VILNIUS UNIVERSITY
CENTER FOR PHYSICAL SCIENCES AND TECHNOLOGY

Ieva
ŽIČKIENĖ

Investigation of semiconductor nanostructures using terahertz and optical pulses

DOCTORAL DISSERTATION

Natural Sciences
Physics N002

VILNIUS 2019

This dissertation was written between 2015 and 2019 in the Center for Physical Sciences and Technology. The research was supported by Research Council of Lithuania:
Grants – P-DAK-18-149, DOK-1703;
Mobility funding – P-DAK-18-237;
Projects – MIP-054/2014.

Academic supervisor:
dr. Ramūnas Adomavičius (Center for Physical Sciences and Technology, Natural Sciences, Physics – N 002).

This doctoral dissertation will be defended in a public meeting of the Dissertation Defence Panel:
Chairman – prof. habil dr. Žilvinas A. Kancleris (Center for Physical Sciences and Technology, Natural Sciences, Physics – N 002).
Members:
doc. dr. Ramūnas Aleksiejūnas (Vilnius University, Natural Sciences, Physics – N 002);
doc. dr. Vytautas Karpus (Center for Physical Sciences and Technology, Natural Sciences, Physics – N 002);
prof. dr. Arkady Major (University of Manitoba, Canada, Natural Sciences, Physics – N 002);
dr. Evaldas Stankevičius (Center for Physical Sciences and Technology, Natural Sciences, Physics – N 002).

The dissertation shall be defended at a public meeting of the Dissertation Defence Panel at 2 p. m. on 14th November 2019 in room A101 of the Center for Physical Sciences and Technology.

Address: Saulėtekio av. 3, A101, Vilnius, Lithuania. Tel. +37052648884; e-mail: office@ftmc.lt.

The text of this dissertation can be accessed at the libraries of Center for Physical Sciences and Technology and Vilnius University, as well as on the website of Vilnius University: www.vu.lt/lt/naujienos/ivykiu-kalendorius

VILNIUS UNIVERSITETAS
FIZINIŲ IR TECHNOLOGIJOS MOKSLŲ CENTRAS

Ieva
ŽIČKIENĖ

Puslaidininkinių nanodarinių tyrimai terahercinės spinduliuotės ir optiniais impulsais

DAKTARO DISERTACIJA

Gamtos mokslai
Fizika N002

VILNIUS 2019

Disertacija rengta 2015–2019 metais Fizinių ir Technologijos mokslų centre. Mokslinius tyrimus rėmė Lietuvos mokslo taryba:
Stipendija – P-DAK-18-149, DOK-17033;
Parama išvykoms – P-DAK-18-237;
Projektai – MIP-054/2014.

Mokslinis vadovas:
dr. Ramūnas Adomavičius (Fizinių ir technologijos mokslų centras, gamtos mokslai, fizika – N 002).

Gynimo taryba:
Pirmininkas – prof. habil dr. Žilvinas A. Kancleris (Fizinių ir technologijos mokslų centras, gamtos mokslai, fizika N 002).
Nariai:
doc. dr. Ramūnas Aleksiejūnas (Vilniaus universitetas, gamtos mokslai, fizika N 002);
doc. dr. Vytautas Karpus (Fizinių ir technologijos mokslų centras, gamtos mokslai, fizika N 002);
prof. dr. Arkady Major (Manitobos universitetas, Kanada, gamtos mokslai, fizika N 002);
dr. Evaldas Stankevičius (Fizinių ir technologijos mokslų centras, gamtos mokslai, fizika N 002).

Disertacija ginama viešame Gynimo tarybos posėdyje 2019 m. lapkričio mėn. 14 d. 14 val. Fiznių ir technologijos mokslų centro A101 auditorijoje. Adresas: Saulėtekio av. 3, Vilnius, tel. +37052648884; el. paštas: office@ftmc.lt .

Disertaciją galima peržiūrėti Fizinių ir technologijos mokslų centro bei VU bibliotekose ir VU interneto svetainėje adresu:
https://www.vu.lt/naujienos/ivykiu-kalendorius.

Padėka

Doktorantūros studijų metais įvairiomis aplinkybėmis teko bendrauti daugeliu žmonių, kurie vienaip ar kitaip prisidėjo prie galutinio šios disertacijos varianto. Norėčiau jiems visiems nuoširdžiai padėkoti.

Mama ir tėti, ačiū kad gražiai mane užauginote ir visada labai palaikėte. Taip už sugaudytus artikelius ir pagerintą sakinių struktūra.
Edmundai, ačiū už rūpestį, domėjimąsi mano darbais, kitokį požiūrio kampą, kūrybiškumą ir visokeriopą pagalbą.

Ramūnai, ačiū už neišsenkančią kantrybę, perduotą patirtį, pagilintas fizikos žinias, vertingus patarimus bei pastebėjimus tiek atliekant tyrimus, tiek rašant šį darbą.

Renata, ačiū už galimybę iš arčiau susipažinti su MBE ir savo rankomis išbandyti nanovielelių auginimo metodiką. Taip pat už optimizmo ir geros nuotaikos užtaisą.
Arūnai, ačiū už visada vertingus patarimus ir naujas idėjas.
Gintarai, ačiū už suteiktas galimybes dalyvauti puikiose konferencijose.
Evelina, ačiū už meilę mokslui, visas bendras konferencijas, pokalbius prie kavos ir pietų metu apie fiziką ir ne tik.
Sandra, ačiū už puikią atmosferą kabinete, galvosūkius ir pasidalinimą patirtimi.
Vaidai, Ignai, Ričardai, Andriau, Andrejau, Andžejau, Daniele, Tadai, Martynai ir visi kiti nepaminėti Optoelektronikos skyriaus kolegos, ačiū už vienokią ar kitokią pagalbą visų doktorantūros studijų metu.

Brangūs draugai, mieli šokėjai ir pažįstami, ačiū kad pagelbėjote, palaikėte, patarėte, pamokėte ar padėjote pailsėti nuo mokslinio darbo, kad vėl galėčiau kibti į jį su naujomis jėgomis.

Abbreviation	Meaning
THz	Terahertz, 10^{12} Hz
THz pulse	(In this work) $\sim$ 1 ps duration electromagnetic pulses that spectral components reache few THz
THz spectroscopy	Spectroscopy in terahertz region
TDS	Time Domain Spectroscopy
OR	Optical Rectification
EFIOR	Electric Field Induced Optical Rectification
FEL	Free Electron Laser
QCL	Quantum Cascade Laser
LT–GaAs	Low Temperature growth gallium arsenide
SI GaAs	Semi-Insulating gallium arsenide
MBE	Molecular Beam Epitaxy
MOCVD	Metalorganic Chemical Vapor Deposition
RNA	Ribonucleic Acid
DNA	Deoxyribonucleic Acid
SHG	Second Harmonic Generation
SFG	Sum Frequency Generation
DFG	Difference Frequency Generation
EO	Electro-Optic
MISFET	Metal-Insulator-Semiconductor Field Effect Transistor
MESFET	MEtal-Semiconductor-Field Effect Transistor
MSM	Metal-Semiconductor-Metal
NS GaAs	Non-Stoichiometric GaAs
NWs	Nanowires
SEM	Scanning Electron Microscope
TEM	Transmission Electron Microscope
AFM	Atomic Force Microscope
LIPSS	Laser Induced Periodic Surface Structures
HSFL	High Spacial Frequency LIPSS
LSFL	Low Spacial Frequency LIPSS
SPP	Surface Plasmon Polariton
VLS	Vapour-Liquid-Solid method for the nanowires growth

SLS	Solution-Liquid-Solid method for the nanowires growth
FET	Field Effect Transistor
PNA	Peptide Nucleic Acid
IR	Infra-red region

Phrase	Meaning
Optical table plane	It is a plane parallel to the incidence optical (excitation) beam, reflected optical beam and generated THz beam. For most experiments, THz detector's knobs lay in this plane as well.
Detection plane	In this work, it is a plane in THz detector where the semiconductor interface and metallic detector's knobs meet.
(n times) Stronger THz pulse	In this work, it means that THz pulse peak-to-valley amplitude is n times higher than that of the reference signal.
THz emitting electric dipole	This phrase is more a tribute to the tradition rather than accurate term. For instance, R. Inouce [1] used term *electric dipole moment*, while M. B. Johnson call it *THz dipole* [2]. Of course, it would be more accurate to speak about a vector of the derivative of the photocurrent or a vector of the second derivative of the dipole moment. However, due to the simplicity the term *THz emitting electric dipole* was chosen.

Table of Contents

1 Introduction **11**

1.1 Major Goal . . . 12
1.2 Tasks of this Work . . . 12
1.3 Scientific Novelty . . . 13
1.4 Statements of Defence . . . 13
1.5 Contribution of the Author . . . 14
1.6 Publications . . . 14

2 Time Domain Terahertz Spectroscopy – an Overview **18**

2.1 THz region: brief history and applications . . . 18
2.2 THz emission from semiconductor surfaces . . . 21
2.2.1 Surface electric field . . . 25
2.2.2 Photo-Dember effect . . . 26
2.2.3 Non-linear optical effects . . . 28
2.2.3.1 Optical rectification . . . 29
2.2.3.2 Electric field-induced optical rectification 31
2.2.4 Anizotropic photocurrent . . . 32
2.3 THz emission from semiconductor nanostuctures . . . 33

3 THz emission methods used for investigation **37**

3.1 Main principles of THz TDS . . . 37
3.2 Standard THz emission spectroscopy methods . . . 40
3.2.1 THz excitation spectroscopy . . . 40
3.2.2 Azimuthal dependencies . . . 41
3.3 Double-pump-pulse THz emission method . . . 42
3.4 Methods to determine THz emitting electric dipole orientation . . . 46
3.4.1 Method I . . . 48
3.4.2 Method II . . . 51
3.5 Setups for investigation . . . 54

4 Non-stoichiometric GaAs **55**

4.1 Production of the non-stoichiometric GaAs . . . 55
4.2 Applications of non-stoichiometric GaAs . . . 57

4.3 Investigation of Non-stoichiometric GaAs 59
4.3.1 Samples 59
4.3.2 THz pulse emission from non-stoichiometric GaAs samples 60
4.3.3 Investigation of NS GaAs sample with hill like structure – Ga4 61
4.3.4 Investigation of NS GaAs sample with grooves like structure – Ga15 63
4.3.5 Promising material for surface based THz emitters 64
4.3.6 Conclusions 66

5 LIPSS **67**
5.1 Formation of LIPSS 67
5.2 Applications of LIPSS 69
5.3 Investigation of LIPSS 72
5.3.1 Samples 72
5.3.2 First series. THz pulse amplitudes and azimuthal dependencies 73
5.3.3 Second series. THz emission azimuthal dependencies 77
5.3.4 Orientation of THz emitting electric dipole 78
5.3.5 DPP measurements 79
5.3.6 Discussion on the origin of THz emission 80
5.3.7 Conclusions 82

6 Nanowires **84**
6.1 Growth of the nanowires 84
6.2 Applications of nanowires 88
6.3 Investigation of InAs and composition-tunable InGaAs nanowires 91
6.3.1 Samples 91
6.3.2 THz emission from InAs NWs 92
6.3.3 THz emission from InGaAs NWs 95
6.3.4 THz excitation spectra of InGaAs NWs 97
6.3.5 Conclusions 99
6.4 Investigation of tilted to the surface GaAs nanowires . . . 99

6.4.1 Samples 100
6.4.2 THz emission from nanowires 100
6.4.3 THz emission dependence on an excitation angle 102
6.4.4 THz emission azimuthal dependencies 103
6.4.5 Discussion on THz emission from GaAs NWs . . 105
6.4.6 Conclusions 108

7 Main Results and Conclusions **109**

8 Santrauka **111**
8.1 Įvadas 111
8.2 Literatūros apžvalga 113
8.3 Tyrimo metodikos 114
8.4 Tyrimas 115
8.5 Pagrindiniai rezultatai ir išvados 138

References **140**

9 Publications **159**

Notes **197**

1. Introduction

In recent years terahertz time domain spectroscopy (THz-TDS) finds its application in various fields. It could be used in security systems for drugs and explosives detection [3] in medicine as a non-invasive way for cancer diagnostic [4], in the food industry for quality control [5], in the art for heritage restoration [6], and etc. Moreover, THz spectroscopy is a good tool to investigate semiconductors and their structures: it could be used to determine electron mobility, relaxation time, semiconductor bandgap, intervalley separation [7], and etc. For all these applications an effective, compact, easy to use and cheap THz emitter is needed.

Nowadays, there exist various types of THz sources such as quantum cascade lasers [8], diodes [9], field effect transistors [10], non-linear crystals [11], photoconductive antennas [12] and similar. However, most of them are expensive, requires specific operational conditions such as low temperature or external bias, others are bulky and hard to position. An alternative could be the bare semiconductor surfaces illuminated by ultrashort optical pulses. Such THz emitters have some advantages over other THz sources. First of all, they are small, compact and easily manageable. Second, they could be activated in a wide wavelength range of optical pulses. And third, such emitters does not need external bias which makes them cheaper and more durable. However, semiconductor surfaces are not such effective THz emitters as, for instance, photoconductive antennas. On the other hand, recently it has been reported that semiconductor nanostructures in comparison with their bulk counterparts are able to enhance THz emission from optically excited surfaces for a few times. An enhancement was observed in InN nanorods [13], Si nanoneedles [14], InP porous

membrane [15] and nanowires made from wide variety of semiconductors, such as Si [16], Ge [17], InGaAs [18], GaAs [19] and InAs [20]. Despite the promising results, the THz generation mechanism, as well as the origin of THz emission enhancement in semiconductor nanostructures, is still unknown. Thus, in order to create better THz emitters, these things must be revealed. Therefore, the main goal of this dissertation is to enlarge the existing knowledge and stimulate further works regarding the semiconductor nanostructures.

1.1 Major Goal

To find out the cause of an enhancement of laser pulse induced THz pulse emission from nanostructured semiconductor surfaces.

1.2 Tasks of this Work

- To develop a complex measurement methodology suitable for the investigation of THz pulse emission from semiconductor structures.
- To investigate the THz pulse emission from non-stoichiometric GaAs and laser induced periodic surface structures (LIPSS) on GaAs substrate dependence on different optical excitation conditions. To determine the influence of GaAs surface nanostructurization on THz emission efficiency.
- To investigate the THz pulse emission properties of the perpendicular to the substrate surface InGaAs nanowires. To find out the dependence of THz radiation generation efficiency on the composition of nanowire.
- To investigate the THz pulse emission properties of the tilted GaAs nanowires. To explain the reasons behind effective THz pulse emission from these nanowires.

1.3 Scientific Novelty

- A novel method to determine the orientation of a THz pulse emitting electric dipole in respect to the substrate surface has been developed. It was found that the orientation of this dipole changes after the nanostructurization of semiconductor surface.

- It was found out that the entirety of laser-excited nanowires emit THz pulses as a thin layer with a particular refractive index n_0. Since n_0 is smaller than the refractive index of the substrate, the direction of THz generation becomes more favourable in respect to the THz emitting dipole axis which results in enhanced THz pulse emission.

- The THz pulse emission from non-stoichiometric GaAs and LIPSS on GaAs was investigated for the first time. A modification of non-stoichiometric GaAs, which efficiently emits THz pulses even though the excitation beam falls perpendicular to the semiconductor surface, has been found.

1.4 Statements of Defence

- The enhancement of THz emission from non-stoichiometric GaAs and LIPSS can be explained by the experimentally observed formation of parallel to the surface component of THz emitting electric dipole after photoexcitation and the surface electric field enhancement after nanostructurization.

- InGaAs nanowires, that consist of a similar amount of Ga and In atoms, emits THz radiation most effectively. Weaker THz emission from low Ga-concentration nanowires is related mainly to the electrons scattering by the surface defects.

- By regarding GaAs nanowires as a thin layer with a refractive index n_0, it is possible to describe the THz emission properties of GaAs nanowires quite accurately. According to this model, better THz generation direction in respect to the electric dipole axis is

the main reason of THz emission enhancement in semiconductor nanowires.

1.5 Contribution of the Author

All experimental set-ups were assembled and all measurements were performed by the author of this dissertation. Moreover, author took part in the experimental data analysis and preparation of scientific publications. Additionally, author presented the results in conferences either in oral or in poster sessions. All non-original work is referenced.

1.6 Publications

The main results of the dissertation were published in 5 scientific publications and 17 conference reports. All publications and conference reports were prepared under author's maiden name (Beleckaitė).

Scientific publications

P1 A. Arlauskas, J. Treu, K. Saller, **I. Beleckaitė**, G. Koblmüller and A. Krotkus. Strong terahertz emission and its origin from catalyst-free InAs nanowire arrays. *Nano Letters*, **14**(3), pp 1508–1514, 2014. DOI: 10.1021/nl404737r

P2 **I. Beleckaitė**, R. Adomavičius, R. Butkutė, V. Pačebutas, G. Molis, V. Bukauskas, A. Selskis and A. Krotkus. Non-stoichiometric GaAs – prospective material for compact THz emitters. *Electronics Letters*, **54**(23), pp 1954-1956, 2016. DOI: 10.1049/el.2016.2517

P3 **I. Beleckaitė**, J. Treu, S. Morkötter, M. Döblinger, X. Xu, R. Adomavičius, J. J. Finley, G. Koblmüller, and A. Krotkus. Enhanced THz emission efficiency of composition-tunable InGaAs nanowire arrays. *Applied Physics Letters*, **110**(20), p. 201106, 2017. DOI: http://dx.doi.org/10.1063/1.//4983641

P4 **I. Beleckaitė**, L. Burakauskas and R. Adomavičius. Study of surface electric field and photocarrier dynamics in InAs by means of a modified double-pump-pulse terahertz emission method. *Lithuanian Journal of Physics*, **58**(1), pp 116–125, 2018. DOI: 10.3952/physics.v58i1.3657

P5 **I. Beleckaitė** and R. Adomavičius. Determination of the terahertz pulse emitting dipole orientation by terahertz emission measurements. *Journal of Applied Physics*, **125**(22), p. 225706, 2019. DOI: 10.1063/1.5096952

Conference Reports

1. **I. Beleckaitė**, A. Šiušys, R. Adomavičius, A. Reszka, A. Krotkus and J. Sadowski. *Teraherz pulse emission from InGaAs and GaMnAs nanowires*. 44th „Jaszowiec" International School and Conference on the Physics of Semiconductors, Wisla, Poland, June 20–25, 2015 (Poster presentation)

2. **I. Beleckaitė**, G. Molis, R. Adomavičius, A. Šiušys, A. Reszka, A. Krotkus and J. Sadowski. *Terahertz emission from non-vertically aligned semiconductor nanowires*. 40th International Conference on Infrared, Millimeter, and Terahertz Waves, Hong Kong, China, August 23–28, 2015 (Poster presentation)

3. **I. Beleckaitė**, R. Adomavičius, A. Arlauskas, R. Butkutė, V. Pačebutas, A. Selskis, V. Bukauskas and A. Krotkus. *Terahertz emission from non-stoichiometric Ga-rich GaAs layer*. 59th Scientific Conference for Students of Physics and Natural Sciences "Open Readings 2016", Vilnius, Lithuania, March 18–25, 2016 (Oral presentation) **Award for the best oral presentation in the field of semiconductor physics.**

4. **I. Beleckaitė**, R. Adomavičius, R. Butkutė, V. Pačebutas, A. Arlauskas, A. Šiušys, A. Reszka, J. Sadowski, A. Krotkus. *Terahertz emission from semiconductor nanowires and non-stoichiometric layers: similarities and differences*. 45th "Jaszowiec" International School and Conference on the Physics of Semiconductors, Szczyrk, Poland, June 18 – 24, 2016 (Oral presentation)

5. **I. Beleckaitė**, R. Adomavičius, R. Butkutė, V. Pačebutas, V. Bukauskas and A. Krotkus. *Characterization of THz surface emitter based on non-stoichiometric Ga-rich GaAs layer*. 18th International Conference-School Advanced Marerials and Technologies, Palanga, Lithuania, August 27–31, 2016 (Poster presentation)

6. **I. Beleckaitė**, R. Adomavičius, G. Molis, A. Šiušys, A. Reszka, T. Wojciechowski, J. Sadowski and A. Krotkus. *Characterization of non-vertically aligned semiconductor nanowires by THz emission measurements*. 41st International Conference on Infrared, Milimetr and Terahertz Waves IRMMW-THz 2016, Copenhagen, Denmark, September 24–30, 2016 (Poster presentation)

7. **I. Beleckaitė**, R. Adomavičius, R. Butkutė, V. Pačebutas, V. Bukauskas, A. Selskis ir A. Krotkus. *Terahercinės spinduliuotės emisija iš puslaidininkinių nanovielelių ir nestechiometrinių GaAs sluoksnių.* 6th Scientific Conference for PhD students an young researches FizTeCh 2016, Vilnius, Lithuania, October 26–27, 2016 (Oral presentation)

8. **I. Beleckaitė**, R. Adomavičius. *Determination of terahertz radiating electric dipole orientation by terahertz emission measurements*. 60th Scientific Conference for Students of Physics and Natural Sciences "Open Readings 2017", Vilnius, Lithuania, March 14–17, 2017 (Oral presentation)

9. **I. Beleckaitė**, R. Adomavičius, A. Krotkus, M. Gedvilas, M. Gaidys and G. Račiukaitis. *Laser induced periodic surface structures on the GaAs surface investigated by THz emission measurements*. 19th International Conference-School Advanced Marerials and Technologies, Palanga, Lithuania, August 27–31, 2017 (Poster presentation)

10. **I. Beleckaitė** and R. Adomavičius. *Terahercinius impulsus spinduliuojančio dipolio orientacijos puslaidininkyje nustatymas laikinės terahercų spektroskopijos metodais*. 42-oji Lietuvos Nacionalinė Fizikos konferencija, Vilnius, Lithuania, September 4–6, 2017 (Poster presentation)

11. **I. Beleckaitė**, R. Adomavičius, A. Krotkus, M. Gedvilas, M. Gaidys ir G. Račiukaitis. *Lazeriu graviruotų periodinių paviršinių struktūrų ant GaAs padėklų tyrimas THz impulsų emisijos metodais* 7th Scientific Conference for PhD students and young researches FizTeCh 2017, Vilnius, Lithuania, October 24–25, 2017 (Oral presentation) **Award for the best oral presentation.**

12. **I. Beleckaitė**, R. Adomavičius, A. Krotkus, M. Gedvilas, M. Gaidys ir G. Račiukaitis. *Terahertz emission enhancement by forming LIPSS structures on the surface of GaAs*. Advanced Properties and Processes in Optoelectronic Materials and Systems APROPOS 2018, Vilnius, Lithuania, October 10–12, 2018 (Oral presentation)

13. **I. Beleckaitė**. *THz spektroskopijos metodai THz emiterių bei detektorių charakterizavimui.* 7th conference for young scientists "Physical and technological science interdisciplinary investigations", Vilnius, Lithuania, February 9, 2017 (Oral presentation)

14. **I. Beleckaitė**, L. Burakauskas and R. Adomavičius. *Investigation of a p-type InAs using a novel modified double-pump-pulse terahertz emission method*. 61st Scientific Conference for Students of Physics and Natural Sciences "Open Readings 2018", Vilnius, Lithuania, March 20–23, 2018 (Oral presentation)

15. **I. Beleckaitė**, L. Burakauskas and R. Adomavičius. *Investigation of semiconductors using modified double-pump-pulse terahertz emission method*. International Conference on the Physics of Semiconductors ICPS2018, Montpellier, France, July 29th – August 3rd, 2018 (Oral presentation)

16. **I. Beleckaitė**, L. Burakauskas and R. Adomavičius. *Double-pump-pulse terahertz emission method as a novel tool to investigate ultrafast processes in semiconductors*. 43rd International Conference on Infrared, Milimetr and Terahertz Waves IRMMW-THz 2018, Nagoya, Japan, September 9–14, 2018 (Poster presentation)

17. **I. Beleckaitė**, L. Burakauskas, R. Adomavičius. *Ultrasparčių procesų tyrimai puslaidininkiuose dvigubo žadinimo terahercinės emisijos metodu*. 8th Scientific Conference for PhD students and young researches FizTeCh 2018, Vilnius, Lithuania, October 17–18, 2018 (Oral presentation) **Award for the best oral presentation.**

2. Time Domain Terahertz Spectroscopy – an Overview

This chapter offers a brief introduction to THz region and applications of THz spectroscopy. A lot of attention will be drawn to the most important mechanisms of THz generation in semiconductors, such as photo-Dember effect, surface electric field driven photocurrent, non-linear optical effects (OR and EFIOR) and anisotropic photocurrent effect. At the end of this chapter an overview of THz pulse emission from various semiconductor nanostructures will be given.

2.1 THz region: brief history and applications

The terahertz (THz) region is electromagnetic spectrum range typically defined as a range from 0.1 THz up to 10 THz [21]. 1 THz $= 10^{12}$ Hz – it is a frequency, that corresponds to a single vibration within a picosecond, a wavelength of 0.3 mm and photon quantum energy of 4.1 eV. It is obvious, that THz region lies between microwaves and infrared range (Fig. 2.1).

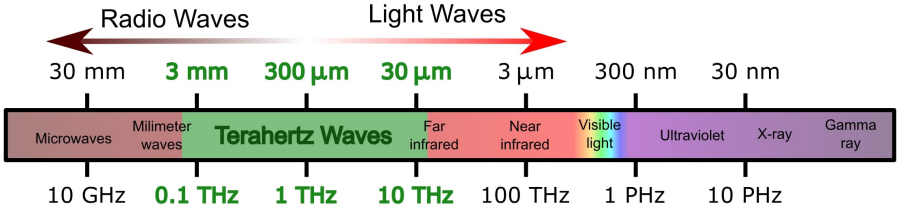

$$1THz \rightarrow 1ps \rightarrow 300\mu m \rightarrow 33cm^{-1} \rightarrow 4.1meV \rightarrow 48K$$

Figure 2.1: Electromagnetic spectrum and THz range.

The oldest artificial source of THz radiation is far infrared gas laser. This is an optically driven gas laser system, where a CO_2 laser is used to excite rotational molecular levels, usually methanol gases. Such a laser can operate in

a range from 0.3 to 5 THz. Unfortunately, in recent years, this technology is no longer being improved, even though such lasers are still used in spectroscopy and plasma diagnostics. THz frequency radiation can also be obtained using several high-frequency diodes such as Gunn diode, IMPATT and TUNNET diodes. They work in an area from 0.2 to 1 THz [9]. In 2003, in Novosibirsk (Russia), was demonstrated the first stage of high power free electron laser (FEL), based on an accelerator–recuperator and an energy recovery line. Such a laser, in a full scale, operates in a range from 1.2 μm to 0.24 mm [10]. However, FEL requires strong electric and magnetic fields, it also needs high electron density, because a large number of electrons recombine due to a metal shell. All last-mentioned features greatly complicate the practical application of such a device. The rapid development of semiconductor nanotechnologies has opened up an opportunity for the production of terahertz electronics. In 2002, the first quantum cascade laser (QCL) with the photon energy corresponding to 4.4 THz was demonstrated [8]. The main disadvantage of such lasers is that most of them operate only at low temperatures (several tens of kelvins). However, they find excellent application in some THz spectroscopy systems and as a high power THz sources in THz imaging systems. [22]

During the last decade of the 20th century, the fast development of laser and semiconductor technologies evoked a strong interest in an electrical pulses travelling through transmission lines. The pioneers of this research field were Dan Grischkowsky (IBM Watson Research Center), Martin Nuss (Bell Laboratories) and David H. Auston (Columbia University, Department of Physics) [23]. In 1984, David H. Auston for the first time suggested an idea, that the optical pulse could not only trigger a photoconductor, but it could also generate a photocurrent in a dipole antenna that would cause the emission of electromagnetic pulse. Later in the same year, Auston with colleagues introduced the first prototype of time domain spectroscopy system that was capable of generating and recording very short electromagnetic pulses emitted in the free space [24]. Several years later, in 1989, it was announced about the first far infrared electromagnetic pulses propagating from the emitter to the detector in the free space [25]. It was also pointed out that by placing the sample between such elements, the transmission spectra of the sample could be measured. After a few more years, it was shown that the semiconductor surface illuminated with an ultrashort optical pulse emits electromagnetic pulse in a THz range [26,27]. From then, many scientific groups focused on searching for the best semiconductor materials for THz emitters and THz detectors. For a long time, the best material was believed to be the silicon layers on the sapphire substrate. However, in 1990, all of the best devices at that time were surpassed by the THz system with photoconductive components made of GaAs layers grown at a

low temperature (LT) by molecular beam epitaxy (MBE) [28]. LT GaAs is still one of the most widely used materials, although the high potential is shown by the GaBiAs [29] and InGaAs [30] layers.

Based on THz time domain spectroscopy (TDS) achievements in recent years, THz visualization systems have been developed. They allow visualizing the objects that are hidden behind plastic, wooden, cardboard or paper shield [31]. THz spectroscopy imaging systems are well suited for detecting explosives [32] and illicit drugs [3, 33], as well as weapons containing low-metal concentration or made of ceramics [34], as all these materials have a characteristic spectrum in the THz range. There has been noticed, that healthy and cancer damaged tissues could be clearly distinguished in the THz range [4]. Thus, THz visualization systems are a great tool for a medical diagnostics of cancer cells, as THz radiation does not disrupt tissues and is non-ionizing. So, THz imagining is a much safer way than biopsy or X-ray tomography. Another area of application in medicine is the measurement of medicaments ageing. Medicaments, that are too old to use, change their crystalline structure and these changes are clearly reflected in the THz spectrum [35]. Since the water molecules have strong resonant lines in the THz range, product visualization in THz spectrum can show internal and external damage to the fruit or vegetables, as a higher concentration of water is found in the areas affected by rotating. It is also possible to detect poison, narcotic or some other dangerous inclusions in food [5, 36]. After the birth of spectroscopy systems working in THz frequencies, it was noticed that many important biological components such as proteins, polysaccharides, ribonucleic acid (RNA) and deoxyribonucleic acid (DNA) have resonant frequencies in the THz range. Thus, these molecules can be studied by means of THz spectroscopy. This method enables the observation of vibrational and rotational levels of organic and some inorganic molecules [37]. Additionally, THz spectroscopy also could be applied to investigate semiconductors [7], thin metal layers [38], polar gases and their mixtures [39], some polymeric materials and organic electro-optical crystals [40].

Another advantage of THz-TDS systems is very precise and fast sample thickness measurements. Such a capability could be very useful for producing equipment that requires strictly control of scratches or bumps. Moreover, THz imaging could be used in plastic industry for quality control, especially to supervise the quality of the weld joints of a plastic part, which can be considerably weakened by inclusions, voids or delaminations [41]. Speaking about a more exotic application, THz spectroscopy can be used in art restoration. THz imaging of the painting could not only expose the image hidden behind the front layer of paint, but it also could reveal the composition of the original

dye [6, 42]. In recent years, THz spectroscopy finds its path towards communication technologies. There appear first attempts to create high quality and fast wireless information transmission lines working in THz range [43, 44].

2.2 THz emission from semiconductor surfaces

Since the beginning of THz spectroscopy, at the end of the 20th century, a lot of effort was put to the investigation and development of THz sources. Some of them (such as QCL, various diodes, FEL) were already mentioned in a previous chapter. However, during the years of investigation, many more THz sources were successfully applied in spectroscopy systems. One of the most popular THz emitters is photoconductive antenna – a semiconductor layer on which two metallic contacts with a gap in between are formed. Such a device is activated by ultrashort optical pulse and requires external bias for operation [12]. Another popular type of THz emitters is various crystals with high nonlinear dielectric sensitivity [11]. Speaking about unbiased THz emitters, bare semiconductor surfaces illumination by femtosecond laser pulse should be mentioned [45]. Finally, it is worth to point out, that in recent years, there were presented some extraordinary THz pulse sources such as air-plasma [46] or even liquid water film [47]. However, as this work is concentrated on the investigation of nanostructures formed from semiconductor materials, in the later chapters the main focus would be drawn on the THz generation mechanisms in semiconductor surfaces.

But before moving to the detailed descriptions of THz generation mechanisms, a reminder on why accelerated charged particles emit electromagnetic radiation would be given. In general, the explanation should be based on of Maxwell's equations, but J. J. Thomson offers a more intuitive approach to the problem, thus the later discussion will be based on his model [48]. Let us start with the charged carrier in a stationary position. Such carrier has an electric field around it (Fig. 2.2a) and this field could be described by Coulomb's law:

$$E_r = \frac{1}{4\pi\varepsilon_0} \cdot \frac{q}{r^2} \tag{2.1}$$

where E_r is a radial component of the electric field, q is the charge of a carrier, r is the radial distance from the carrier and ε_0 is permittivity of free space. If the carrier is moving at a constant velocity it produces a constant magnetic field and no electromagnetic radiation is emitted. In order to radiate electromagnetic wave, a carrier needs to accelerate. It is important to remember, that acceleration can be achieved either by changing the carrier's velocity (electrons moving in an electric field) or its moving direction (electrons vibration in a lat-

tice). Both types of velocity changes will produce electromagnetic radiation.

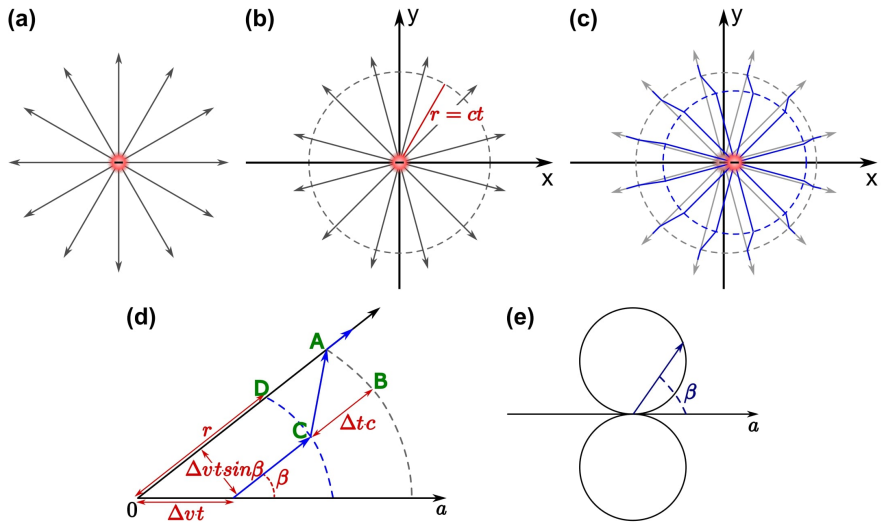

Figure 2.2: Illustration of J.J. Thomson's model of evaluating the radiation of an accelerated charged particle. (a) A stationary electron is surrounded by a radial electric field. (b) At time $t = 0$ the electron is at the origin of the coordinate system. We consider a sphere which is at a distance $r(= ct)$ away from the centre. (c) The diagram shows schematically the configuration of electric field lines (blue) at time t due to a charge accelerated to a velocity v in time Δt. The primary situation is shown in grey. (d) Illustration of elements necessary to evaluate the strength of the azimuthal component E_β of the electric field due to the acceleration of the electron. (e) The polar diagram of the emitted electric field E_β as a function of polar angle β with a respect to the instantaneous acceleration vector a. Adapted from [48].

Now, consider a charged carrier at the origin (O) of a coordinate system at a time $t = 0$. We will focus on the electric field inside and outside the sphere of a radius $r = ct$ and centred at the origin of a coordinate system (Fig. 2.2b). Let us consider, that this charged carrier is accelerated in a time Δt along the x axis to a velocity Δv. We also assume that $\Delta v \ll c$ so that relativistic effects could be excluded. At a time t, carrier has moved a distance Δvt to right along the x axis. The sphere of interest is very large compared to the distance moved by the electron, thus electric field lines outside the sphere do not yet notice that the charge has moved from the original position because information cannot travel faster than the speed of light. So, electric field lines outside the sphere are still centred at O. On the contrary, inside the sphere closer the carrier, the electric field lines are centred on the moving charge (Fig. 2.2c). It is obvious, that there exist a transition region (so called a thin shell of a thickness Δtc) were the new field lines (blue) connect with the old field lines (grey). The

direction of the electric field in the shell is from point A to point C (Fig. 2.2d) It is clear, that AC could be divided into two electric field components: radial E_r and tangential E_β. The radial one was described earlier so let us focus on the tangential one.

The tangential component of electric field could be found using a pure geometrical approach. From the Fig. 2.2d it is obvious that the ratio between E_β and E_r could be written as follows:

$$\frac{E_\beta}{E_r} = \frac{\Delta v t \sin\beta}{\Delta t c} \tag{2.2}$$

The radial component was described in eq. 2.1 so we can write:

$$E_\beta = \frac{q}{4\pi\varepsilon_0}\frac{\Delta v}{\Delta t}\sin\beta\frac{t}{rrc} \tag{2.3}$$

$\Delta v/\Delta t$ is the acceleration $|\vec{a}|$ of the charge carrier, and $r = ct$, hence

$$E_\beta = \frac{q|\vec{a}|\sin\beta}{4\pi\varepsilon_0 rc^2} \tag{2.4}$$

So, this equation describes the pulse of electromagnetic radiation which is produced by an accelerating charge carrier. At this point, it is important to outline some features of such radiation:

- It depends on the acceleration $\vec{a}$ of the charged particle: the larger the acceleration the stronger the electromagnetic pulse.
- The polar diagram of the radiation has a dipolar form: the electric field strength varies as $\sin\beta$, where β is the angle with respect to the acceleration vector of the particle (Fig. 2.2e). It is important to notice that there is no radiation along the acceleration vector and the strongest radiation is in the direction perpendicular to the acceleration vector.
- The radiation is polarised: the electric field vector, in a far field, is lying in the direction of the acceleration vector of the particle.

One more thing that is worth the discussion is the distribution of electromagnetic radiation from a group of charged particles instead of a single carrier. In general, these distributions could be totally different. Let us come back to the THz radiation. Semiconductor surface is usually illuminated by the optical beam that diameter is much bigger than the wavelength of THz radiation. Then in the every spot of illuminated area THz emitters that radiates electromagnetic radiation in every direction emerge (like shown in Fig. 2.2e). From the first view, it might look like the total THz emission should propagate in

every direction as well, however, due to destructive interference THz radiation propagates mostly in two specific directions.

Usually, optical beam impinges the sample at some non-zero angle α_i, thus the wave-front of the radiation reaches the surface points at different times – point a is reached earlier than point b (Fig. 2.3). For constructive interference at the wave-front ef the optical paths cae and dbf must be equal. If this condition is not be satisfied, the destructive interference takes place and THz radiation would not propagate in this direction or its intensity would be strongly reduced.

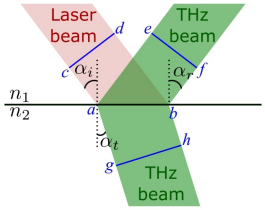

Figure 2.3: THz radiation propagation direction after sample excitation with an optical beam, which diameter is much larger than THz radiation wavelength.

The paths cae and dbf will be equal only when:

$$n_{1,opt} \sin \alpha_i = n_{1,THz} \sin \alpha_r \tag{2.5}$$

here α_i is an angle of incidence for optical radiation, α_r – an angle of reflection for THz radiation, $n_{1,opt}$ and $n_{1,THz}$ indexes of refraction in the first medium for optical and THz radiation respectively. If the first medium is air (as it often is) $n_{1,opt} \approx n_{1,THz} \approx 1$, then $\alpha_i = \alpha_r$ – THz radiation propagates in the same direction as reflected optical light.

The same algorithm could be applied for the THz pulses propagating in transmission direction. Here the optical paths cag and dbh must be equal. It is so, when

$$n_{1,opt} \sin \alpha_i = n_{2,THz} \sin \alpha_t \tag{2.6}$$

where α_t is an angle of refraction for THz radiation and $n_{2,THz}$ is the indexes of refraction for THz radiation in a second medium. It is worth to mention that in the second medium $n_{1,opt}$ might not be equal to $n_{1,THz}$, and propagation directions for optical and THz radiation might differ.

Now, let us speak about the situation, when an optical beam is tightly focused and excitation spot diameter is comparable or even smaller than THz radiation wavelength. In this case, the difference in optical paths cae and dbf (or cag and dbh) would be too small compared with THz radiation wavelength

and destructive interference would be noneffective, thus THz radiation propagates in every direction. Of course, THz radiation would be stronger in the reflection direction (defined by α_r).

To sum up, semiconductor illumination with an optical pulse generates photocarriers. These carriers are moving deeper into semiconductor creating an electric current. As the velocity of photocarriers is not a constant, they generate an electromagnetic pulse. If the alternation of photo induced electric current (motion of photocarriers) is ultra-fast and lasts for a few picoseconds, the emitted pulse is in the THz frequency range. The generated THz radiation follows the direction of reflected and refracted optical light. Moreover, the directionality of THz radiation depends on the optical beam diameter: the smaller the diameter, the bigger THz radiation spread angle.

The main mechanisms (surface electric field, photo-Dember effect, nonlinear effects and anisotropic photocurrent) that cause ultra-fast electron motion after photoexcitation will be discussed in the following chapters.

2.2.1 Surface electric field

On the surface of each semiconductor crystal always exist some allowed electronic states in the forbidden energy band gap. The origin of these surface states could vary, yet most common cause is a termination of a periodic structure of a crystal lattice. In other words, there are no covalent bonds created at the surface so there emerge dangling bonds. It is worth to mention, that surface states exist only close to the semiconductor surface (in a range of a few lattice constants). These states has no equivalent in the band structures of the bulk crystal and are particularly independent of bulk doping level. Depending on the material, surface states could be described using Shockley [49] (suitable for metals and narrow gap semiconductors) or Tamm [50] (suitable for transitional metals and wide gap semiconductors) formalism. However, there is no real physical distinction between these two descriptions, only the mathematical approach in describing surface states is different. Historically, the Shockley states arises as solutions of Schrödinger equation in a framework of the nearly free electron approximation, while the Tamm states are calculated in the framework of a tight-binding model.

Surface states could be donors or acceptors, depending on which carriers (electrons or holes) they did catch near the semiconductor surface. By capturing charged carriers surface states become charged itself, thus the potential near the semiconductor surface differs from the bulk potential and semiconductor's valence and conduction bands bend (Fig. 2.4) resulting in the appearance of a surface electric field [51].

When semiconductor with such states is illuminated with femtosecond

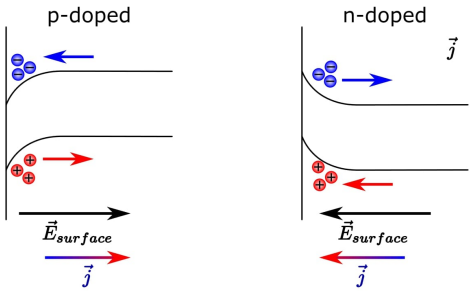

Figure 2.4: Band bending at the surface due to surface states, and photocarrier moving directions after photoexcitation.

optical pulse, which photon energy exceeds semiconductor bandgap, created photocarriers are accelerated by a surface electric field. Separated electrons and holes result in THz pulse emitting electric dipole, which orientation is essential for THz emission efficiency (as will be shown in later chapters). As the field is perpendicular to the surface, it enhances photocarriers motion (photocurrent) in the same axis. The rise time of this photocurrent is in the order of a laser pulse duration. After that, photocurrent decreases and reaches zero after free carriers transits across the depletion layer.

The surface electric field depends on the doping type, the electron bands could bend up or down, thus the direction of surface electric field could be against the surface or towards it. Thus, the phase of THz pulse generated from p-type and n-type semiconductors differs by 180 degrees [52]. According to that, THz pulse emission measurement from p- and n-doped semiconductors is one of the best ways to determine, that THz generation in this particular semiconductor is driven by the surface electric field. It must be mentioned, that this THz generation mechanism is dominant when photocarriers are excited close to the conduction band and their excess energy is quite small. For instance, if Ti:Sapphire laser (central wavelength $\sim$ 800 nm) is used for excitation, surface electric field caused THz emission dominates in GaAs [52], InP [53] and etc. When the excess energy of photocarriers becomes larger, the photo-Dember effect takes place.

2.2.2 Photo-Dember effect

Semiconductor surface illumination with ultrashort optical pulse creates electron and hole pairs in the illuminated area. Due to the concentration gradient photocarriers diffuse from this area into its surroundings. As the electrons have much larger mobility, they move deeper into the semiconductor than much slower holes (electron mobility in InAs and InSb is about 100 times

larger than holes mobility [54,55]). The negative net charge moves ahead of positive (Fig. 2.5a), that causes a photocurrent flow near the surface, which results in THz pulse emission. Later, the photo-Dember electric field between fast electrons and slow holes becomes so strong, that holes, which are much heavier than electrons, forces the electrons to slow down. Finally, photocurrent flow stops, as there forms a neutral particle – electron and hole dipole. [56,57]

As it is obvious from Fig. 2.5a photocarriers move in all directions after photoexcitation and, in general, there form photo-Dember dipoles (THz emitting electric dipoles) in all directions as well. For the simplicity, let us assume that there occur perpendicular to the surface electric dipole (black arrow in Fig.2.5b) and two parallel to the surface dipoles (grey arrow in Fig.2.5b) near semiconductor surface. In standard semiconductor photocarriers motion in every direction is even, thus both parallel dipoles are the same strength, just of an opposite sigh. These two dipoles compensate each other's contribution in total THz radiation due to the destructive interference. Generally speaking, every dipole that is non-perpendicular to the surface has a symmetrical one, thus they compensate each other. That lefts only one uncompensated dipole – perpendicular to the surface. However, this dipole orientation is not favourable, as the majority of its generated radiation propagates in the direction parallel to the surface.

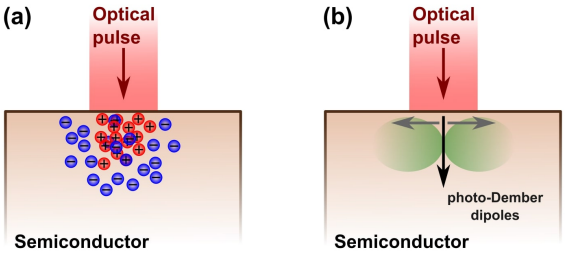

Figure 2.5: Schematic illustration of the photo-Dember effect. (a) The distribution of photocarriers. (b) The orientation of photo-Dember dipoles. As parallel to the surface (grey) dipoles are the same strength but opposite in sign, they compensate each other's contribution in total THz radiation and only perpendicular to the surface (black) dipole remains relevant.

The best THz emitting dipole orientation is parallel to the surface. This could be achieved due to a lateral photo-Dember, by creating a photocarrier gradient parallel to the surface [58]. For this purpose, on the semiconductor surface are formed metallic stripes, that partially covers optical beam (Fig. 2.6a). The stripe is thicker along one side than the other. Such stripe creates strong lateral concentration gradient near the thicker side, as it is opaque for optical radiation, and much weaker gradient on the thinner side, where only

some optical photons can transmit trough the thin metal film. The stronger concentration gradient results in stronger electric dipole (black line in Fig. 2.6a), which dominates its opposite competitor (grey line in Fig. 2.6a).

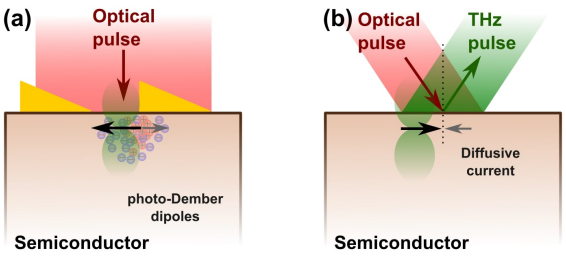

Figure 2.6: (a) Schematic illustration of THz emitter based on lateral photo-Dember effect. (b) Illustration of uncompensated diffusive photocurrent due to off-normal axis photoexcitation. As the parallel to the surface (black and grey) dipoles differ in strength, they no longer compensate each other's contribution, and total THz radiation comes from dominant parallel dipole (black).

Speaking about the lateral photo-Dember effect, it is worth to mention work by Mueckstein *el al* [59]. Here authors investigated THz emission in the near field from GaAs and Fe-doped InGaAs and explained results by the appearance of the uncompensated diffusive photocurrent due to off-normal axis photoexcitation as illustrated in Fig. 2.6b. In this case, the optical beam impinges the sample at non-zero incidence angle ($\sim 50°$) which means, that the right side of the beam reaches surface earlier than the left side. Immediately, when the photocarriers are excited at the right side of the beam they move in the direction parallel to the surface due to the strong concentration gradient (black arrow in the Fig 2.6b). As the front of the optical beam travels trough the illumination area it creates photocarriers along its path faster than these carriers can diffuse, thus concentration gradient towards the centre of the beam is reduced. In result, that diffusion photocurrent, which occurs on the left side of the optical beam is much weaker (grey arrow in the Fig 2.6b) than that on the right side. So, according to the authors, THz emission arises from the photocarriers motion indicated by the black arrow (Fig. 2.6b).

Photo-Dember effect is considered to be the main THz generation mechanism in InAs [56], InSb [60] and other materials owing to high electron mobility. However, some THz emission features could not be explained in terms of either surface electric field, nor photo-Dember effect.

2.2.3 Non-linear optical effects

THz pulses arising from the surface electric field and photo-Dember effects do not depend on crystallographic orientation of the sample, as the linear di-

electric properties of cubic crystals are isotropic. However, it was noticed that THz pulse amplitude depends on the optical polarization of excitation beam in respect to the crystallographic axis in InAs [61], GaAs [62], GaTe [63] and etc. Further investigation of these dependencies allows scientists to develop a novel approach to the origin of THz generation based on non-linear optical effects, such as optical rectification (OR) and electric field-induced optical rectification (EFIOR), which would be discussed further.

Let us begin with the reminder on a material interaction with an incident light. During the interaction, the material re-emits electromagnetic radiation of the same frequency when the optical excitation fluencies are low. However, when the electric field strength of the electromagnetic wave becomes comparable to the inter-atomic electric fields, atoms in the lattice begin to fluctuate not only at the frequency of the falling electromagnetic wave, but also at the other frequencies. As a result, the frequency of the transmitted light changes. In general, the frequencies that occur after the wave interaction with the material can be various (THz range included) depending on the material properties and electromagnetic wave characteristics.

Generally, the polarization density of a material is a non-linear function of an electric field ($\vec{E}$) and could be expressed as [64]:

$$\begin{aligned}\vec{P}(t) &= \varepsilon_0(\chi^{(1)}\vec{E}(t) + \chi^{(2)}\vec{E}^2(t) + \chi^{(3)}\vec{E}^3(t) + ...) \\ &= \vec{P}^{(1)}(t) + \vec{P}^{(2)}(t) + \vec{P}^{(3)}(t) + ... \\ &= \varepsilon_0\chi^{(1)}\vec{E}(t) + \vec{P}_{NL}(t)\end{aligned} \tag{2.7}$$

where $\chi^{(1)}$, $\chi^{(2)}$ and $\chi^{(3)}$ are the first-, second- and third-order electric susceptibility tensors, respectively, ε_0 – dielectric permittivity, $\vec{P}_{NL}(t)$ – non-linear polarization. Electric susceptibility tensors depend on many factors, such as crystal symmetry, its orientation, doping concentration, temperature and etc. For anyone's interest, actually measured higher order susceptibilities for many materials could be found in [65].

2.2.3.1 Optical rectification

For the simplicity, let's start with the material that has only the second order non-linearity. Thus

$$\vec{P}_{NL}(t) = \varepsilon_0\chi^{(2)}\vec{E}^2(t) \tag{2.8}$$

Consider the case where optical excitation fluency is high and the electromagnetic radiation travelling through this material consist of two distinct fre-

quency components, which are represented in the form:

$$\vec{E}(t) = E_1(e^{-i\omega_1 t} + e^{i\omega_1 t}) + E_2(e^{-i\omega_2 t} + e^{i\omega_2 t}) \tag{2.9}$$

Then non-linear polarization could be obtained by combining eq. 2.9 and eq. 2.8:

$$\begin{aligned} \vec{P}_{NL}(t) = \varepsilon_0 \chi^{(2)} [& E_1^2(e^{-i2\omega_1 t} + e^{i2\omega_1 t}) + && \text{(SHG)} \\ & E_2^2(e^{-i2\omega_2 t} + e^{i2\omega_2 t}) + && \text{(SHG)} \\ & 2E_1E_2(e^{-i(\omega_1+\omega_2)t} + e^{i(\omega_1+\omega_2)t}) + && \text{(SFG)} \\ & 2E_1E_2(e^{-i(\omega_1-\omega_2)t} + e^{i(\omega_1-\omega_2)t}) + && \text{(DFG)} \\ & 2(E_1^2 + E_2^2)] && \text{(OR)} \end{aligned} \tag{2.10}$$

Thus, two frequency components of an excitation electromagnetic waves give rise to second-harmonic generation (SHG) at frequencies $2\omega_1$ and $2\omega_2$, sum-frequency generation (SFG) $\omega_1 + \omega_2$, difference-frequency generation (DFG) $\omega_1 - \omega_2$, and the frequency independent electric field – the optical rectification (OR).

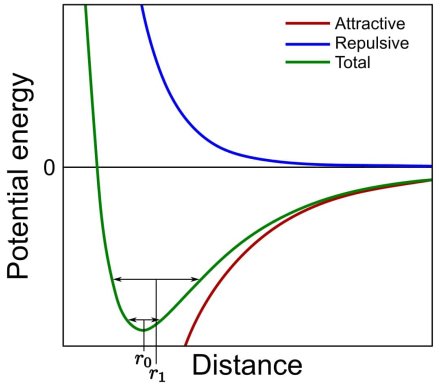

Figure 2.7: The typical energy potential of interatomic forces dependence on a distance between two atoms. r_0 indicates low intensities, where the potential is approximately parabolic, while r_1 indicates higher intensities, where the potential is non-parabolic.

In order to better understand OR effect, let's analyse an electron potential energy dependence on a distance between two atoms (Fig. 2.7). Electron potential energy has two components related to attractive and repulsive forces. Repulsive potential energy stronger depends on a distance between atoms than attractive energy, thus total potential energy curve has an asymmetrical shape. After sample illumination, electromagnetic wave vector affects electrons in the crystals lattice by forcing them to oscillate around their balance position r_0. While the electric field vector is small, electrons move the same distance in both

directions, thus the average distance remains the same – r_0. On the contrary, with increasing electric field vector, oscillations become asymmetric (motion distance in one direction is larger than in the other), thus the average distance increase (r_1). In a result, atom gains a constant dipole moment (constant polarization), which increases together with the illumination light intensity. If the sample is excited with an optical pulse, the crystal lattice constant polarization follows the intensity of the optical pulse, thus it becomes time-dependent and generates its own pulse of electromagnetic radiation. If optical pulse duration corresponds to the period of THz frequency, the newly generated electromagnetic pulse will be in THz range.

On the other hand, the difference-frequency generation (DFG) could also cause THz pulse emission. The sample is excited with a short optical pulse, that has many spectral components. Thus in non-linear medium DFG occurs between every possible pair of spectral components which might result in many various frequencies belonging to THz range. It should be pointed out that THz pulses caused by DFG have the same characteristics as THz pulses arising from OR effect.

OR effect was reported for the first time in 1962 by Bass *et al.* [66]. There was observed an appearance of constant voltage caused by DC polarization when the laser beam travels through the crystal. OR effect as THz generation mechanism was first discussed in the work of Zhang *et al.* in 1992 [62]. Here it was used to explain azimuthal dependencies (sample is rotated around the normal to the surface) observed in (111) crystallography orientation bulk GaAs. In later years, THz emission from such crystals as GaP, ZnTe, $LiNbO_3$ was also assigned to OR effect [67].

2.2.3.2 Electric field-induced optical rectification

In the previous chapter, for the simplicity of calculation only second-order bulk electric susceptibility was included into account. However, more general approach would be to use, so called, effective second-order susceptibility [68]:

$$\chi_{ijk}^{(2)eff} = \chi_{ijk}^{(2)bulk} + 3\chi_{ijk_z}^{(3)} E_z^{surf} \tag{2.11}$$

where $\chi_{ijk}^{(2)bulk}$ is a second-order susceptibility tensor determined by the symmetry properties of the bulk material, while $\chi_{ijk_z}^{(3)}$ is the third-order susceptibility tensor that specifies the symmetry properties of radiation from the near-surface region which is under the influence of a surface electric field E_z^{surf}. It should be pointed out, that in the crystals with inversion symmetry second-order susceptibility tensor equal to zero ($\chi_{ijk}^{(2)bulk} = 0$) and $\chi_{ijk_z}^{(3)}$ becomes particularly significant.

Now, one can repeat the calculations done for OR effect. The only difference is that non-linearity now depends on the surface electric field, that justifies the name given to this mechanism – electric field induced optical rectification. EFIOR, as a possible THz generation mechanism, was first presented in a work by Chuang *et al* in 1992 [69]. This method clearly explains THz emission from Ge crystals [70]. However, in many cases both methods, OR and EFIOR, must be considered [71].

2.2.4 Anizotropic photocurrent

Last but not least THz generation mechanism is anisotropic photocurrent model suggested by V.L. Malevich [72, 73]. This model is based on an idea, that anisotropic photocurrent originates from the optical alignment of photoexcited electron momenta. The optical momentum alignment effect in semiconductors results from the selection rules for interband electron transitions. When the semiconductor is illuminated by the linearly polarized light, which quantum energy exceeds its energy bandgap, created photocarriers exhibit an anisotropic momentum distribution due to optical alignment. In cubic semiconductor, such as InAs or InSb the momenta of electrons excited from heavy holes lie mainly in the plane perpendicular to the optical polarization vector (blue arrows in Fig. 2.8a), while the momenta of electrons excited from light holes lie in the plane parallel to the optical polarization vector (green arrows in Fig. 2.8a). Due to the much larger density of states, there are excited 3 times more electrons from heavy holes than from light holes, thus electrons from heavy holes play the key role.

For stationary excitation, optical alignment is usually observed only at cryogenic temperatures, due to a short carrier momenta relaxation time. However, in semiconductor excited with femtosecond optical pulse, THz emitting photocurrent achieves its peak value in a time scale comparable to the carrier momenta relaxation time. Thus, optical alignment becomes significant and could cause the anisotropy of photocurrent.

Consider semiconductor that has a surface electric field. When such a material is excited with the polarized optical pulse, electrons momenta are distributed as shown in Fig. 2.8a. Then electrons having momenta aligned in the same direction as surface electric field will be slowed down and lose their energy, while the electrons moving in the opposite direction will be accelerated and their energy will grow. Due to nonparabolicity of the electron conduction band, the effective masses of these two groups of electrons becomes different, thus electron motion in one direction becomes dominant and there occurs uncompensated photocurrent, which may result in THz pulse emission. If the sample is excited at the non-zero incidence angle the uncompensated pho-

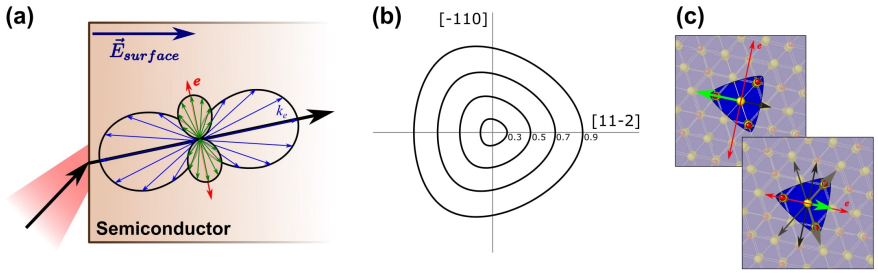

Figure 2.8: (a) Optical alignment of the momenta of electrons excited from the heavy hole subband by the linearly polarized light beam impinging on the semiconductor surface at non-zero incidence angle. e is the optical polarization vector, $k_e$is the electron wave vector; blue arrows represent electron excited from heavy holes, green – from light holes. (b) Cross-sections of the conduction band iso-energetic surfaces in InSb. Numbers near iso-energetic surfaces denote electron excess energy in electronvolts. Adapted from [74]. (c) Illustration of uncompensated electron motion in semiconductor under excitation of p- and s-polarized light.

tocurrent has two components: perpendicular to the surface and parallel to the surface.

It is worth to mention that uncompensated photocurrent could occur even when there is no surface electric field. Consider that electrons are excited very high in the conduction band, where the band is non-spheric and nonparabolic (Fig. 2.8b). Then electrons moving in one direction and in the opposite direction will have different effective mass and different mobility, which leads to uncompensated photocarriers motion in one specific direction. Parallel to the surface component of such motion will depend on the azimuthal angle (the angle between one of crystallographic axis and optical polarization vector) as it is illustrated in Fig. 2.8c.

Anisotropic photocurrent effect was described in details including a theoretical explanation in papers [72] and [73]. It was experimentally observed and analysed in InAs [75] and InSb [74].

2.3 THz emission from semiconductor nanostuctures

The best-known surface-based THz pulse emitter to date is p-type InAs [76, 77]. However, this material might have a competitor – the semiconductor nanostructures. It was noticed that nanostructurization of the semiconductor surface leads to the enhanced THz radiation, which could be a few

times stronger in comparison with a bulk semiconductor. For example, the THz pulse emitted from InN nanorods arrays was reported to have three times higher peak amplitude than that from InN film [13]. This enhancement was found to be closely related to the surface-to-volume ratio, which is much higher for nanorods than for InN film. In a result, the authors stated, that increased effective surface area results in a stronger absorption of excitation light, which might lead to the enhanced THz emission. Another example might be black silicon – needle like nanostructures on silicon surface obtained via reactive ion etching. It was shown that these structures effectively emit THz pulses, while bulk Si does not emit THz radiation at all. Hoyer *et al.* [14] explained THz emission from black silicon by the absorption of the whole optical pulse power at the very surface of nanostructures. On the other hand, Blumroder *et al.* [78] contradicted to this idea and suggested that effective THz emission is related to the increased number of carriers created along the silicon needle, where the THz radiation outcoupling is more effective than from bulk material. However, in all these nanostructures THz generation was explained due to the photo-Dember effect. In contrast, to explain THz generation in InP porous membrane was proved to be more difficult. Nevertheless, it was shown that THz radiation emission from such a membrane exceeds that of bulk InP by almost two orders of magnitude in power. Reid *et al.* [15] considered the observed increase to be related to the enhancement of the local electric field in the porous network, as well as to the modification of the flow direction of transient photocurrent which results in the THz emitting electric dipole.

Despite the wide variety of potential semiconductor nanostructures for THz pulse generation, semiconductor NWs are the most popular material under investigation for today. In 2010, Jung *et al.* [16] reported on THz emission from vertically aligned Si NWs synthesized via Ag nanoparticles assisted chemical etching. They also noticed that effective THz emission is related to the more efficient THz radiation outcoupling from NWs, as well as to the enhanced optical light absorption in the NW layer. Authors of [16] also investigate THz emission dependence on the length of the NWs: the intensity increases up to the length of 3 μm and then saturates. The maximum intensity is related to the overall absorption of the excitation light by the NWs. As all light power is absorbed in the NWs of the length of 3 μm, the longer NWs could not absorb more power, thus, there could not be created more photocarriers that could move along the NW and THz emission saturates. The origin of THz generation was explained to be the surface electric field and photo Dember effect. Tingzon *et al.* compared THz emission from vertically and non-vertically aligned Si NWs, and reported enhancement in non-vertical NWs due to the more favourable orientation of THz emitting electric dipole [79]. Yim *et al.*

compared THz emission from aligned and less-aligned InGaAs NWs. They reported THz emission from aligned NWs to be much stronger and more polarized. Yim *et al.* also stated that electron diffusion along the NW is the dominant THz radiation mechanism [18]. In 2013, the first observation of enhanced THz emission from Ge NWs was reported. The observed enhancement was attributed to an extensive surface area where more photons could be collected via multiple paths [17]. The interesting result were obtained investigating GaAs-InGaAs core-shell NWs. Authors reported THz emission of a wider spectrum from core-shell NWs compared to just the GaAs core. The broader bandwidth was related to the shorter carrier lifetimes in AlGaAs shell than in GaAs core. THz radiation is generated by the photocarriers moving along the NW and the THz pulse is emitted during the stage of ballistic carrier transport. In this picture, carriers moving at higher velocity contribute to higher-frequency THz emission, while slower carriers correspond to lower THz frequencies. As photocarriers have a short lifetime in AlGaAs shell, they are expected to generate higher-frequency THz emission. On the contrary, photocarriers with a longer lifetime in GaAs core are expected to slow down and generate lower-frequency THz emission [80].

The major effort to explain the THz generation mechanism and THz radiation enhancement in NWs was put by Seletskiy *et al.* [20]. They demonstrated THz radiation power efficiency from InAs NWs to be 15 times higher than from n-type InAs substrate, taking into account that the fill factor of NWs is equal to 0.03. The origin of the THz generation was attributed to the cold plasma that occurs in the NW layer. While the THz emission enhancement in NW structures is related to the much better THz radiation outcoupling from the NW layer based on the model of emission cone [56]. The authors of [20] calculated that THz radiation outcoupling from bulk InAs takes place in a narrow emission cone with an apex angle of $\sim 15°$. The THz rays that impinge the semiconductor-air interface at the greater angles suffer the total reflection and are trapped in the semiconductor. A THz emitting electric dipole is oriented perpendicular to the sample surface in bulk InAs. Such dipole does not radiate in the direction along its axis, thus the radiation pattern is oriented parallel to the surface and only a very small portion of the total THz radiation falls in an emission cone. Such a problem does not occur in case of NWs, thus the outcoupling in these structures is more effective. At this point, it is worth to mention that this explanation is valid only if the THz radiation is generated from the point source. However, in the most experiments laser beam is focused to relatively wide spot (few millimetres), thus every point of illuminated area acts as THz pulse emitter and the propagation direction of THz radiation is mainly determined by the constructive interference.

Another attempt to understand the origin of THz generation in NWs was made by Trukhin *et al.* [19]. They had investigated p-doped and undoped GaAs NWs grown by VLS method using Au and Ga nanodroplets as catalysts. After the NW growth, the catalyst cap remains on top of the NW and creates Schottky (in case of Au) contact, which determines the formation of contact electric field. After optical excitation, optically created electron and holes are forced to move in this field, resulting in a drift current. Due to the photocarriers concentration gradient in the NW, the diffusion current occurs as well. As the direction of the contact field depends on the type of doping of the NWs, the drift and diffusion currents might flow in one direction, enhancing THz generation, or in opposites, reducing THz generation in comparison with self-catalysed NWs. In the latter case, there forms an ohmic contact between Ga cap and NW, thus no contact electric field occurs. The best THz emission was observed in undoped GaAs NWs with Au catalyst, where both currents are oriented in the same direction. Even though such a model explains enhanced THz emission for some types of NWs, it is not suitable for catalyst-free NWs. However, it was shown that GaAs NWs, grown by selective-area epitaxy, generates THz radiation more effectively than p-type InAs [81]. The results were explained in terms of Mie resonances: the electromagnetic field amplification due to the resonance excitation of the leaky modes in NWs arrays. The most efficient THz emission was achieved when the distance between the NWs was of the order of the excitation light wavelength.

To sum up, despite the unquestionable THz emission enhancement observed in various semiconductor nanostructures and few attempts to understand its origin and THz generation mechanism in such structures, there are still left many questions related to the THz pulse emission from nanostructured surfaces. For instance, many authors agree that THz generation in semiconductor NWs is caused by the photocarriers moving along the NW [19,80], however, the origin of such a motion is still not known. One of the most convincing explanation was that photocarriers are moving in the Schottky electric field originating at the semiconductor/metallic catalyst interface [19]. However, such a mechanism does not explain strong THz pulse emission from catalyst-free NWs [82] or black Si [14]. The other idea, that THz generation is caused by photo-Dember effect [78] still does not have enough proof and is under discussion. The main drawback of this idea is that due to the small diameter of semiconductor NWs, excitation light goes through the all NWs layer resulting in similar photocarriers concentration along the whole nanoneedle. The following part of this work is dedicated to enlarge the existing knowledge and stimulate further discussions and investigations regarding the semiconductor nanostructures.

3. THz emission methods used for investigation

The main mission of this chapter is to introduce the reader to the THz emission spectroscopy and to give a detail discussion on the THz emission techniques that were developed during the years of the dissertation as well as on the standard THz spectroscopy methods. Firstly, the main principles of THz time domain spectroscopy will be presented. Secondly, a short introduction to some standard THz emission methods will be given. Thirdly, the methods to determine the orientation of THz emitting electric dipole will be described in details. Finally, the information of the lasers and THz detectors used for the investigation will be given.

3.1 Main principles of THz TDS

THz generation mechanisms were discussed in the previous chapters. The main focus was on surface based THz emitters where THz generation was driven by a surface electric field, photo-Dember effect, non-linear effects or anisotropic photocurrent. Suchlike THz source usually generates single-cycle THz pulse lasting about 1 ps. The position of THz spectra maximum depends on the emitter characteristics, and the spectral range is quite wide, from 0.2 THz up to a few THz. These pulses could be detected coherently (by sampling THz pulse amplitude at various time delays with photoconductive antennas or electro-optic crystals) or incoherently (by registering THz pulse power with Golay cell, Schottky diode or etc.). Even though, the last-mentioned method is faster, the coherent detection has some significant advantages: it contains information not only about the THz pulse amplitude but it also keeps the phase; moreover it offers broad dynamic range. These two components allow to find out about the complex refractive index of the sample as well as the dielectric permittivity and conductivity. One of the most popular coherent THz detection methods is THz time domain spectroscopy (THz-TDS), which, together

with some modifications, would be further discussed in this chapter.

THz-TDS system consists of the following components: a femtosecond laser, mechanical delay line, THz pulse emitter (a sample in our case) and THz detector (Fig 3.1). A femtosecond laser beam is split into two branches. One of them goes through a delay line, which then illuminates the sample, that emits a few-picosecond-long THz pulse. Emitted THz pulse is directed towards the detector (for this purpose there could be used some parabolic mirrors if necessary). The other optical branch activates the THz detector, which is often made of a short carrier lifetime (< 1 ps) semiconducting material having a bandgap lower than the exciting laser photon energy. Optical pulse creates photocarriers, which are forced to move by the electric field of THz pulse, that results in a photocurrent, which could be registered by a lock-in amplifier. It is important that the optical path travelled by both branches would be equal at the detection plane, as here would be the delay line position of the THz pulse maximum. By moving the delay line the whole THz pulse could be sampled.

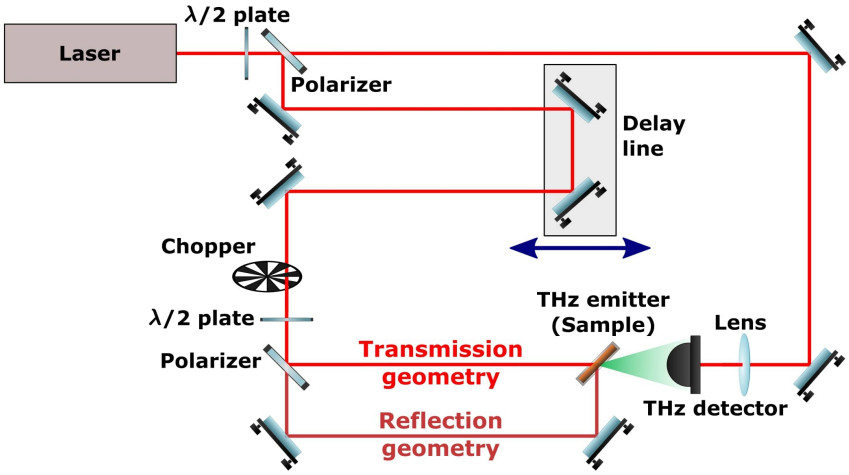

Figure 3.1: A typical THz emission time domain spectroscopy system setup.

The most important part of the THz-TDS system, despite THz emitter, is THz detector. For coherent detection, there could be used electro-optic (EO) sampling or photoconductive antennas. The THz detector based on the photoconductive antenna is usually made of the epitaxial layer of semiconductor, which has the following properties: a high dark resistivity, high electron mobility, short carrier lifetime (desirable $<$ 1ps) and the bandgap lower than the photon energy of an excitation pulse. Nowadays, the most popular THz-TDS systems are based on the mode-locked Ti:Sapphire lasers that emit femtosecond optical pulses at a central wavelength around 800 nm. Thus the most popular material for THz detectors fabrication is low temperature (LT) GaAs

[28, 83]. Nevertheless, expensive and bulky Ti:Sapphire lasers in a short time might be defeated by the more compact and cost-effective solid state or fiber lasers. Yet lasers are operating in the spectral ranges of around 1–1.5 μm, thus new materials for THz detectors must be found. Although it should be pointed out that there were reports on LT GaAs based THz detectors operating with activation of 1.55 μm femtosecond laser pulses due to the two-step photoabsorption mediated by midgap states in LT GaAs [84]. Another candidate for THz detectors is GaBiAs [29], which is still rising material with very promising characteristics.

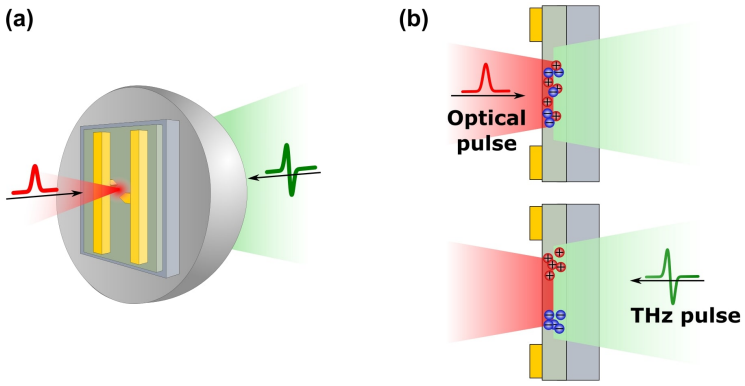

Figure 3.2: THz pulse detection with a photoconductive antenna. (a) 3D illustration of the detector. (b) Schematic THz pulse detection.

As it was mentioned photoconductive antenna is fabricated of the epitaxial layer of semiconductor. On top of this layer, there are formed two metallic ohmic contacts, usually in a shape of letter H – two parallel micro-strips that have knobs in the middle, by means of electron beam lithography. There exist many different variations of the contacts, such as bow-tie [85], plasmonic nano-antennas [86] and etc., but the main focus will be put on the H-type antennas as they were used for all experiments described here. On the other side of the semiconductor, there is placed a hemispherical silicon lens, that focuses the incoming THz radiation. The illustration of an antenna-based THz detector could be found in Fig. 3.2a. Such a detector is activated by the femtosecond optical pulse, illuminating the gap between the metallic contacts, which creates the electron-hole pairs in the semiconductor layer (Fig. 3.2b upper image). Then THz pulse arrives from the other side and is focused by the silicon lens to the same gap between the metallic contacts. The photocarriers are forced to move by the electric field of THz pulse, resulting in photocurrent between the contacts, which is then detected by the lock-in amplifier (Fig. 3.2b lower image) [87]. At this point, it is worth to mention that detection with lock-in

amplifier requires periodical signal modulation and for this purpose, the mechanical chopper is placed in the path of one of the optical branches (Fig. 3.1). Moreover, it should be noted that these detectors are polarization-sensitive, which means that they detect only THz polarization (THz electric field) that is parallel to the metallic knobs.

Speaking about the other type of THz detectors, EO detectors, there is used an electro-optic effect, in other words, the operation of the THz detector is based on the ellipsoid of the index of refraction dependence on the applied electric field. For THz pulse registration both optical and THz pulses are required. First, the THz pulse electric field initiates the changes in EO crystal index of refraction ellipsoid. Then, the polarized optical pulse is transmitted through the EO crystal and its polarization is changed. These changes later are detected by the polarization analyser. By shifting optical pulse in time with a respect to the THz pulse, the whole THz signal is sampled. For today, the most popular EO crystals are ZnTe, $LiTaO_3$, $LiNbO_3$ [88] ar GaP [89]. Despite the high signal to noise ratio and wide spectral range, EO sampling is more difficult to implement than photoconductive antennas.

3.2 Standard THz emission spectroscopy methods

After illuminating the semiconductor surface with an ultrashort optical pulse, it generates a THz pulse that could be detected in reflection or transmission geometry. From such measurements, a lot of information about the sample could be obtained. Nevertheless, simple THz emission measurement could not reveal all the interesting features of the sample. Thus, there were created some variations of THz emission measurements: there could be added external magnetic field to change the movement direction of photocarriers; measurements could be done varying excitation wavelength and optical fluence; during the experiment the sample could be rotated around the azimuthal or spacial angle; two excitation pulses could be used instead of one. Each method would reveal some new features of the material under investigation. In the following chapters, most of these THz emission spectroscopy variations would be discussed in details.

3.2.1 THz excitation spectroscopy

THz excitation spectroscopy was first mentioned in 2005 [90]. Measurement results – THz pulse amplitude dependence on an excitation wavelength. Usually, at each wavelength the whole THz pulse is measured. Then, the peak-to-valley THz pulse amplitude is extracted from the measurement. Finally, all obtained amplitudes should be normalized to the same number of photons. In

order to keep the normalization process reliable THz pulses must be measured in the linear regime (the correlation between THz pulse amplitude and optical power of the excitation beam must be linear).

THz excitation spectroscopy reveals a lot of information about the electronic structure of the material. First of all, THz emission usually occurs only when electrons are excited up to the conduction band, thus the energy band gap value could be obtained from the measurement. The front of the excitation spectra helps to make a decision on the origin of THz generation: sharp growth of the signal suggests surface electric field while permanent rise offers photo-Dember effect to be responsible for THz emission. The excitation spectra could also reveal information about the intervalley separation in the conduction band. The terahertz pulse amplitude usually increases with the increasing laser photon energy due to larger excess energies of photoexcited electrons. This increase stops with the onset of electron transitions to subsidiary conduction band valleys, thus the stop position indicates the energies of the subsidiary conduction band valleys [7]. In resent years, it was shown that THz excitation spectroscopy method is also a useful tool to determine the heterojunction band off-sets [91].

3.2.2 Azimuthal dependencies

One of THz emission spectroscopy variations is THz emission azimuthal dependencies. During the measurement the sample is rotated around the normal to the sample surface (Fig. 3.3). And at each azimuthal angle ϕ THz pulse amplitude is measured. The measurement could be done both in transmission and in reflection geometry.

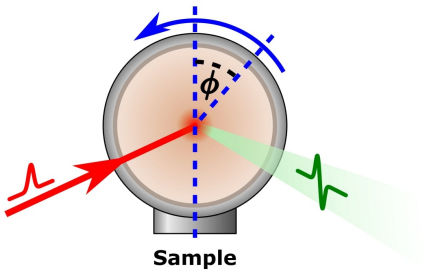

Figure 3.3: The illustration of the THz emission azimuthal dependencies measurement.

Such a method is the primary tool to investigate the origin of THz generation in various semiconductors. It is known that THz generation mechanisms based on non-linear effects (for more information please refer to subsection 2.2.3) exhibit strong azimuthal dependencies. As the non-linear effects

strongly depend on the crystallography of the crystal, azimuthal dependencies differ from each other at various crystallographic orientation. It also depends on the optical and THz light polarization. Nevertheless, such measurement is a good tool to distinguish OR and EFIOR effects. In Table 3.1 the possible THz pulse amplitude azimuthal dependencies for zinc-blende crystals excited with p polarized light is presented.

Certainly, it is worth to mention, that azimuthal dependencies could be observed not only due to THz generation by non-linear effects. In the sample, where exist stationary tilted THz radiating electric dipole, $\sim \sin\phi$ azimuthal dependence is also visible. For instance, such dependencies were detected in non-stoichiometric GaAs samples [92] and tilted nanowires GaAs NWs [93]. Moreover, azimuthal dependence measurements are a very promising tool even to investigate temporally existing tilted electric dipoles or parallel to the surface dipoles that occur only at specific sample orientations.

Table 3.1: THz pulse amplitude dependence on azimuhtal angle when generating from zinc-blende crystals excited with p polarized light. The first row specifies crystal orientations and THz pulse polarization. Constants a and b does not depend on an azimuthal angle. Adapted from [68].

	(100)	(110)	(111)
OR; s THz pol.	$\sim \cos 2\phi$	$\sim a\sin\phi + b\sin 3\phi$	$\sim a + b\sin 3\phi$
OR; p THz pol.	$\sim \sin 2\phi$	$\sim a\cos\phi + b\cos 3\phi$	$\sim \sin 3\phi$
EFIOR; s THz pol.	0	$\sim \sin 2\phi$	$\sim a + b\cos 3\phi$
EFIOR; p THz pol.	$\sim b$	$\sim a + b\cos 2\phi$	$\sim \sin 3\phi$

3.3 Double-pump-pulse THz emission method

Another THz emission spectroscopy variation is so called double-pump-pulse (DPP) THz emission method. The main idea of this method is to use two excitation pulses instead of a usually used one. The first pulse magnifies free carrier concentration, changes the surface electric field strength and might change its orientation as well. The second pulse reaches the sample with a time delay and generates THz radiation that reflects the last-mentioned changes. This method allows monitoring the dynamics of the electric field and photocarrier relaxation in the sample on a picosecond time scale.

Such a method was first mentioned in 2002 by the Tonouchi *et al* [94]. In their article, the investigation of the optoelectronic switch based on low-temperature gallium arsenide (LT-GaAs) was presented. Authors have noted

that THz generation efficiency decreases due to the screening of bias electric field by generated photocarriers, while the recovery of the THz signal was related to the electron relaxation and recombination processes. Two years later Siebert *et al* [95] performed a similar experiment and find out that results should be interpreted in terms of radiation-field-induced screening rather than of space-charge-induced screening. Based on this statement, they pointed carrier trapping as the main channel for DPP signal relaxation. In previously discussed works, the motion of photoexcited carrier as well as THz pulse generation process was driven by the external electric field. As it is known, there are other ways to generate THz pulses. DPP method was proved to be a useful tool to investigate a physical mechanism of THz generation in various semiconductors. For instance, using this method for $CuInSe_2$ layer [90] it was found out that THz emission is caused by the electrons and holes moving in the built-in surfaces electric field rather than photo-Dember effect or optical nonlinearity of the crystal. Moreover investigating $CuInSe_2$ was demonstrated by the first time that excitation of the samples with the first pump pulse could enhance the efficiency THz emission initiated by the second pump pulse [90]. In recent years, the DPP method with sharply focused optical beams was applied for the evaluation of solar cells [96]. The authors have indicated that the DPP signal reflects the lifetime of photocarriers in heavily doped silicon layers, which was difficult to obtain with PL imaging. They also highlighted high spatial and temporal resolution of the DPP method that allows them to visualize the changes in the electric field of the screening effect in the emitter layer.

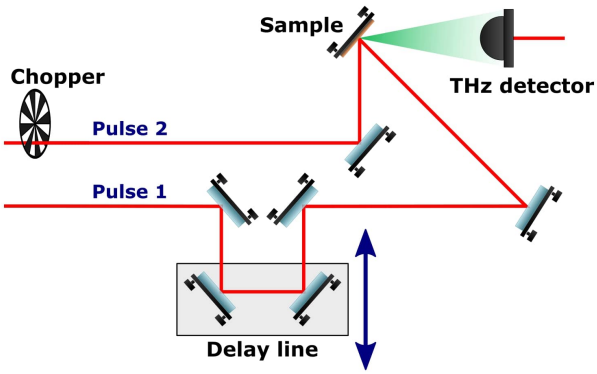

Figure 3.4: The illustration of the experimental set-up for DPP measurement.

The experimental set-up for DPP measurements is shown in Fig. 3.4. Here the first pulse (pulse 1) goes through a delay line so its position in time can be changed and impinges the sample at 0° excitation angle. The second pulse (pulse 2) has a fixed position in time, at a THz pulse peak, is chopped and

usually impinges at 45° excitation angle. It should also be defined, that time is positive when pulse 1 reaches the sample before pulse 2, and time is negative when pulse 2 comes before pulse 1. In general, both pulses generate THz radiation, but as the pulse 1 illuminates the sample at 0° excitation angle, the majority of its generated THz beam is expected to propagate backwards in the same direction and do not reach the detector. However, when working in tight focus condition, due to the strong diffraction of THz radiation some part of this radiation reaches the detector. Luckily, due to the condition of synchronous detection it should be able to measure THz radiation generated only by the pulse 2, as this pulse is chopped. For a long time it was generally assumed that in negative time delays only the THz radiation generated by the pulse 2 is detectable, while the pulse 1 has no noticeable effect. On the contrary, in the positive time delay detected THz pulse could be described by two components: THz radiation generated by the pulse 2 and the difference in THz generation due to the influence of pulse 1. This could be summarised in the following equation:

$$\underbrace{E_2(t)}_{\Delta t<0} \longrightarrow \underbrace{E_2(t)+\Delta E_{1\to 2}(t)}_{\Delta t>0} \tag{3.1}$$

where $E_2(t)$ is the THz pulse generated by the optical pulse 2 (without the pulse 1) and $\Delta E_{1\to 2}$ is the difference, induced by the optical pulse 1, in THz generation by the optical pulse 2. In other words, this term represents how pulse 1 modulates pulse 2. Only in recent years, almost at the same time, it was noticed that the equation 3.1 is correct only at very specific conditions and usually does not match with the real experiment [97,98]. It was found out that a peak in DPP kinetics at time delays close to 0, which was earlier attributed to the in THz emission enhancement, is false and results from large diffraction of THz radiation generated by pulse 1. It was proved that such a peak occurs at negative time delays, and the eq. 3.1 should be modified as follows:

$$\underbrace{E_2(t)+\Delta E_{2\to 1}(t)}_{\Delta t<0} \longrightarrow \underbrace{E_2(t)+\Delta E_{1\to 2}(t)}_{\Delta t>0} \tag{3.2}$$

where $\Delta E_{2\to 1}(t)$ is the difference, induced by the optical pulse 2, in THz generation by the optical pulse 1.

The main goal of the DPP experiment is to measure the $\Delta E_{1\to 2}(t)$. The problem is that existence of $\Delta E_{2\to 1}(t)$ heavily complicates the interpretation of DPP THz emission kinetic curves. To overcome this problem, one must know where the exact zero is and to eliminate $E_2(t)$ from the eq. 3.2 by measuring

THz generation by pulse 2, when pulse 1 is blocked:

$$\underbrace{E_2(t)}_{\Delta t<0} \longrightarrow \underbrace{E_2(t)}_{\Delta t>0} \tag{3.3}$$

and extracting it from the DPP measurement. That way we are left only with the (eq. 3.2 - eq. 3.3):

$$\underbrace{\Delta E_{2\to1}(t)}_{\Delta t<0} \longrightarrow \underbrace{\Delta E_{1\to2}(t)}_{\Delta t>0} \tag{3.4}$$

Then it would be relatively easy to separate two different modes: $\Delta t < 0$, where the pulse of interest is shifting in time, and $\Delta t > 0$, where it has a fixed position. Both modes could be used for DPP measurement and are equally correct. Which mode to use depends only on the will of the researcher. For faster measurements, $\Delta t > 0$ mode might be more suitable as the pulse of interest has a fixed position it time and the direct measurement of the DPP kinetic is possible. On the other hand, working in $\Delta t < 0$ range will take more time, as the whole THz pulse must be measured at each time delay, but it provides more information about the changes initiated by optical excitation. For more information please refer to P4.

DPP method could reveal interesting results even about well-known materials, such as – SI GaAs (Fig. 3.5). It was noticed that very weak excitation with the pulse 1, initiates significant changes in THz generation and even changes the sign of the THz pulse (Fig. 3.5). It is known that in SI GaAs exist strong built-in surface electric field, that is the origin of THz generation. Photocarrier

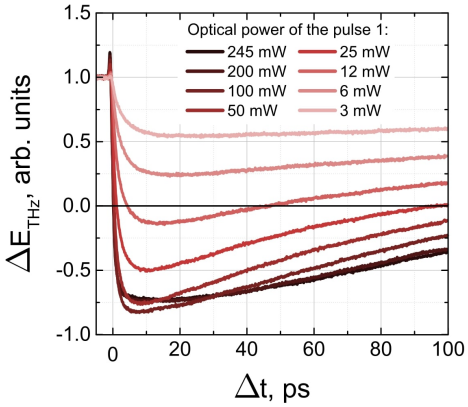

Figure 3.5: DPP measurement of SI GaAs under different optical power of pulse 1. It should be poiten out that small exicitation power (only 12 mW) is enought to change the sign (to overcome the surface electric field) of THz pulse.

created by the optical pulse 1 in the first few moments after the photoexcitation are moving due to the concentration gradient (photo-Dember effect) and creating their own electric field which is of opposite direction to the built-in surface electric field in SI GaAs. This newly created electric field overcomes the built-in field at relatively small excitation power (12 mW) and becomes the main force for the THz generation by the pulse 2. The change in the electric field direction results in the reversed sign THz pulse.

From the Fig. 3.5 it is clear that DPP method is very sensitive for a small changes in free carrier concentration. It can detect changes a few tenth times smaller than, for example, optical pump – THz probe method (OPTP). Additionally, the time resolution of DPP method is a few hundreds of femtoseconds, therefore rapid processes, for example, the ballistic electron transport, could be measured. Moreover, the spatial resolution is limited only by the ability to focus optical beam, that could be down to a few μm. While in OPTP, the spatial resolution depends on the diameter (d_{THz}) of THz beam, which is much harder to focus (d_{THz} usually is $\cong 1-2$mm).

3.4 Methods to determine THz emitting electric dipole orientation

The necessity to determine the orientation of THz emitting electric dipole comes from the desire to create the most effective THz emitters. Speaking about surface-based emitters, after its illumination with an ultrashort optical pulse, generated photocarriers moves deeper into the semiconductor due to the photo-Dember effect [99] or built-in surface electric field [52]. Both effects lead to a formation of perpendicular to the surface THz emitting electric dipole. The problem is that such dipole orientation is not favourable for outcoupling THz radiation from the semiconductor into free space. Thus, it is important to find a way to change dipole orientation into a more appropriate one (parallel to the surface). External magnetic field [100], as well as a certain configuration of metallic contacts [58], could create a parallel to the surface component of THz emitting electric dipole and enhance THz emission. The same result could be obtained due to a laser-induced strong nonlinear optical phenomena [68] or anisotropic photocurrent effect [72]. Also, it is very likely that parallel THz emitting electric dipole component occurs after nanostructurization of semiconductor surfaces [92]. However, when working on the ways to tilt THz emitting dipole, it is necessary to have tools to evaluate the results. Therefore, it is important to have methods to determine the orientation of the THz source (electric dipole/photocurrent) with respect to the semiconductor surface.

In 2009, R. Inoue *et al* [1] were first to suggest a method to determine the orientation of the THz emitting electric dipole. According to this method, firstly, one should measure the THz peak amplitude dependence on a detected angle, and secondly, using the model based on W. Lukosz theory [101] one should find the best fit of the results by varying the tilt angle (θ) of the dipole. Using such method R. Inoue *et al* [1] has investigated p-type InAs and SI GaAs under the influence of the external magnetic field. They found out that in p-type InAs non-zero tilt angle exists even under zero magnetic field ($\theta = 10.1°$). On the contrary, no such effect was observed for SI GaAs. However, R. Inoue *et al* declared a linear relationship between the angle θ and the magnetic field; for SI GaAs the proportionality constant was found to be equal to $10°/T$. Despite the obvious benefits of the method, it is difficult to implement as a fibre-based THz detector and the precise mechanics to rotate that detector around the sample is required. Another disadvantage is that only a very small part of the total THz radiation reaches the detector, which can greatly affect the accuracy of the method. Thus, it was essential to prepare new methods to determine THz radiating dipole orientation, where the diameter of laser beam at the surface of a semiconductor would be higher than the THz radiation wavelength, so it would minimize the divergence of THz radiation, and the majority of generated THz radiation would be collected in the detector.

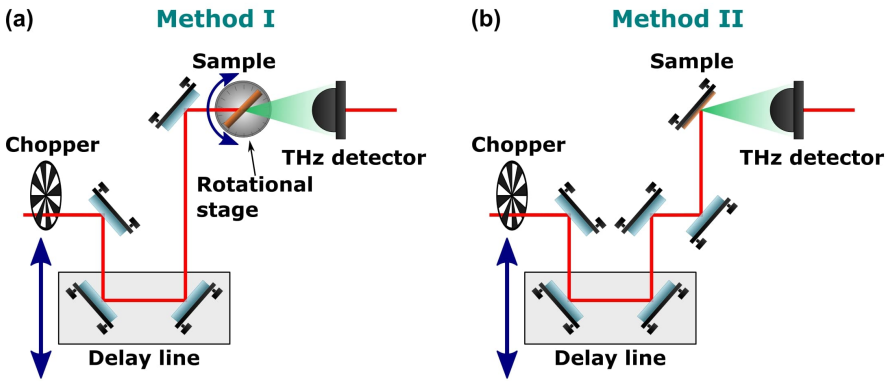

Figure 3.6: The illustration of the experimental set-up for method I in transmission (a) and method II in reflection (b) geometry.

Actually, there were developed two methods to determine the orientation of the THz radiating electric dipole: method I based on the measurements of THz emission dependence on an angle of incidence and determination of critical excitation angle; method II based on the THz emission measurement in reflection geometry and determination of the ratio between the second and the first emitted THz pulses. Experiment for the method I should be carried out in

transmission geometry, by rotating the sample around the axis perpendicular to the optical table (Fig. 3.6(a)). To implement the measurement here is quite simple, because then the laser beam axis, the sample and the THz detector are in one straight line. During the experiment, only the angle between the sample surface and the laser beam axis is changing. For method II, measurements should be done in reflection geometry, and no sample rotation is needed (Fig 3.6(b)). It is worth to mention that the sample must be transparent for THz radiation in order to be investigated by either of these methods.

3.4.1 Method I

This method is based on the observation that the spacial distribution of THz radiation as well as the efficiency of THz emitting electric dipole could be predicted by knowing the tilt angle θ. These dependencies could be calculated based on the W. Lukosz suggested model of electric dipole radiation [101,102]. During the experiment, the sample is rotated around the axis perpendicular to the detection plane, thus the angle between the sample surface and the laser beam axis (α_1) is changed. At each α_1 emitted THz pulse is measured and the THz pulse amplitude dependence on α_1 is plotted for the further analysis.

The radiated THz field dependence on the angle of incidence and the dipole tilt angle could be expressed as follows [52]:

$$E_{THz}(\alpha_1, \phi, \theta) = (1 - R_{opt}(\alpha_1))E_{td}(\alpha_1, \phi, \theta)t_{THz}(\alpha_1) \tag{3.5}$$

where ϕ and θ are azimuthal and polar angles of the dipole, and α_1 is the angle of incidence (Fig. 3.7a). The first factor, $1 - R_{opt}$, comes from the photocarrier density, which is proportional to the amount of the optical radiation power density that gets into the semiconductor. Here R_{opt} is a power reflection coefficient for optical radiation. The second factor, E_{td}, describes the radiation pattern of the dipole, and the third factor, t_{THz}, is the transmission coefficient for the THz wave electric field amplitude. The reflection coefficient of laser radiation, R_{opt}, strongly depends on polarization. For s-polarized laser radiation, the R_{opt} can be expressed as:

$$R_{opt}(\alpha_1) = \left(\frac{\cos\alpha_1 - n_{opt}\cos\alpha_{2,opt}}{\cos\alpha_1 + n_{opt}\cos\alpha_{2,opt}} \right)^2 \tag{3.6}$$

where n_{opt} is the index of refraction of semiconductor for laser radiation, and $\alpha_{2,opt}$ is the refracted optical beam angle, which can be calculated from Snell's law. For most common p-polarized terahertz radiation, the transmission coef-

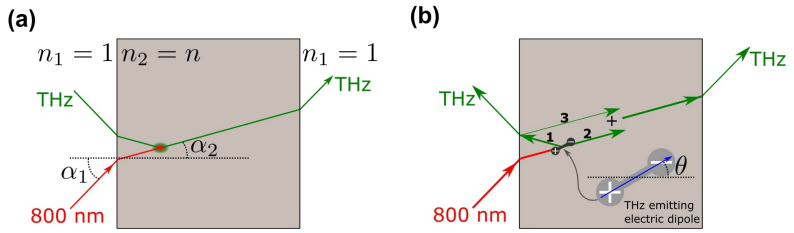

Figure 3.7: The propagation of THz radiation after photoexcitation. (a) Optical and THz radiation propagation directions. (b) Formation of THz radiating electric dipole in reflection and transmission directions according to the model represented in [101].

ficient through the semiconductor-air interface can be expressed as:

$$t_{THz}(\alpha_1) = \frac{2\sqrt{n_{THz}\cos\alpha_{2,THz}\cos\alpha_{1,THz}}}{\cos\alpha_{2,THz} + n_{THz}\cos\alpha_{1,THz}} \tag{3.7}$$

where n_{THz} is the index of refraction of semiconductor for terahertz radiation, $\alpha_{1,THz}$ and $\alpha_{2,THz}$ are the THz beam angles measured from the normal of the semiconductor-air boundary for propagation in air and semiconductor, respectively. If refractive indexes of terahertz and optical waves have very close values then, according to Huygens' principle, the directions of THz and optical beams coincide inside the semiconductor, therefore $\alpha_{2,opt} = \alpha_{2,THz} \approx \alpha_2$ and $\alpha_1 \approx \alpha_{1,THz}$. Thus, it could be assumed that α_1, α_2 and n was the same for optical and THz radiation.

In this work, the terahertz radiation pattern inside the semiconductor sample was modelled on the basis of W. Lukosz [101,102] theory. According to this theory, THz radiation going deeper in semiconductor from the electric dipole located close to the semiconductor-air interface consists of two beams: one emitted in the transmission geometry and second emitted to the reflection geometry and reflected back from the interface (Fig. 3.7b). Then the superposition of these two beams could be expressed as follows:

$$E_{td}(\alpha_1, \phi, \theta) = \frac{\cos\alpha_2(\cos\theta\sin\alpha_2 + n\sin\theta\cos\alpha_1\cos\phi)}{\cos\alpha_2 + n\cos\alpha_1} \tag{3.8}$$

Here, and in all following cases, THz pulse electric field is normalized to the electric field that would be measured in the detector if the THz pulse emitting electric dipole is located in air.

At a certain angle $\alpha_1 = \alpha_{cr}$, the numerator of the right-hand side of equation (3.8) is equal to zero. Then, the E_{td}, and as a result, E_{THz} become equal to zero too. If $\phi = 0$ (the dipole lies in the plane of incidence), the critical angle α_{cr}

and angle θ are related by the equation:

$$\tan \alpha_{cr} = n^2 \tan \theta \tag{3.9}$$

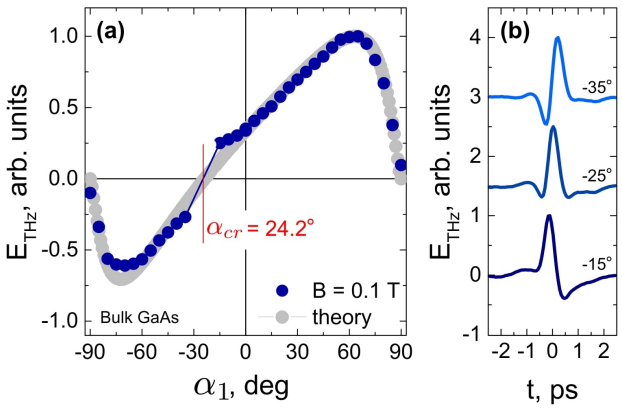

Figure 3.8: (a) Dependence of THz pulse amplitude on an excitation angle. (b) The temporal chape of THz pulse at various excitation angles. Experimental results (represented in dots) show THz pulse peak-to-valley amplitude and polarity. In the area $\alpha_1 \approx \alpha_{cr}$, the temporal shape of THz pulses change drastically, so the values corresponding to their amplitudes are difficult to define. The theoretical curve was calculated by the equation 3.5 using electric dipole tilt angle θ that was calculated by eq. 3.9 after experimentally having determined the angle α_{cr}.

The method I involves experimentally finding the angle α_{cr}, at which THz signal shifts into the opposite sign, and then to calculate the angle θ using the eq. 3.9. For the visualization of Method I in action, the experimental results for SI-GaAs under an external magnetic field is shown as blue dots in Fig. 3.8a. It could be seen that in the vicinity of α_{cr}, THz pulse is experiencing fundamental changes (Fig. 3.8b); its complicated shape progressively changes from one polarity to another. This might be explained by the dual nature of THz emitting electric dipole. Under the external magnetic field, the electrostatic force determines the formation of a perpendicular to the surface electric dipole component, while the Lorentz force determines the formation of the parallel one. These components cause the emission of different temporally shaped THz pulses. In a THz detector, constructive or destructive interference of these pulses can occur depending on the values of α_1 and B. In the case of constructive interference, differences between THz pulses are not very important, while in the case of destructive interference, the signal amplitude decreases, and the temporal shape of THz pulse changes, but the signal does not disappear (Fig. 3.8b). So, strictly speaking, the emission of THz radia-

tion in a magnetic field should be described by the THz emission from two perpendiculars to each other electric dipoles, which actually complicates the method. Luckily, the points, where pulse polarity was not clear, could be eliminated from Fig. 3.8a, and a linear approximation could be used to determine α_{cr} value. Such an approximation was proved to be valid as theoretical (obtained after angle θ determination) and experimental results are in a very good agreement (Fig. 3.8a).

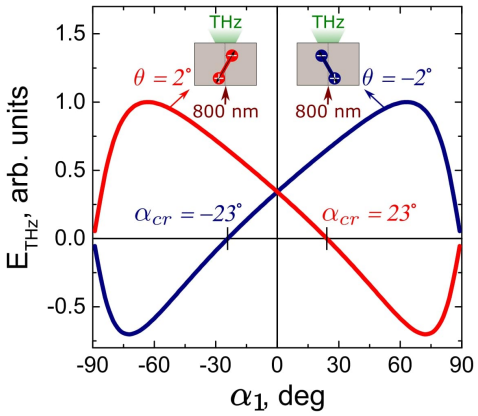

Figure 3.9: THz pulse amplitude dependence on an excitation angle calculated for two opposite directions THz radiating electric dipoles.

It is worth to mention that this method allows to determine the orientation of the THz emitting electric dipole very precisely: it gives not only the absolute value of angle θ, but also the sign of θ. That allows telling in which direction exactly the dipole is tilted (Fig. 3.9). For more information please refer to P5. Moreover, it should be pointed out that an eq. 3.5 precisely describes azimuthal dependencies, when the dipole tilt angle is known.

3.4.2 Method II

Method II is based on the THz emission measurement in reflection geometry. Samples to be investigated with this method must be sufficiently thick. Then after the photoexcitation by the laser pulse, at least two THz pulses can be detected in the reflection direction. A THz wave emitted in the reflection direction forms the first pulse, while the wave emitted in the transmission direction and reflected from the back surface of the sample is visible in the second THz pulse (Fig. 3.10a). Keeping in mind radiation pattern of Hertzian dipole, it is obvious that the ratio between the electric field amplitudes of these two THz pulses strongly depends on a tilt angle of the dipole (Fig. 3.10b). Estimating the reflection loss from the back surface of the sample, the last-mentioned ratio

could be calculated as follows:

$$\frac{E_{THz\_II}}{E_{THz\_I}} = \frac{-E_{td}(\alpha,\phi,\theta)r_{THz}(\alpha_1)t_{THz}(\alpha_1)}{E_{rd}(\alpha,\phi,\theta)} \tag{3.10}$$

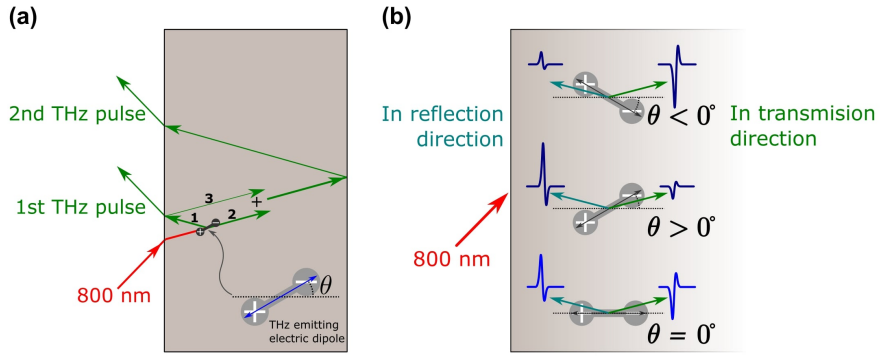

Figure 3.10: (a) The illustration of THz pulse sequence formation in a semiconductor substrate. (b) The illustration of THz pulses emitted in transmission and reflection geometry at a different electric dipole tilt angle.

In the equation (3.10) the $E_{rd}(\alpha,\phi,\theta)$ refers to the amplitude of THz pulse emitted in the reflection direction (the transmission coefficient of the front interface is included), while $E_{td}(\alpha,\phi,\theta)$ is the amplitude of the THz pulse emitted in the transmission direction. $r_{THz}(\alpha_1)$ and $t_{THz}(\alpha_1)$ are the sample surface transmission and reflection coefficients for THz radiation. Expressions for $E_{td}(\alpha,\phi,\theta)$ and $t_{THz}(\alpha_1)$ have been described previously in equations (3.8) and (3.7) while the $E_{rd}(\alpha,\phi,\theta)$ and $r_{THz}(\alpha_1)$ could be expressed as follows:

$$r_{THz}(\alpha_1) = -\frac{\cos\alpha_2 - n\cos\alpha_1}{\cos\alpha_2 + n\cos\alpha_1} \tag{3.11}$$

and

$$E_{rd}(\alpha,\phi,\theta) = \frac{\sqrt{n\cos\alpha_1\cos\alpha_2}(\cos\theta\sin\alpha_2 - \sin\theta\cos\alpha_2\cos\phi)}{\cos\alpha_2 + n\cos\alpha_1} \tag{3.12}$$

Fig. 3.11 presents theoretical results for the E_{THz_I}, E_{THz_II} and E_{THz_II}/E_{THz_I} ratio calculated using the formulas described above. The determination of the dipole orientation with method II consists of three stages illustrated in Fig. 3.12. Firstly, the THz emission in reflection geometry should be measured. Then the ratio E_{THz_II}/E_{THz_I} should be calculated using the measured amplitudes of first and second THz pulses. Finally, based on the obtained ratio, the tilt angle θ should be determined using the dependence calculated using eq. 3.10. It should be noted, that method II, similarly to the

method I, also tells the sigh of θ and describes in which direction the dipole is tilted.

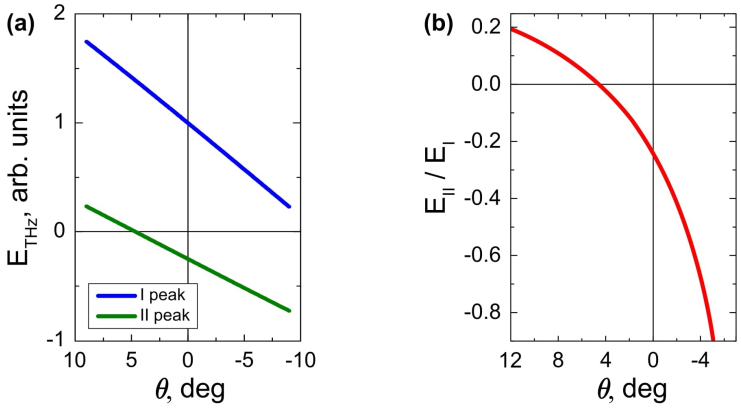

Figure 3.11: The first (Ist) and second (IInd) THz pulse amplitudes (a) and their ratio (b) dependence on an angle θ calculated by the equation (3.10).

The credibility of the method I and method II was tested with SI GaAs under external magnetic field. It is known, that added magnetic field changes the movement direction of the charged carriers due to the Lorentz's force. The electrons, which, in SI GaAs, are naturally moving perpendicular to the surface, due to built-in surface electric field, are forced to move in the direction parallel to the sample surface. Thus, in the sample forms tilted THz emitting electric dipole. By changing the strength of the magnetic field, the tilt angle could be controlled. Both methods described above give similar results and show the linear relationship between dipole tilt angle and magnetic field strength as it was observed in the work by R. Inoue [1]. The investigation of SI GaAs by methods I and II also lead to an assumption, that the magnetic field induced changes of the dipole tilt angle is proportional to the mobility of electrons. For more information please refer to **P5**.

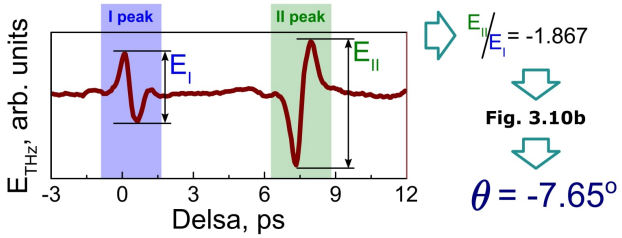

Figure 3.12: Schematic illustration of THz emitting electric dipole orientation evaluation using Method II.

It should be noted, that both methods are good choices to determine the

orientation of the THz emitting dipole. However, it is obvious that method I is more complicated than method II. For example, the THz radiation transmission function changes when the laser beam diameter becomes comparable to the THz radiation wavelength. In addition, this diameter depends on α_1, which results in drastically changing excitation conditions when α_1 approaches 90°. Therefore, in most cases, method II is a better choice as it is easier, faster and more precisely described mathematically. However, in certain cases, the $E_{THz}(\alpha_1)$ measurement could be more informative than the method II. For instance, in case of a very thin sample, method II is noneffective, because pulses overlap in time. Another example – semiconductor nanostructures, in which θ often depends on the angle α_1. In this case, the measurement of $E_{THz}(\alpha_1)$ together with the azimuthal dependencies $E_{THz}(\phi)$ is the primary tool to see a general picture of the THz emission characteristics in such structure.

3.5 Setups for investigation

The majority of the experiments were done using three stages "Coherent" femtosecond laser system. In the first stage there is a laser diode matrix which is used to pump neodymium-doped yttrium aluminium garnet (Nd:YAG) "Verdi" laser in the second stage. In the third stage there is a titanium:sapphire (Ti:Sa) laser "Mira" pumped by the second harmonic of Ng:YAG oscillator. Femtosecond laser system generates 150 fs duration and 800 nm wavelength optical pulses at a repetition rate of 76 MHz and the pulse energy of 6.5 nJ. Polarization-sensitive LT-GaAs photoconductive antenna was used to detect THz radiation (Teravil Ltd.).

Other part of the experiments was carried out using an amplified ytterbium-doped potassium gadolinium tungsten (Yb:KGW) laser system (PHAROS, Light Conversion Ltd.) operating at 1030 nm with a pulse duration of 160 fs, the pulse repetition rate of 200 kHz, and 7 W average power. Output laser beam is divided into two parts: the smaller one (about 0.5 W) is directly used in the experiments while the other one (about 6.5 W) is directed to a cavity-tuned optical parametric oscillator (ORPHEUS, Light Conversion, Ltd.) that generates 140-160 fs duration pulses with a central wavelength tunable from 640 nm to 2600 nm and average power ranging from 100 to 500 mW depending on the wavelength. Polarization-sensitive GaAsBi photoconductive antenna was used to detect THz radiation (Teravil Ltd.).

4. Non-stoichiometric GaAs

Non-stoichiometric (NS) semiconductor is a term used for semiconductor compounds that have an elemental composition the proportion of which cannot be represented by integers. This is mainly caused by three reasons: an atom missing from the lattice structure, which causes the other atoms to change their oxidation states to maintain neutrality; the presence of extra atoms in the lattice; the missing atoms are replaced by the atoms of a different element, maintaining the neutral charge of the material. It was noticed that non-stoichiometry of the crystal may result in nanostructurization of its surface: there might form grooves or hills like structures (Fig. 4.1). In the following chapters, an overview of NS semiconductors will be given and an investigation of nanostucturized NS-GaAs will be presented.

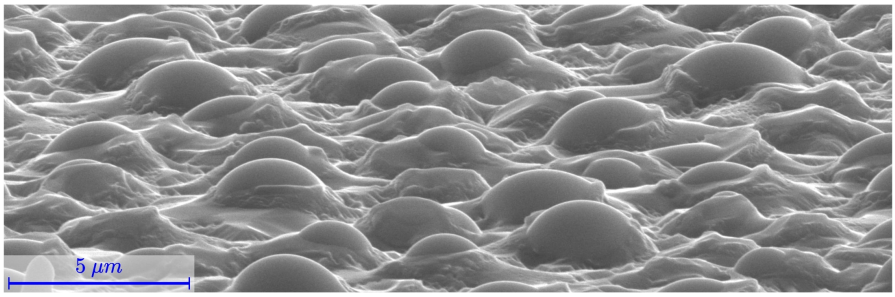

Figure 4.1: SEM image of non-stoichiometric grown GaAs layer. Growth performed by R. Butkutė and V. Pačebutas (Center for Physical Sciences and Technology, Vilnius, Lithuania), SEM image is done by A. Selskis (Center for Physical Sciences and Technology, Vilnius, Lithuania).

4.1 Production of the non-stoichiometric GaAs

Most semiconductors and their structures, that are of major interest for investigators, these days are grown by Metalorganic Chemical Vapour Deposition (MOCVD) or Molecular Beam Epitaxy (MBE). Even though both tech-

niques result in high quality semiconductor layer deposition, MBE allows better control of layer growth. Additionally, it was chosen for the preparation of the samples under investigation, thus only MBE technique will be presented in details. This growth technique performed in an ultra-high vacuum and based on a reaction of molecules and atoms with the heated crystalline substrate, which results in an atomic layer by layer deposition. The term *"Molecular Beam Epitaxy"* was first mentioned in the work of A. Y. Cho in 1971 [103]. The term *"Molecular Beam"* refers to a directional flow of molecules or atoms without any collisions among them. The term *"Epitaxy"* is composed of two Greek words *"epi"*, meaning *"upon"*, and *"taxis"*, meaning *"order"*. Thus the epitaxial growth refers to a growth of one crystalline layer on another crystalline layer, maintaining the same or closely related crystal structure. The molecular beam is created by evaporating the source material, that is resistively heated. In front of the sources, the shutters are placed that allows to turn on and off the particular molecular beam, which results in almost monolayer control of semiconductor material growth. Moreover, the MBE technique allows precise control of material composition and purity, as well as a real-time, in situ monitoring [104]. Due to the precise control of material stoichiometry, this method could be used to growth both stoichiometric and non-stoichiometric semiconductors.

One of the best known non-stoichiometric semiconductors is NS GaAs. In general, there could be grown both, Ga-rich GaAs [105] that have excess Ga, and As-rich GaAs [106] that has excess As, depending on the flux ration of the two species and substrate temperature. Usually, high quality GaAs is grown in a substrate temperature range of 500-640°C. At higher temperatures, without As overpressure, As evaporates from the surface leaving Ga droplets and resulting in Ga-rich GaAs. In order to obtain As-rich GaAs one needs to maintain large As to Ga flux ratio at high temperatures. While at low temperatures it is much easier to obtain such material. The As-rich GaAs is usually referred to as low temperature grown GaAs (LT GaAs), as the growth is performed in a substrate temperature range of 200-300°C. At these conditions, as much as 1.5% of excess As could be incorporated into GaAs layer, leading to a strong non-stoichiometry of the sample [107].

Another way to produce highly non-stoichiometric GaAs is the implantation of GaAs crystal by large doses of high energy As [108] or Ga [109] ions. The thickness of the non-stoichiometric region created by implantation depends on the weight and energy of the ions. Lighter Ga ions incorporate deeper in the bulk GaAs crystal than heavier As ions. Therefore, layer with excess Ga will appear deeper in the crystal, while the layer with excess As will be closer to the surface. However, As ions with an energy in a range of MeV might

be incorporated sufficiently deep into the GaAs crystal. In comparison to low temperature growth, ion implantation offers better control of the incorporated amount of excess material. Moreover, it allows creating non-stoichiometry in the localized region of the crystal [110].

4.2 Applications of non-stoichiometric GaAs

Non-stoichiometry in As-rich GaAs is always complemented by the formation of As antisite defects (As_{Ga}) and Ga vacancy point defects (V_{Ga}). Since the As_{Ga} is a deep double donor, the high concentration of these point defects has a considerable impact on the electrical properties. It was shown that LT GaAs exhibits short carrier lifetime, high carrier mobility and high resistivity of the material. These features were associated with ionised As_{Ga} defects which are the main electron traps in LT GaAs. The concentration of As_{Ga} defects is much larger than that of V_{Ga}, thus only a few percents of As antisites are ionized and participate in electron trapping, while the rest remains inactive. Therefore, it was suggested to activate neutral As_{Ga} defects by additional doping of LT GaAs with compensating acceptor impurities, for instance, beryllium [111].

All in all, the LT GaAs exhibits a lot of properties that are essential for effective THz emitters and detectors [28]. Tani *et al.* investigated THz emission from several types (dipole, bow tie, and strip line) of photoconductive antennas fabricated on LT GaAs and compared the results with those obtained using SI GaAs based antennas. The radiation spectra of LT GaAs and SI GaAs based antennas was found to be very similar. However, LT GaAs based antennas show better saturation properties against pump intensity and a higher breakdown field [112]. Photoconductive antennas for THz pulse detection were also fabricated on LT GaAs and good detection properties up to 4 THz were demonstrated [90]. Most of LT GaAs based THz detectors reach the detection range up to 6-7 THz, however, in 2000 it was reported the ultrabroadband detection up to 20 THz, when LT GaAs photoconductive dipole antenna was gated with 15 fs light pulses [60]. Additionally to THz pulse emitters and detector, LT GaAs photoconductive switches were used to realize continuous wave imaging system working in a range between 0.2 and 1.5 THz. Such a system produces high quality image that could be formed from both amplitude and phase data similarly to THz pulse systems [113]. After it was found that As ion implanted and then annealed GaAs has electrical and recombination properties very close to those of LT GaAs, it was also used as potential material for THz spectroscopy devises [108, 111]. With the development of laser technology, the lossless 1.55 mm wavelength window gains more and more attention in the field of optical communication. Unfortunately, GaAs is not sensitive in

that wavelength range, as its bandgap in a room temperature corresponds to a wavelength of 867 nm. However, there were reports on LT GaAs based THz detector operating under activation of 1.55 μm pulses due to two-step photoabsorption mediated by midgap states in LT GaAs [84]. The spectral range of such detectors was shown to be up to 4.5 THz, with a peak signal to noise ratio of 29 dB [114].

Of course, NS GaAs could be used not only for THz components. An emission of picosecond infrared pulses at the wavelength of 10.6 μm using LT GaAs based optical semiconductor switch was reported [115]. It was also suggested that by optimizing LT GaAs switching time ultrashort pulses at almost any wavelength in the mid- and far-infrared range could be generated. Another promising field for NS GaAs is in fabrication of field-effect transistors. As the LT GaAs has high resistivity, it was chosen as a buffer layer to eliminate backgating in metal-semiconductor field-effect transistor (MESFET) [116]. An excellent microwave power performance was demonstrated for GaAs metal-insulator-semiconductor field-effect transistor (MISFET) where LT GaAs was used as a gate insulator. This MISFET exhibited a high breakdown voltage, high microwave power density and allowed to achieve low gate current [117]. In 2002 a novel LT GaAs based long-absorption-length metal–semiconductor–metal (MSM) travelling wave photodetectors operating in a long wavelength regime (around 1300 nm) was demonstrated. This device was shown to be at least an order of magnitude better than conventional MSM photodetectors [118]. In addition, the features of NS GaAs were found to be useful in the production of photoconductive switches suitable for an on-chip study of magnetization dynamics excited by a subterahertz electromagnetic field pulse. For example, it was shown that using LT GaAs it is possible to generate 0.6 T and 3 ps long magnetic field pulses [119]. There was also expressed an expectation that with some modifications to the photoconductive antenna design the pulses field strength could be increased up to a few teslas. One of the newest works related to NS GaAs reports the fabrication of GaAs nanowires (NWs) covered with non-stoichiometric low-temperature grown GaAs shell. Authors demonstrate successful incorporation of excess As atoms in the GaAs matrix resulting in a short carrier lifetime and a low electrical conductivity. Thus, further these NS GaAs NWs are expected to be chosen for a novel THz and photoconductive applications [120].

Despite the NS GaAs potential as an excellent material for fast photoconductive antennas favourable for THz pulse emission and detection, there were no attempts to evaluate the contribution of surface morphology in effective THz pulse emission from bare NS GaAs surface. In the next chapter, the inves-

tigation of two types of nanostructures, grooves, and hills, that appeared on the NS GaAs surface during the MBE growth, will be presented. Both structures were found to exhibit interesting and useful features, that might lead to a novel type of surface based THz emitters.

4.3 Investigation of Non-stoichiometric GaAs

4.3.1 Samples

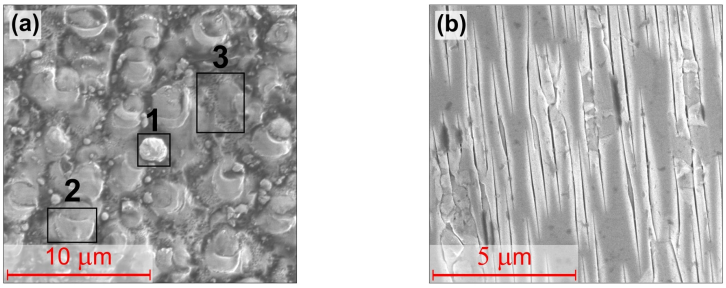

Figure 4.2: SEM images of two non-stoichiometric GaAs samples. (a) Ga4 with a hill like nanostructures on the surface. (b) Ga15 with grooves like nanostructures.

Samples were fabricated in the Department of Optoelectronics at a Center for Physical Sciences and Technology. Non-stoichiometric (NS) GaAs were grown by solid source MBE using SVTA reactor equipped with a metallic Ga and a two-zone arsenic valved-cracker source to produce As_2 dimers. The semi-insulating (100) crystallographic orientation GaAs wafers were used as substrates. NS GaAs layers were grown at a substrate temperature of 540°C and As_2 and Ga beam equivalent pressure ratio close to 5.8. There were prepared two types of the samples, which would be referred as Ga4 and Ga15. The thickness of the NS GaAs layer was about 5–6 µm for G4 and 3-4 µm for Ga15. The Scanning Electron Microscope (SEM) images have revealed that these samples have a very different surface morphology (Fig. 4.2), even though nanostructures were found on both surfaces. Ga4 shows hill like structures with a diameter of 3 µm and height of 400 nm, as could be seen in the Atomic Force Microscope (AFM) image (Fig. 4.3a). The other sample, Ga15, exhibits grooves like structures (Fig 4.3b) that has a depth of $\sim$ 200 nm, the width of $\sim$ 400 nm and the length of 5 µm. Both samples were proved to be Ga-rich as the elemental Ga/As ratio was found to be 1.2 for the sample Ga15, 1.6, 1.4 and 1.2 for sample Ga4 in the regions 1, 2 and 3, respectively (Fig. 4.2a).

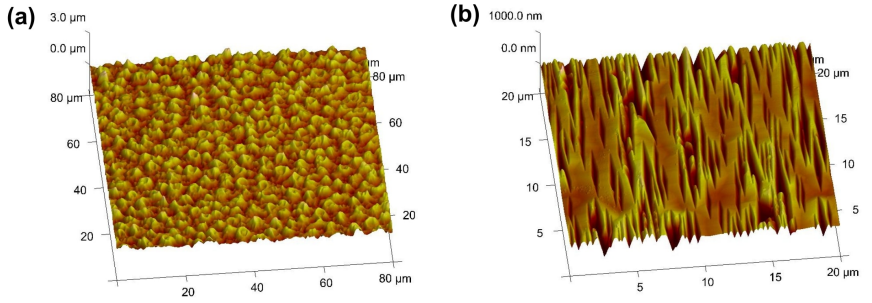

Figure 4.3: AFM image of non-stoichiometric GaAs samples: (a) Ga4 nad (b) Ga15.

4.3.2 THz pulse emission from non-stoichiometric GaAs samples

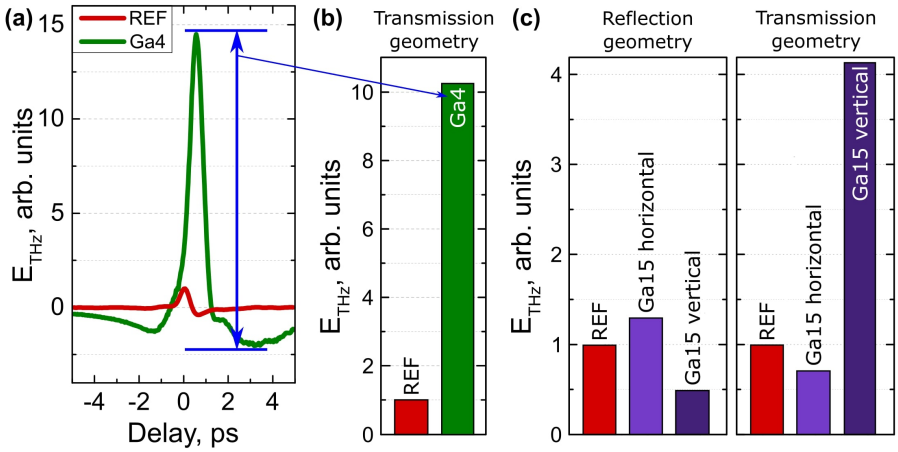

Figure 4.4: (a) THz pulses emitted from non-stoichiometric GaAs sample Ga4 and SI GaAs (REF), measured in transmission geometry. The azimuthal angle was chosen to correspond to the maximum THz signal. (b) Peak-to-valley THz pulse amplitudes of last-mentioned THz pulses. (c) THz pulse amplitudes of non-stoichiometric GaAs sample Ga15, measured for two specific Ga15 orientations in transmission and reflection geometries.

To begin with, THz pulse emission in transmission and reflection geometries was measured and compared with a reference sample – SI GaAs (REF). As it could be seen in Fig. 4.4a THz pulse emitted from Ga4 sample is much stronger than that emitted from a reference sample. In order to simplify the comparison process, the peak-to-valley amplitudes of measured THz pulses in Fig 4.4a are shown as the bars of a histogram in Fig. 4.4b. Now, it is clear

that Ga4 emits 10 times stronger THz pulse than that of SI GaAs. Speaking about other NS GaAs sample, Ga15, two specific orientations were distinguished: when grooves are oriented parallel (Ga15 horizontal) and perpendicular (Ga15 vertical) to the optical table. In Fig. 4.4c peak-to-valley amplitudes of emitted THz pulses at these two sample orientation are summarized in transmission and reflection geometries. In reflection geometry, no noticeable THz emission enhancement was observed, however in transmission geometry 4 times stronger THz pulses were measured for vertical grooves orientation. The origin of THz emission enhancement in NS GaAs samples will be discussed in later chapters.

In addition, THz pulse emission under external magnetic field was investigated (Fig. 4.5). The measurements were done at 0° excitation angle. Without magnetic field sample Ga15 does not emit THz radiation, while THz pulse emitted from the sample Ga4 is quite strong. When the 0.5 T strength magnetic field was applied, the THz emission behaviour of sample Ga15 drastically changes – there occurs THz pulse, while THz emission from sample Ga4 experiences only negligible changes. These results suggest, that the THz generation mechanism in these samples are completely different.

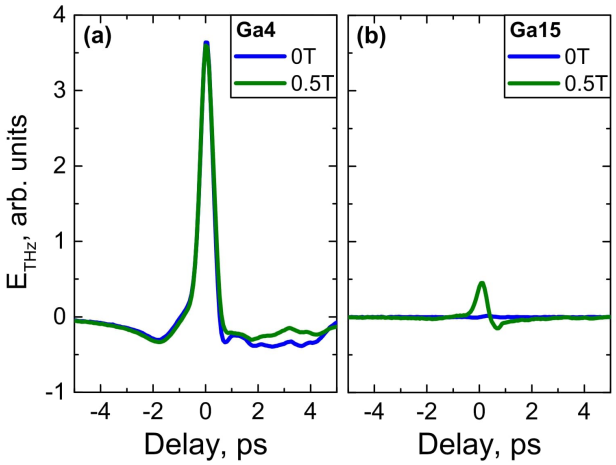

Figure 4.5: THz pulses emitted from non-stoichiometric GaAs for samples Ga4 (a) and Ga15 (b) with and without an external magnetic field.

4.3.3 Investigation of NS GaAs sample with hill like structure – Ga4

For further investigation of NS GaAs samples, THz pulse amplitude dependence on an angle of incidence was measured. In Fig. 4.6a the results for sample Ga4 and SI GaAs are shown.

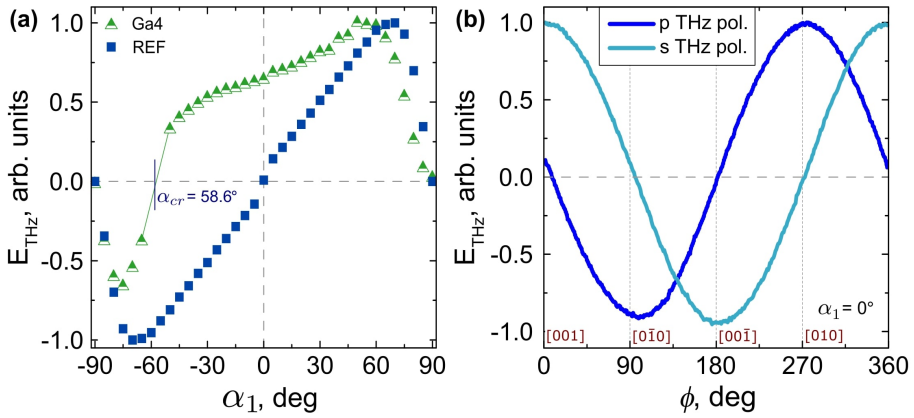

Figure 4.6: (a) THz pulse amplitude dependence on an excitation angle for non-stoichiometric sample Ga4 and SI GaAs (REF). (b) THz pulse amplitude azimuthal dependencies for non-stoichiometric GaAs sample Ga4 measured in transmission geometry under s- and p-polarized light excitation and $\alpha_1 = 0°$. The azimuthal angle is measured starting from the sample crystallographic direction [001] being parallel to the THz detector antenna knobs when the detector is positioned for p polarization detection.

The sample is rotated around the axis perpendicular to the optical table, thus changing the excitation angle. It is worth reminding, that in such measurement the strength of THz pulse at each angle depends on the orientation of THz emitting electric dipole. The measured curves show huge difference near the excitation angle equal to 0° suggesting that there exist a tilted dipole in Ga4 sample. From obtained results, α_{cr} was determined and then using Method I (described in chapter 3.4.1) the electric dipole tilt angle in Ga4 sample was determined to be $\theta = 8°$.

The existence of parallel to the surface electric dipole component in Ga4 was further confirmed by the azimuthal dependencies measurement (Fig. 4.6b). This figure represents azimuthal dependencies measured in transmission geometry at 0° excitation angle for s and p THz polarization. As the measurements were done at normal excitation angle, perpendicular to the surface component has no influence on the results. Ga4 sample exhibits a clear single-cycle azimuthal dependence, which has 90° shift when comparing s and p THz polarization.

However, the origin of tilted electric dipole in Ga4 is still not clear, nevertheless, some ideas might be discussed. THz generation mechanism in this sample might be related to the non-linear optical effects. In the previous works, it was noticed that various processes, such as chemical etching, tend to follow [110] direction resulting in nano- and micro- structures elongated along with

it [121]. It is obvious that the [110] direction exhibits some specific features, so it is not unlikely that under certain GaAs growth conditions there might occur stronger lattice strain along the last-mentioned direction. This may result in an increase of nonlinear-optical constants. From Fig. 4.6b it could be seen that parallel component of THz emitting electric dipole is lying along [010] crystallographic axis which is actually a projection of [110] crystallographic axis to the (100) plane. Thus the appearance of parallel to the surface component of THz emitting electric dipole might be the result of the specific features, that occur during the NS GaAs growth and are related to [110] crystallographic direction.

Previously described results are published in P2.

4.3.4 Investigation of NS GaAs sample with grooves like structure – Ga15

NS GaAs sample Ga15, with grooves like structure on the surface, exhibits very different THz emission characteristics from the Ga4. First of all, Ga15 does not emit THz pulse when excited at 0° incidence angle (Fig. 4.7a), thus one can guess that parallel to the surface dipole does not exist here. However, this sample has a lot of interesting features. It was already mentioned that there

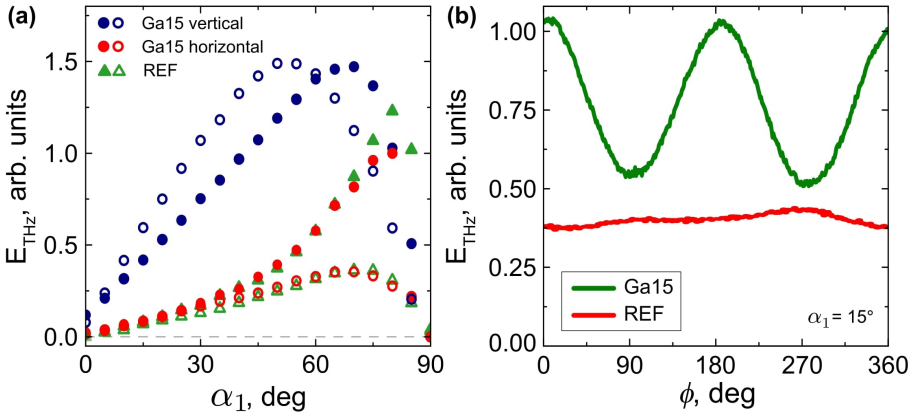

Figure 4.7: (a) THz pulse amplitude dependence on an excitation angle for two orientations of non-stoichiometric sample Ga15 and SI GaAs (REF). Open points for s-polarized, full points for p-polarized excitation light. (b) THz pulse amplitude azimuthal dependencies for non-stoichiometric GaAs sample Ga15 and REF sample measured in transmission geometry under p-polarized light excitation and $\alpha_1 = 15°$.

exist two specific orientations in sample Ga15: grooves oriented vertically and horizontally in respect to the optical table. THz pulse amplitude dependence

on an excitation angle has a very different shape for vertical and horizontal Ga15 orientation. The curves for horizontal orientation (red dots in Fig. 4.7a) follows the results of REF sample (green dots in Fig. 4.7a), whereas the data obtained from the vertical orientation has completely different dependence on an excitation angle (blue dots in Fig. 4.7a). These results could be related to the appearance of the parallel the surface THz emitting electric dipole component. It is worth to mention, that tilted electric dipole does not appear at $\alpha_1 = 0°$ and its strength depends on an excitation angle (the bigger the excitation angle, the larger the shadow on one slope).

Further, NS GaAs sample Ga15 was investigated by measuring azimuthal dependencies. The experiment was performed in transmission geometry at 15° excitation angle. The results were compared with reference GaAs sample. The REF sample does not exhibit a strong dependence on an azimuthal angle, while NS GaAs sample Ga15 shows clear two-cycle ($\cos 2\phi$) dependence (Fig. 4.7b). At first glance, this dependence could be attributed to the OR effect. However, previous measurements of THz emission dependence on an excitation angle shows that nor OR, neither EFIOR should affect THz generation. So, obtained $\cos 2\phi$ azimuthal dependence must be explained in another way. It is obvious that the result is related to the orientation of the grooves: maximum THz signal occurs when grooves are vertical and minimums when they are horizontal. As the measurement is done at non zero excitation angle, THz generation from perpendicular to the surface electric dipole is visible at every azimuthal angle and remains the constant value in a whole angle range. When the sample is oriented vertically, there occurs parallel to the surface electric dipole (due to shadowing effect), which emitted THz pulse constructively interferes with the one emitted from the perpendicular dipole, resulting in enhanced THz emission. On the contrary, when the grooves are horizontal, only THz emission from the vertical electric dipole is detected.

4.3.5 Promising material for surface based THz emitters

As mentioned above, parallel to the surface THz radiating dipoles are more preferable for compact effective THz surface emitters due to better THz radiation outcoupling into free space and possibility to be activated by the laser beam perpendicularly. Such an activation angle simplifies the positioning of THz emitter as well as allows creating more compact THz TDS systems. Since the sample Ga4 corresponds to this requirement (there is a non-vanishing parallel to the surface component of THz radiating dipole), the emitted THz pulses from this material were compared with those obtained from other THz surface emitters operating at 0° excitation angle like tilted GaAs NWs and (111)-cut p-InAs. As it could be seen from Fig. 4.8a, Ga4

emits at least two times stronger THz pulse than the other two materials. Further, the NS GaAs layer has been tested as a bias-free THz emitter in Teravil Ltd THz spectroscopy system. For this purpose, the Ga4 was mounted into a commercial THz emitter holder with silicon lens and placed into a THz spectrometer. Emitted THz pulses were detected using a 16-bit analogue to digital converter based coherent detection system. In addition, the low noise

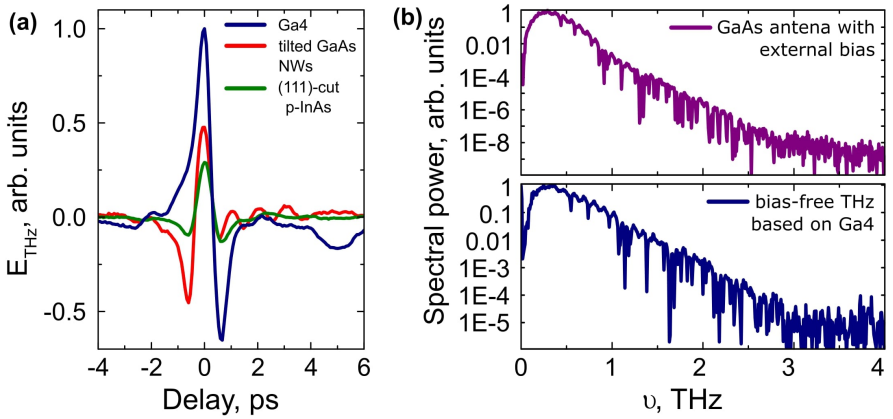

Figure 4.8: (a) Emitted THz pulses from the non-stoichiometric GaAs layer (Ga4) compared with THz pulses emitted from tilted GaAs NWs and (111)-cut p-InAs at 0° excitation angle. (b) Emitted THz pulse spectra for the commercial biased GaAs antenna. (c) THz pulse spectra of bias-free THz emitter based on Ga4 layer.

amplifier connected directly to the detector antenna was used to amplify the THz signal to the measurable level. 116 ps range was scanned ten times per second using a voice coil driven delay line with a feedback loop for speed control. The average of 1000 curves was used to obtain the THz spectra (Fig. 4.8c). The obtained results were similar to the results of a standard THz emitter – GaAs dipole antenna biased with a 100 V DC (Fig. 4.8b). Despite the smaller amplitude of THz pulse emitted from the NS GaAs layer, the obtained spectrum was up to 3 THz and the dynamic range was more than ∼50 dB. In addition, in comparison with commercial THz sources (biased antennas), the THz emitter based on the NS GaAs layer has some important advantages. Firstly, no external bias is necessary for device operation which opens the possibility to make smaller, compact and easily manageable THz emitters suitable for THz microscopy and mounting together with a detector. Secondly, the polarization of emitted THz pulse can be controlled simply by rotating the emitter around the normal to the surface. These advantages are very important for optical components capable to control polarisation in a broad THz spectrum region.

4.3.6 Conclusions

1. Photoexcited electrons motion in the directions perpendicular and parallel to the surface is the main cause of THz generation in sample Ga15. The direction and strength of the parallel to the surface component depends on the grooves orientation in respect to the impinging direction of an excitation light.
2. THz emission from Ga4 does not depend on the external magnetic field, so it is likely that the generation of THz radiation is determined not by the free electrons but by the valence electrons (nonlinear optical effects).
3. The orientation of the THz emitting electric dipole in sample Ga4 is fixed and rotates together with the sample, when the azimuthal angle is changing.
4. Strong THz emission at 0° excitation angle is a unique feature of sample Ga4, which could be used for bias-free, surface-based, polarization rotating THz emitters.

5. LIPSS

Laser-induced periodic surface structures (LIPSS), often termed ripples (Fig. 5.1), are a universal phenomenon that occurs on solids upon irradiation with linearly polarized laser radiation. LIPSS usually emerge as a surface relief composed of (quasi-) periodic lines, which exhibit a clear correlation to the wavelength and polarization of the radiation. These structures can be generated on almost any material (metals, semiconductors, and dielectrics) and can be formed in a huge range of pulse durations, ranging from continuous wave irradiation down to only a few femtoseconds. Such structures were found to be useful material in many fields, starting from optical up to biological applications, that will be presented in the following chapter. Another chapter will be dedicated to the LIPSS formation techniques. And finally, the investigation of LIPSS using THz emission spectroscopy will be discussed.

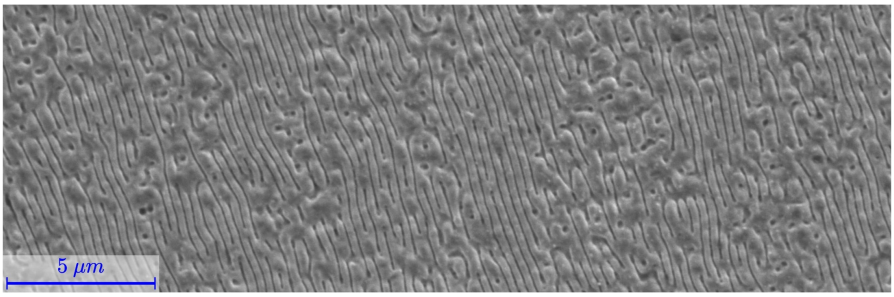

Figure 5.1: SEM image of LIPSS formed on GaAs substrate. Formation and imaging were done in Center for Physical Sciences and Technology, Vilnius, Lithuania by M. Gedvilas, M. Gaidys and G. Račiukaitis.

5.1 Formation of LIPSS

LIPSS were first observed by Birnbaum in 1965 [122]. He reported parallel grooves formation on Ge, Si, GaAs, GaSb, InSb, and InAs crystal surfaces after irradiation by a focused ruby laser beam. Birnbaum suggested that sur-

face relief formation is attributed to a diffraction effect, while parallel grooves are formed by the material removal at the maxima of electric field intensity. Almost ten years later, Emmony *et al.* suggested a novel explanation after observation of periodical damage on germanium under illumination by TEA CO_2 laser beam. They reported that grooves result from interference of the incident laser beam with the light that was scattered at surface defects and scratches [123]. Later, this idea was extended by Keilmann and Bai [124], as they proposed that interference occurs between the incident laser light and surface polaritons propagating along the irradiated surface. In the same years, the term LIPSS was suggested by van Driel *et al.*, who were first to demonstrate the formation of periodic structure using circularly polarized light. They also developed an extended theory of LIPSS formation based on the interference of an incidence light with surface scattered field [125].

In general, LIPSS can be formed either in static mode via irradiation of a single surface spot or in dynamic mode via a scanning process, where the laser beam or/and the sample surface are moved relative to each other at a constant velocity. The tidiness, period and orientation of obtained ripples depend mostly on the characteristics of the light sources, such as optical fluence, light wavelength, polarization, and pulse duration. As the ripples formation require a sufficient surface mobility provided to the material, it was noticed, that LIPSS are more likely to form at long pulse duration or at a large number of short laser pulses (typically exceeding a few thousands). Commonly, LIPSS could be divided into two categories: high spatial frequency LIPSS (HSFL) and low spatial frequency LIPSS (LSFL). LSFL, which are considered to be a classical type of LIPSS, exhibits period (Λ_{LSFL}) close to or slightly smaller than the irradiation wavelength ($\lambda/2 \leq \Lambda_{LSFL} \leq \lambda$). On the contrary, HSFL has a period (Λ_{HSFL}) smaller than the half of irradiation wavelength ($\Lambda_{HSFL} < \lambda/2$). Further, both LSFL and HSFL could be divided into two sub-categories, depending on ripples period and depth [126].

The first type of LSFL, called LSFL-I, exhibits ripples oriented perpendicular to the irradiation light polarization and has a period close to the wavelength ($\Lambda_{LSFL} \sim \lambda$, for simplicity, LIPSS period is often linked to surface plasmon polariton (SPP) wavelength $\Lambda_{LSFL} = \Lambda_{SPP}$ [126]). Such LIPSS usually form on strongly absorbing materials, like semiconductors and metals. Their generation is explained by an interaction of incidence light and scattered electromagnetic wave, and in many cases the excitation of SPP is involved [127]. However, this LIPSS generation mechanism was found to be suitable for plasmonic non-active materials as well, as these materials could be turned into the metallic state, once critical free electron density is exceeded. This allows direct excitation of SPP, which is believed to play a key role in LSFL-I formation [128]. It

should be mentioned, that LIPSS could be formed with pulses that energy is lower than an ablation threshold by triggering self-assembly of molecular units via local melting and rapid solidification. This process takes place in a narrow laser fluence window in between melting and ablation threshold [129]. Another type of LSFL, referred to as LSFL-II, is usually observed on dielectric materials or in cases, when irradiation photon energy is smaller than the bandgap of illuminated material. These structures have a period close to $\Lambda_{LSFL} = \lambda/n$, where n is an index of refraction, and are typically oriented parallel to the laser beam polarization [130]. LSFP-II formation is associated with specific non-radiative and non-propagating electromagnetic field mode close to the surface.

The second category of LIPSS, HSFL, with a period smaller than $\lambda/2$, are usually formed at fluencies very close to the ablation threshold of the material and typically for pulse duration in the femtosecond and picosecond range. In this case, ripples could be oriented in either parallel or perpendicular direction in respect to the irradiation polarization depending on the material [131]. HSFL could be divided into two sub-categories depending on the depth of the nanostructure. Type HSFL-I consists of narrow periodic grooves, which depth might reach up to several hundred nanometers [132] thus exceeding their period and resulting in depth-to-period ratio $A > 1$. This type is common for dielectric and semiconductor materials. In contrast, second type HFSL-II grooves have a depth of few tens of nanometers, resulting in depth-to-period ratio being much smaller than 1 ($A << 1$). This type is often observed on metal surfaces [133]. The origin of HSFL is still under discussion despite of wide variety of formation mechanism that was already mentioned in the literature. The most popular of them are associated with twinning effect during re-solidification, superficial oxidation, second harmonic generation, self-organization, and involvement of different plasmonic effects [126].

5.2 Applications of LIPSS

Since the discovery of LIPSS structures in 1965, this topic attracts great attention among the various groups of scientists. Especially in a last decay, as, with the development of laser technology, LIPSS could be formed via a simple single-step process in an air environment, avoiding expensive vacuum technology or lithography methods, while offering the ability to tailor optical, mechanical and chemical surface properties. Thus, let us discuss some of the main LIPSS applications fields, such as optics, fluidics, biology, medicine, and tribology.

Maybe the most obvious application arises from the fact that LIPSS act as diffractive gratings, thus generating structural colour, which might be at the

desired light range. The first observation of colour metals was reported by Vorobyev and Guo in 2008. They demonstrated visual and spectral measurements of the different structural colours (golden, black, grey, iridescent) produced on Al samples. They also showed, that depending on size and orientation of the ripples, as well as on the angle of incidence of light and an angle of observation, the LIPSS provides a controllable modification of optical properties of metals in the spectral range from UV up to THz [134]. A few years later, Dusser *et al.* present a systematical investigation of the influence of laser pulse energy, light polarization and laser spot size on the resulting LIPSS and their optical properties. Additionally, they demonstrated the processing of a portrait painting of van Gogh on a polished stainless steel surface just by using various LIPSS [135]. Another interesting application if LIPSS in the field of optics, arises from their ability to notably enhance light absorption, which, according to Kirchhoff's law, should lead to an increased emission of thermal radiation. Such idea was proposed and proved by Vorobyev *et al.* via processing LIPSS on a tungsten incandescent lamp filament, which dramatically brightened the lamp and enhanced its emission efficiency. Furthermore, they demonstrated a partially polarized light emission from the LIPSS based tungsten lamp [136]. In 2011, for the first time, was reported of an antireflection effect of LIPSS in a wide wavelength range of 250 – 2500 nm. It was showed that femtosecond pulse induced surface grating significantly suppress the total and specular reflectance from a Si surface, even though the antireflectance effect is stronger in the visible than in the infrared region [137].

Next to the optical features, also the wetting properties of LIPSS changes in comparison with non-structured surfaces. In general, the wettability of solid surface by a liquid depends on the viscosity of the liquid, surface energy of both materials, and the surface morphology of the solid. The last factor could be changed by forming various ripples on the surface. Kietzing *et al.* had investigated various metals and their alloys and noticed that upon LIPSS formation the surface could exhibit both superhydrophilic and superhydrophobic behaviour. Immediately after femtosecond laser irradiation, the metallic surfaces were hydrophilic, while after some time they became superhydrophobic. The change in wetting behaviour was found to correlate with the amount of nonpolar carbon on the surface. Directly after the laser treatment, there was not enough carbon to cover the entire surface and shield the initial hydrophilicity of the metal sheet. Moreover, the surface hydrophilicity was amplified by the surface roughness. However, over time, carbon dioxide reaction takes place and nonpolar carbon accumulates in the ripples resulting in superhydrophobic behaviour [138]. A very interesting result on transforming regular Si surface to superwicking was reported in [139]. There were formed the ripples, that

renders liquid to move vertically uphill against the gravity. Authors explained such unusual behaviour by a supercapillary effect arising from created LIPSS. Furthermore, LIPSS covered surfaces were reported to show self-cleaning ability, which makes the water and dirt repel from the surface [140, 141].

LIPSS covered surface is also of huge interest for medical and biological application, as they could be used to control orientation, migration and even growth properties of the cells. It was shown, that the LIPSS formed on a commercially available smooth polystyrene film accelerates rat glioma cells to attach and adhere, while suppresses their migration. Additionally, it was observed that cells are more likely to migrate and orient along the ripples [142]. Such behaviour was also fortified while studying the growth of different kinds of mammalian cells on polystyrene films, although it was pointed out that the cell alignment along the ripples takes place only when the periodicity of the ripples is above a critical value which depends on the cell type [143]. Moreover, it was reported that adhesion and proliferation of cells are enhanced on LIPSS covered films compared to smooth ones. On the contrary, it was shown that on titanium-based materials cell adhesion is reduced, while osteointegration was enhanced, which results in an increased integration and life span of the implants. For instance, it was reported that even in the presence of a mixed cell population from human bone marrow LIPSS tends to encourage cell proliferation and supports the solid attachment of bone marrow [144]. Recently, Cunha *et al.* reported on the ripples formed on the titanium film, that successfully reduces the adhesion of *Staphylococcus aureus* bacteria. According to the author, femtosecond laser-induced surface texturing is a promising tool for creating dental and orthopedic titanium implants, that exhibits antibacterial properties, thus reducing the risk of implant-associated infections [145].

Apart from the previously discuses applications, additional utilization of LIPSS covered surfaces were proposed during the last few years. A lot of reports related to the LIPSS expedience in the Surface Enhanced Raman Spectroscopy (SERS) applications. Chang *et al.* presented a nanostructured Ag surface, which shows 15 times greater SERS intensity of reference chemical compared with untreated Ag substrate [146]. Such behaviour was attributed to the plasmonic excitation and field enhancement effects in the vicinity of a rough surface. Great results were achieved by forming LIPSS on the dielectric material and then coating it with noble metal films. In case of Au coating, SERS signal was showed to be 15 times higher in comparison with the smooth substrate, while in case of Ag coated ripples the enhancement of more than 2000 times was observed [147]. Another potential application of nano- and microstructured surfaces is associated with the catalytic activity in the electrochemical process. Lange *et al.* recently reported a detailed investigation of platinum

electrodes covered with grooves, spikes and LIPSS. They showed that modified surface morphology could enhance electrochemical activity by a factor of 1500 after the laser treatment, due to the enlarged active surface area. However, it should be pointed out that LIPSS were found to be not the most favourable surface morphology for the electrochemical reaction [148]. Another unusual application was reported by Romoli *et al.* in a work on fuel injection in car engine. LIPSS were formed on the inner walls of a stainless steel gasoline direct injection nozzles. Such a modification of standard nozzles improved the fuel atomization via a reduction of an average fuel droplet size by 10% and increased the spray cone angle by 20 % [149]. Last but not least application of laser-induced ripples is found in the field of tribology. It was shown that LIPSS covered steel surface exhibits reduced value of a friction coefficient compared to the smooth surface. This phenomenon was explained by combining adhesion, trapped wear particles, and asperity deformation effects [150].

Despite a wide variety of LIPSS application, there were no previous attempts to use these structures in a field of THz spectroscopy, for example, as THz pulse emitters. Although, one should expect THz emission enhancement after fabrication of LIPSS on the semiconductor surface, as enhanced THz pulse emission was observed from various semiconductor nanostructures [13,15,19,78]. Thus, in the following chapter, the very first results of THz pulse emission from LIPSS covered GaAs substrate will be presented.

5.3 Investigation of LIPSS

5.3.1 Samples

Samples were fabricated in the Department of Laser Technologies at a Center for Physical Sciences and Technology. LIPSS were prepared on 3 different substrates: n-type GaAs (100) crystallographic orientation, i-GaAs (100) and i-GaAs (111). There were formed two series of LIPSS changing optical power, ablation speed (First series) and light polarization (Second series). LIPSS fabrication was done using an industrial-grade diode-pumped picosecond laser (Atlantic, Ekspla) with the central wavelength of 355 nm and a pulse duration of 10 ps. The formed LIPSS were attributed to the type LSFL-I.

In the First series, LIPSS were formed changing the optical power of the laser pulse (0.02 W, 0.04 W, 0.08 W) and the surface scanning velocity (5 mm/s, 10 mm/s, 20 mm/s), while polarization was kept constant. In these LIPSS preparation conditions, the direction of emerging ripples is perpendicular to the light polarization, in this particular case, the obtained ripples were oriented along the [110] crystallographic axis of GaAs crystals. There were formed 9

different samples on each of the 3 substrates, resulting in 27 samples of the First series in total. The sample surfaces were first investigated by SEM (Fig 5.2a). As it could be seen, the surface morphology strongly depends on the optical power: the tidiest LIPSS structures were obtained at the lower optical power (0.02 W). On the contrary, the dependence on the scanning velocity is not clearly seen.

After the investigation of the First series by means of THz emission spectroscopy, optimal LIPSS preparation conditions were determined and then later used for the Second series preparation. In this case, optical power and surface scanning velocity were kept 0.02 W and 5 mm/s respectively, while the polarization of optical radiation was changed. The ripples were formed at 0°, 45°, 90° and 135° angles in respect to the [110] crystallographic axis. There were fabricated 4 different samples on each of the 2 substrates (i-GaAs (100) and i-GaAs (111)), resulting in 8 samples of the Second series in total. In Fig 5.2b SEM images of Second series samples are presented. Additional SEM image of a larger surface area is presented in Fig. 5.1.

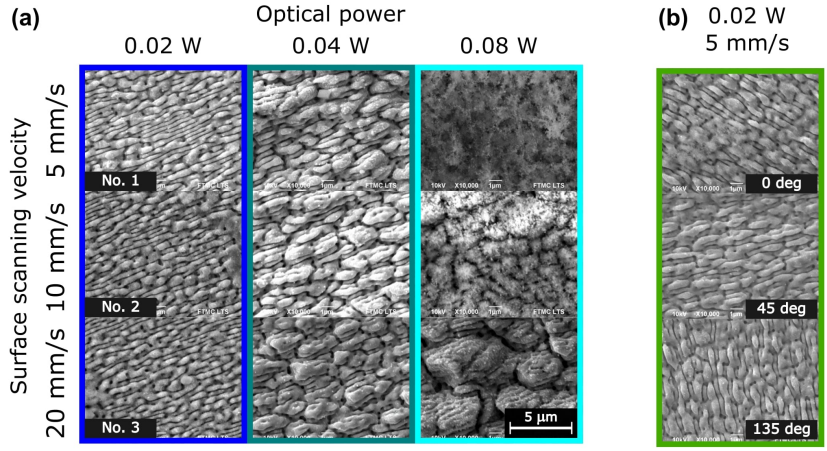

Figure 5.2: SEM image of LIPSS formed on a i-GaAs (111) substrate. (a) First series. Samples were fabricated changing the optical fluence and surface scanning velocity. (b) Second series. Samples were fabricated changing the polarization of laser light (an angle between ripples and [110] crystallographic axis of the sample is indicated in the bottom right of each image).

5.3.2 First series. THz pulse amplitudes and azimuthal dependencies

The first task was to find optimal preparation conditions of LIPSS best suitable for THz pulse generation. From SEM images (Fig 5.2a), it could be seen

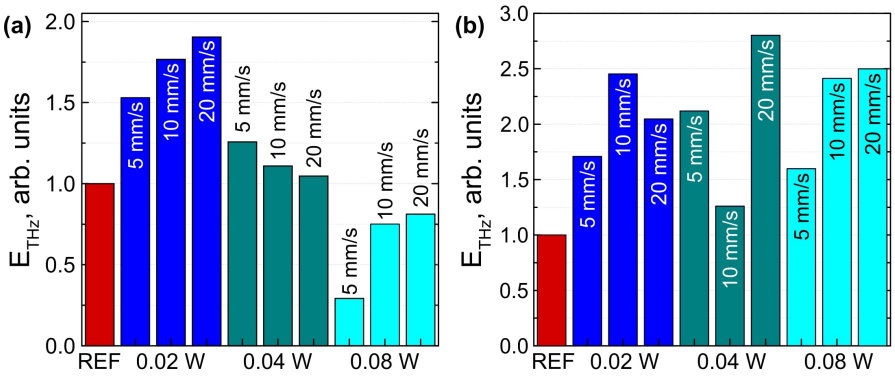

Figure 5.3: The amplitudes of THz pulses emitted from various LIPSS samples formed on (a) n-GaAs (100) and (b) i-GaAs (111) substrates and GaAs substrates before nanostructurization (REF). Measurements were done in reflection geometry.

that surface morphology strongly depends on the optical power of the laser pulse. As it is expected that THz emission depends on the surface structure, LIPSS samples were divided into three groups according to the optical power that was used to form the ripples (0.02 W, 0.04 W, 0.08 W). To begin with, THz pulse emission from all samples of the First series was measured in transmission and reflection geometries. Fig. 5.3 summarizes the amplitudes of THz pulses emitted from LIPSS formed on n-GaAs (100) (Fig. 5.3a) and i-GaAs (111) (Fig. 5.3b) in reflection geometry. It could be seen from Fig. 5.3a that LIPSS fabricated using lower optical power exhibits higher amplitude THz pulses, while samples formed using higher optical power emits THz radiation even worth than a reference sample. This result suggests that tidiest surface nanostructures lead to better THz pulse emission. However, all samples formed on i-GaAs (111) substrate emits stronger THz pulses than the reference sample (Fig. 5.3b) and no clear dependence on the LIPSS preparation conditions could be seen. For further investigation, azimuthal dependencies of all samples were measured. As it could be seen from Fig. 5.4, ripples formed at 0.02 W optical power shows very similar azimuthal dependencies which follows the $\sin 3\phi$ pattern inherent from the substrate. The second group, 0.04 W, shows still similar to each other yet more chaotic dependence on an azimuthal angle. The ripples fabricated at 0.08 W optical power show even more chaotic results, which does not follow the reference pattern. Azimuthal dependencies of the sample formed on i-GaAs (100) substrate also have a similar tendency when speaking about dependence on preparation conditions (Fig. 5.5). LIPSS fabricated at lower optical power shows $\cos 2\phi$ dependence, while those formed at higher intensities exhibits more unpredictable results. These mea-

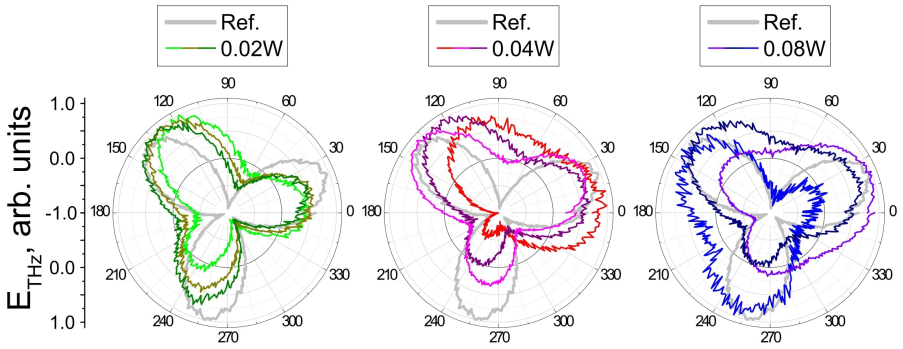

Figure 5.4: THz pulse amplitude azimuthal dependencies for LIPSS samples formed on i-GaAs (111) substrate.

surements further proved that ripples fabricated with the optical power close to ablation threshold exhibit most predictable results. Thus for further investigation, the samples formed at 0.02 W optical power were chosen (they are labeled in Fig. 5.2a).

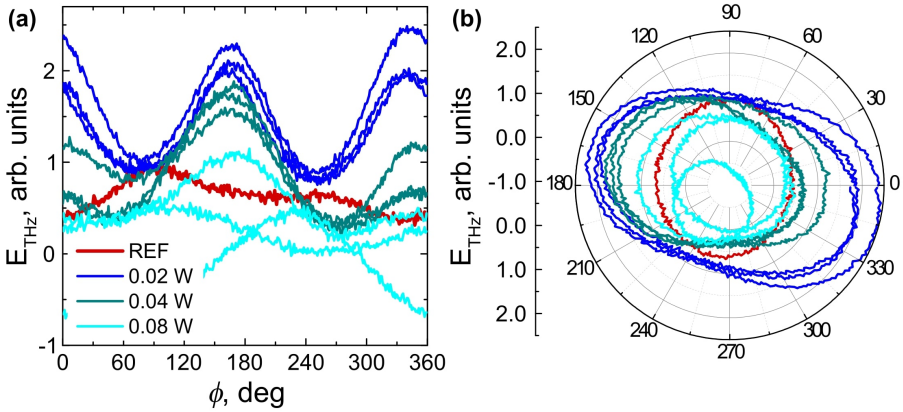

Figure 5.5: THz pulse amplitude azimuthal dependencies for LIPSS samples formed on i-GaAs (100) substrate in (a) Cartesian and (b) polar coordinate system.

LIPSS formed on i-GaAs (100) substrate show $\cos 2\phi$ azimuthal dependence which is very similar to the NS GaAs sample Ga15 (for more information see chapter 4.3.4). Due to non-linear effects non-ablated GaAs sample might have such dependence [151], however, it is almost invisible for the reference sample (Fig. 5.5 red curve). On the contrary, after nanostructurization process takes place the dependence becomes quite strong. Moreover, it was noticed that obtained results could be related to the orientation of the ripples, similarly as it was related to the orientation of the grooves for sample Ga15. When

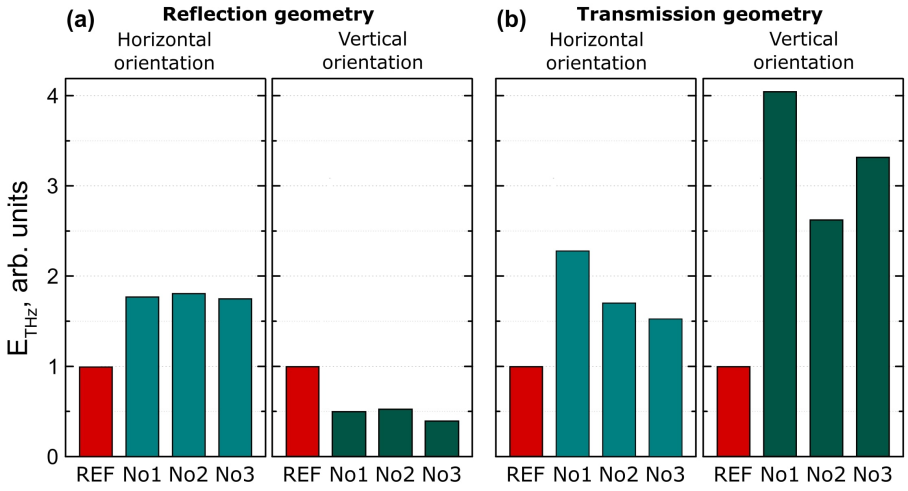

Figure 5.6: THz pulse amplitudes measured in (a) reflection and (b) transmission geometries for ripples oriented vertically and horizontally in respect to the optical table. The results are shown for LIPSS formed on i-GaAs (100) at optical power 0.02 W and surface scanning velocity 5 mm/s (No. 1), 10 mm/s (No. 2), and 20 mm/s (No. 3)

LIPSS are oriented horizontally to the optical table there are minimums and when LIPSS are oriented vertically there are maximums in azimuthal dependence. Nevertheless, THz emission enhancement is obtained for both orientations: for horizontal orientation, it is 1.5–2 times, while for vertical orientation the enhancement rises up to 4 times (Fig. 5.6). The results are almost identical for the ones obtained with NS GaAs Ga15, yet, for horizontal grooves in Ga15 THz emission enhancement was much smaller in reflection geometry, while there was no enhancement at all in transmission geometry. In the case of NS GaAs, THz emission enhancement for vertical grooves orientation was related to the appearance of tilted THz emitting electric dipole. The same explanation might be applied for LIPSS as well. However, it remains unclear if non-linear effects could be completely eliminated as the significant sample orientation coincides with the crystallographic axis of the sample, thus complicating the separation of the influence of sample crystallography and surface nanostructurization. The problem with NS GaAs, as well as with some similar surface nanostructures obtained by etching [121], is that it is impossible to control the orientation of emerging grooves, as their appearance is always related to the sample crystallography. On the contrary, the direction of LIPSS could be controlled by choosing the polarization of laser radiation during the preparation process. Thus it opens a possibility to distinguish ripples direction from the main crystallographic axis, which was realized in the second series of LIPSS

samples.

5.3.3 Second series. THz emission azimuthal dependencies

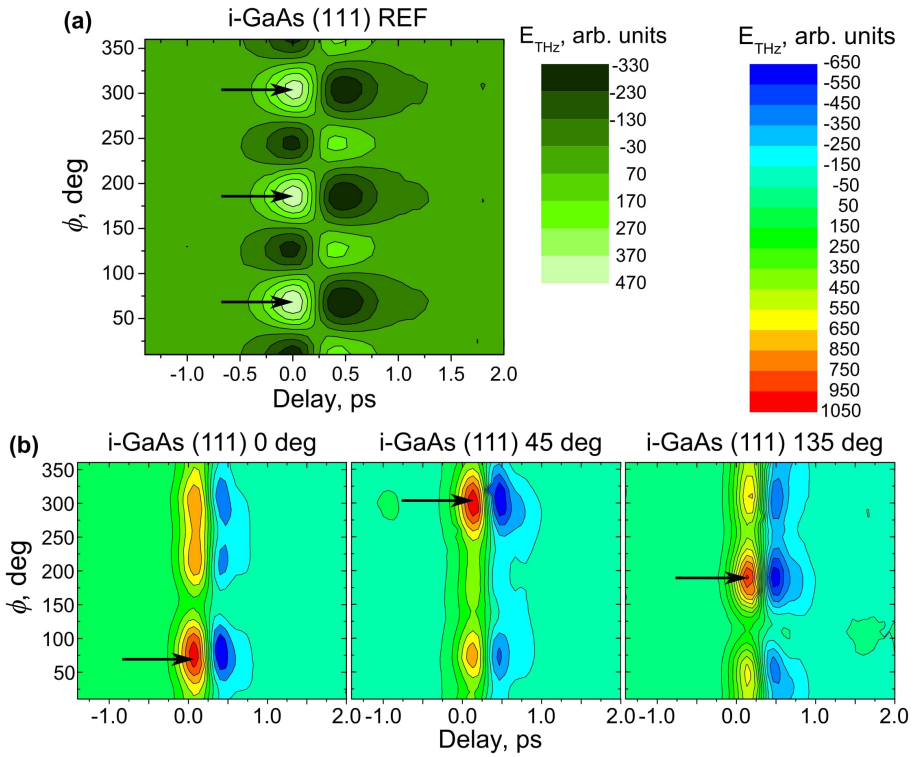

Figure 5.7: 2D graphs of azimuthal dependencies (a) for reference sample and (b) for second series LIPSS formed on i-GaAs (111) substrate. Black arrows indicate the peak positions of the REF sample.

In this section main focus was put on the THz emission azimuthal dependencies of LIPSS formed on i-GaAs (111) substrate. However, after the LIPSS were fabricated, it was noticed that the temporal shape of THz pulse becomes complicated and the peak position THz pulse slightly shifts in time when the azimuthal angle is changing. In the result, simple azimuthal dependencies measurement (usually done at one-time delay matching the peak position) becomes inappropriate. Thus, in order to obtain the full view temporal shape of the THz pulse was measured at each azimuthal angle and summarized in 2D azimuthal plots (Fig. 5.7). The i-GaAs (111) substrate, before nanostructurization, has substantial $\sin 3\phi$ azimuthal dependencies due to a strong nonlinear effect (Fig. 5.7a). After the LIPSS were fabricated, $\sin 3\phi$ azimuthal dependence evidence remains, yet, instead of 3 main peaks, there remains one,

which position follows the one of the peaks of the reference sample and varies depending on ripples orientation. Such results imply that both, sample crystallography and the direction of surface nanostructures, have a significant influence in THz emission characteristics.

5.3.4 Orientation of THz emitting electric dipole

After the investigation of the second LIPSS series, it was proved that THz emission features are mostly related to the direction of the ripples and not to the sample crystallography (which however might still be important). Thus, following the relation to the NS GaAs sample Ga15, it was considered of great importance to determine the orientation of THz emitting dipole. Previously, there was mentioned that THz pulse amplitude dependence on an excitation angle α_1 could be used for this purpose. However, this method is suitable only if the dipole orientation is fixed in the sample and does not depend on the angle α_1. It was shown that this requirement is not satisfied with NS sample Ga15 and in LIPSS as well. This leaves the necessity to use the Method II (for more information please refer to chapter 3.4.2) to determine the THz emitting electric dipole orientation.

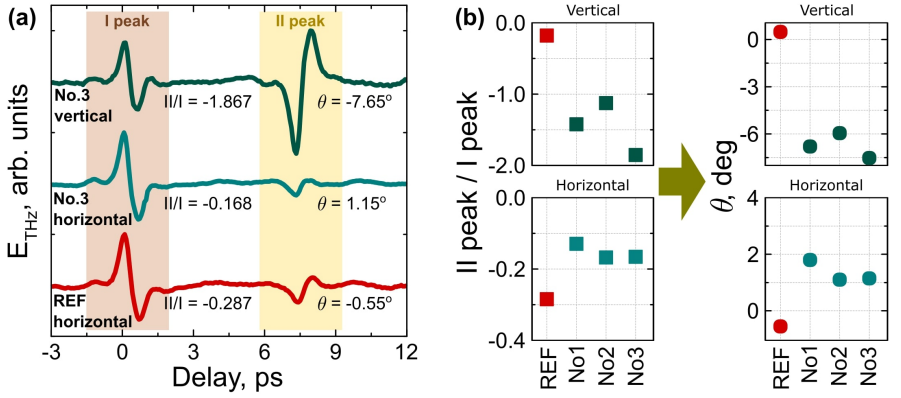

Figure 5.8: Determination of the orientation of THz pulses emitting electric dipole using method II (described in 3.4.2). (a) THz pulses measured in reflection geometry for vertical and horizontal ripples orientation compared with the reference sample. (b) The ratio between IInd and Ist THz peaks and corresponding tilt angle of THz emitting electric dipole for LIPSS on i-GaAs (100).

For Method II THz pulse emission from LIPSS structures formed on GaAs (100) substrate should be measured in reflection geometry (Fig. 5.8a). Then, the ratio between peak I and peak II was calculated, and later used to determine the tilt angle of the THz emitting electric dipole (Fig. 5.8b). Interesting thing is that the non-zero tilt angle was found out for both horizontally and

vertically oriented ripples. For the horizontal orientation, positive tilt angle with the value $\sim 2°$ was found, while for vertical orientation dipole is tilted in another direction having a negative angle $\theta \approx -6.5°$. Now, it is clear that THz emission enhancement is a consequence of non-perpendicular THz emitting electric dipole. However, the more information on this dipole still needs to be find out.

5.3.5 DPP measurements

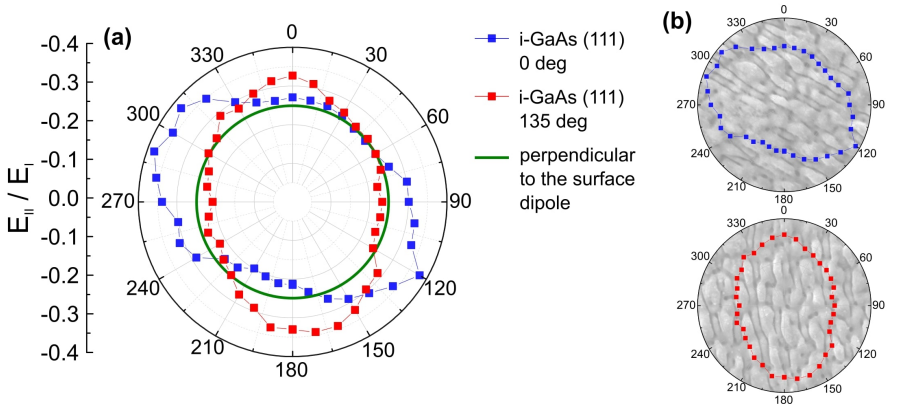

Figure 5.9: (a) The azimuthal dependence of the E_{II}/E_I ratio of DPP signal for Second series i-GaAs (111) 0 deg and i-GaAs (111) 135 deg samples. Green line represents the situation when the screened electric dipole is perpendicular to the sample surface. (b) E_{II}/E_I ellipsoids correlation with the orientation of LIPSS.

For further investigation of LIPSS, the double pump pulse (DPP) THz emission method (presented in chapter 3.3) was used. First, THz pulses generated under the illumination with one optical pulse (THz pulse I) and under the illumination with two optical pulses (THz pulse II) were measured at each azimuthal angle. Then the difference THz pulse (DPP signal = THz pulse II – THz pulse I) was obtained and the ratio between peak I and peak II of the last-mentioned THz pulse was calculated. This ratio for samples i-GaAs (111) 0 deg and i-GaAs (111) 135 deg was plotted as a function of the azimuthal angle (Fig. 5.9a). The obtained ellipsoids represent the THz emitting electric dipole that exists in LIPSS under the influence of the first optical pulse. It should be pointed out that these plots obtained an ellipsoidal shape, which is elongated along the direction of the ripples as could be seen in Fig. 5.9b. If the dipole would be oriented perpendicular to the sample surface at every azimuthal angle, the plot should maintain a circular shape

(Fig. 5.9a green line). However, the obtained results imply that the dipole has a small tilt angle ($\theta = -1.1°$ for sample i-GaAs (111) 135 deg and $\theta = -1.6°$ for sample i-GaAs (111) 0 deg), when the ripples are oriented horizontally in respect to optical table, and is perpendicular, when the ripples are oriented vertically.

5.3.6 Discussion on the origin of THz emission

The ability to determine THz emitting electric dipole orientation provides a straight knowledge of the electron motion direction in the sample. Usually, perpendicular to the sample surface THz pulse emitting electric dipole forms in semiconductor after the photoexcitation. Yet in LIPSS samples, similarly to the the NS GaAs sample Ga15, the existence of tilted electric dipole suggests that there occurs parallel to the surface uncompensated electron motion in the direction which depends on the orientation of the ripples. When ripples are oriented horizontally, the calculated tilt angle is positive which means that electrons are moving to the right along the ripples as shown in Fig. 5.10a. On the contrary, when ripples are oriented vertically, the tilt angle is negative and photoexcited electrons are moving in the opposite direction – to the left (Fig. 5.10b). The origin of such motion is not obvious, however, one can guess that surface morphology should play a key role here.

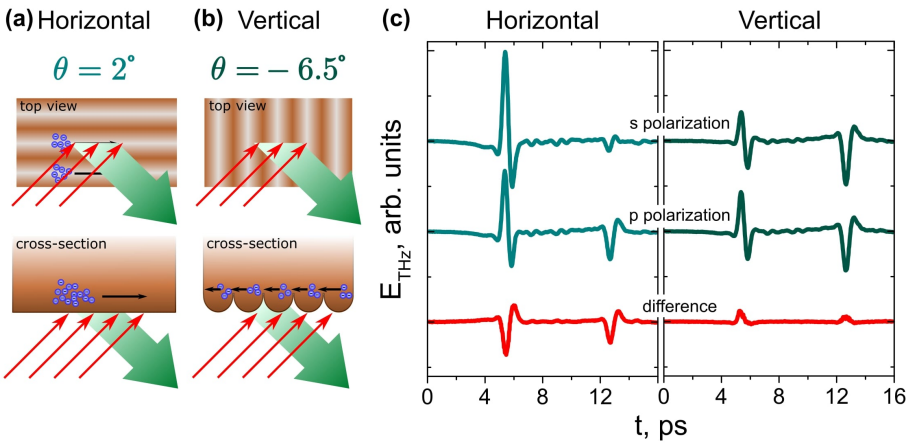

Figure 5.10: Schematic illustration of electrons motion in horizontally (a) and vertically (b) oriented ripples. (c) THz pulses measured under p- and s-polarized laser illumination of vertically and horizontally oriented ripples formed on i-GaAs (100) substrate (green curves). Red curves represent the difference THz signal (THz emission under p-polarized laser illumination – THz emission under s-polarized laser illumination).

The appearance of parallel to the surface component of THz emitting elec-

tric dipole could be related to the surface photovoltaic effect [152]. When semiconductor surface is excited with a p polarized light, the electron momentum distribution immediately after photoexcitation is oriented along (for electrons excited from heavy holes sub-band) or perpendicular (for electrons excited from light holes sub-band) to the refracted light beam axis (Fig. 2.8a). At non-zero excitation angle electron distribution is tilted in respect to the surface. In general, parallel to the surface component of electron's motion towards the surface and motion in opposite direction should compensate each other. However, it is true only if the interface semiconductor/air could be regarded as specular surface. In other cases, electrons are scattered diffusively [153], which leaves uncompensated parallel to the surface component of electrons motion. After the LIPSS formation the diffuseness coefficient of those samples might be enhanced, which results in the formation of parallel to the surface component of THz emitting electric dipole. It should be mentioned, that this effect could be observed only for excitation with p-type optical light [152], as for s-type polarization electron momentum distribution always has spherical symmetry. Last-discussed effect could explain the THz emission from LIPSS samples dependence on the polarization of an excitation light for both ripples orientation (Fig. 5.10c). Red curves in Fig. 5.10c represent the difference THz signal (THz emission under p-polarized laser illumination – THz emission under s-polarized laser illumination). The ratio of the amplitudes of II and I THz peaks of this signal equals to 0.64, which, according to Method II (described in chapter 3.4.2), corresponds to the almost parallel to the surface THz emitting electric dipole. This result confirms that surface photovoltaic effect takes place in LIPSS samples and it is stronger for horizontal ripples orientation. However, the appearance of tilted to the surface THz emitting electric dipole was observed for both polarizations of excitation light. Which means that there should be more effects that affects photocarriers motion. It is possible that ripples could act as an optical lens. The ripples are believed to have a spherical shape, which illuminated at some angle, might focus laser radiation to the right side of the ripple (Fig. 5.10b bottom). Then, due to photo-Dember effect, electrons move from high concentration gradient region to the low concentration gradient region in the left side of the ripple which results in an appearance negative tilt angle of THz emitting electric dipole.

Even though the origin of THz generation in LIPSS structures is not completely clear, the THz pulse emission enhancement up to 4 times after ripples formation is unquestionable. Such an enhancement is a result of the appearance of tilted THz pulse emitting electric dipole, however, the question is if this explanation is enough. Fig. 5.11b represents the calculations of the dependence of THz pulse emission enhancement on the tilt angle θ of THz

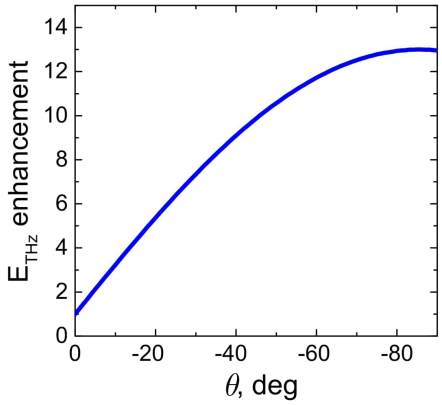

Figure 5.11: THz pulse amplitude dependence on the dipole tilt angle at the detection plane in transmission geometry. Results normalized to the THz pulse emitted from the perpendicular to the sample surface electric dipole. Calculations were done with $\alpha_1 = 45°$ and $n = 3.6$.

pulse emitting electric dipole in transmission geometry. According to these calculations, the LIPSS sample with the highest dipole tilt angle of 7.5° should emit THz pulse 2.7 times more effective than the reference GaAs. However, the experimentally measured THz emission enhancement is 3.4 times, which means that there must be an additional mechanism to explain these results. For instance, as the laser ablation heavily changes the semiconductor surface, it might lead to increased strength of the surface electric field. In the case where all other conditions for the last-mentioned LIPSS sample are kept constant, the surface electric field enlargement of 1.25 times would be enough to explain measured THz emission enhancement.

5.3.7 Conclusions

1. Laser-induced periodic structures on the semiconductor surface can enhance THz emission for a few times. The strongest emission and the most predictable results were obtained from the structures that could be achieved using excitation fluence close to the ablation threshold.

2. The enhancement of THz emission could be explained by the appearance of the parallel to the sample surface component of THz radiating electric dipole. The orientation of this dipole is responsible for better THz emission in transmission geometry.

3. Parallel to the sample surface component of THz radiating electric dipole has azimuthal dependencies that are the result of both: the direction of LIPSS and the semiconductor crystallographic orientation.

4. The THz emission dependence on an optical light polarization could be related to the surface photovoltaic effect.

6. Nanowires

Semiconductor nanowires (NWs) are few tens of nanometres in diameters and few microns lengths stripes that might be formed vertically or at some angle in respect to the substrate surface (Fig. 6.1). Such nanostructures attracted great interest in the last two decades. During that time there were developed various NWs formation techniques: from etching to the growth in MBE or MOCVD chambers. NWs find application in many fields: optoelectronic, optical radiation detection, solar cells and others. Thus in a few following chapters the NWs fabrication processes and main application areas will be introduced. Then an overview of NWs suitability in THz spectroscopy systems will be given. Finally, in the last two chapters the investigation of InAs, InGaAs and GaAs NWs will be presented.

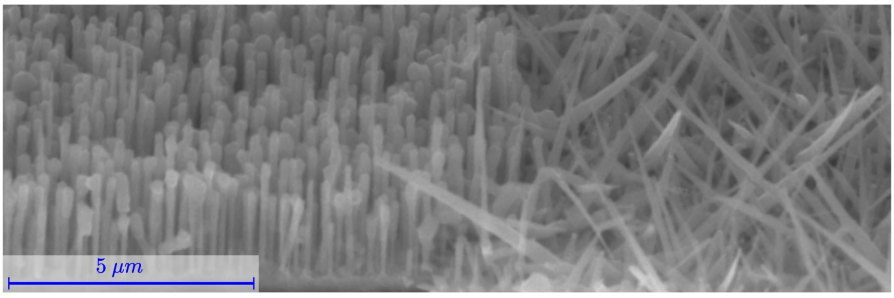

Figure 6.1: SEM images of GaAs nanowires grown on GaAs substrate. The difference in NWs alignment between the right and the left side of the image is mainly the result of the non-even distribution of native SiO_2. NWs were grown by the author of the dissertation under-supervision of R. Butkutė in Center for Physical Sciences and Technology, Vilnius, Lithuania. SEM image was done by A. Maneikis (Center for Physical Sciences and Technology, Vilnius, Lithuania).

6.1 Growth of the nanowires

The fabrication of semiconductor nanowires must be a very precisely controlled process, because even the smallest deviation from the desired param-

eters could be critical. For example, in NWs laser technology, uniformity of NW's diameter is essential for the NW's performance as a resonant cavity [154]. For NWs application in the field of optoelectronics, crystallographic phase control plays the key role, since the defects in crystal lattice effectively trap the photocarriers and act as a non-radiant recombination centres [155]. Precise control of the doping concentration and composition of the NWs is crucial for devices based on NW heterostructures [156].

Semiconductor nanowires could be fabricated via a wide variety of approaches that could be classified into two main categories: top-down and bottom-up. Fabricating NWs with the top-down technique involves the growth of desired semiconductor layer on the substrate and then the optical or electron beam lithography and etching processes take place. Such a method demonstrates its superiority in the nanometre control of NWs placement. However, the difficulty to focus a laser beam, limits the accuracy of NW's parameters' control in the few nanometre scale. The second method is based on the chemical synthesis process, which allows accurate control and tuning of the NW parameters during the growth. Compared to the top-down approach, the bottom-up techniques allow the control of the NW dimensions of an atomic precision, a fabrication of heterostructures, a production of exotic channel materials that may not be accessible in the bulk wafer form, and full control of the crystal surface facets formed during NW growth [157]. It is obvious that the bottom-up is more appropriate for the fabrication of high-quality NWs with the precisely controlled parameters. Moreover, this approach was used to fabricate NWs investigated in this work, therefore, only the bottom-up procedure will be described below.

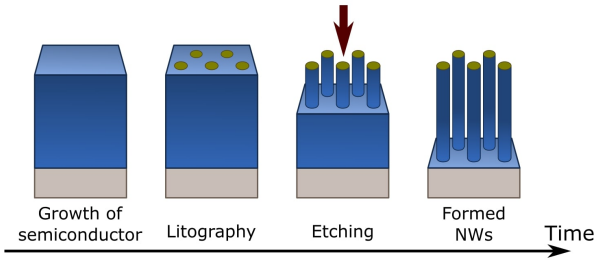

Figure 6.2: Schematic illustration of the top-down technique.

One of the bottom-up NWs fabrication methods is the growth performed on specific mask templates, allowing NW elongation in only one dimension while physically restraining growth in other directions. For instance, SiO_2 coated Si substrate might serve as a perfect template for NWs growth after the SiO_2 layer was processed either by nanoimprint lithography or by sim-

ple wet chemical etching to form site-selective mask [158]. Additionally, templates may be porous metal layers, polymer matrices, triangular grooves and etc. [159]. The main drawback of this technology is that high temperatures may trigger the chemical reactions between the template and NWs material, so the material of the template limits the choice of materials for NWs [160]. Another technology is a vapour-liquid-solid (VLS) method using a catalyst. The VLS mechanism was established 55 years ago by Wagner and Ellis in the growth of Si whiskers of micron sizes [161]. A catalyst, usually gold (Au), is deposited on the substrate and heated in order to form Au droplets. Then the vapour precursor of desired semiconductor (for instance Si) is released into the growth chamber. When precursor vapour interacts with liquid Au, Si is incorporated in Au droplet forming an alloy nanoparticle. Later, the Si-Au alloy becomes oversaturate by Si and Si atoms crystallize on a semiconductor substrate, forming a Si column that has a diameter approximately equal to the size of the Au droplet [161]. The NW growth by VLS method is illus-

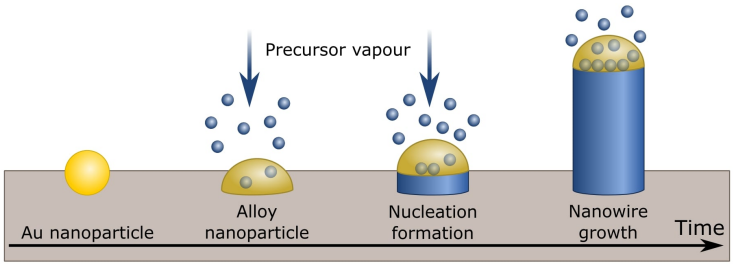

Figure 6.3: Schematic illustration of the VLS growth of semicodnuctor nanowires using an Au catalyst particle.

trated in Fig. 6.3. The NW growth using Au catalyst may cause some disadvantages: Au atoms may be incorporated into the NW resulting in deep level traps [158]. Thus, self-catalysed VLS method was established. According to this method, the nucleation of GaAs NW starts in the Ga droplets formed in the SiO_2 pinholes. It is worth mentioning that the growth direction of the NWs, grown by VLS method, depends on the crystallographic orientation of the substrate [162, 163]. In one of the latest works was reported the fabrication of dual-type semiconductor NWs by combining both template-directed and VLS techniques [164]. This technology might be very promising for the fabrication of NWs solar cells and LEDs as the wider spectrum range might be achieved. There exist some variation of VLS method, such as the Solution-Liquid-Solid (SLS) method. The NW growth process is analogous to VLS, only the components that make up the NWs do not come from the vapour phase, but from the solution. This method also requires a catalyst, which commonly is low melting metal, In, Bi, Sn nanoparticles [165]. The SLS method has sev-

eral advantages over VLS technology: it offers a systematic control of the NW's diameter and surface passivation level as well as the ability to produce large quantities of NWs simultaneously. On the other hand, fabrication of NWs using VLS method makes it much easier to control the growth direction and the crystalline structure of NWs [166].

The last but not least thing that should be discussed in this chapter is the crystalline structure of the semiconductor NWs. During the last decades, it was found out that III-V semiconductor nanowires can adopt either zinc-blende (ZB) structure, for instance, GaAs NWs on GaAs (111)B substrate [167], or wurtzite (WZ), for example, InAs NWs on Si (111) substrate [82], structure. The main difference between cubic ZB and hexagonal WZ crystal structure is the stacking of bilayers composing the crystal. The stacking sequence of ZB lattice is ABCABC (Fig. 6.4 the lower left image), where each letter represents a bilayer of III–V pairs. Whereas, the WZ lattices follow an ABABAB stacking sequence (Fig. 6.4 the upper left image). While growing the semiconductor NWs some planar defects might occur. The most common defect types are twin planes (Fig. 6.4 middle images) and stacking faults (Fig. 6.4 right images). The twin plane occurs when a single bilayer is mis-stacked so that the stacking sequence changes direction mirroring the previous stacking sequence. For instance, in ZB crystal, in sequence ABCACBA, C is the mis-stacked bilayer which creates the twin plane A. Another type of defects, stacking fault, occurs when a single bilayer is misplaced. For instance, in the WZ structure, sequence ABABACACA contains a stacking fault at bilayer C [154]. The importance of determining and controlling the crystalline structure of NWs lies in the fact that different crystal structures can have different optical and electrical properties. Thus, in some cases, it might be essential to determine the crystal structure of the NWs which is usually done by TEM measurements.

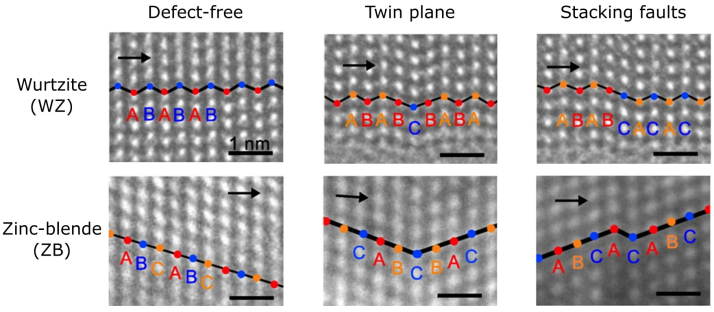

Figure 6.4: TEM images with the stacking sequences in InAs and InAsSb nanowire illustrating pure phase WZ and ZB together with some kinds of defects including twin planes and stacking faults. Adapted from [168].

6.2 Applications of nanowires

Semiconductor nanowires could be used in many electronic and optoelectronic applications, such as lasers, light emitting diodes, transistors, solar cells, detectors and etc. So, in this section, let us overview some of these fields.

In the development of semiconductor electronic and photonic devices, the mechanical and thermal stability of the materials is very important. Semiconductor NWs are characterized by much a lower melting point in comparison to bulk semiconductors. This is a great advantage in producing semiconductor devices that require extremely low defect concentration, because in order to reduce the number of defects NWs could be annealed in a few times lower temperature than bulk semiconductor. In addition, cutting, interconnecting, and welding of NWs could be done under "soft" conditions (in relatively low temperature), which greatly facilitate their integration into polymer matrices and organic semiconductor devices. It was also noticed that semiconductor NWs are about twice as strong as their bulk counterparts due to a reduction in the number of defects per unit length in NWs. On the other hand, when the diameter of the NWs is reduced to a smaller and smaller length scale, their thermal stability may become extremely sensitive to environmental changes such as temperature fluctuation, then if NW thickness becomes sufficiently thin or the bonding between constituent atoms is too weak, NWs can split into segments even at a room temperature [160].

Opportunity to create materials with high carrier mobility, and well-developed NWs fabrication and doping technologies are attractive conditions to produce NWs based electronic devices such as field transistors (FET) [169]. In FET production, the main advantage of NWs is their small dimensions which allow reducing device size to nanometre-scale thus increasing the density of the devices in an area unit for a 1000 times in comparison with bulk semiconductor-based FETs [166]. Usually, NWs transistors are made from horizontally lying NW with a gate contact on the top or at the bottom of NW. However, in 2006 there was presented an operating vertically integrated NW FET [170]. Such configuration allowed to further increase the transistor number per area unit. In this case, FETs may be fabricated directly on a substrate on which NWs are grown, thus reducing the costs of a device. The main problem with the production of NWs FETs is the self-formation of Schottky contacts after the deposition of a metal droplet on the NW. Luckily, further researches showed that ohmic contacts form after an annealing process [169]. The fast development of the NWs fabrication technology not only allows achieving the precise doping concentration when creating n- and p-type transistor channels, but also opens the possibility to create various

semiconductor heterojunctions inside the NW. For example, in 2003 there was created a single-electron transistor based on an axial heterojunction NW [171]. In addition, there could be formed a radial heterojunction NWs with a thin shell layer around the NW core. Such heterojunctions facilitate the formation of ohmic contacts in comparison with homogeneous NWs. Furthermore, the NWs with radial heterojunctions show better charge carriers injection into the contacts as well as reduced carrier scattering process in the NW core [169]. As Si-based technology is one of the best developed technologies in the world, the majority of the studies related to the NWs FETs was concentrated on the transistors formed from Si NWs [172]. However, nowadays a lot of attention is given to FETs based on GaAs NWs [173], InAs NWs [174] and Ge NWs [156].

Semiconductor NWs FETs could be used as the basis for the chemical and biological sensors as well as for the modern electromagnetic radiation detectors. Recently, Hahm *et al.* [175] presented a DNA sensor based on the peptide nucleic acid (PNA) receptor-modified p-type Si NW FET. PNA receptors become negatively charged by bonding DNA molecules, thus inducing a conduction channel in the transistor. In a result, the conductance of a device is enhanced and depends on the concentration of the attached DNA molecules [175]. NW conductance also changes by absorbing gas molecules on the surface. For example, ZnO NWs based detectors are very sensitive for oxygen molecules: O_2 molecules absorbed on the NW surface effectively captures electrons thus reducing the conductance of the NW [176]. In addition, the ZnO NW's energy bandgap matches ultraviolet range (3.37 eV), so the conductivity of ZnO NWs increases several times after illumination with UV radiation. Such feature is not only essential for an ultraviolet radiation photodetector but it also can be used in creating an optically controlled electronic switch analogue [177]. By choosing an appropriate materials for NW FET, one can create detectors that would cover most of the electromagnetic radiation ranges, including long-wave infrared (THz) range [178]. Due to small dimensions of NWs photodetectors, they are particularly attractive in the fabrication of an electromagnetic radiation sensor matrix or optically controlled logic circuits.

Another interesting feature of NWs is light trapping, thereby giving rise to enhanced optical absorption (in semiconductor NWs layer compared to their bulk counterparts) at specific resonance wavelengths depending on the size of the NWs. This, together with the possibility to increase the number of p-n junctions in the area unit, due to the small dimension of NWs, was the main stimulus to apply the NWs layer for solar cell [155]. The NWs, with a radial p-n junction, are considered as the most promising for solar cells' application, because in such structure the separation of charge carriers takes place not in the direction along the NW, but perpendicular to it. In this case, the distance

that photocarriers have to overpass while moving towards the pn-junction becomes close or equal to their diffusion length. In a result the number of photocarriers that were effectively separated increases dramatically. Additionally, lower quality materials can be used in such NW geometry compared to p-n junctions of bulk semiconductor, which leads to the reduced cost of the final device [179, 180]. Effective solar cells are also manufactured from NWs with axial p-n junctions. Such structures can withstand higher voltage and operate efficiently even with low doping concentrations of p and n layers, while radial p-n junction NWs operate effectively only when the doping concentration of the semiconductor is sufficiently large [181]. Similarly to NWs FET technology, in the field of NWs based solar cells, the main focus is put on Si NWs [182]. However, high efficiency is achieved by axial GaAs NWs [181] and InP NWs [183] based solar cells.

A device, which operation is based on the process, reversed to the one occurring in solar cells, is called light-emitting diode (LED). In NWs based LEDs the charge carriers are electrically injected into the NWs, where they recombine resulting in an electromagnetic radiation emission in the visible, ultraviolet and infrared range. Opportunity to grow NWs from different materials and combine them into various heterostructures leads to the creation of a wide variety of NWs based LEDs, which emission spectra overlap the entire range of electromagnetic radiation. Moreover, it was demonstrated that the GaN NWs layer containing a few InGaN/GaN disk-in-nanowire heterostructures could work as a powerful white light emitting diode [184]. It is worth to mention, that single ZnO NW LED operating at room temperature was demonstrated a few years ago [185]. Small NWs size, their stability, and controlled composition open the possibility to combine NWs with organic layers, which results in the birth of the powerful, flexible optoelectronic devices. Nowadays, technological opportunities allow easy optimization of the device performance, by changing the properties of organic and inorganic elements. Additionally, the organic matrix provides chemical stability of an active component, such as ZnO NWs, and protects it from mechanical deformation [186]. Detail investigation of a single NW revealed that it can act as a Fabri-Pero resonator. Furthermore, stimulated emission from NWs could be achieved after optical excitation. Firstly, the ultraviolet lasing was observed in ZnO NWs layers, and almost immediately there appeared reports of stimulated emissions from a single ZnO NW excited by picosecond laser pulses [187]. A few years later lasing from GaAs/GaAsP NW [188] and GaN NW [189] was reported. NW lasers are one of the most potential light sources in a high resolution near field microscopy because the properties of the coherent electromagnetic radiation from such a laser could be controlled by selecting the composition of NW.

In recent years, one more application field for semiconductor NWs has emerged. It is the fabrication of THz TDS system components: emitters, detectors, modulators. Two years ago very first demonstration THz emission from semiconductor NWs based biased THz emitter was reported. InGaAs NWs were fabricated in between integrated electrodes pattern via electron beam lithography and plasma etching. THz emission from such device was about 3 times stronger in comparison with an unbiased state [190]. Since the III-V semiconductor NWs posses high carrier mobilities, picosecond lifetimes and direct bandgap, they were suggested as an ideal alternative for THz photoconductive detectors. Moreover, due to inherent anisotropy, NWs could be a very promising material for polarization sensitive THz radiation detection. In 2017, Peng *et al.* presented a single InP NW detector with an optimized bow-tie antenna structure. Such a device exhibited excellent sensitivity, high signal-to-noise ratio of 50 dB, and a broad detection bandwidth up to 2 THz [191]. More advanced THz systems, suitable for ultrafast wireless THz communication, requires effective THz modulators that combine high modulation depth, fast optical switching speed, and broad operation bandwidth. Recently, NWs were proved to be excellent candidates for such an application. The performance of ultrafast THz modulator based on GaAs NWs arranged in a wire-grid configuration was demonstrated. There was achieved the switching time of less than 5 ps and dynamic range of -9 dB, and THz modulation in a range of 0.1 – 4 THz [192].

6.3 Investigation of InAs and composition-tunable InGaAs nanowires

6.3.1 Samples

Samples were fabricated in Walter Schottky Institut, Physik Department, Technische Universität München. InAs and InGaAs NWs were grown in a completely catalyst-free, selective area epitaxial growth mode on SiO_2/Si template using solid source MBE. The SiO_2/Si template was prepared on (111) p-type Si substrate with a 20 nm thick thermally grown SiO_2 mask prepatterned by nanoimprint lithography. The template exhibits a periodic pattern of 60 nm wide holes separated by 250 nm pitch. This enables the growth of NWs in a site-selective, highly periodic manner with minimal size distribution and homogeneous NW densities (Fig. 6.5a). InAs NWs were grown at the substrate temperature of 480°C in As-rich conditions (As/In ration = 12). In the first series, there were prepared InAs NWs of three different lengths 0.7 μm (NW0.7um), 1.8 μm (NW1.8um) and 3.3 μm (NW3.3um). In the second

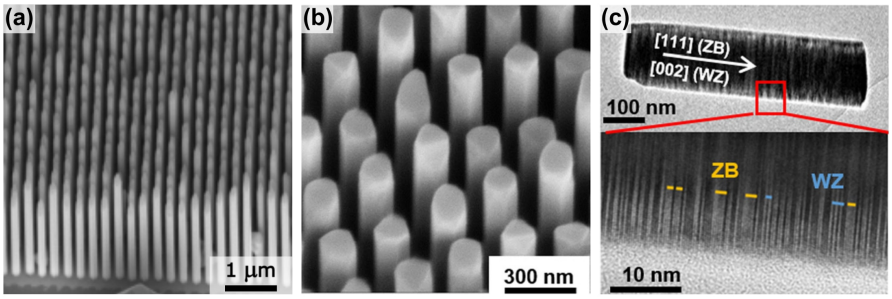

Figure 6.5: (a) SEM image of InAs NWs (1.8 µm length) recorded in a bird's eye view. (b) SEM image of InGaAs NW (x(Ga) = 0.48) along with the corresponding TEM data obtained from a single NW from the same sample, showing (c) the disordered layer stacking composed of ZB- and WZ-polytypes.

Table 6.1: InAs NWs samples.

Sample description	Abbreviation	Sample description	Abbreviation
0.7 µm length InAs NW	NW0.7um	InAs NWs with $InAs_{85\%}P_{15\%}$ shell	NW1_15%
1.8 µm length InAs NW	NW1.8um	InAs NWs with $InAs_{70\%}P_{30\%}$ shell	NW2_30%
3.3 µm length InAs NW	NW3.3um	InAs NWs with $InAs_{40\%}P_{60\%}$ shell	NW3_60%

series there were fabricated $\sim$ 3µm length passivated InAs NWs: the NW core of InAs was overlaid by thin, a few nm thick, $InAs_{1-x}P_x$ shell with P concentration of 15% (NW1_15%), 30% (NW2_30%) and 60% (NW3_60%). There was also a reference sample – InAs NWs without a shell (NW_ref). And in the last series there were grown $\sim$ 1µm length InGaAs NWs with different Ga concentration: x(Ga) = 0.00, 0.28, 0.40, 0.48 and 0.63. All NWs were oriented vertically along [111] direction as it was expected from the epitaxial relation with the Si (111) substrate. The NWs exhibits mostly hexagonal shape (Fig. 6.5b) and six sidewall facets are related to the {110} family of planes. From transmission electron microscope (TEM) images (Fig. 6.5c), it was found out that InAs NWs and InGaAs NWs with low Ga concentration (x(Ga)=0.28) are mostly wurtzite (WZ) crystalline phase with some stacking faults. With increasing Ga concentration intermix of WZ/ZB (zincblende) phases occur, while at high Ga concentration ZB phases become dominant.

6.3.2 THz emission from InAs NWs

The investigation of vertically aligned NWs starts from the THz emission measurements of three InAs NWs samples in reflection geometry. Peak-to-valley amplitudes of THz pulses emitted from different length InAs NWs are

summarized in Fig. 6.6a and compared with the best known THz surface emitter – p-type InAs. The measurements are done under s-polarized laser excitation. There could be seen, that the longer the NWs, the better the THz emission. Nevertheless, none of the InAs NWs samples exceeds THz emission efficiency of p-type InAs, however, the THz pulse amplitude of the longest NWs reaches up to 80% of the amplitude emitted from p-InAs under excitation by Ti:Sapphire laser ($\lambda = 800\,\text{nm}$). For further investigation of THz emission char-

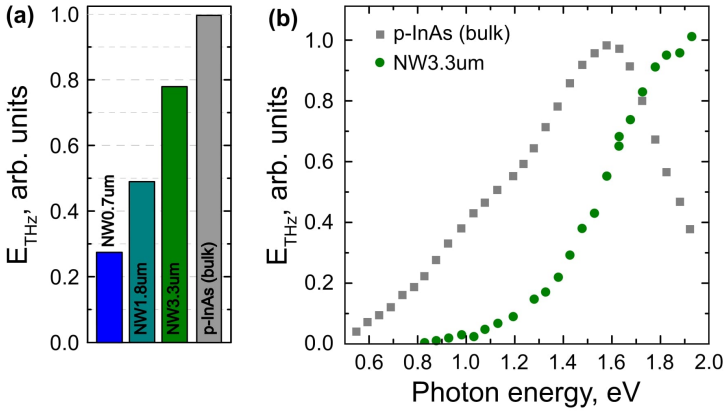

Figure 6.6: (a) THz pulses emitted from the different length InAs NWs after excitation by s-polarized Ti:sapphire laser pulses (the excitation fluence was 27 nJ/cm^2). (b) THz excitation spectra of the longest InAs NWs compared to the one obtained from bulk p-InAs (the excitation fluence was ∼50 nJ/cm^2).

acteristics and THz pulse generation mechanism in InAs NWs, the excitation wavelength (in an energy range from 0.55 eV to 1.95 eV) dependent THz emission measurements were performed. In Fig. 6.6b there are summarized the results for reference sample, bulk p-InAs, and the longest InAs NWs. Here, the two main differences between bulk and nanostucturized samples occur: (1) in case of NWs no THz emission efficiency maximum could be seen; (2) THz generation starts at higher excitation energies. The same tendency was observed for InAs NWs of all lengths. THz emission efficiency maximum in InAs is attributed to the intervalley scattering of photoexcited electrons [193]. In details, at first, increasing photon energy leads to an enhanced THz emission, due to an increase in initial photoexcited electron velocity. This statement is valid as long as the excess energy of photoexcited electrons in the main Γ valley of conduction band does not reach the energy separation between the high mobility Γ and subsidiary L and X valleys. At this point, THz emission starts to decrease due to the photoexcited electron transition to the valleys with the larger effective mass and lower mobility. However, it is obvious that in InAs NWs this process has an only minor effect in photoexcited carrier movement

and THz emission characteristics. This could be explained in terms of a momentum relaxation time in NWs ($\tau = \mu m^*/e$). The electron mobility in InAs NWs is at least 10 times smaller than in bulk InAs [82], thus the momentum relaxation time is also smaller and becomes comparable to the intervalley scattering time, which is in order a few hundreds of femtoseconds. As a result, only a very small amount of electrons is scattered into the subsidiary valleys. Short momentum relaxation time in InAs NWs is a result of a high density of donor-type point defects that occur in the surface accumulation layer at the native oxide/InAs interface and has electron densities that can exceed 10^{18} cm^{-3}. Last-mentioned defects are also responsible for the high intrinsic electron density in small diameter InAs NWs. In a result, in NWs with a diameter less than $\sim$ 100 nm, this intrinsic electron density might easily exceed 10^{17} cm^3 [194]. This might be the reason of a blue-shift in the THz emission spectral dependencies (Fig. 6.6b), as the conduction band might be filled and/or the photocarrier movement might be screened by the intrinsic electrons. Nevertheless, surface defects in NWs highly increase intrinsic electrons concentration and effectively scatter photoexcited electrons, thus lowering their mobility. Both effects weaken THz emission efficiency in NWs. (Previously described results are published in P1). Thus, in order to alleviate these effects and increase THz generation efficiency, surface-passivated InAs NWs, such as core-shell InAs-InAsP NWs, might be a good choice to try.

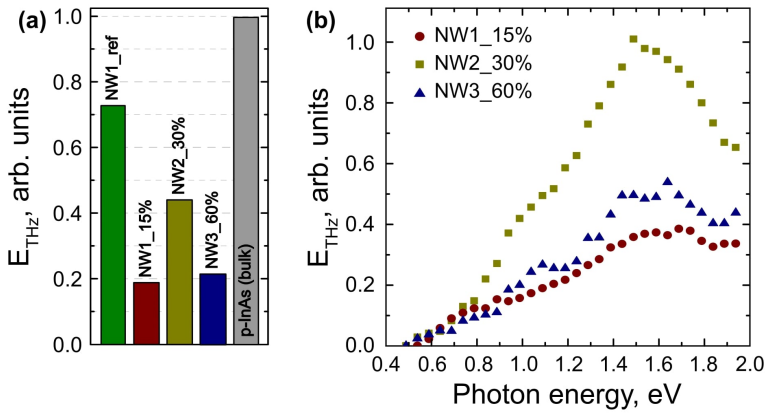

Figure 6.7: (a) THz pulses emitted from the passivated InAs NWs after excitation by s-polarized Ti:sapphire laser pulses (the excitation fluence was 27 nJ/cm^2). (b) THz excitation spectra of the passivated InAs NWs (the excitation fluence was $\sim$60 nJ/cm^2).

THz emission from passivated InAs NWs is summarized in Fig. 6.7a. It could be seen that $\sim$ 3 μm non-passivated InAs NWs (NW_ref) emits THz radiation as well as the longest (3.3 μm) InAs NWs of the first series. However

after passivation THz emission efficiency drastically decreases. The best THz emission was observed from the NWs with 30% of P in a NW shell, where the THz pulse amplitude remains 61% of the amplitude emitted from reference, non-passivated, NWs. Moreover, it could be seen from THz emission spectral dependencies (Fig. 6.7b) that a number of intrinsic electrons might be reduced as no blue-shift of THz peak amplitude is observed. Additionally, THz emission maximum in a spectral range of 1.4-1.6 eV, specific for bulk InAs, is now clearly visible for core-shell InAs-InAsP NWs with 30% of P, which also suggests that surface point defect concentration is reduced after the NWs passivation. However, it was not enough to obtain high efficiency THz emitters and another approach must be found.

6.3.3 THz emission from InGaAs NWs

As the NW's passivation does not give desired results, the alternatives are required and there comes an idea to try composition-tunable InGaAs NWs. THz pulses emitted from InGaAs NWs are shown in Fig. 6.8 where they are compared with bulk p-type InAs as a reference. When Ga concentration in InGaAs NWs is low $x(\mathrm{Ga}) < 0.3$, THz emission efficiency reaches only 30% of the respective peak-to-valley amplitude of bulk p-InAs. With increasing Ga content, THz pulse amplitude of InGaAs NWs increases and reaches its maximum, of about 70% compared to bulk p-InAs, at $x(\mathrm{Ga}) = 0.48$. For higher Ga concentration ($x(\mathrm{Ga}) > 0.6$), THz emission starts to decrease, which suggests that highly Ga-rich InGaAs NWs become less efficient due to increased bandgap values and associated lower carrier excess energy, lifetime and mobility. The intervalley scattering is also increased when approaching the limit of GaAs. At this point it is important to mention that InGaAs NWs are much shorter (their length is $\sim 1\mu$m) than the best emitting InAs NWs sample NW3.3um (their length was determined to be 3.3μm) presented in the previous chapter. Nevertheless being 3 times shorter InGaAs NWs with the $x(\mathrm{Ga}) = 0.48$ show THz pulse amplitude as high as 87% of the respective amplitude of the sample NW3.3um, which confirms that a change in NWs composition was a right step towards the more effective surface-based THz emitters.

In general, weak THz emission from low Ga concentration InGaAs NWs might be related to the three effects: (1) THz radiation absorption by the intrinsic electrons, (2) electron-electron scattering and (3) the electron scattering by the surface defects. The first effect can be neglected, as the InGaAs NWs samples show high THz radiation transmission coefficient (close to 90%). Speaking about second effect, the photocarrier mobility dependence on an intrinsic electron concentration should be discussed. In InAs NWs with a diameter less than ~ 100 nm, intrinsic electron density might exceed 10^{17} cm^3 [194], while

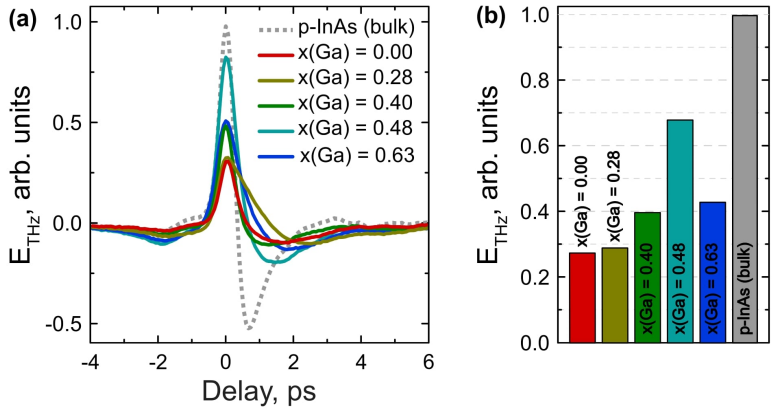

Figure 6.8: (a) THz pulses emitted from the surfaces of InGaAs NW arrays after excitation by s-polarized Ti:sapphire laser pulses. (b) Corresponding amplitude normalized to the peak-to-valley amplitude of bulk p-type InAs. The excitation fluence was 27 nJ/cm^2 for all measurements.

in medium Ga concentration InGaAs NWs it is reduced to 10^{16} cm^3 [195], as it was estimated from the works by our colleagues from Technische Universität München, who fabricated NW samples investigated in this dissertation. However, electron mobility in InAs is reduced only 1.5 times when going from electron concentration of 10^{16} cm^3 to 10^{17} cm^3 [196]. This suggests, that electron-electron scattering very weakly affects THz emission efficiency. This leaves the electrons scattering by the surface defects to be the main reason of weaker THz emission from low Ga concentration InGaAs NWs. Recently, x-ray photoemission spectroscopy studies and correlated semi-quantitative space charge calculations of the surface electronic structure of the as-grown In-rich InGaAs NWs, performed by our colleagues, reveal that native oxides indeed cause donor-type surface states [195], which reduce electron mobility thus reducing THz emission efficiency. Moreover, other discoveries shows, that electron mobilities in InAs NWs with diameters from 70 to 150 nm are in the range of $\sim 800-2000$ cm^2/(V s) values [194,197] which are more than 10 times smaller than the bulk electron mobility of InAs at room temperature (i.e., $>$ 20000 cm^2/(V s) [198]). For Ga concentration in the mid-compositional range, the elimination of surface electron accumulation layer was observed, which leads to the flat-band conditions [195] and higher THz generation efficiency. THz emission decreases at higher Ga concentration due to the lower excess energy of photoexcited electrons.

6.3.4 THz excitation spectra of InGaAs NWs

To obtain a full view of THz generation characteristics in composition-tunable InGaAs NWs, the measurements of THz emission dependence on an excitation photon energy was performed (Fig. 6.9). It could be noted, that at photon energies close to the energy bandgap THz pulse amplitude emitted by Ga-rich InGaAs NWs increases faster than those emitted by In-rich InGaAs NWs. This behaviour might be explained as follows. In In-rich InGaAs NWs,

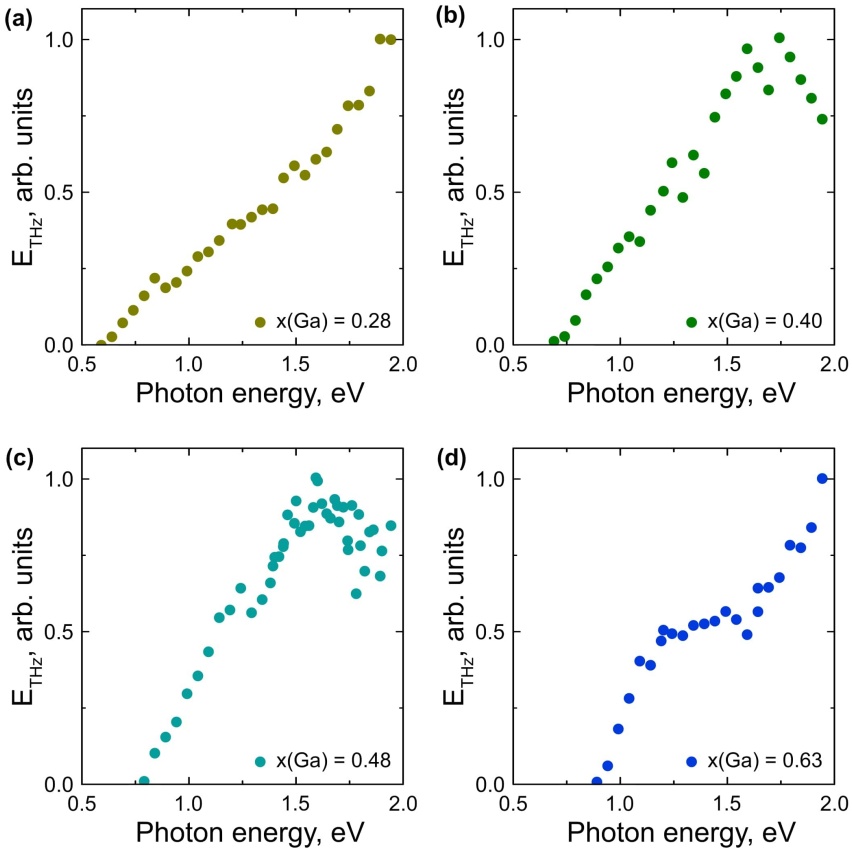

Figure 6.9: THz excitation spectra of InGaAs NW samples with different Ga-contents (a)–(d) measured as a function of laser photon energy with a pump fluence of 60 nJ/cm^2.

THz generation is attributed to the photocarrier's diffusion due to their concentration gradient. This effect is weaker near the energy bandgap and slowly increases with the higher photon energies where the photoexcited electron's excess energy and carrier density gradient is higher (Fig. 6.9a and 6.9b). On the contrary, in Ga-rich InGaAs NWs the THz emission efficiency increases much faster which suggests that there exist a surface electric field, which, from

the very beginning of optical absorption, separates photoexcited electron and hole resulting in THz emitting electric dipole (Fig. 6.9c and 6.9d).

For further investigation THz emission of composition-tunable InGaAs NWs was measured under excitation of three technologically relevant excitation wavelengths: 780 nm, 1030 nm, and 1500 nm (Fig. 6.10). The choice of wavelengths depends on their utility in THz-TDS systems. As it could be expected from the previous measurements (Fig. 6.9) THz pulse amplitudes decrease with increasing excitation wavelength. THz pulse amplitudes exhibit in general similar dependence as shown in Fig. 6.8, except that the strongest THz pulse is emitted from the InGaAs NWs with $x(\mathrm{Ga}) = 0.4$ rather than NWs with $x(\mathrm{Ga}) = 0.48$. This inconsistency could be attributed to the different laser

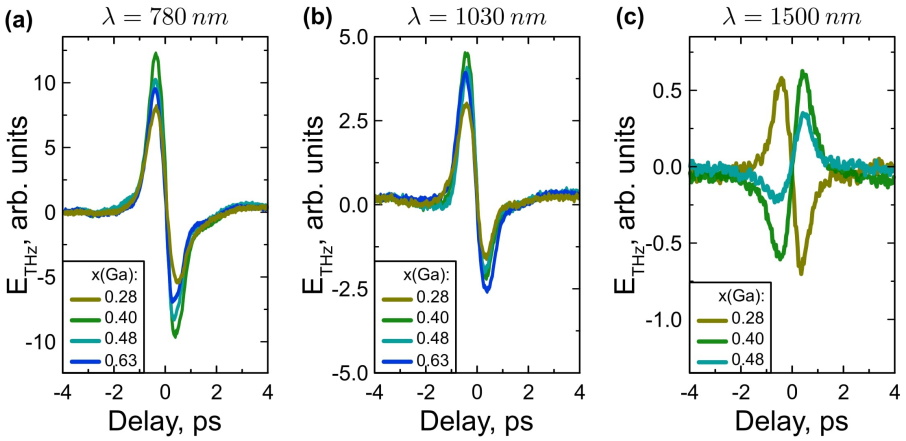

Figure 6.10: THz pulses emitted from the InGaAs NWs with different Ga-contents $x(\mathrm{Ga})$ excited at three technologically relevant wavelength: (a) 780 nm, (b) 1030 nm, and (c) 1500 nm. Samples were excited at the 45° excitation angle in the reflection geometry with a pump fluence of 60 nJ/cm^2.

pulse repetition rate of the laser systems used for the later measurements an for the previous ones. Previously, measurements were done with Ti:Sapphire laser system with the pulse repetition rate of 76 MHz, while the later experiments were performed with the system with a pulse repetition rate of 200 kHz. At higher pulse repetition rate, the time between two optical pulses is shorter than photocarrier relaxation time in semiconductor, which results in photocarriers accumulation in the semiconductor conduction band. As some of the conduction band states are already filled, newly arrived optical pulse creates fewer photocarriers, which means weaker THz radiation emission. However, the most interesting thing here is the phase change of THz pulse (phase shift) at the excitation wavelength of 1500 nm in the InGaAs NWs with $x(\mathrm{Ga}) = 0.4 - 0.5$. It should be pointed out that Ga-rich InGaAs NWs ($x(\mathrm{Ga})$

= 0.63) emits too weak THz pulse at this wavelength and it is not shown here. It was concluded, that the phase shift indicates the different origin of THz generation. In general, THz pulse is generated by the photocarriers moving along the nanowire due to built-in surface electric field or concentration gradient. At high excitation wavelength, the optical radiation absorption is less effective in the whole body of the NW, thus fewer photocarriers are mowing in the upper part of the NW. On the contrary, more photocarriers start to move in the direction of a built-in electric field at the NW/Si substrate heterojunction, which forces electrons to move in the opposite direction than their associates in the upper part of the NW [199]. When the motion of the photocarriers at the NW/Si interface becomes dominant, the sign of emitted THz pulse changes. Previously described results are published in P3.

6.3.5 Conclusions

- The efficiency of THz emission from $In_{1-x}Ga_xAs$ NWs dependence on Ga concentration reaches its maximum at $x(\mathrm{Ga}) = \sim 0.4 - 0.5$.
- The weaker THz emission from In-rich InGaAs NWs and InAs NWs is related to the high concentration of the donor-type surface defects.
- At first, with increasing $x(\mathrm{Ga})$ THz pulse amplitude increases while the effects related to the donor-type surface defects are more important that the decreasing excess energy of photoexcited electrons. At higher $x(\mathrm{Ga})$, THz pulse amplitude starts to decrease as the influence of lower electron's excess energy becomes dominant.

6.4 Investigation of tilted to the surface GaAs nanowires

The main difference of the NWs investigated in the previous chapters and the NWs in this chapter is the NWs orientation with respect to the substrate surface. InAs and InGaAs NWs were perpendicular to the surface – the most common orientation of NWs. However, this orientation is not favourable for THz radiation outcoupling from the sample. Nevertheless, strong THz emission or even its enhancement was observed in many works [17, 20, 82]. Here comes an idea that this enhancement is related to the lower index of refraction (n) of semiconductor NWs layer than of their bulk counterpart, as the lower n means easier THz radiation transmission through the interface NWs layer/air. Thus measurements of n should be the next step towards a better understanding of THz emission from NW arrays. It will be shown in the follow-

ing chapters that this might be done by calculating the contribution of parallel and perpendicular to the surface electric dipole components in the THz emission dependence on an azimuthal or excitation angle. However, the InAs and InGaAs NWs does not have a parallel to sample surface component, thus they could not be used for the last-mentioned experiment. Whereas GaAs NWs forms a non-zero tilt angle to the surface, which means that THz emitting electric dipole has both, parallel and perpendicular, electric dipole components. Thus, GaAs NWs were chosen for the determination of n.

6.4.1 Samples

Tilted GaAs NW samples were grown in MAX-lab, Lund University, Sweden, by MBE on high temperature (550°C) GaAs (110) substrates. The NWs growth was induced by gold droplets. The length of the NWs is approximately 4 μm, their diameter is in the range of 70 – 100 nm. Four types of NW samples have been fabricated: GaAs NWs (NW1), GaAs core – GaMnAs shell NWs (NW2), GaAs base – InGaAs core – GaMnAs shell NWs (NW3) and GaAs core – GaMnAs shell NWs (NW4). It should be pointed out that NWs was grown on GaAs (110) substrate forms $\sim 55°$ angle between the NW and the surface (Fig. 6.11a). The sample NW4 was removed from the substrate by embedding NW layer into epoxy resin, then placing sample into cryostat and cooling down to 15 K. At such low temperature due to different GaAs substrate's and epoxy resin's coefficient of thermal expansion, epoxy resin layer seceded from the substrate. The NWs lift-off process is illustrated in Fig. 6.11b.

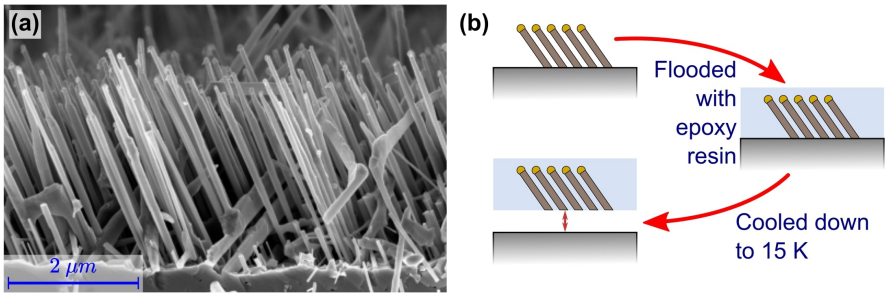

Figure 6.11: (a) SEM image of the sample NW3. (b) Schematic illustration of sample NW4 preparation.

6.4.2 THz emission from nanowires

As always, the investigation starts from the THz pulse emission measurements under excitation with Ti:sapphire laser pulses in reflection geometry (Fig. 4.4). All investigated samples emit THz pulses of the amplitude 3–6 times

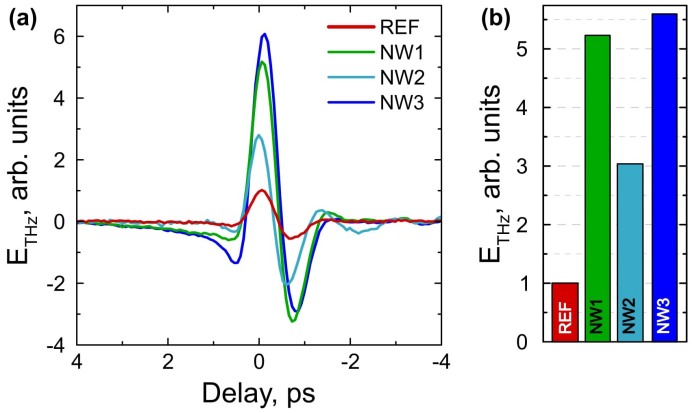

Figure 6.12: (a) THz pulse emission from tilted semiconductor NWs compared with SI GaAs substrate (REF) in reflection geometry. (b) Corresponding amplitudes of these pulses normalized to the peak-to-valley amplitude of SI GaAs substrate.

higher than the reference SI GaAs substrate. In the case of NWs, the dipole orientation and position are known, as it is known that photocarriers are moving along the NWs in a built-in electric field. As GaAs NWs were grown by VLS method and has a metallic (gold) cap on the top, the origin of the previously mentioned electric field is attributed to the Schottky contact which occurs at the interface metallic cap/NW [19]. As investigated GaAs NWs are non-vertically align, THz emitting electric dipole in these samples is tilted. Such a dipole could be analysed as a combination of parallel and perpendicular to the surface electric dipoles.

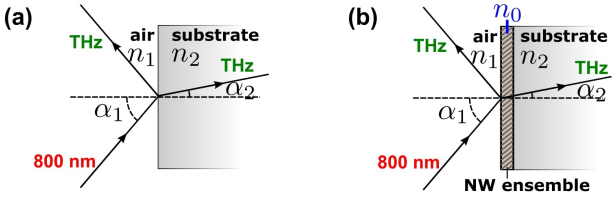

Figure 6.13: Illustration of two media (a) and three media (b) models that were used to simulate the radiation behaviour of tilted electric dipoles.

In order to better understand the physical processes in NWs it is worth to simulate radiation behaviour of these dipoles. For this purpose theoretical calculations based on W. Lukosz theory [101] was developed. The formulas describe THz generation in semiconductors and radiation outcoupling into air. The schematic illustration of this idea is shown in Fig. 6.13a. A THz electric

field ($E^p(\alpha_1,\phi)$) is defined as

$$E^{(p)}(\alpha_1,\phi) = \sqrt{\frac{3}{2\pi n}}\cos\alpha_1 \frac{\cos\theta\sin\alpha_2 + \sin\theta\cos\alpha_2\cos\phi}{\cos\alpha_2 + n\cos\alpha_1} \tag{6.1}$$

where $n = n_2/n_1$. n_1 and n_2 are refraction indexes of air and semiconductor respectively, α_1 is an excitation angle, α_2 is the angle of refraction, and ϕ – the azimuthal angle. The angle θ describes the orientation of electric dipole. A tilted to the surface THz radiating dipole can be decomposed into a perpendicular ($\theta = 0°$) and parallel ($\theta = 90°$) to the surface components. The perpendicular dipole always radiates the same field while the radiation field of parallel dipole depends on the azimuthal angle ϕ as $\cos\phi$.

The two media model does not consider the contribution of NWs, thus the formula was extended from two to three media (air, NW ensemble and substrate (Fig. 6.13b)) model to simulate THz emission from NWs layer. It is worth to mention, that is this case NW arrays are regarded not as separated NWs but as a thin layer of the refractive index n_0. The calculated angular dependencies strongly depend on n_0 [200]:

$$[E^p(\alpha_1,\phi)]_{1,0,2} = (\frac{n_2}{n_0})^{\gamma/2} E^p(\alpha_1,\phi) \tag{6.2}$$

here $E^p(\alpha_1,\phi)$ is the efficiency of THz radiation in air of the same dipole located in the substrate at the interface to air when the intermediated NWs layer is absent [101]. Parameter γ refers to dipole orientation: $\gamma = 5$ for perpendicular and $\gamma = 1$ for parallel. Eq. 6.2 has two main parameters: α_1 and ϕ that could be changed during the experiment. As a result, the measurement of THz emission dependence on each, excitation (α_1 is changing and ϕ is fixed) or azimuthal (α_1 is fixed and ϕ is changing) angle, could be used to determine refractive index if NWs layer.

6.4.3 THz emission dependence on an excitation angle

If the azimuthal angle position is fixed and α_1 is changing, the THz emission dependence on an excitation angle would be obtained. Dots in Fig 6.14a represent such a dependence of the tilted NWs sample NW4. In this case THz radiation pattern could be successfully described by the same equations 6.1 and 6.2 with only a small change (the illustration of the idea could be found in Fig. 6.14b). The tilt angle is known in this sample and equal $\theta = 35°$. Thus the calculations could be done by varying the refraction index n_0 in order to find the best match between the theory and experiments. From the best fit (Fig 6.14a red line), the effective index of refraction of NWs layer was determined to be $n_0 = 2.6$. In comparison the green line (Fig. 6.14a) represents the calculated

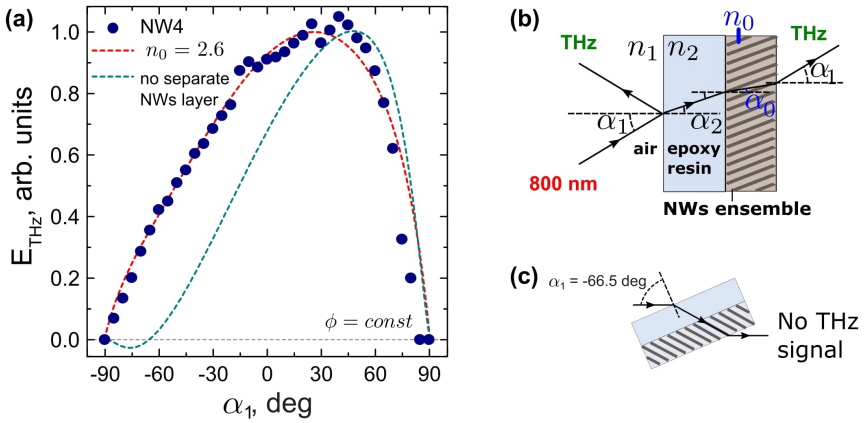

Figure 6.14: (a) THz emission dependence on an excitation angle compared to theoretical calculations. Red and green curves are obtained using two media and three media models (Fig. 6.13) respectively. The parameters used for calculation are $\theta = 35°$, $n_1 = 1$, $n_2 = 1.6$ and $n_0 = 2.6$. (b) Illustration of three media model that was used to simulate the radiation behaviour of tilted electric dipole in substrate free NWs sample. (c) Illustration of THz pulse emission at the excitation angle $\alpha_1 = -66.5°$ in case the NWs ensemble is not treated as a separate layer.

behaviour of NWs ensemble, when it is not treated as a thin layer. It is clear that such curve poorly describes experimental results. The main difference occurs at the excitation angle $\alpha_1 = -66.5°$. In the case of a two media model, at this excitation angle, according to the Huygens principle, the direction of propagation of the THz radiation should be directed along the axis of the nanowires. The THz pulse emitting electric dipole is also oriented along this axis, so the THz radiation generated in this case should be very weak. However, experimental results show quite strong THz pulse emission at this α_1. These results can only be explained when the refractive index of the NWs ensemble is significantly higher than the refractive index of the epoxy resin (1.6). This requires using a three-media model (Fig. 6.13b). Using this model, the best agreement between experimental and theoretical results is obtained when $n_0 = 2.6$,

6.4.4 THz emission azimuthal dependencies

To obtain more information about processes happening in GaAs NWs, THz emission azimuthal dependencies were measured (Fig. 6.15a). All samples exhibits a single-cycle ($\cos\phi$) azimuthal dependencies, that could be explained by the electric dipole orientation in the sample. This dipole has a fixed position in NWs and rotates together with the sample when the azimuthal angle is changing similarly to non-stoichiometric GaAs sample Ga4 that was dis-

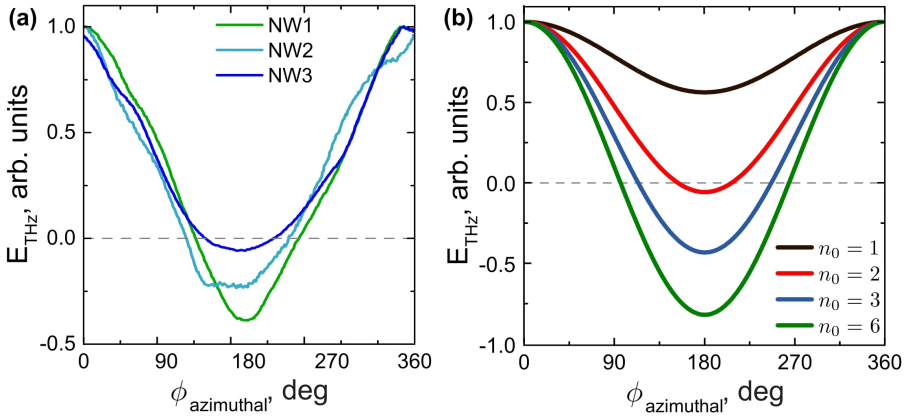

Figure 6.15: (a) THz emission azimuthal dependencies of tilted NWs samples. (b) Theoretical calculations of THz emission azimuthal dependencies for the tilted semiconductor NWs ensemble on GaAs substrate with a different effective index of refraction.

cussed in chapter 4.3.3. As it was mentioned such a dipole could be divided into two components. The contribution of perpendicular and parallel dipoles in azimuthal dependencies changes with respect to n_0. One of the possible explanations of such behaviour can be as follows. According to Snell's law $\sin\alpha_0 = n_1/n_0 \sin\alpha_1$. Moreover, the influence of perpendicular dipole in the efficiency on THz radiation behaves as $\sin\alpha_0$ and of parallel dipole as $\cos\alpha_0$ where α_0 is the angle of refraction in NW ensemble. As α_0 decreases with increasing refraction index n_0 the role of perpendicularly oriented dipole decreases while for parallel it remains almost the same (for small angle of refraction $\sin\alpha_0 \to 0$ while $\cos\alpha_0 \approx 1$). As a consequence, the azimuthal dependence becomes more symmetrical with respect to the $E_{THz} = 0.0$ axis as could be seen in Fig. 6.15b.

The formulas, presented in chapter 6.4.2, was used to simulate the THz radiation behaviour of tilted GaAs NWs (Fig 6.16 dashed lines) and compared to the experimental results (Fig 6.16 solid lines). After the comparison of theoretical calculations and experimental results (Fig. 6.16), n_0 was estimated to be 2.8, 2.5 and 2.0 for NW1, NW2 and NW3 samples respectively.

It is worth to mention that it would be hardly possible to measure refraction index of NWs layer by means of traditional THz TDS methods. For instance calculated THz radiation reflection coefficient for GaAs substrate is approximately 0.555 and for NW sample (in case of NW length – 3 μm and $n_0 = 2.5$) on GaAs substrate it changes only by 0.2%. Such a small change is bellow the sensitivity limit of THz TDS spectrometer due to intensity fluctuations of a femtosecond laser.

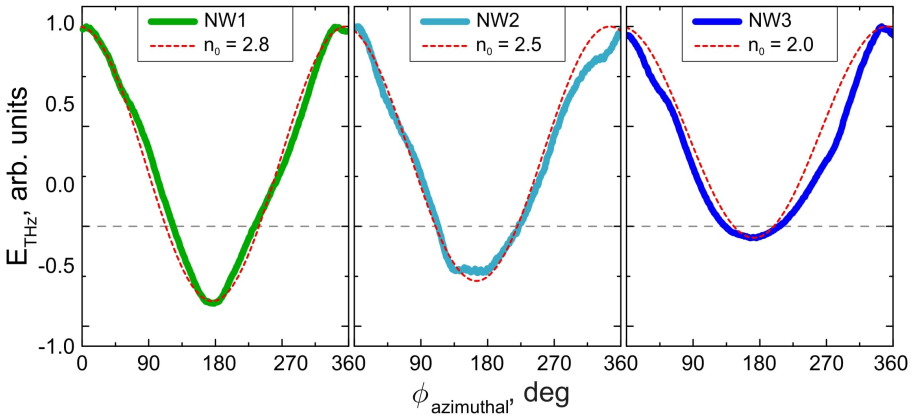

Figure 6.16: THz emission azimuthal dependencies of non-vertically aligned GaAs NWs samples (NW1, NW2, NW3) compared with theoretical calculations based on equation 6.2, when $\alpha_1 = const$ (dashed lines).

6.4.5 Discussion on THz emission from GaAs NWs

In the previous section, it was shown that THz emission from NWs is well described by the three media model, where NWs layer has an effective index of refraction n_0 that differs from the refractive index n of the substrate. For GaAs NW, n_0 was found to be less than n. It will be shown below that the model allows determining how much times THz emission from NWs layer is stronger than that of the substrate. To begin with, it is worth to examine the most common case – THz emission from vertically aligned NWs in the reflection geometry. The analysis starts with the equation for orthogonal dipoles derived by W. Lukosz [200]:

$$[E^p(\alpha_1,\phi)]_{1,0,2} = (\frac{n}{n_0})^{5/2} E^p(\alpha_1,\phi) \tag{6.3}$$

where $E^p(\alpha_1,\phi)$ is described in eq. 6.1.

This equation predicts an increase in THz pulse amplitude if the n_0 of the emitting layer is smaller than the n of the substrate (when the dipole dynamics is independent of the properties of the layer). For the values of n_0 determined previously (Fig. 6.14 and Fig. 6.16), the equation predicts an increase in THz amplitude from 2 to 5 times (Fig. 6.17a, green dots). There are two main factors that determine the THz radiation enhancement. First of all, the angle between the THz emitting electric dipole axis and the direction of propagation of the THz radiation is bigger in the layer with the lower index of refraction. This results in an increase of THz pulse amplitude by n/n_0 times. Another effect is related to the change in the solid angle of electromagnetic radiation at the

semiconductor-air interface. The ratio of solid angles of radiation in semiconductor and air is described by the equation [102]:

$$\frac{d\Omega_1}{d\Omega_2} = n^2 \frac{\cos\alpha_2}{\cos\alpha_1} \tag{6.4}$$

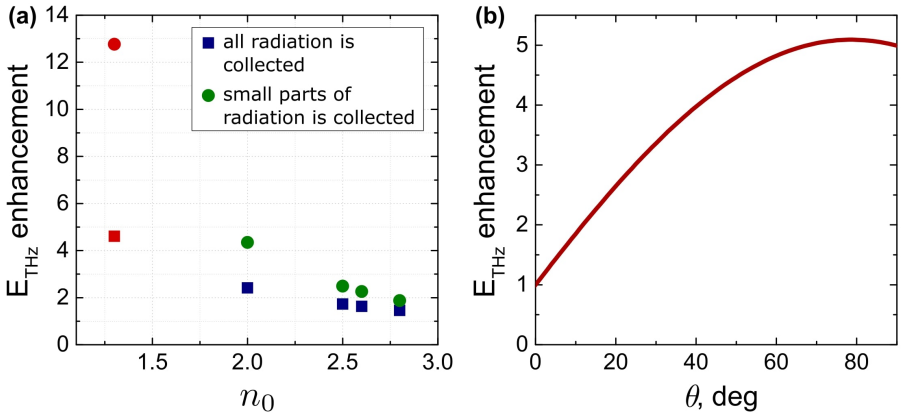

Figure 6.17: (a) The dependence of THz emission enhancement on the effective index of refraction n_0 of the NW layer. The calculations are done for perpendicular to substrate surface NWs. Red dots represents the situation when n_0 is close to 1. (b) THz pulse amplitude dependence on the dipole tilt angle at the detection plane in reflection geometry. Results normalized to the THz pulse emitted from the perpendicular to the sample surface electric dipole. Calculations were done with $\alpha_1 = 45°$ and $n = 3.6$.

According to this equation, the solid angle of radiation emitted from the THz emitting electric dipole located in the NWs layer to the air is $(n/n_0)^2$ times smaller than when the dipole is located in the substrate. Moreover, the energy density of THz radiation per unit area is reduced by the same number of times. Thus, the amplitude of the emitted THz pulse would increase by n/n_0 times. However, this is true only in case of a large divergence of THz radiation or THz detector with a small aperture. In contrast, in all experiments the efforts have been put to generate THz beams with the smallest possible divergence that almost all the THz radiation could be collected in the detector. In this case, the W. Lukosz equation (eq. 6.3) transforms into:

$$[E^p(\alpha_1,\phi)]_{1,0,2} = (\frac{n}{n_0})^{3/2} E^p(\alpha_1,\phi) \tag{6.5}$$

The THz pulse emission enhancements for GaAs NWs samples calculated using this eq. 6.5 are shown in Fig. 6.17a as blue dots. In practice, in order to have the most effective THz generation conditions, the divergence of THz radiation is kept in medium-range and then the THz emission enhancement

values are somewhere between blue and green dots (Fig. 6.17a). It should be noted that the values of n_0 of GaAs NWs layers obtained in this work are higher than it would be expected by evaluating the small semiconductor/air volume ration in NWs layer ($n_0 \approx 1.3$). Thin layer properties in the THz region were also investigated by TDS spectroscopy and a higher-than-expected electric conductivity of this layer was obtained [201]. It is not yet clear what causes the higher refractive index and conductivity values of the layers, but if the n_0 of the NWs layer could be reduced, a further increase in THz pulse amplitude could be expected (Fig. 6.17a red dots).

The possibility to growth tilted NWs is a unique way to rotate the THz emitting electric dipole and thereby further increase the THz pulse amplitude. Such an increase as a function of the dipole tilt angle, when the THz source is located in the substrate with $n = 3.6$ and the measurements are done in reflection geometry, is shown in Fig. 6.17b. If the refractive index is lower, the influence of θ on the THz emission enhancement decreases. For instance, the amplitude of THz pulse emitted from the electric dipole located in the media with $n_0 = 2.6$ and tilted at the angle $\theta = 35°$ (sample NW4) should be 2.5 times larger than from perpendicular dipole located in GaAs substrate (To gain such an enhancement in GaAs substrate the dipole should be tilted at $\theta = 18°$). The total increase in THz amplitude according to the calculations described for the sample NW4 is $2.5 * 1.6 = 4$, where the factor 2.5 is determined by the more favourable dipole orientation in tilted NWs and the factor 1.6 is related to the reduced NWs layer refractive index in comparison with the substrate. In the literature, enhancement of THz emission from semiconductor nanostructures is often related to the better THz radiation outcoupling into free space. Interestingly, according to the model used in this work, THz radiation outcoupling from the THz pulse-emitting layer is always 100% and does not depend on n_0, while the main mechanism of THz emission enhancement is more favourable direction of THz radiation propagation in respect to the THz emitting electric dipole axis.

It could be stated, that the described model explains the THz pulse enhancement shown in Fig. 6.12 quite well. The calculations predict about 4 times higher amplitude of the THz pulse, while experimentally obtained values are slightly higher. This small mismatch can be explained by the change in the THz radiation solid angle discussed above. To sum up, the dynamics of photoexcited charged carrier in the investigated GaAs NWs and GaAs substrate are very similar. Moreover, similar THz emitting electric dipoles are created in both materials. While, THz emission enhancement in case of NWs is mostly related to the smaller index of refraction of the NWs layer.

6.4.6 Conclusions

- Theoretical calculations based on three media (air, NW ensemble and substrate) model is suggested.
- From theoretical calculations the effective index of refraction n_0 of the NW layer is determined.
- The index of refraction n_0 of the NW layer is smaller than that of SI GaAs substrate, which means the bigger angle between THz generation direction and THz emitting electric dipole axis. This results in enhanced THz emission from GaAs NWs.

7. Main Results and Conclusions

In this work, several types of semiconductor nanostructures have been investigated using conventional and newly developed laser-assisted THz pulse emission techniques. Also, the models, that explains the characteristics of THz pulse emission from semiconductor nanostructures, have been suggested and the main reasons of THz emission enhancement have been identified.

1. Nanostructurization of semiconductor substrates often results in a formation of longitudinal structures on the surface (Ga15 and LIPSS). The investigation have shown that such a surface geometry is very important as it leads to an uneven distribution of photoexcited charge carriers and to the emergence of a parallel to the surface photocurrent. This photocurrent causes the tilting of the THz emitting electric dipole and is the main reason of THz emission enhancement.

2. In rarer cases, nanostructures can significantly change the optical properties of the semiconductor surface (Ga4). In this case, the enhancement of THz emission results from the change in nonlinear-optical constants associated with nanostructured semiconductor crystallography.

3. InAs nanowire layers are no better THz sources than InAs substrate due to the negative influence of surface defects on the THz generation process. By increasing the amount of Ga in InGaAs nanowires the influence of the surface on the THz generation process gradually decreases. As the number of Ga concentration approaches the $x(\mathrm{Ga}) = 50\%$, the highest THz emission efficiency is achieved. A layer of sufficiently long nanowires of this composition could be expected to be several times more efficient THz pulse emitter than a reference p-InAs substrate.

4. The analysis of THz pulse emission features of semiconductor nanowires could be done by regarding semiconductor NWs as a thin layer with a refractive index n_0 which is smaller than refractive index of the substrate of the same semiconductor. Due to smaller n_0, the angle between the THz generation direction and the THz emitting electric

dipole axis is increased resulting in enhanced THz emission. Such a model denies the widespread belief that the main mechanism of THz emission enhancement in NWs is the better THz radiation outcoupling from semiconductor to the air.

8. Santrauka

8.1 Įvadas

Pastaraisiais metais laikinė terahercinių dažnių spektroskopija (THz-TDS) yra vis dažniau naudojama įvairiose mokslo bei pramonės šakose. Tai puiki metodika narkotinių bei sprogių medžiagų aptikimui saugumo sistemose [3], vėžio diagnostikai medicinoje [4], kokybės kontrolei maisto pramonėje [5], paveikslų restauracijai mene [6] it t.t. Be to THz-TDS nepamainomas įrankis puslaidininkinių medžiagų bei jų darinių tyrimuose: ji leidžia nustatyti elektronų judrį, relaksacijos trukmę, draustinį juostų tarpą, atstumus tarp laidumo juostos slėnių [7] ir kt. Visiems minėtiems taikymams reikalingi efektyvūs, kompaktiški, pigūs ir paprastai naudojami THz spinduliuotės emiteriai.

Šiandien galima rasti pačių įvairiausių THz spinduliuotės šaltinių, tokių kaip kvantų kaskadų lazeriai [8], įvairūs diodai [9], lauko tranzistoriai [10], netiesiniai kristalai [11], fotolaidžios antenos [12] ir kt. Deja, dauguma jų yra brangūs, dirba tik tam tikromis sąlygomis, pvz. prie itin žemų temperatūrų, kitiems reikalingi įtampos šaltiniai, dar kiti yra didelių gabaritų, sudėtingai montuojami ir dar sudėtingiau pozicionuojami. Alternatyva anksčiau išvardintiems THz spinduliuotės šaltiniams galėtų būti paviršiniai emiteriai – tai ultratrumpais optiniais impulsais sužadinami puslaidininkių paviršiai, kurie pasižymi keletu privalumų. Pirma, tokie emiteriai yra maži, kompaktiški bei paprastai montuojami. Antra, jie gali būti aktyvuojami plačiame optinių bangų ruože. Trečia, šiems THz spinduliuotės šaltiniams dirbti nereikalinga pridėta įtampa, tad jie yra pigesni bei ilgaamžiškesni. Deja, minėti emiteriai nėra tokie efektyvūs, kaip, pvz. fotolaidžios antenos. Nepaisant to, paviršiniai emiteriai yra patrauklūs kandidatai THz spinduliuotės šaltiniams. Be to, pastaruoju metu vis daugėja pranešimų, kad nanostruktūrizavus puslaidininkio paviršių, galima net kelis kartus sustiprinti THz spinduliuotės emisiją. Kelis kartus didesnės amplitudės THz impulsai buvo stebėti iš InN nanostulpelių [13], Si nanoadatėlių [14], porėto InP paviršiaus [15] bei Si [16], Ge [17], InGaAs [18], GaAs [19] ir InAs [20] nanovielelių. Nepaisant puikių rezulta-

tų, THz spinduliuotės generacijos mechanizmai, taip pat kaip ir THz emisijos sustiprėjimo priežastys puslaidininkinėse nanostruktūrose vis dar nėra žinomos. Taigi, pagrindinė šios disertacijos paskirtis yra praplėsti turimas žinias bei paskatinti tolesnius tyrimus susijusius su THz spinduliuotės emisija iš puslaidininkinių nanostruktūrų.

Darbo tikslas

Išsiaiškinti lazerio impulsais inicijuotos THz impulsų emisijos sustiprėjimo puslaidininkiniuose nanodariniuose priežastis.

Darbo uždaviniai

- Sukurti kompleksinę matavimo metodiką, tinkamą puslaidininkinių darinių THz emisijai tirti.
- Ištirti nestechiometrinio GaAs ir lazeriu graviruotų GaAs bandinių THz emisijos priklausomybes nuo įvairių optinio žadinimo sąlygų. Išsiaiškinti GaAs paviršiaus nanostruktūrizavimo įtaką THz emisijos efektyvumui.
- Ištirti statmenų padėklui InGaAs nanovielelių THz emisijos ypatybes. Išsiaiškinti THz spinduliuotės generavimo efektyvumo priklausomybę nuo nanovielelių sudėties.
- Ištirti pasvirusių padėklo atžvilgiu GaAs nanovielelių THz emisijos ypatybes. Paaiškinti GaAs nanovielelių THz emisijos efektyvumą lemiančias priežastis.

Darbo naujumas

- Sukurta nauja metodika, leidžianti nustatyti THz impulsus generuojančio dipolio orientaciją puslaidininkinio padėklo atžvilgiu. Nustatyta, kad šio dipolio orientacija pasikeičia padėklo paviršiuje suformavus nanodarinius.
- Nustatyta, kad lazeriu sužadintų nanovielelių visuma THz impulsus spinduliuoja kaip tam tikro lūžio rodiklio n_0 plonas sluoksnis. Nustatyta, kad mažesnis nei padėklo n_0 lemia palankesnę THz spinduliuotės generavimo kryptį THz impulsus emituojančio dipolio ašies atžvilgiu, kas ir yra pagrindinė THz spinduliuotės emisijos sustiprėjimo pasvirose GaAs nanovielelėse priežastis.

- Pirmą kartą ištirta nestechiometrinio GaAs ir LIPSS darinių THz impulsų emisija. Atrasta nestechiometrinio GaAs modifikacija efektyviai spinduliuojanti THz impulsus žadinančiam spinduliui krintant statmenai į puslaidininkio paviršių.

Ginamieji teiginiai

- THz emisijos iš nestechiometrinio GaAs ir LIPSS darinių sustiprėjimas gali būti paaiškintas eksperimentiškai stebimu lygiagretaus paviršiui elektrinio dipolio susiformavimu po fotosužadinimo ir paviršiaus elektrinio lauko sustiprėjimu po nanostruktūrizavimo.
- Efektyviausiai terahercinius impulsus spinduliuoja InGaAs nanovielelės, susidedančios iš panašaus In ir Ga atomų kiekio. THz emisijos susilpnėjimas mažos Ga koncentracijos junginiuose susijęs su elektronų sklaida paviršiniais defektais.
- GaAs nanovielelių visumą laikant tam tikro lūžio rodiklio n_0 plonu sluoksniu galima gana tiksliai aprašyti GaAs nanovielelių terahercinės spinduliuotės emisijos ypatybes. Šis modelis atskleidžia pagrindinę THz emisijos sustiprėjimo puslaidininkinėse nanovielelėse priežastį – geresnę generuojamos THz spinduliuotės kryptį spinduliuojančio elektrinio dipolio ašies atžvilgiu.

Autorės indėlis

Disertacijos autorė surinko visus eksperimentinius stendus, kurie buvo naudojami ruošiant disertaciją, bei atliko visus matavimus. Taip pat dalyvavo atliekant gautų duomenų analizę ir rengiant mokslinius straipsnius. Be to autorė parengė ir pristatė žodinius bei stendinius pranešimus konferencijose. Visos publikacijos ir konferencijų pranešimai parengti autorės mergautine pavarde (Beleckaitė).

8.2 Literatūros apžvalga

Elektromagnetinių bangų sritis nuo 0.1 iki 10 THz vadinama terahercinių (THz) diapazonu [21]. Pirmasis žmogaus sukurtas THz spinduliuotės šaltinis buvo dujinis lazeris, kurio spinduliuojamų bangų dažnis siekė nuo 0.3 iki 5 THz [9]. Vėliau estafetę perėmė aukštadažniai diodai [9], laisvų elektronų lazeriai [10], kvantų kaskadų lazeriai [8], optiškai žadinami puslaidininkiniai paviršiai [76] bei fotolaidžios antenos, davusios pradžia laikinės THz spektroskopijos (THz-TDS) sistemoms [24]. Pastarosios rado pritaikymus įvairio-

se mokslo, pramonės bei meno srityse, nuo puslaidininkinių medžiagų tyrimų [7] iki paveikslų restauracijos [6]. Nepaisant to vis dar vyksta aktyvios THz spinduliuotės emiterių paieškos.

Pastaruoju metu nemažai dėmesio sulaukia paviršiniai THz impulsų šaltiniai – tai optiškai žadinami įvairių puslaidininkių, tokių kaip InAs [56], GaAs [52], GaTe [63], InSb [60], InP [53] ir kt., paviršiai. THz spinduliuotės generacija šiuose puslaidininkiuose aiškinama paviršinio elektrinio lauko [52], foto-Demberio [57], optino lyginimo [66], paviršinio elektrinio lauko indukuoto optinio lyginimo [70] arba anizotropinės fotosrovės efektais [72]. THz spinduliuotės emisija taip pat buvo stebėta iš įvairių puslaidininkinių nanostruktūrų: porėtų sluoksnių [15], nanoadatėlių [14] bei nanovielelių [20]. Svarbu pažymėti, kad šiai dienai skaičiuojama apie 12 mokslinių straipsnių, kuriuose pristatomas THz impulsų emisijos iš puslaidininkinių nanostruktūrų sustiprėjimas lyginat su lygiais puslaidininkiniais paviršiais. Tačiau vis dar trūksta žinių apie minėtose struktūrose vykstančius fizikinius procesus, tad tolesni puslaidininkių nanostruktūrų tyrimai yra labai svarbūs.

Darbe tiriamos trijų tipų nanostruktūros: susiformavusios nestechiometrinio GaAs auginimo metu, lazeriu indukuotos periodinės paviršinės struktūros (LIPSS) ir nanovielelės. Disertacijoje, prieš kiekvienos nanostruktūros tyrimus pateikta trumpa literatūros apžvalga, kurioje aptarti konkrečios nanostruktūros formavimo būdai, bei apžvelgtos panaudojimo galimybės.

8.3 Tyrimo metodikos

Visi tyrimai atlikti taikant įvairias laikinės THz spektroskopijos metodikas. Visos naudotos metodikos rėmėsi THz impulsų emisija iš tiriamojo bandinio. Eksperimentams buvo naudojamos tiek standartinės (THz impulsų emisijos priklausomybė nuo žadinančio kvanto energijos; THz impulsų emisijos azimutinės priklausomybės), tiek naujos metodikos (dvigubo impulsinio žadinimo THz impulsų emisija (DPP, publikuota P4 straipsnyje); THz impulsus emituojančio elektrinio dipolio pasvirimo nustatymo iš pralaidumo (1 metodas) ir atspindžio (2 metodas) matavimų metodikos (publikuota P5 straipsnyje). Dauguma eksperimentų atlikti naudojant trijų pakopų "Coherent" Ti:safyro lazerinę sistemą, kuri spinduliuoja 150 fs trukmės impulsus, kurių bangos ilgis yra 800 nm, pasikartojimų dažnis 76 MHz ir impulso energija 6.5 nJ. Prie šios sistemos THz impulsų detekcijai buvo naudojama THz spinduliuotės poliaziracijai jautri fotolaidi antena iš žemoje temperatūroje auginto GaAs (UAB Teravil). Priklausomybės nuo kvanto energijos matavimai buvo atlikti su lazerine sistema, kurią sudaro Yb:KGW lazerinis (PHAROS, Šviesos konversija Ltd.) ir parametrinis stiprintuvas (ORPHEUS, Šviesos konversija, Ltd.). Yb:KGW

lazerio centrinis dažnis 1030 nm, impulso trukmė 160 fs, pasikartojimų dažnis 200 kHz, vidutine galia 6,5 W. Parametrinis stiprintuvas generuoja 140 – 160 fs trukmės impulsus, centrinis dažnis derinamas gana plačiame diapazone, nuo 640 nm iki 2600 nm, vidutinė išėjimo galia 100 – 500 mW, priklausomai nuo generuojamo bangos ilgio. Prie šios sistemos THz impulsų detekcijai buvo naudojama THz spinduliuotės poliaziracijai jautri fotolaidi antena iš GaAsBi (UAB Teravil).

8.4 Tyrimas

Nestechiometrinio GaAs tyrimai

Bandiniai

Bandiniai paruošti Optoelektronikos technologijų laboratorijoje, FTMC. Nestechiometrinio (NS) GaAs sluoksniai buvo auginami molekulinių pluoštelių epitaksijos (MBE) metodu ant savitojo laidumo (100) kristalografinės orientacijos GaAs padėklų. Auginimo metu padėklo temperatūra siekė 540°C, o As ir Ga srautų santykis buvo 5.8. Po auginimo atlikta NS sluoksnių elementinės sudėties analizė parodė, kad abu bandiniai yra praturtinti Ga. Bandinio Ga4 sluoksnio storis 5-6 μm, o paviršiaus struktūros yra kalnelių pavidalo (diametras 3 μm, aukštis of 400 nm). Bandinio Ga15 storis 3-4 μm, paviršinė struktūra – grioveliai, kurių gylis $\sim$ 200 nm, plotis $\sim$ 400 nm ir ilgis 5 μm. Abiejų bandinių skenuojančio elektronų mikroskopo (SEM) nuotraukos pateiktos pav. 8.1.

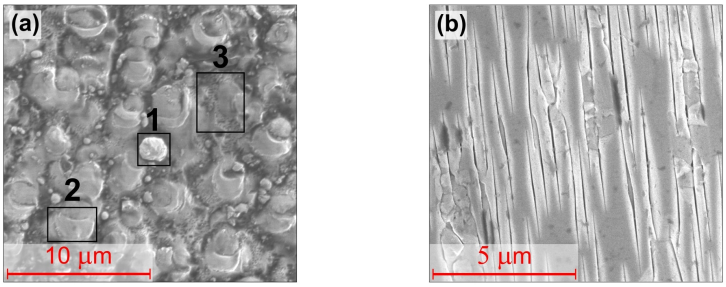

8.1 pav.: NS GaAs bandinių SEM nuotraukos. (a) Bandinys Ga4 su kalnelius primenančiomis nanostruktūromis. (b) Bandinys Ga15 su griovelių formos nanostruktūromis.

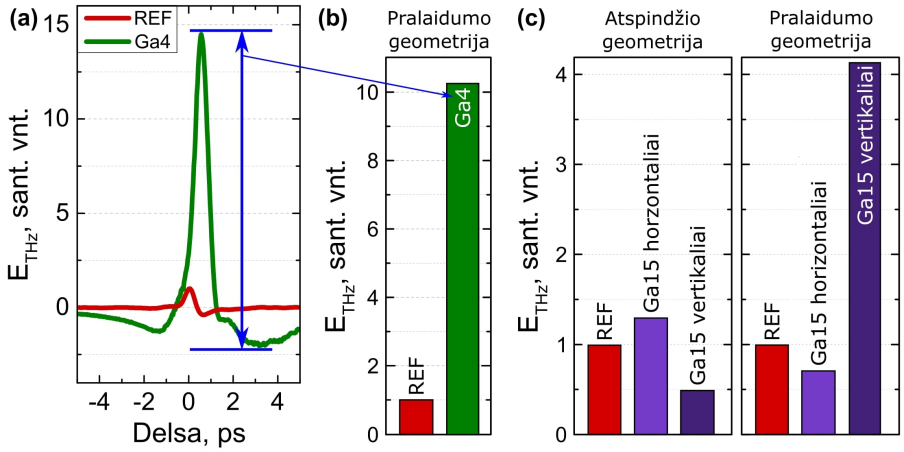

8.2 pav.: (a) Bandinio Ga4 ir savojo laidumo GaAs (REF) spinduliuojami THz impulsai išmatuoti pralaidumo geometrijoje. Azimutinis kampas pasirinktas taip, kad detektuojamas signalas būtų maksimalus. (b) Minėtų THz impulsų amplitudės. (c) Bandinio Ga15 spinduliuojamų THz impulsų amplitudės išmatuotos atspindžio ir pralaidumo geometrijoje, esant dviems specifinėms bandinio orientacijoms.

THz impulsų emisija iš nestechiometrinio GaAs

Pirmiausia buvo išmatuoti NS GaAs bandinių emituojami THz impulsai, jie palyginti su atraminiu bandiniu – SI GaAs (REF) (pav. 8.2). Tam kad THz impulsų amplitudžių skirtumas būtų aiškiau matomas, bandinių emituojamų impulsų pilnos amplitudės, nuo signalo minimumo iki maksimumo, (toliau amplitudės) buvo sunormuotos į REF bandinio THz impulso amplitudę ir atidėtos histogramose (pav. 8.2b ir pav. 8.2c). Iš čia akivaizdu, kad bandinys Ga4 emituoja 10 kartų didesnės amplitudės THz impulsus negu SI GaAs. Tuo tarpu, bandiniui Ga15 buvo išskirtos 2 specifinės orientacijos: kai grioveliai yra orientuoti statmenai (Ga15 vertikaliai) ir lygiagrečiai (Ga15 horizontaliai) optinio stalo plokštumai. Iš pav. 8.2c matosi, kad THz emisijos sustiprėjimas atspindžio ir pralaidumo geometrijoje smarkiai skiriasi: atspindžio geometrijoje sustiprėjimo beveik nėra, o pralaidumo geometrijoje bandinio Ga15 emituojamo THz impulso amplitudė net 4 kartus didesnė už atraminio bandinio.

Taip pat buvo atlikti ir THz impulsų emisijos priklausomybės nuo išorinio magnetinio lauko tyrimai (pav. 8.3). Matavimai atlikti žadinant bandinį 0° kampu. Be magnetinio lauko, bandinys Ga4 efektyviai emituoja THz spinduliuotę, o THz spinduliuotės emisija iš bandinio Ga15 nestebima. Pridėjus 0.5 T magnetinį lauką, THz impulsų emisija iš Ga4 beveik nepasikeičia, o štai Ga15 pradeda emituoti THz impulsus. Gauti rezultatai leidžia teigti, kad THz spinduliuotės generavimo mechanizmai šiuose bandiniuose yra visiškai skirtingi.

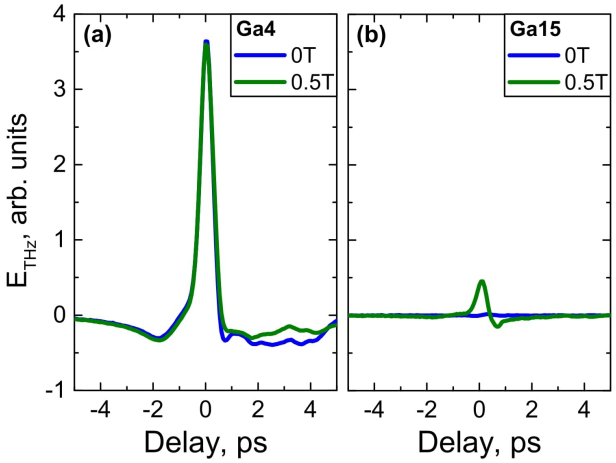

8.3 pav.: NS GaAs bandinių Ga4 (a) ir Ga15 (b) emituojami THz impulsai su ir be išorinio magnetinio lauko.

NS GaAs bandinio su kalnelių pavidalo struktūromis (Ga4) tyrimas

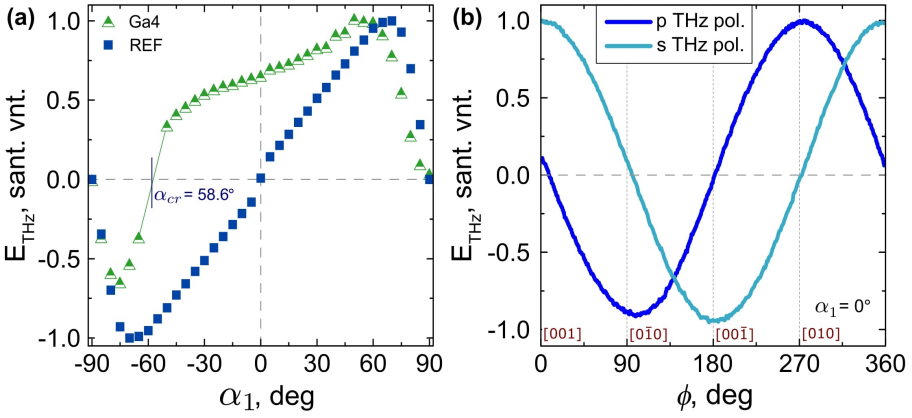

8.4 pav.: (a) Bandinio Ga4 ir savojo laidumo GaAs (REF) spinduliuojamų THz impulsų amplitudės priklausomybė nuo žadinančios spinduliuotės kritimo kampo. (b) Bandinio Ga4 spinduliuojamų THz impulsų amplitudės priklausomybė nuo bandinio azimutinio kampo žadinant s-tipo arba p-tipo poliarizacijos optine spinduliuote. Matavimai atlikti pralaidumo geometrijoje, kai $\alpha_1 = 0°$, o THz detektorius orientuotas taip, kad detektuotų p-tipo poliarizacijos THz spinduliuotę. $\phi = 0°$, atitinka situaciją kai bandinio [001] kristalografinė kryptis yra lygiagreti detektoriaus auselėms.

Siekiant daugiau sužinoti apie bandinį Ga4 buvo atlikti THz impulsų emisijos nuo žadinančios spinduliuotės kritimo kampo matavimai (pav. 8.4a).

Bandinys buvo sukamas aplink ašį, statmeną optiniam stalui, tokiu būdų keičiant optinės spinduliuotės kritimo kampą. Eksperimento metu buvo detektuojama THz spinduliuotė, iš bandinio išėjusi pralaidumo kryptimi. Gauti rezultatai palyginti su gautais tokiu pat būdu tiriant REF bandinį (pav. 8.4a, mėlyni taškai). Pagrindinis skirtumas tarp Ga4 ir REF bandinio matomas ties $\alpha_1 = 0°$, kuomet REF bandinio amplitudė nukrenta iki 0, o Ga4 bandinyje THz spinduliuotės emisija išlieka pakankamai efektyvi. Toks rezultatas leidžia teigti, kad bandinyje Ga4 egzistuoja lygiagrečią bandinio paviršiui komponentę turintis elektrinis dipolis. Pasinaudojus 1 elektrinio dipolio pasvirimo kampo nustatymo metodu (aprašytu skyriuje 3.4.1) buvo nustatyta, kad bandinyje Ga4 po optinio sužadinimo susiformuoja kampu $\theta = 8°$ pasviręs elektrinis dipolis.

Lygiagrečios paviršiui elektrinio dipolio komponentės egzistavimas taip pat buvo patvirtintas ir THz emisijos azimutinės priklausomybės matavimais (pav. 8.4b). Matavimai buvo atlikti pralaidumo geometrijoje, žadinant bandinį statmenai paviršiui bei detektuojant s-tipo (žydra kreivė) arba p-tipo (mėlyna kreivė) THz spinduliuotės poliarizaciją. Kadangi matavimai atlikti optiškai žadinant kampu $\alpha_1 = 0°$, statmena paviršiui THz emituojančio elektrinio dipolio komponentė neturi jokios įtakos rezultatams, tad išmatuotos $\cos\phi$ formos kreivės atspindi tik lygiagrečios paviršiui komponentės savybes. Pav. 8.4b stebimas 90° poslinkis tarp s-tipo ir p-tipo THz spinduliuotės poliarizacijos, liudija, kad pasviro elektrinio dipolio padėtis bandinyje Ga4 yra fiksuota, t.y. nepriklauso nei nuo žadinančios spinduliuotės kritimo, nei nuo bandinio azimutinio kampo.

Šiame skyrelyje aprašyti rezultatai publikuoti P2 straipsnyje.

NS GaAs bandinio su griovelių pavidalo struktūromis (Ga15) tyrimas

THz spinduliuotės emisijos priklausomybės nuo žadinančios spinduliuotės kritimo bei bandinio azimutinio kampo tyrimai buvo atlikti ir su kitu NS GaAs bandiniu Ga15 (pav. 8.5). Gauti rezultatai smarkiai skyrėsi nuo Ga4 bandinio. Pirma, šis neemituoja THz impulsų žadinamas kampu $\alpha_1 = 0°$. Antra, jam galima išskirti dvi specifines orientacijas: grioveliai orientuoti vertikaliai ir horizontaliai optinio stalo atžvilgiu. Pirmiausia, reiktų pastebėti, kad priklausomybės nuo žadinančios spinduliuotės kritimo kampo vertikaliai ir horizontaliai bandinio Ga15 orientacijai smarkiai skiriasi. Horizontaliai orientuotas Ga15 (raudoni taškai pav. 8.5a) praktiškai nesiskiria nuo atraminio SI GaAs bandinio (žali taškai pav. 8.5a), o vertikaliai orientuotas Ga15 (mėlyni taškai pav. 8.5a) pasižymi visiškai kitokia priklausomybe. Pastaroji gali būt susijusi su lygiagretaus paviršiui THz emituojančio elektrinio dipolio atsiradimu.

Svarbu paminėti, kad pastarasis dipolis neatsiranda žadinant bandinį statmenai paviršiui ir jo stipris priklauso nuo žadinančios spinduliuotės kritimo kampo (kuo didesni sužadinimo kampas, tuo didesnė vieno griovelio krašto dalis lieka šešėlyje).

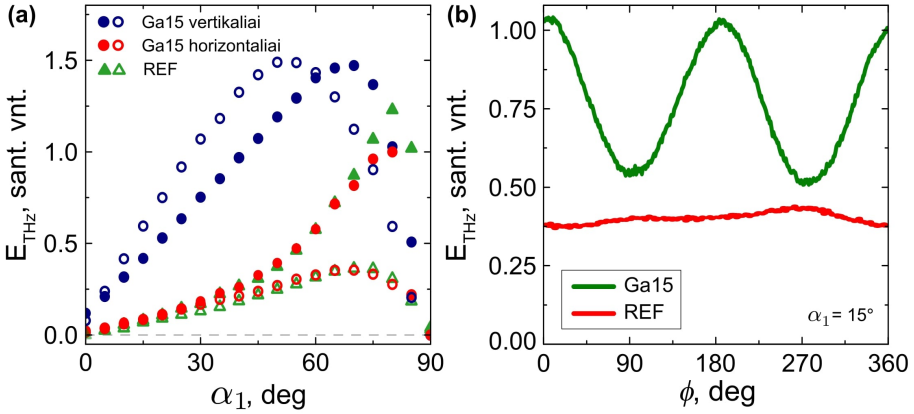

8.5 pav.: (a) Bandinio Ga15 ir savojo laidumo GaAs (REF) spinduliuojamų THz impulsų amplitudės priklausomybė nuo žadinančios spinduliuotės kritimo kampo išmatuota dviems specifinėms bandinio Ga15 orientacijoms. Tuščiaviduriai taškai atitinka s-tipo poliarizacijos, pilnaviduriai – p-tipo poliarizacijos žadinančią spinduliuotę. (b) Bandinio Ga15 ir savojo laidumo GaAs (REF) spinduliuojamų THz impulsų amplitudės priklausomybė nuo azimutinio kampo. Matavimai atlikti pralaidumo geometrijoje, kai $\alpha_1 = 15°$ ir žadinama p-tipo poliarizacijos optine spinduliuote.

Bandinio Ga15 THz spinduliuotės emisijos priklausomybės nuo bandinio azimutinio kampo matavimų rezultatai (pav. 8.5b) taip pat smarkiai skiriasi tiek nuo anksčiau aptarto bandinio Ga4, tiek nuo atraminio SI GaAs. Atraminis bandinys nepasižymi ryškia azimutine priklausomybe, Ga4 turėjo ryškią $\cos\phi$, o Ga15 – $\cos 2\phi$ priklausomybę. Nors iš pirmo žvilgsnio tokia priklausomybė galėtų būt susieta su optinio lyginimo ar elektriniu lauku indukuoto optinio lyginimo efektais, anksčiau stebėta THz spinduliuotės emisijos priklausomybė nuo žadinančios spinduliuotės kritimo kampo rodo, kad minėti netiesiniai efektai nėra dominuojantis THz impulsų generacijos mechanizmas tad negali nulemti bandinio azimutinės priklausomybės. Tad akivaizdu, kad $\cos 2\phi$ priklausomybė yra susijusi su bandinio griovelių orientacija: signalas yra maksimalus, kai grioveliai orientuoti vertikaliai ir minimalus, kai horizontaliai. Matavimai buvo atlikti pralaidumo geometrijoje bandinį žadinant $\alpha_1 = 15°$ kampu, tad statmenos paviršiui THz emituojančio elektrinio dipolio komponentės indėlis į THz impulsų emisiją stebimas ties visais azimutiniais kampais (žalia kreivė pav. 8.5b yra pakilusi virš tiesės $E_{THz} = 0$), tačiau jos dydis išlieka pastovus. Kai bandinys yra orientuotas vertikaliai, dėl šešėliavimo efekto atsi-

radusio lygiagretaus paviršiui elektrinis dipolis emituojama THz spinduliuotė konstruktyviai interferuoja su THz spinduliuote išspinduliuota iš statmeno paviršiui dipolio, tokiu būdų sustiprindama bendrą THz spinduliuotės signalą. Kai bandinys orientuotas horizontaliai, lygiagretus dipolis neatsiranda (šešėliavimo nėra) ir detektuojamas tik statmeno paviršiui dipolio emituojamas THz impulsas.

Apibendrinimas

1. Bandinio Ga15 THz emisiją lemia elektronų judėjimas statmenai ir lygiagrečiai bandinio paviršiui. Lygiagrečiosios srovės komponentės dydis ir kryptis priklauso nuo griovelių orientacijos žadinančios šviesos kritimo plokštumos atžvilgiu.
2. Bandinio Ga4 THz emisijos nepakeičia pridėtas magnetinis laukas, todėl tikėtina, kad THz spinduliuotės generavimą nulemia ne laisvieji elektronai.
3. Keičiant bandinio Ga4 azimutinį kampą, THz impulsus spinduliuojantis elektrinis dipolis išlieka pastovaus dydžio ir sukasi kartu su bandiniu.
4. Išskirtinė bandinio Ga4 savybė – efektyvi THz emisija žadinant statmenu paviršiui lazerio spinduliu. Ši NS GaAs sluoksnių savybė gali būti pritaikyta kuriant kompaktiškus THz impulsų šaltinius.

LIPSS tyrimai

Bandiniai

Bandiniai paruošti Lazerinių technologijų skyriuje, FTMC. LIPSS struktūros buvo formuojamos ant trijų tipų padėklų: n-tipo GaAs (100) kristalografinės orientacijos, savojo laidumo GaAs (SI-GaAs) (100) kristalografinės orientacijos ir SI-GaAs (111) kristalografinės orientacijos. Graviravimui buvo naudojamas diodais kaupinamas pikosekundinis lazeris (Atlantic, Ekspla), kurio centrinis bangos ilgis 335 nm, o impulso trukmė 10 ps. Eksperimentams buvo paruoštos dvi bandinių serijos. Pirmoje serijoje graviravimo metu buvo keičiama optinė lazerinės spinduliuotės galia (0.02 W, 0.04 W, 0.08 W) ir skenavimo greitis (5 mm/s, 10 mm/s, 20 mm/s) (pav. 8.6a). Suformuotos bangelės einančios išilgai [110] kristalografinės ašies. Iš viso pirmą seriją sudarė 27 bandiniai. Antros serijos metu buvo keičiama lazerinės spinduliuotės poliarizacija, o optinė galia (0.02 W) ir skenavimo greitis (5 mm/s) laikomi pastoviais. Bangelės buvo suformuotos 0°, 45°, 90° ir 135° kampu [110] kristalografinės ašies atžvilgiu (pav. 8.6b). Iš viso antrąją seriją sudarė 8 bandiniai.

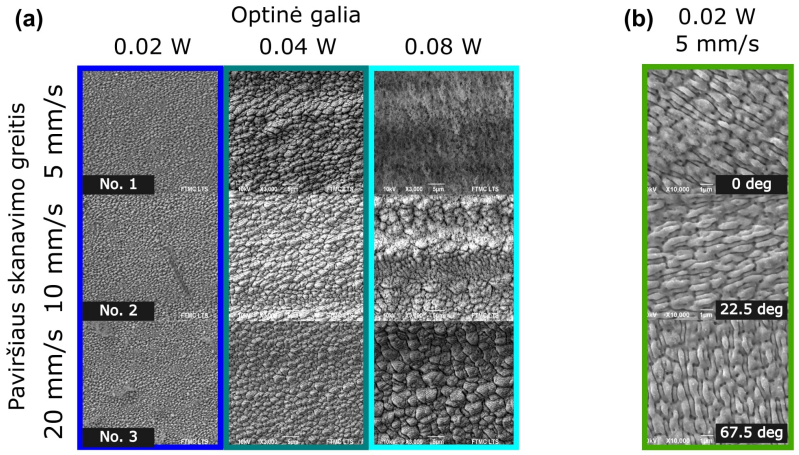

8.6 pav.: LIPSS bandinių SEM nuotrauka (a) Pirmoji serija. Struktūrų formavimo metu buvo keičiama optinė lazerinės spinduliuotės galia ir skenavimo greitis. (b) Antroji serija. Struktūrų formavimo metu buvo keičiama lazerinės spinduliuotės poliarizacija (nuotraukų apačioje nurodutas kampas tarp suformuotų bangelių ir [110] kristalografinės ašies).

Pirmoji serija. THz spinduliuotės emisija ir jos azimutinės priklausomybės

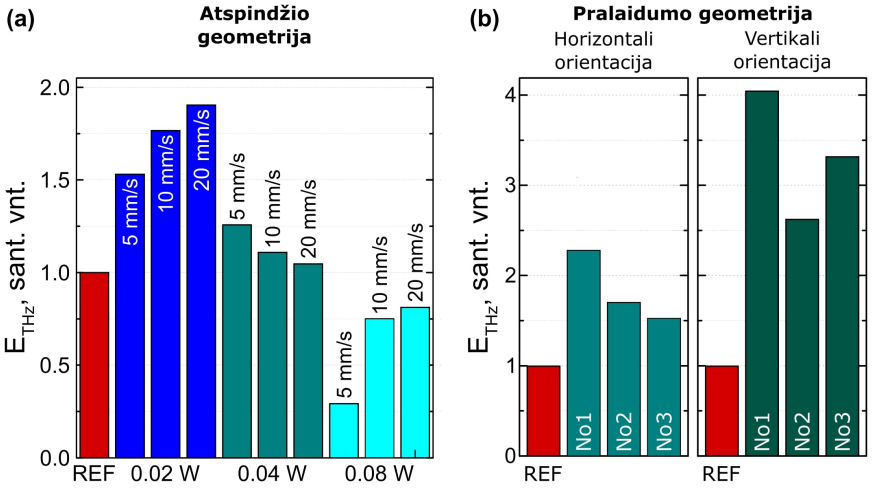

8.7 pav.: (a) THz impulsų, išspinduliuotų iš įvairių LIPSS bandinių, suformuotų ant n-GaAs (100) padėklų, amplitudės, išmatuotos atspindžio geometrijoje. (b) Pralaidumo geometrijoje išmatuotos amplitudės, THz impulsų išspinduliuotų iš LIPSS bandinių suformuotų ant i-GaAs (100) padėklų, kai LIPSS bangelės orientuotos vertikaliai ir horizontaliai optinio stalo atžvilgiu.

Pirmos serijos LIPSS bandiniai buvo suskirstyti į 3 grupes priklausomai nuo jiems suformuoti naudotos lazerinės spinduliuotės optinės galios: 0.02 W, 0.04 W ir 0.08 W. Pirmiausia buvo atlikti THz spinduliuotės emisijos iš LIPSS bandinių tyrimai. Visi bandiniai buvo tirti tiek atspindžio, tiek pralaidumo geometrijose. Pav. 8.7 atvaizduoti LIPSS bandinių suformuotų ant n-GaAs (100) padėklo rezultatai atspindžio geometrijoje (pav. 8.7a) bei ant i-GaAs (100) padėklo pralaidumo geometrijoje (pav. 8.7a). Iš atliktų matavimų akivaizdu, kad tvarkingiausios struktūros bandiniai, suformuoti naudojant mažiausios optinės galios lazerinę spinduliuotę, geriausiai emituoja THz impulsus. Siekiant daugiau sužinoti apie LIPSS bandinius buvo atlikti jų THz spinduliuotės emisijos nuo azimutinio kampo matavimai. Iš pav. 8.8 matosi, kad bandiniams suformuotiems ant i-GaAs (100) padėklo būdinga $\cos 2\phi$ azimutinė priklausomybė, kuri yra ryški ir atsikartojanti 0.02 W bandinių grupei. Grupei 0.04 W, ši priklausomybė silpnesnė ir mažiau atsikartojanti, o 0.08 W grupė pasižymi itin chaotiška azimutine priklausomybe. Bandiniai suformuoti ant kitų padėklų irgi atkartojo tą pačią tendenciją: LIPSS suformuoti su mažiausios optinė galios spinduliuote, pasižymėjo labiausiai atsikartojančiomis azimutinėmis priklausomybėmis. Šie rezultatai leido daryti išvadą, kad THz emisijai palankiausi tvarkingiausios struktūros LIPSS bandiniai.

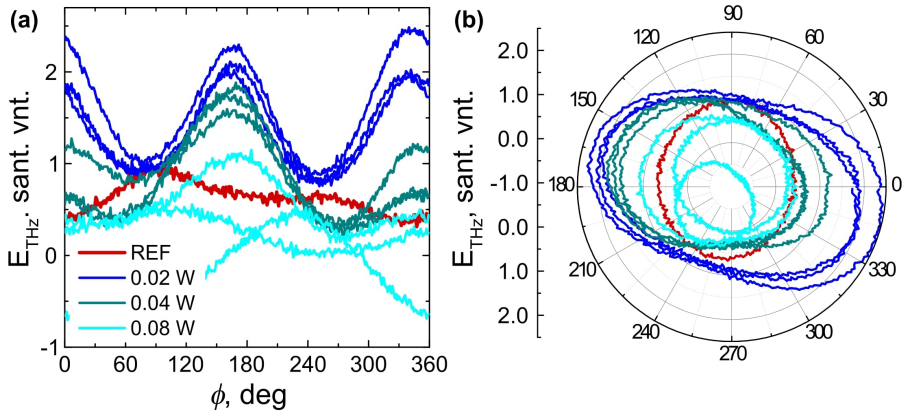

8.8 pav.: LIPSS bandinių, suformuotų ant i-GaAs (100) padėklo spinduliuojamų THz impulsų amplitudės priklausomybė nuo bandinio azimutinio kampo atvaizduota Dekarto (a) ir polinėje (b) koordinačių sistemose.

LIPSS struktūros ant i-GaAs (100) padėklų pasižymi tokiomis pačiomis azimutinėmis priklausomybėmis kaip ir ankstesniame skyriuje aptartas NS GaAs bandinys Ga15. Be to, azimutinių priklausomybių minimumų ir maksimumų padėtis atitinka LIPSS bangelių horizontalią ir vertikalią orientacijas optinio stalo atžvilgiu. Nors THz spinduliuotės emisija sustiprinama abiems orientacijoms, kai bangelės orientuotos vertikaliai sustiprėjimas siekia tik 1.5-2

karto, o kai vertikaliai – net 4 kartus. NS GaAs bandinio atveju, THz spinduliuotės emisijos sustiprėjimas buvo susietas su lygiagretaus paviršiui THz impulsus emituojančio elektrinio dipolio atsiradimu. Toks paaiškinimas tinkamas ir LIPSS bandiniams, tačiau vis dar lieka klausimas, ar netiesinius optinius efektus tikrai galima visiškai eliminuoti, mat pastariesiems būdinga tokia pati $\cos 2\phi$ azimutinė priklausomybė, o tiek LIPSS bangelių, tiek NS GaAs Ga15 griovelių kryptis sutampa su bandinio kristlografinėmis ašimis. Minėtas faktas smarkiai apsunkina bandinio kristalografijos bei paviršiaus nanostruktūrizavimo įtakos THz spinduliuotės emisijai atskyrimą. Kadangi LIPSS suteikia galimybę valdyti bangelių kryptį keičiant lazerinės spinduliuotės poliarizaciją formavimo metu, buvo paruošta Antroji bandinių serija, kurioje bangelės buvo suformuotos įvairiais kampai [110] kristografinės ašies atžvilgiu.

Antroji serija. THz spinduliuotės emisijos azimutinės priklausomybės

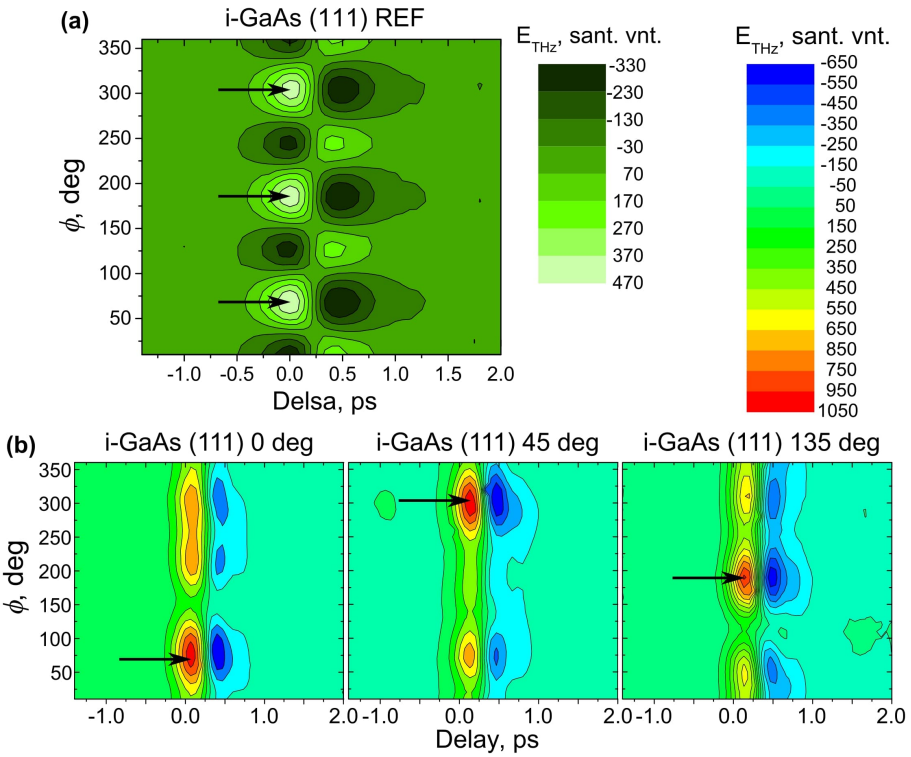

8.9 pav.: Atraminio bandinio (a) ir antros serijos LIPSS bandinių, suformuotų ant i-GaAs (111) padėklo, spinduliuojamų THz impulsų amplitudžių priklausomybės nuo bandinio azimutinio kampo atvaizduotos 2D grafikuose. Juodos rodyklės rodo pikų padėtis atraminio bandinio atveju.

Tiriant Antrosios serijos LIPSS bandinius, didžiausias dėmesys buvo sutelktas į struktūrų, suformuotų ant i-GaAs (111) padėklų, THz spinduliuotės emisijos azimutinių priklausomybių tyrimus. Pradėjus tirti šios serijos bandinius buvo pastebėta, kad po paviršiaus nanostruktūrizacijos laikinė THz impulso forma pasikeitė ir piko padėtis laike šiek tiek svyruoja keičiant bandinio azimutinį kampą. Dėl šios priežasties standartinis azimutinės priklausomybės matavimas (atliekamas ties delsa, atitinkančia piko padėtį) tapo nekorektiškas. Todėl, atliekant tyrimus laikinė THz impulso forma buvo išmatuojama ties kiekvienu bandinio azimutiniu kampu, o gauti rezultatai reziumuojami 2D grafikuose (pav. 8.9). Atraminis bandinys, i-GaAs (111) padėklas prieš nanostruktūrizaciją, turėjo ryškią $\sin 3\phi$ azimutinę priklausomybę, nulemtą netiesinių optinių efektų, kurių įtaka į THz impulsų generaciją tokio tipo bandiniuose yra didelė (pav. 8.9a). Po LIPSS suformavimo ant tokio padėklo, $\sin 3\phi$ priklausomybės pagrindas išliko, tačiau vietoj 3 vienodo stiprumo pikų, išliko po vieną ryškų piką, kurio pozicija kinta priklausomai nuo LIPSS bangelių krypties, tačiau atitinka vienos iš 3 padėklo smailių padėtį. Gauti rezultatai leidžia teigti, kad tiek bandinio kristalografija, tiek paviršiaus nanostruktūros turi didelės įtakos THz spinduliuotės emisijos charakteristikoms.

THz impulsus emituojančio elektrinio dipolio orinentacija

Siekiant suprasti THz impulsų generacijos mechanizmus bei THz spinduliuotės emisijos sustiprėjimą bandiniuose buvo pabandyta įvertinti THz impulsus emituojančio dipolio padėtį bandinuose. Pasinaudojus 2 kampo nustatymo metodą (plačiau apie tai 3.4.2 skyriuje), paremtą II ir I THz impulso pikų santykio atspindžio geometrijoje matavimu (pav. 8.10a), buvo gauti dipolio pasvirimo kampai vertikaliai ir horizontaliai LIPSS bangelių orientacijai (pav. 8.10b) pirmos serijos bandiniams ant i-GaAs (100) padėklo. Svarbu pastebėti, kad abiem bandinio orientacijoms gaunamas pasviras elektrinis dipolis, tik horizontalioms LIPSS bangelėms pasvirimo kampas yra teigiamas $\theta \sim 2°$, o vertikalios – neigiamas $\theta \sim -6.5°$. Lygiagrečios paviršiui elektrinio dipolio komponentės atsiradimas gali būti susijęs su paviršiniu fotovoltiniu efektus [152], kuris taip pat paaiškina šiuose bandiniuose stebėtą gana smarkią priklausomybę nuo žadinančios šviesos poliarizacijos. Tačiau, minėtas efektas gali pasireikšti tik žadinant bandinį p-poliarizuota optine spinduliuote. Kadangi, pasviro elektrinio dipolio atsiradimas buvo užfiksuotas žadinant ir s-poliarizuota optine spinduliuote, akivaizdu, kad reikalingi papildomi efektas THz impulsų generacijai LIPSS bandiniuose paaiškinti.

Nepaisant to, kad THz impulsų generacijos mechanizmas LIPSS bandiniuose nėra visiškai aiškus, THz spinduliuotės emisijos sustiprėjimas iki 4 kartų po LIPSS suformavimo ant paviršiaus yra nenuginčijamas. Akivaizdu, kad

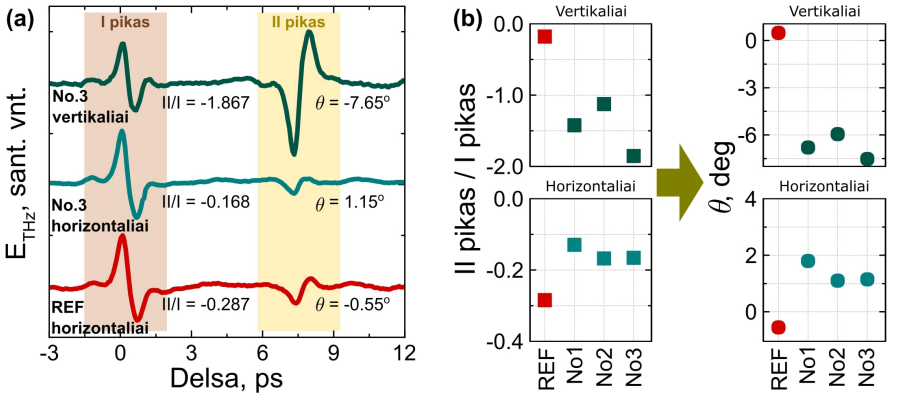

8.10 pav.: THz impulsus emituojančio elektrinio dipolio pasvirimo kampo nustatymas naudojant II metodą (aprašytą 3.4.2 skyriuje). (a) Vertikaliai ir horizontaliai orientuotų LIPSS bandinio No.3 bei atraminio bandinio spinduliuojami THz impulsai išmatuoti atspindžio geometrijoje. (b) Išmatuoti II ir I pikų santykiai ir juos atitinkantys THz impulsus spinduliuojančio elektrinio dipolio pasvirimo kampai LIPSS bandiniams suformuotiems ant i-GaAs (100) padėklų.

THz impulsus emituojančio elektrinio dipolio pasvirimas yra svarbus veiksnys lemiantis THz spinduliuotės emisijos sustiprėjimą. Atlikti skaičiavimai parodo, kad bandinys su didžiausiu dipolio pasvirimo kampu $\theta = 7.5°$, turėtų emituoti 2.7 karto didesnės amplitudės THz impulsus, nei atraminis GaAs padėklas. Tačiau eksperimentiškai stebimas padidėjimas yra 3.4 karto, o tai reiškia, kad turi būti dar vienas THz spinduliuotės emisijos sustiprinimo mechanizmas. Pavyzdžiui, sustiprėjęs paviršinis elektrinis laukas, dėl puslaidininkio paviršiaus graviravimo lazerine spinduliuote. Užtektų 1.25 karto sustiprinti paviršinį elektrinį lauką, kad jis būtų pakankamas stebimam THz spinduliuotės emisijos sustiprėjimui paaiškinti.

Apibendrinimas

1. Ant puslaidininkio paviršiaus lazeriu indukuotos periodinės struktūros kelis kartus sustiprina THz spinduliuotės emisiją iš šių paviršių lyginant su nestruktūrizuotais paviršiais. Ryškiausias THz emisijos padidėjimas bei labiausiai nuspėjami rezultatai buvo gauti LIPSS bandiniams, suformuotiems naudojant lazerinę spinduliuotę, kurios optinė galia artima abliacijos slenksčiui.

2. THz emisijos padidėjimas LIPSS bandiniuose yra susijęs su paviršiui lygiagrečios THz impulsus emituojančio elektrinio dipolio komponentės atsiradimu. Minėto dipolio orientacija bandiniuose lemia didesnį THz

spinduliuotės emisijos sustiprėjimą pralaidumo nei atspindžio geometrijoje.

3. Lygiagrečiai THz impulsus emituojančio elektrinio dipolio komponentei būdinga azimutinė priklausomybė, kurią lemia tiek LIPSS kryptis, tiek bandinio kristalografija.

4. THz emisijos priklausomybė nuo žadinančios spinduliuotės poliarizacijos gali būti paviršinio fotofoltinio efekto pasekmė.

Nanovielelių tyrimai

InAs ir InGaAs nanovielelių tyrimai

Bandiniai

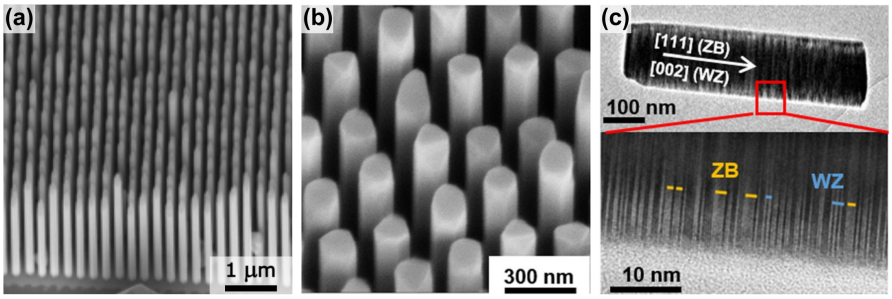

8.11 pav.: (a) InAs NV (1.8 µm ilgio) SEM nuotrauka. (b) InGaAs NW (x(Ga) = 0.48) SEM nuotrauka. (c) InGaAs NW (x(Ga) = 0.48) TEM nuotrauka vaizduojanti WZ ir ZB kristalografinės struktūros segemntus.

Bandiniai buvo užauginti Technische Universität München, Miunchene, Vokietijoje MBE būdu ant SiO_2/Si padėklų nenaudojant katalizatoriaus. Auginimas buvo vykdomas per SiO_2/Si šabloną suformuotą ant p-tipo Si (111) kristalografinės orientacijos padėklų. Šabloną sudaro 20 nm storio SiO_2 sluoksnis su 60 nm pločio skylutėmis, išdėstytomis 250 nm atstumu viena nuo kitos. Toks šablonas leidžia užauginti griežtai periodiškai išdėstytas, vienodo diametro, paviršiui statmenas NV (pav. 8.11a). InAs NV buvo auginamos 480°C temperatūroje, As persotintoje atmosferoje. Buvo paruoštos 3 bandinių serijos. Pirmąją seriją sudarė n-tipo InAs NV, kurių ilgis priklausomai nuo auginimo trukmės – 0,7 µm, 1,8 µm ir 3,3 µm. Antrąją seriją sudarė $\sim$ 3µm ilgio InAs NV su $InAs_{1-x}P_x$ apvalkalu, kur P koncentracija buvo 15%, 30% ir 60% (Šios serijos tyrimas į Disertacijos santrauką neįtrauktas). Pirmos ir antros serijos NV bandinių žymėjimai pateikti 8.1 lentelėje. Trečiąją seriją sudarė $\sim$ 1µm ilgio InGaAs NV su skirtinga Ga koncentracija (pav. 8.11b): x(Ga) = 0.00, 0.28, 0.40,

8.1 lentelė: InAs NV bandiniai.

Bandinio apibūdinimas	Žymėjimas	Bandinio apibūdinimas	Žymėjimas
0.7 μm ilgio InAs NV	NW0.7um	InAs NV su $InAs_{85\%}P_{15\%}$ apvalkalu	NW1_15%
1.8 μm ilgio InAs NV	NW1.8um	InAs NV su $InAs_{70\%}P_{30\%}$ apvalkalu	NW2_30%
3.3 μm ilgio InAs NV	NW3.3um	InAs NV su $InAs_{40\%}P_{60\%}$ apvalkalu	NW3_60%

0.48 ir 0.63. Atlikti pastarosios serijos NV tunelinio elektroninio mikroskopo (TEM) matavimai (pav. 8.11c) atskleidė kad InAs ir InGaAs NV su maža Ga koncentracija ($x(\mathrm{Ga}) = 0.28$) yra daugiausias vurcitinės (WZ) kristalografinės struktūros, didėjant Ga koncentracijai atsiranda WZ/ZB (cinko blizgučio) kristalinių fazių maišymasis ir galiausiai kai $x(\mathrm{Ga}) = 0.63$ ZB kristalinė fazė tampa dominuojanti.

THz spinduliuotės emisija iš InAs NV

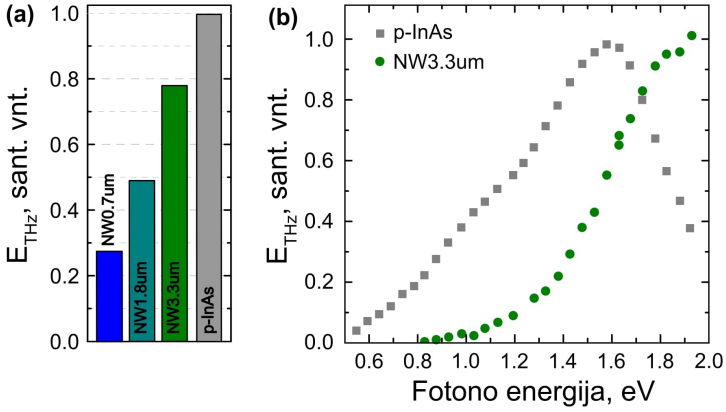

8.12 pav.: (a) THz impulsai, išspinduliuoti iš skirtingo ilgio InAs NV ir p-tipo InAs padėklo, sužadinus bandinio paviršių s-tipo poliarizacijos titano:safyro lazerio impulsais. (b) InAs NV bandinių bei p-tipo InAs padėklo emituojamų THz impulsų amplitudės priklausomybė nuo žadinančio spinduliuotės fotono energijos.

Skirtingo ilgio InAs NV tyrimas prasidėjo nuo THz spinduliuotės emisijos matavimo. Bandinių bei šiuo metu geriausio žino paviršinio THz emiterio – p-tipo InAs padėklo (p-InAs) išspinduliuotų THz impulsų amplitudės palygintos pav. 8.12a. Akivaizdu, kad THz spinduliuotės emisijos efektyvumas tiesiogiai priklauso nuo NV ilgio: kuo ilgesnės NV, tuo stipresnė THz spindu-

liuotės emisija. Nors nė vienas NV bandinys emisijos efektyvumu nepranoko p-InAs, ilgiausių InAs NV emituojamo THz impulso amplitudė siekia net 80% p-InAs emituojamo THz impulso amplitudės. Siekiant daugiau išsiaiškinti apie InAs NV vykstančius fizikinius procesus, buvo atlikti THz emisijos efektyvumo priklausomybės nuo žadinančio spinduliuotės kvanto energijos (intervale nuo 0.55 eV iki 1.95 eV) matavimai. Pav. 8.12b atvaizduoti rezultatai gauti p-InAs bei 3.3 μm ilgio InAs NV bandiniams. Tirtame žadinančios spinduliuotės fotonų energijų intervale, minėtiems bandiniams išryškėja du pagrindiniai skirtumai: (1) NV atveju nestebimas THz emisijos efektyvumo maksimumas būdingas InAs padėklui; (2) NV bandinyje THz impulsų generacija prasideda ties aukštesne kvanto energija. Analogiška tendencija buvo stebėta visų ilgių InAs NV bandiniams. p-InAs būdingas THz emisijos efektyvumo maksimumas priklausomybės nuo kvanto energijos kreivėje, siejamas su fotosužadintų elektronų tarpslėnine sklaida [193]. Tačiau, iš pav. 8.12b akivaizdu, kad šis efektas turi mažai įtakos InAs NV sužadintiems krūvininkams bei THz spinduliuotės emisijos charakteristikoms. To priežastys gali būti tokios. Elektronų judris InAs NV yra maždaug 10 kartų mažesnis, nei tūriniame InAs [82], kas rodo, kad impulso relaksacijos trukmė ($\tau = \mu m^*/e$) InAs NV sumažėja bei tampa palyginama su tarpslėninės sklaidos trukme (keli šimtai femtosekundžių). Tai lemia, kad tik nedidelė dalis elektronų yra išsklaidoma į gretimus laidumo juostos slėnius. Tikėtina, kad maža impulso relaksacijos trukmė InAs NV yra didelio donorinio tipo taškinių defektų pasekmė. Tokio tipo defektai atsiranda NV paviršiuje ties natūraliai susidariusio oksido/InAs riba. Šie defektai taip pat lemia dideles savitąsias elektronų koncentracijas InAs NV, pvz.NV, kurių diametras mažesnis nei ~ 100 nm, savitoji elektronų koncentracija gali siekti 10^{17} cm^3 [194]. Dėl tokios didelės koncentracijos apatiniai laidumo juostos lygmenys gali būti užpildyti, o fotosužadintų krūvininkų judėjimas stabdomas. Dėl šių priežasčių stebimas mėlynasis poslinkis THz spinduliuotės emisijos spektrinėse priklausomybėse (pav. 8.12b). Apibendrinant, didelė paviršinių defektų koncentracija InAs NV efektyviai sklaido fotosužadintus elektronus bei mažina jų judrį. Abu minėti veiksniai neigiamai veikia THz spinduliuotės emisijos efektyvumą. Šiame skyriuje pristatyti rezultatai publikuot P1 straipsnyje.

THz spinduliuotės emisija iš InGaAs NV

Akivaizdu, kad, norint sustiprinti THz spinduliuotės emisiją iš InAs NV, reikia sumažinti paviršinių taškinių defektų koncentraciją. Vienas iš pasiūlytų šios problemos sprendimo variantų – pakeisti nanovielelių cheminę sudėtį, įterpiant Ga atomų į InAs NV. Skirtingą Ga atomų koncentraciją savo sudėtyje turinčių InGaAs NV emituojami THz impulsai palyginti su p-InAs ir pateikti

pav. 8.13. In praturtintų InGaAs NV ($x(\mathrm{Ga}) < 0.3$) THz spinduliuotės emisijos efektyvumas siekia tik 30% tūrinio p-InAs efektyvumo. Didinant Ga atomų koncentraciją InGaAs NV, THz impulso amplitudė didėja ir pasiekia maksimumą tieks Ga koncentracija $x(\mathrm{Ga}) = 0.48$. Toliau didinant Ga koncentraciją ($x(\mathrm{Ga}) > 0.6$), THz spinduliuotės emisija iš InGaAs NV silpnėja. Šis silpnėjimas tikėtina yra didesnio draustinio energijos tarpo vertės bei su tuo susijusių mažesne krūvininkų pertekline energija bei mažesnių krūvininkų judrio ir gyvavimo trukmės verčių pasekmė. Svarbu paminėti, kad InGaAs NV yra gerokai trumpesnės (jų ilgis $\sim 1\mu$m) nei geriausiai THz impulsus emituojantis InAs NV bandinys NW3.3um (jų ilgis 3.3μm). Nepaisant to, 3 kartus trumpesnių InGaAs NV su $x(\mathrm{Ga}) = 0.48$ emituojamo THz impulso amplitudė siekia net 87% NW3.3um emituojamo THz impulso amplitudės.

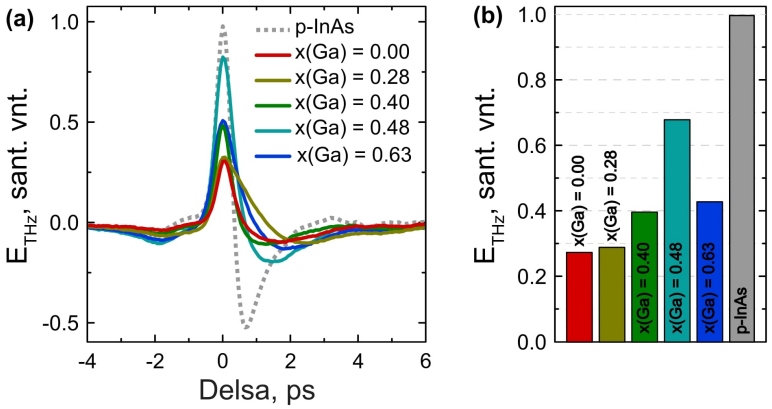

8.13 pav.: (a) THz impulsai išspinduliuoti iš skirtingo ilgio InGaAs NV ir p-tipo InAs padėklo, sužadinus bandinio paviršių s-tipo poliarizacijos titano:safyro lazerio impulsais. (b) Minėtų impulsų amplitudės sunormuotos į atraminio bandinio p-tipo InAs padėklo emituojamo THz impulso amplitudę.

Silpną THz spinduliuotės emisiją iš mažos Ga koncentracijos InGaAs NV gali nulemti trys veiksniai: (1) THz spinduliuotės sugertis laisvaisiais elektronais, (2) elektron-eletroninė sklaida bei elektronų sklaida paviršiniais defektais. Pirmasis efektas buvo atmestas, nes išmatuotas aukštas InGaAs NV pralaidumo THz spinduliuotei koeficientas (artimas 90%). Elektron-eletroninė sklaida labiausiai pasireiškia prie didelių savitųjų elektronų koncentracijų. InAs nanovielelėse, kurių diametras mažesnis nei ~ 100 nm ši koncentracija buvo nustatyta išties didelė – 10^{17} cm^3 [194], o vidutinės Ga koncentracijos InGaAs NV ji sumažėja iki 10^{16} cm^3 [195]. Tačiau, fotosužadintų elektronų judris dėl tokio savitosios elektronų koncentracijos pokyčio pasikeičia tik 1.5 karto [196], kas rodo jog elektron-elektroninė sklaida daro tik silpną įtaką THz emisijos efektyvumui. Tad labiausiai tikėtina, kad silpna

THz spinduliuotės emisija yra susijusi su didele paviršinių donorinio tipo defektų koncentracija mažos Ga koncentracijos InGaAs NV. Neseniai, rentgeno fotoemisijos spektroskopijos tyrimai papildyti elektroninės struktūros In praturtintų InGaAs NV paviršiuje skaičiavimais parodė, kad paviršiuje esantis oksido sluoksnis tikrai lemia donorinio tipo paviršines būsenas [195], kurios efektyviai sklaido elektronus ir sumažina jų judrį daugiau nei 10 kartų lyginant su tūriniu InAs [194, 197]. Toks elektronų judrio sumažėjimas turi didelės neigiamos įtakos THz spinduliuotės emisijos efektyvumui. Kai Ga koncentracija InGaAs NV pasiekia vidutines vertes, buvo stebėtas akumuliacinio sluoksnio išnykimas, kuris lemia laidumo ir valentinės juostos išlinkimo prie paviršiaus sumažėjimą [195] ir THz spinduliuotės padidėjimą.

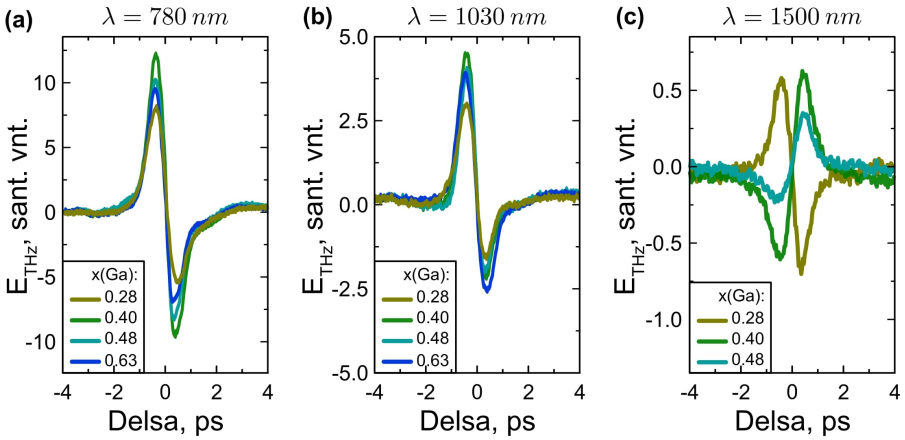

8.14 pav.: InGaAs NV su skirtinga Ga atomų koncentracija $x(\mathrm{Ga})$ sudėtyje emituojami THz impulsai išmatuoti žadinant bandinį trim skirtingais technologiškai svarbiais bangos ilgiais: (a) 780 nm, (b) 1030 nm, ir (c) 1500 nm (ties šiuo bangos ilgiu bandinio $x(\mathrm{Ga}) = 0.63$ THz spinduliutės emisija itin silpna dėl to nėra atvaizduota). Matavimai atlikti atspindžio geometrijoje, kai $\alpha_1 = 45°$.

Kadangi InGaAs NV tikimasi taikyti THz spektroskopijos sistemose, THz spinduliuotės emisija iš šių bandinių detaliau ištirta žadinant juos ties trim THz-TDS sitemose dažniausiai naudojamais bandos ilgiais: 780 nm, 1030 nm ir 1500 nm (pav. 8.14). Kaip ir galima tikėtis iš ankstesnių matavimų THz impulso amplitudės mažėja didėjant žadinančios spinduliuotės bangos ilgiui. Įdomiausias aptariamų matavimų rezultatas yra bandinių $x(\mathrm{Ga}) = 0.4 - 0.5$ emituojamo THz impulso fazės apsivertimas žadinant 1500 nm bandos ilgio spinduliuote (pav. 8.14c). Jis galėtų būti paaiškintas THz spinduliuotės generacijos ypatybėmis. Bendru atveju, THz impulsas yra generuojamas išilgai NV judančių krūvininkų, kurių judėjimą lemia paviršinis elektrinis laukas bei koncentracijos gradientas. Ties dideliais bangos ilgiais, optinės spinduliuotės

sugertis per visą NV ilgį nėra tolygi ir vis mažiau fotokrūvininkų juda viršutinėje NV dalyje lyginant su situacija kai žadinama trumpo bangos ilgio spinduliuote. Tačiau apatinėje NV dalyje vis daugiau krūvininkų juda elektriniame lauke susidariusiame riboje InGaAs NV/Si padėklas. Svarbu paminėti, kad šis laukas verčia krūvininkus judėti priešinga kryptimi nei koncentracijos gradientas viršutinėje NV dalyje [199]. Bandinio emituojamo THz impulso fazė apsiverčia, kai fotokrūvininkų judėjimas apatinėje NV dalyje tampa dominuojančiu THz spinduliuotės generacijos mechanizmu. Šiame skyriuje pristatyti rezultatai publikuot P3 straipsnyje.

Apibendrinimas

1. $In_{1-x}Ga_x$ As nanovielelių THz emisijos efektyvumo priklausomybė nuo Ga kiekio pasiekia savo maksimumą apytiksliai ties $x(\mathrm{Ga}) = \sim 0.4 - 0.5$.
2. THz emisijos susilpnėjimas mažo $x(\mathrm{Ga})$ junginiuose susijęs su didele paviršiaus donorinių būsenų koncentracija.
3. Didėjant $x(\mathrm{Ga})$, THz signalas auga kol donorinių būsenų efektai išlieka svarbūs, o po to mažėja, nes svarbesnis tampa sužadintų elektronų energijos mažėjimas.

Pasvirų GaAs nanovielių tyrimai

Bandiniai

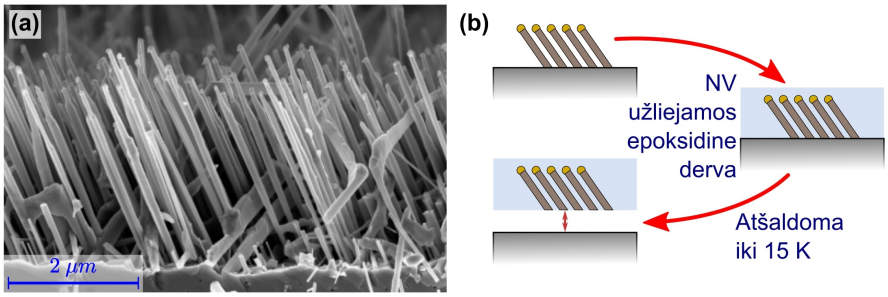

8.15 pav.: (a) Bandinio NW3 SEM nuotrauka. (b) Bandinio NW4 nukėlimo nuo padėklo iliustracija.

Bandiniai paruošti MAX-lab, Lundo universitete, Švedijoje. Nanovielelės (NV) užaugintos MBE kameroje, and (100) kristalografinės orientacijos GaAs padėklų 550°C temperatūroje augimą inicijuojant Au katalizatoriumi. Gautų NV ilgis apie 4 μm, diametras 70–100 nm. Buvo paruošti 4 bandiniai: GaAs NV (NW1), NV su GaAs šerdimi – GaMnAs apvalkalu (NW2), NV su GaAs

baze – InGaAs šerdimi – GaMnAs apvalkalu (NW3) ir NV su GaAs šerdimi – GaMnAs apvalkalu (NW4). Visų bandinių NV sudarė $\sim 55°$ kampą su padėklo paviršiumi (pav. 8.15a). Bandinys NW4 buvo nukeltas nuo padėklo. NV sluoksnis buvo aplietas epoksidine derva, tuomet patalpintas į kreostatą, kur atšaldytas iki 15 K. Tokioje žemoje temperatūroje dėl skirtingo terminio plėtimosi koeficiento epoksidinės dervos sluoksnis kartu su NV atsiskiria nuo GaAs padėklo (pav. 8.15b).

THz spinduliuotės emisija iš GaAs NV

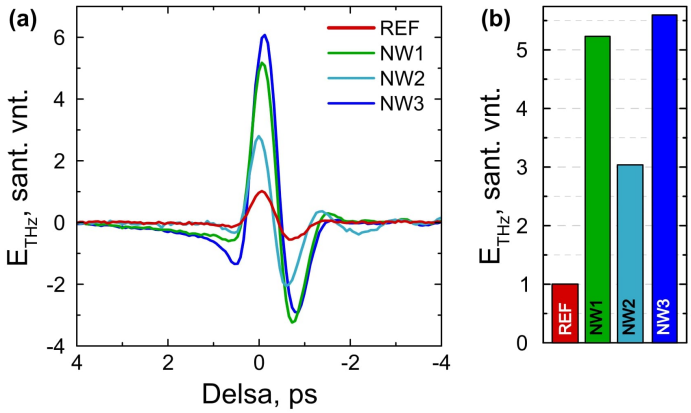

8.16 pav.: (a) Pasvirų GaAs NV ir SI GaAs (REF) emituojami THz impulsai išmatuoti atspindžio geometrijoje. (b) Reziumuotos minėtų impulsų amplitudės normuotos į REF bandinio amplitudę.

Pirmiausia atliktas THz impulsų emisijos tyrimas žadinant GaAs NV bandinius Titano:safyro lazeriu (pav. 8.16). Visi tirti bandiniai spinduliavo 3-6 kartus didesnė amplitudės THz impulsus, nei atraminis SI GaAs padėklas (REF). Yra žinoma, jog po sužadinimo fotokrūvininkai juda išilgai NV paviršiniame elektriniame lauke, THz impulsus emituojančio elektrinio dipolio orientacija NV bandiniuose visada yra išilgai NV ašies. Minėtas laukas atsiranda NV augintose VLS metodu (plačiau 6.1 skyriuje) naudojant metalo katalizatorių dėl Šotki kontakto susidariusio riboje katalizatorius/NV [19]. Kadangi tiriamos GaAs NV yra pasvirusios padėklo atžvilgiu, THz impulsus emituojantis elektrinis dipolis jose taip pat yra pasviręs. Toks dipolis gali būt analizuojamas kaip dviejų, statmeno ir lygiagretaus paviršiui, dipolių visuma.

Siekiant geriau suprasti NV vykstančius fizikinius procesus verta atlikti tokių dipolių spinduliavimo simuliacijas. Tam tikslui buvo pasitelktas W. Lukosz [101] pasiūlytas dviejų terpių matematinis modelis. Jis aprašo THz spinduliuotės generaciją puslaidininkyje ir jos ištrūką į laisvą erdvę. Analizuojama

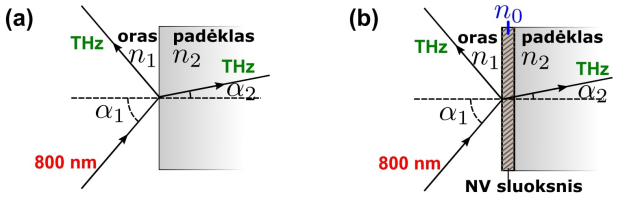

8.17 pav.: Dviejų terpių (a) ir trijų terpių (b) modelis naudotas THz spinduliuotės emisijai iš pasvirų elektrinių dipolių simuliuoti.

situacija pavaizduota pav. 8.17a. Emituojamo THz impulso elektrinis laukas ($E^p(\alpha_1,\phi)$) yra aprašomas formule:

$$E^{(p)}(\alpha_1,\phi) = \sqrt{\frac{3}{2\pi n}}\cos\alpha_1 \frac{\cos\theta\sin\alpha_2 + \sin\theta\cos\alpha_2\cos\phi}{\cos\alpha_2 + n\cos\alpha_1} \tag{8.1}$$

čia $n = n_2/n_1$. n_1 ir n_2 yra atitinkamai oro ir puslaidininkio lūžio rodikliai, α_1 – optinės spinduliuotės kritimo kampas, α_2 – optinės spinduliuotės lūžio kampas, o ϕ – bandinio azimutinis kampas. Kampas θ yra THz impulsus emituojančio dipolio pasvirimo kampas. Statmenam paviršiui dipoliui šis kampas yra 0°, lygiagrečiam – 90°. Svarbu paminėti, kad keičiant bandinio azimutinį kampą ϕ, statmenas paviršiui dipolis visada spinduliuoja vienodos amplitudės THz impulsą, o lygiagretaus paviršiui generuojamo THz impulso amplitudė kinta dėsniu $\cos\phi$.

Aptartas modelis skirtas simuliuoti THz impulsų generaciją puslaidininkyje, o norint analizuoti THz spinduliuotės emisiją iš suformuotų NV modelis buvo praplėstas iki trijų terpių (pav. 8.17b). Šiuo atveju, NV traktuojamos kaip vientisas plonas sluoksnis turinti efektinį lūžio rodiklį n_0. THz impulsų emisijos kampinės priklausomybės labai priklauso nuo n_0 [200]:

$$[E^p(\alpha_1,\phi)]_{1,0,2} = (\frac{n_2}{n_0})^{\gamma/2} E^p(\alpha_1,\phi) \tag{8.2}$$

čia $E^p(\alpha_1,\phi)$ yra THz emisijos efektyvumas ore, kai dipolis yra padėkle šalia ribos oras/padėklas, o tarpinis NV sluoksnis neegzistuoja [101]. Parametras γ priklauso nuo THz impulsus emituojančio elektrinio dipolio orientacijos: $\gamma = 5$ statmenam, o $\gamma = 1$ lygiagrečiam dipoliui. Formulėje 8.2 yra du parametrai, α_1 ir ϕ, kurie gali būti keičiami eksperimento metu. Taigi, THz spinduliuotės emisijos priklausomybės tiek nuo optinės spinduliuotės kritimo kampo (keičiamas α_1, o ϕ padėtis yra fiksuota), tiek nuo bandinio azimutinio kampo (α_1 padėtis fiksuota, o ϕ yra keičiamas) matavimai gali būti naudojami NV sluoksnio efektinio lūžio rodiklio n_0 nustatymui.

GaAs NV sluoksnio lūžio rodiklio nustatymas

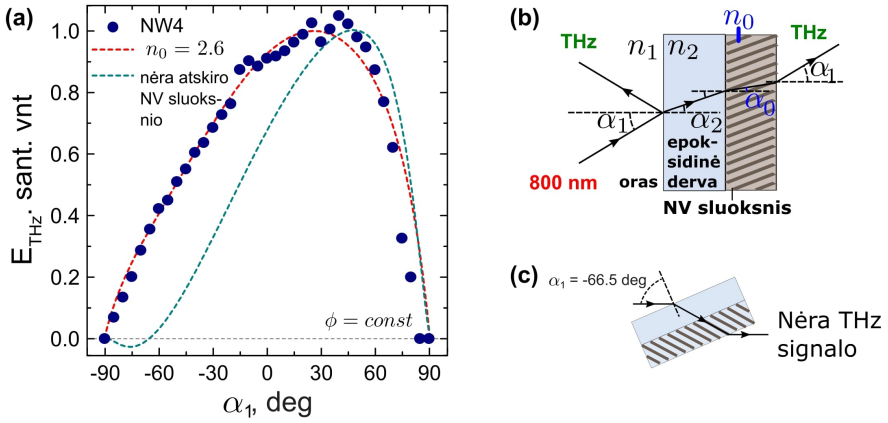

8.18 pav.: (a) THz impulsų emisijos priklausomybė nuo optinės spinduliuotės sužadinimo kampo palyginta su teorinėmis kreivėmis, kai $\phi = const$. Raudona ir žalia linijos skaičiuotos pagal dviejų ir trijų terpių modelius (pav. 8.17) atitinkamai. Skaičiavimai atlikti naudojant tokius parametrus: $\theta = 35°$, $n_1 = 1$, $n_2 = 1.6$ ir $n_0 = 2.6$ (b) Trijų terpių modelio variacija nuo padėklo nukeltoms GaAs NV. (c) Iliustracija vaizduojanti THz impulsų emisija žadinant bandinį kampu $\alpha_1 = -66.5°$.

Kai bandinio azimutinis kampas yra fiksuotas, o matavimo metu keičiamas kampas α_1, gaunama THz spinduliuotės emisijos priklausomybė nuo bandinio sužadinimo kampo. Taškai pav. 8.18a atvaizduoja tokią priklausomybę GaAs NV bandiniui NW4. Šiuo atveju, minėta priklausomybė gali būt aprašoma formulėmis 8.1 ir 8.2 su minimaliais pakeitimais (modelio schema pavaizduota pav. 8.18b). Kaip jau minėta anksčiau, THz impulsus emituojančio dipolio pasvirimo kampas NV bandiniuose yra žinomas $\theta = 35°$. Taigi, teorinė kreivė geriausiai aprašanti eksperimentinius rezultatus gali būti randama varijuojant efektinio lūžio rodiklio n_0 vertę. Suradus geriausią teorijos ir eksperimento atitikimą bandiniui NW4 (raudona kreivė pav. 8.18a), gauta n_0 vertė 2.6. Palyginimui, pav. 8.18a žalia kreive atvaizduota situacija, kai skaičiavimai atlikti GaAs NV ansamblio neaproksimuojant plonu sluoksniu (dviejų terpių modelis). Akivaizdu, kad toks metodas netinka eksperimento rezultatams aprašyti. Pagrindiniai eksperimento ir teorijos neatitikimai stebimi ties optinės spinduliuotės kritimo kampu $\alpha_1 = -66.5°$. Žadinant šiuo kampu, dviejų terpių modelio atveju, generuojamos THz spinduliuotės sklidimo kryptis pagal Hiuigenco principą turėtų būti nukreipta išilgai nanovielelių ašies. THz impulsus spinduliuojantis dipolis taip pat nukreiptas išilgai šios ašies, todėl šiuo atveju sugeneruota THz spinduliuotė turėtų būti labai silpna. Tai neatitinka eksperimentinių rezultatų. Šie rezultatai gali būti paaiškinti tik tada, kai lūžio

rodiklis NV aplinkoje yra gerokai didesnis nei epoksidinės dervos lūžio rodiklis (1.6). Tokiam atvejui reikalingas trijų terpių modelis (pav. 8.17b pav.) . Taikant šį modelį, geriausias eksperimento ir teorinio modeliavimo rezultatų sutapimas gaunamas kai $n_0 = 2.6$.

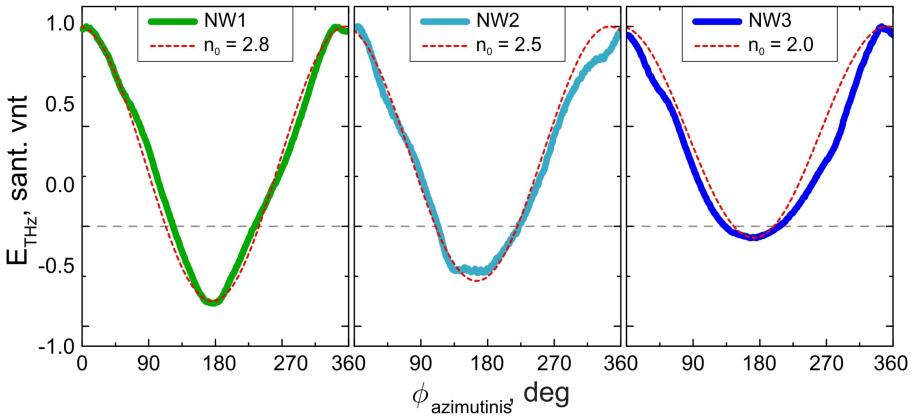

8.19 pav.: GaAs NV bandinių (NW1, NW2 ir NW3) emituojamų THz impulsų priklausomybės nuo bandinio azimutinio kampo palyginimas su teoriniais skaičiavimais pagal formulę 8.2, kai $\alpha_1 = const$ (punktyrinės linijos).

Aptartas modelis pritaikytas ir THz spinduliuotės emisijos priklausomybių nuo bandinio azimutinio kampo matavimams kitiems GaAs NV bandiniams. Formulės 8.1 ir 8.2 buvo panaudotos apskaičiuoti teorines THz spinduliuotės azimutines priklausomybes (punktyrinės linijos pav. 8.19), kurios palygintos su eksperimento rezultatais (ištisinės linijos pav. 8.19). Iš atlikto palyginimo buvo nustatytos n_0 vertės 2.8, 2.5 ir 2.0 bandiniams NW1, NW2 ir NW3 bandiniams atitinkamai.

THz emisijos iš GaAs NV sustiprėjimo priežastys

Ankstesniame skyriuje buvo parodyta, kad THz spinduliuotės emisija iš NV gerai aprašoma trijų terpių modeliu, kuriame NV sluoksnio lūžio rodiklis n_0. Toliau bus parodyta, kad minėtas modelis leidžia kiekybiškai įvertinti kiek kartų THz spinduliuotės emisija iš NV sluoksnio yra efektyvesnė už emisiją iš to paties puslaidininkio padėklo. Pirmiausia verta panagrinėti paprasčiausią atvejį – THz spinduliuotės emisiją iš padėklui vertikalių NV atspindžio geometrijoje. Analizė prasideda nuo W. Lukosz išvestos formulės statmeniems dipoliams [200]:

$$[E^p(\alpha_1, \phi)]_{1,0,2} = (\frac{n}{n_0})^{5/2} E^p(\alpha_1, \phi) \tag{8.3}$$

kur $E^p(\alpha_1, \phi)$ yra aprašytas formule 6.1.

Formulė 8.3 aprašo THz impulso amplitudės padidėjimą, jei spinduliuojančio sluoksnio lūžio rodiklis n_0 yra mažesnis už padėklo n (kai dipolio dinamika nepriklauso nuo sluoksnio savybių). Šiame darbe nustatytų n_0 verčių atveju (pav. 8.18 ir pav. 8.19) formulė prognozuoja THz amplitudės padidėjimą nuo 2 iki 5 kartų (pav. 8.20a, žali taškai). Šį signalo padidėjimą lemia du pagrindiniai faktoriai. Visų pirma, mažesnio lūžio rodiklio sluoksnyje susidaro didesnis kampas tarp dipolio ašies ir THz spinduliuotės sklidimo krypties. Tai lemia THz elektrinio lauko amplitudės padidėjimą n/n_0 kartų. Kitas THz emisijos sustiprėjimo efektas susijęs su elektromagnetinės spinduliuotės skėsties kampo pokyčiu puslaidininkis-oras riboje, kuris lemia išspinduliuoto THz impulso amplitudės padidėjimą n/n_0 karto. Tačiau, tai tiesa tik pakankamai didelės THz spinduliuotės skėsties arba mažos apertūros detektoriaus atveju. Priešingai minėtoms sąlygoms, šiame darbe aprašomų eksperimentų atveju buvo stengiamasi generuoti kuo mažesnės skėsties THz pluoštus, kad būtų galima surinkti į detektorių beveik visą sugeneruotą spinduliuotę. Tokiu atveju 8.3 formulė transformuojasi į:

$$[E^p(\alpha_1,\phi)]_{1,0,2} = (\frac{n}{n_0})^{3/2} E^p(\alpha_1,\phi) \tag{8.4}$$

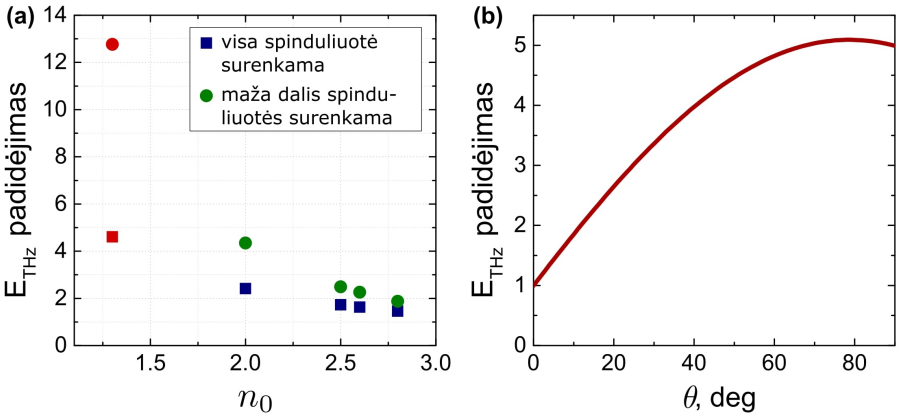

8.20 pav.: (a) THz impulsų emisijos sustiprėjimo priklausomybė nuo NV sluoksnio lūžio rodiklio n_0. Skaičiavimai atlikti statmenų paviršiui NV atveju. Raudoni taškai atitinka situaciją kai n_0 yra artimas 1. (b) THz impulso amplitudės priklausomybė elektrinio dipolio pasukimo kampo atspindžio geometrijoje. Rezultatai sunormuoti į statmeno paviršiui dipolio emituojamo THz impulso amplitudę. Skaičiavimai atlikti kai $\alpha_1 = 45°$ ir $n = 3.6$.

Pagal šią formulę suskaičiuotos THz impulso padidėjimo vertės pavaizduotos pav. 8.20a mėlynais kvadratėliais. Praktikoje, siekiant efektyviausio THz spinduliuotės generavimo, dažniausiai sukuriami vidutinio skėsties dy-

džio THz pluoštai ir tuomet THz signalo padidėjimo vertės yra kažkur tarp mėlynais ir žaliais taškais pažymėtų verčių (pav. 8.20a). Reiktų paminėti, kad šiame darbe nustatyti GaAs NV sluoksnių n_0 yra didesni nei būtų galima tikėtis įvertinus puslaidininkio ir oro užimamų tūrių santykį NV sluoksnyje ($n_0 \approx 1.3$). Kol kas nėra aišku, kas lemia didesnes sluoksnių lūžio rodiklio vertes, tačiau, jei pavyktų dar sumažinti NV sluoksnio lūžio rodiklį, būtų galima tikėtis dar keletą kartų padidinti THz impulso amplitudę (pav. 8.20a raudoni taškai).

Galimybė auginti padėklo atžvilgiu pasvirusias NV yra unikalus būdas pasukti elektrinį dipolį ir tokiu būdu dar labiau padidinti THz impulso amplitudę. Pav. 8.20b parodyta kaip šis padidėjimas priklauso nuo dipolio pasvirimo kampo, THz impulsus registruojant atspindžio geometrijoje. Skaičiavimai atlikti atvejui, kai THz spinduliuotės šaltinis yra $n = 3.6$ lūžio rodiklio padėkle. Jei lūžio rodiklis būtų mažesnis, θ įtaka signalo sustiprėjimui mažėtų. Pavyzdžiui, jei THz impulsus emituojantis dipolis palinkęs padėklo atžvilgiu 35° kampu, o spinduliuojančio sluoksnio $n_0 = 2.6$ (NW4 atvejis), tai registruojamo signalo sustiprėjimo koeficientas bus lygus 2.5 (dipoliui esant GaAs padėkle toks sustiprėjimo koeficientas gaunamas prie $\theta = 18°$). Bendras THz amplitudės padidėjimas pagal aprašytus skaičiavimus NW4 bandinio atveju būtų $2.5 * 1.6 = 4$, kur koeficientą 2.5 lemia nanovielelių pasvirimas, o koeficientą 1.6 – mažesnis nei padėklo lūžio rodiklis. Mokslinėje literatūroje, THz emisijos sustiprėjimo priežastimi dažnai laikoma padidėjusi THz spinduliuotės ištrūka iš nanodarinių. Įdomu tai, kad, pagal šiame darbe skaičiavimams naudotą modelį, THz spinduliuotės ištrūka iš THz impulsus spinduliuojančio sluoksnio yra šimtaprocentinė ir nepriklauso nuo n_0, o pagrindinis THz generavimo sustiprėjimo mechanizmas yra THz spinduliuotės generavimo krypties pokytis dipolio ašies atžvilgiu.

Galima teigti, kad skaičiavimams naudotas modelis gana gerai paaiškina THz impulso padidėjimo rezultatus, atvaizduotus pav. 8.16. Skaičiavimai prognozuoja apie apie 4 kartus didesnę THz impulso amplitudę, o eksperimento metu gaunamos šiek tiek didesnės vertės (Šis mažas neatitikimas gali būti paaiškintas aukščiau aptartu THz spinduliuotės skėsties pokyčiu). Tai reiškia, kad sužadintų krūvininkų dinamika ištirtose GaAs NV ir GaAs padėkle yra panaši, abiejose terpėse sugeneruojami panašūs dipoliai, o THz emisijos padidėjimą daugiausiai lemia mažesnis NW sluoksnio lūžio rodiklis.

Apibendrinimas

1. Pasiūlytas trijų terpių (oras, NV sluoksnis, puslaidininkis) teorinis modelis THz impulsų emisijai iš NV bandinių aprašyti.

2. Naudojantis pasiūlytu modelius buvo nustatytas NV sluoksnio efektinis lūžio rodiklis n_0.

3. Lūžio rodiklis n_0 NV sluoksnyje yra mažesnis nei SI GaAs, kas leidžia padidinti kampą tarp THz spinduliuotės generavimo krypties bei elektrinio dipolio ašies, tokiu būdu padidinant THz spinduliuotės generavimo efektyvumą.

8.5 Pagrindiniai rezultatai ir išvados

Šiame darbe, pasitelkus įprastas bei naujai sukurtas lazeriu žadinamos THz impulsų emisijos tyrimo metodikas, ištirti kelių tipų puslaidininkiniai nanodariniai. Sukurti modeliai, aiškinantys nanodarinių THz spinduliuotės emisijos ypatybes, bei išskirti pagrindiniai veiksniai, lemiantys šios emisijos sustiprėjimą.

1. Puslaidininkinių padėklų nanostruktūrizavimas dažnai lemia išilginių darinių paviršiuje susiformavimą (Ga15 ir LIPSS). Tyrimai parodė, kad tokia paviršiaus geometrija yra labai svarbi, nes ji lemia netolygų sužadintų krūvininkų pasiskirstymą ir paviršiui lygiagrečios fotosrovės atsiradimą. Ši fotosrovė lemia THz impulsus spinduliuojančio elektrinio dipolio pasvirimą ir yra pagrindinė THz emisijos sustiprėjimo priežastis.

2. Retesniais atvejais nanodariniai gali smarkiai pakeisti optines paviršiaus savybes (Ga4). Tokiu atveju THz emisijos sustiprėjimą lemia netiesinių optinių konstantų pasikeitimas, susijęs su nanostruktūrizuoto puslaidininkio kristalografija.

3. InAs nanovielelių sluoksniai nėra geresni THz impulsų šaltiniai nei InAs padėklai dėl neigiamos paviršiaus defektų įtakos generavimo procesui. Didinant Ga kiekį InGaAs nanovielelėse, paviršiaus įtaka THz generavimo procesui laipsniškai mažėja. Ga atomų kiekiui artėjant prie 50% ribos pasiekiamas didžiausias THz emisijos efektyvumas. Pakankamai ilgų tokios sudėties nanovielelių sluoksnis būtų kelis kartus efektyvesnis THz impulsų emiteris už etaloninį p-InAs padėklą.

4. Tiriant THz impulsų emisiją, puslaidininkinių nanovielelių visumą galima aprašyti plonu sluoksniu, kurio lūžio rodiklis n_0 yra mažesnis už to paties puslaidininkio padėklo lūžio rodiklį. Mažesnis n_0 lemia kampo tarp THz spinduliuotės generavimo krypties bei elektrinio dipolio ašies padidėjimą ir tokiu būdu padidina THz spinduliuotės generavimo

efektyvumą. Toks modelis paneigia paplitusią nuomonę, kad pagrindinis THz emisijos iš nanovielelių sustiprėjimo mechanizmas yra geresnė THz spinduliuotės ištrūka iš nanovielelių.

References

[1] R. Inoue, K. Takayama, and M. Tonouchi, "Angular dependence of terahertz emission from semiconductor surfaces photoexcited by femtosecond optical pulses," *Journal of the Optical Society of America B*, vol. 26, p. A14, may 2009.

[2] M. B. Johnston, D. M. Whittaker, A. Corchia, A. G. Davies, and E. H. Linfield, "Theory of magnetic-field enhancement of surface-field terahertz emission," *Journal of Applied Physics*, vol. 91, pp. 2104–2106, feb 2002.

[3] M. Tonouchi, "Cutting-edge terahertz technology," *Nature Photonics*, vol. 1, pp. 97–105, feb 2007.

[4] C. Yu, S. Fan, Y. Sun, and E. Pickwell-MacPherson, "The potential of terahertz imaging for cancer diagnosis: A review of investigations to date," *Quantitative imaging in medicine and surgery*, vol. 2, pp. 33–45, mar 2012.

[5] Z. Yan, Y. Ying, H. Zhang, and H. Yu, "Research progress of terahertz wave technology in food inspection," in *Terahertz Physics, Devices, and Systems* (M. Anwar, A. J. DeMaria, and M. S. Shur, eds.), SPIE, oct 2006.

[6] K. Fukunaga, I. Hosako, I. N. D. III, and M. Picollo, "Terahertz imaging systems: a non-invasive technique for the analysis of paintings," in *O3A: Optics for Arts, Architecture, and Archaeology II* (L. Pezzati and R. Salimbeni, eds.), SPIE, jul 2009.

[7] G. Molis, A. Krotkus, and V. Vaičaitis, "Intervalley separation in the conduction band of InGaAs measured by terahertz excitation spectroscopy," *Applied Physics Letters*, vol. 94, p. 091104, mar 2009.

[8] R. Köhler, A. Tredicucci, F. Beltram, H. E. Beere, E. H. Linfield, A. G. Davies, D. A. Ritchie, R. C. Iotti, and F. Rossi, "Terahertz semiconductor-heterostructure laser," *Nature*, vol. 417, pp. 156–159, may 2002.

[9] pp. 216–221, Comitato Conferenze Elettra, sep 2004.

[10] N. Gavrilov, B. Knyazev, E. Kolobanov, V. Kotenkov, V. Kubarev, G. Kulipanov, A. Matveenko, L. Medvedev, S. Miginsky, L. Mironenko, A. Oreshkov, V. Ovchar, V. Popik, T. Salikova, M. Scheglov, S. Serednyakov, O. Shevchenko, A. Skrinsky, V. Tcheskidov, and N. Vinokurov, "Status of the novosibirsk high-power terahertz FEL," *Nuclear Instruments and Methods in Physics Research Section A: Accelerators, Spectrometers, Detectors and Associated Equipment*, vol. 575, pp. 54–57, may 2007.

[11] D. Auston and M. Nuss, "Electrooptical generation and detection of femtosecond electrical transients," *IEEE Journal of Quantum Electronics*, vol. 24, pp. 184–197, feb 1988.

[12] P. Smith, D. Auston, and M. Nuss, "Subpicosecond photoconducting dipole antennas," *IEEE Journal of Quantum Electronics*, vol. 24, pp. 255–260, feb 1988.

[13] H. Ahn, Y.-P. Ku, Y.-C. Wang, C.-H. Chuang, S. Gwo, and C.-L. Pan, "Terahertz emission from vertically aligned InN nanorod arrays," *Applied Physics Letters*, vol. 91, p. 132108, sep 2007.

[14] P. Hoyer, M. Theuer, R. Beigang, and E.-B. Kley, "Terahertz emission from black silicon," *Applied Physics Letters*, vol. 93, p. 091106, sep 2008.

[15] M. Reid, I. V. Cravetchi, R. Fedosejevs, I. M. Tiginyanu, and L. Sirbu, "Enhanced terahertz emission from porous InP (111) membranes," *Applied Physics Letters*, vol. 86, p. 021904, jan 2005.

[16] G. B. Jung, Y. J. Cho, Y. Myung, H. S. Kim, Y. S. Seo, J. Park, and C. Kang, "Geometry-dependent terahertz emission of silicon nanowires," *Optics Express*, vol. 18, p. 16353, jul 2010.

[17] W.-J. Lee, J. W. Ma, J. M. Bae, K.-S. Jeong, M.-H. Cho, C. Kang, and J.-S. Wi, "Strongly enhanced THz emission caused by localized surface charges in semiconducting germanium nanowires," *Scientific Reports*, vol. 3, jun 2013.

[18] J.-H. Yim, M. Irfan, K.-J. Song, E.-H. Lee, J.-D. Song, and Y.-D. Jho, "Polarized terahertz waves emitted from $in_{0.2}ga_{0.8}as$ nanowires," *Journal of Nanoscience and Nanotechnology*, vol. 15, pp. 6024–6027, aug 2015.

[19] V. N. Trukhin, A. S. Buyskikh, N. A. Kaliteevskaya, A. D. Bourauleuv, L. L. Samoilov, Y. B. Samsonenko, G. E. Cirlin, M. A. Kaliteevski, and A. J. Gallant, "Terahertz generation by GaAs nanowires," *Applied Physics Letters*, vol. 103, p. 072108, aug 2013.

[20] D. V. Seletskiy, M. P. Hasselbeck, J. G. Cederberg, A. Katzenmeyer, M. E. Toimil-Molares, F. Léonard, A. A. Talin, and M. Sheik-Bahae, "Efficient terahertz emission from InAs nanowires," *Physical Review B*, vol. 84, sep 2011.

[21] *Principles of Terahertz Science and Technology*. Springer US, 2009.

[22] B. S. Williams, "Terahertz quantum-cascade lasers," *Nature Photonics*, vol. 1, pp. 517–525, sep 2007.

[23] P. H. Siegel, "Terahertz pioneer: David H. Auston," *IEEE Transactions on Terahertz Science and Technology*, vol. 1, pp. 6–8, sep 2011.

[24] D. H. Auston, K. P. Cheung, and P. R. Smith, "Picosecond photoconducting hertzian dipoles," *Applied Physics Letters*, vol. 45, pp. 284–286, aug 1984.

[25] C. Fattinger and D. Grischkowsky, "Terahertz beams," *Applied Physics Letters*, vol. 54, pp. 490–492, feb 1989.

[26] B. B. Hu, X.-C. Zhang, and D. H. Auston, "Terahertz radiation induced by subband-gap femtosecond optical excitation of GaAs," *Physical Review Letters*, vol. 67, pp. 2709–2712, nov 1991.

[27] X.-C. Zhang, B. B. Hu, J. T. Darrow, and D. H. Auston, "Generation of femtosecond electromagnetic pulses from semiconductor surfaces," *Applied Physics Letters*, vol. 56, pp. 1011–1013, mar 1990.

[28] A. C. Warren, N. Katzenellenbogen, D. Grischkowsky, J. M. Woodall, M. R. Melloch, and N. Otsuka, "Subpicosecond, freely propagating electromagnetic pulse generation and detection using GaAs:as epilayers," *Applied Physics Letters*, vol. 58, pp. 1512–1514, apr 1991.

[29] K. Bertulis, A. Krotkus, G. Aleksejenko, V. Pačebutas, R. Adomavičius, G. Molis, and S. Marcinkevičius, "GaBiAs: A material for optoelectronic terahertz devices," *Applied Physics Letters*, vol. 88, p. 201112, may 2006.

[30] Y. Zhang, X. Zhang, S. Li, J. Gu, Y. Li, Z. Tian, C. Ouyang, M. He, J. Han, and W. Zhang, "A broadband THz-TDS system based on DSTMS emitter and LTG InGaAs/InAlAs photoconductive antenna detector," *Scientific Reports*, vol. 6, may 2016.

[31] B. Recur, A. Younus, S. Salort, P. Mounaix, B. Chassagne, P. Desbarats, J.-P. Caumes, and E. Abraham, "Investigation on reconstruction methods applied to 3d terahertz computed tomography," *Optics Express*, vol. 19, p. 5105, mar 2011.

[32] M. Leahy-Hoppa, M. Fitch, X. Zheng, L. Hayden, and R. Osiander, "Wideband terahertz spectroscopy of explosives," *Chemical Physics Letters*, vol. 434, pp. 227–230, feb 2007.

[33] A. G. Davies, A. D. Burnett, W. Fan, E. H. Linfield, and J. E. Cunningham, "Terahertz spectroscopy of explosives and drugs," *Materials Today*, vol. 11, pp. 18–26, mar 2008.

[34] W. R. Tribe, D. A. Newnham, P. F. Taday, and M. C. Kemp, "Hidden object detection: security applications of terahertz technology," in *Terahertz and Gigahertz Electronics and Photonics III* (R. J. Hwu, ed.), SPIE, apr 2004.

[35] M. Kawase, T. Saito, M. Ogawa, H. Uejima, Y. Hatsuda, S. Kawanisi, Y. Hirotani, M. Myotoku, K. Ikeda, H. Konishi, I. Iga, J. Yamakawa, S. Nishizawa, K. Yamamoto, and M. Tani, "Application of terahertz absorption spectroscopy to evaluation of aging variation of medicine," *Analytical Sciences*, vol. 27, no. 2, p. 209, 2011.

[36] C. Jördens, "Detection of foreign bodies in chocolate with pulsed terahertz spectroscopy," *Optical Engineering*, vol. 47, p. 037003, mar 2008.

[37] D. F. Plusquellic, K. Siegrist, E. J. Heilweil, and O. Esenturk, "Applications of terahertz spectroscopy in biosystems," *ChemPhysChem*, vol. 8, pp. 2412–2431, dec 2007.

[38] M. Walther, D. G. Cooke, C. Sherstan, M. Hajar, M. R. Freeman, and F. A. Hegmann, "Terahertz conductivity of thin gold films at the metal-insulator percolation transition," *Physical Review B*, vol. 76, sep 2007.

[39] D. Mittleman, R. Jacobsen, R. Neelamani, R. Baraniuk, and M. Nuss, "Gas sensing using terahertz time-domain spectroscopy," *Applied Physics B: Lasers and Optics*, vol. 67, pp. 379–390, sep 1998.

[40] P. D. Cunningham, N. N. Valdes, F. A. Vallejo, L. M. Hayden, B. Polishak, X.-H. Zhou, J. Luo, A. K.-Y. Jen, J. C. Williams, and R. J. Twieg, "Broadband terahertz characterization of the refractive index and absorption of some important polymeric and organic electro-optic materials," *Journal of Applied Physics*, vol. 109, pp. 043505–043505–5, feb 2011.

[41] S. Wietzke, F. Rutz, C. Jördens, N. Krumbholz, N. Vieweg, C. Jansen, R. Wilk, and M. Koch, "Applications of terahertz spectroscopy in the plastics industry," in *Terahertz Photonics* (C. Zhang and X.-C. Zhang, eds.), SPIE, nov 2007.

[42] J.-P. Guillet, M. Roux, K. Wang, X. Ma, F. Fauquet, H. Balacey, B. Recur, F. Darracq, and P. Mounaix, "Art painting diagnostic before restoration with terahertz and millimeter waves," *Journal of Infrared, Millimeter, and Terahertz Waves*, vol. 38, pp. 369–379, jan 2017.

[43] H. Elayan, O. Amin, R. M. Shubair, and M.-S. Alouini, "Terahertz communication: The opportunities of wireless technology beyond 5g," in *2018 International Conference on Advanced Communication Technologies and Networking (CommNet)*, IEEE, apr 2018.

[44] J. Federici and L. Moeller, "Review of terahertz and subterahertz wireless communications," *Journal of Applied Physics*, vol. 107, p. 111101, jun 2010.

[45] R. McLaughlin, Q. Chen, A. Corchia, C. M. Ciesla, D. D. Arnone, X. C. Zhang, G. A. C. Jones, E. H. Linfield, and M. Pepper, "Enhanced coherent terahertz emission from indium arsenide," *Journal of Modern Optics*, vol. 47, pp. 1847–1856, sep 2000.

[46] K. Liu, A. D. Koulouklidis, D. G. Papazoglou, S. Tzortzakis, and X.-C. Zhang, "Enhanced terahertz wave emission from air-plasma tailored by abruptly autofocusing laser beams," *Optica*, vol. 3, p. 605, jun 2016.

[47] Q. Jin, Y. E, K. Williams, J. Dai, and X.-C. Zhang, "Observation of broadband terahertz wave generation from liquid water," *Applied Physics Letters*, vol. 111, p. 071103, aug 2017.

[48] M. S. Longair, *Radiation of accelerated charged particles and bremsstrahlung of electrons*, p. 154–177. Cambridge University Press, 3 ed., 2011.

[49] W. Shockley, "On the surface states associated with a periodic potential," *Physical Review*, vol. 56, pp. 317–323, aug 1939.

[50] E. Gerlach, "On the existence of tamm states," *Surface Science*, vol. 15, pp. 549–554, jul 1969.

[51] V. Kažukauskas, *Šiuolaikiniai puslaidininkių mikroelektronikos prietaisai. Fizika ir technologija*, p. 180. Progretus, 2008.

[52] X.-C. Zhang and D. H. Auston, "Optoelectronic measurement of semiconductor surfaces and interfaces with femtosecond optics," *Journal of Applied Physics*, vol. 71, pp. 326–338, jan 1992.

[53] M. Nakajima, M. Hangyo, M. Ohta, and H. Miyazaki, "Polarity reversal of terahertz waves radiated from semi-insulating InP surfaces induced by temperature," *Physical Review B*, vol. 67, may 2003.

[54] P. Gu, M. Tani, S. Kono, K. Sakai, and X.-C. Zhang, "Study of terahertz radiation from InAs and InSb," *Journal of Applied Physics*, vol. 91, pp. 5533–5537, may 2002.

[55] K. Liu, J. Xu, T. Yuan, and X.-C. Zhang, "Terahertz radiation from InAs induced by carrier diffusion and drift," *Physical Review B*, vol. 73, apr 2006.

[56] M. B. Johnston, D. M. Whittaker, A. Corchia, A. G. Davies, and E. H. Linfield, "Simulation of terahertz generation at semiconductor surfaces," *Physical Review B*, vol. 65, mar 2002.

[57] V. Apostolopoulos and M. E. Barnes, "THz emitters based on the photodember effect," *Journal of Physics D: Applied Physics*, vol. 47, p. 374002, aug 2014.

[58] G. Klatt, F. Hilser, W. Qiao, M. Beck, R. Gebs, A. Bartels, K. Huska, U. Lemmer, G. Bastian, M. Johnston, M. Fischer, J. Faist, and T. Dekorsy, "Terahertz emission from lateral
photo-dember currents," *Optics Express*, vol. 18, p. 4939, feb 2010.

[59] R. Mueckstein, M. Natrella, O. Hatem, J. R. Freeman, C. S. Graham, C. C. Renaud, A. J. Seeds, E. H. Linfield, A. G. Davies, P. J. Cannard, M. J. Robertson, D. G. Moodie, and O. Mitrofanov, "Near-field analysis of terahertz pulse generation from photo-excited charge density gradients," *IEEE Transactions on Terahertz Science and Technology*, vol. 5, pp. 260–267, mar 2015.

[60] S. Kono, P. Gu, M. Tani, and K. Sakai, "Temperature dependence of terahertz radiation from n-type InSb and n-type InAs surfaces," *Applied Physics B*, vol. 71, pp. 901–904, dec 2000.

[61] R. Adomavičius, A. Urbanowicz, G. Molis, A. Krotkus, and E. Šatkovskis, "Terahertz emission from p-lnAs due to the instantaneous polarization," *Applied Physics Letters*, vol. 85, pp. 2463–2465, sep 2004.

[62] X.-C. Zhang, Y. Jin, K. Yang, and L. J. Schowalter, "Resonant nonlinear susceptibility near the GaAs band gap," *Physical Review Letters*, vol. 69, pp. 2303–2306, oct 1992.

[63] G. Xu, G. Sun, Y. J. Ding, I. B. Zotova, K. C. Mandal, A. Mertiri, G. Pabst, R. Roy, and N. C. Fernelius, "Investigation of terahertz generation due to unidirectional diffusion of carriers in centrosymmetric GaTe crystals," *IEEE Journal of Selected Topics in Quantum Electronics*, vol. 17, pp. 30–37, jan 2011.

[64] R. W. Boyd, *The Nonlinear Optical Susceptibility*, pp. 1–67. Elsevier, 2008.

[65] O. Madelung, U. Rössler, and M. Schulz, eds., *Group IV Elements, IV-IV and III-V Compounds. Part b - Electronic, Transport, Optical and Other Properties*. Springer-Verlag, 2002.

[66] M. Bass, P. A. Franken, J. F. Ward, and G. Weinreich, "Optical rectification," *Physical Review Letters*, vol. 9, pp. 446–448, dec 1962.

[67] M. C. Hoffmann, K.-L. Yeh, J. Hebling, and K. A. Nelson, "Efficient terahertz generation by optical rectification at 1035 nm," *Optics Express*, vol. 15, no. 18, p. 11706, 2007.

[68] M. Reid, I. V. Cravetchi, and R. Fedosejevs, "Terahertz radiation and second-harmonic generation from InAs: Bulk versus surface electric-field-induced contributions," *Physical Review B*, vol. 72, jul 2005.

[69] S. L. Chuang, S. Schmitt-Rink, B. I. Greene, P. N. Saeta, and A. F. J. Levi, "Optical rectification at semiconductor surfaces," *Physical Review Letters*, vol. 68, pp. 102–105, jan 1992.

[70] A. Urbanowicz, A. Krotkus, R. Adomavičius, and V. Malevich, "Terahertz emission from femtosecond laser excited ge surfaces due to the electrical field-induced optical rectification," *Physica B: Condensed Matter*, vol. 398, pp. 98–101, aug 2007.

[71] V. L. Malevich, A. Krotkus, A. Bičiūnas, and V. Pačebutas, "Terahertz emission from femtosecond laser illuminated (112) surfaces of InSb," *Journal of Applied Physics*, vol. 104, p. 113117, dec 2008.

[72] V. L. Malevich, P. A. Ziaziulia, R. Adomavičius, A. Krotkus, and Y. V. Malevich, "Terahertz emission from cubic semiconductor induced by a transient anisotropic photocurrent," *Journal of Applied Physics*, vol. 112, p. 073115, oct 2012.

[73] Y. V. Malevich, R. Adomavičius, A. Krotkus, and V. L. Malevich, "Anisotropic picosecond photoconductivity caused by optical alignment of electron momenta in cubic semiconductors," *Journal of Applied Physics*, vol. 115, p. 073103, feb 2014.

[74] A. Arlauskas, L. Subačius, A. Krotkus, and V. L. Malevich, "Terahertz emission from InSb illuminated by femtosecond laser pulses," *Journal of Physics D: Applied Physics*, vol. 50, p. 055101, jan 2017.

[75] P. Cicėnas, A. Geižutis, V. L. Malevich, and A. Krotkus, "Terahertz radiation from an InAs surface due to lateral photocurrent transients," *Optics Letters*, vol. 40, p. 5164, nov 2015.

[76] R. Mendis, M. L. Smith, L. J. Bignell, R. E. M. Vickers, and R. A. Lewis, "Strong terahertz emission from (100) p-type InAs," *Journal of Applied Physics*, vol. 98, p. 126104, dec 2005.

[77] M. L. Smith, R. Mendis, R. E. M. Vickers, and R. A. Lewis, "Comparison of photoexcited p-InAs THz radiation source with conventional thermal radiation sources," *Journal of Applied Physics*, vol. 105, p. 063109, mar 2009.

[78] U. Blumröder, M. Zilk, H. Hempel, P. Hoyer, T. Pertsch, R. Eichberger, T. Unold, and S. Nolte, "Influence of structure geometry on THz emission from black silicon surfaces fabricated by reactive ion etching," *Optics Express*, vol. 25, p. 6604, mar 2017.

[79] P. Tingzon, L. Lopez, N. Oliver, N. Cabello, A. Cafe, A. D. L. Reyes, J. Muldera, E. Prieto, C. Que, G. Santos, M. Tani, A. Salvador, E. Estacio, and A. Somintac, "Terahertz emission and photoluminescence of silicon nanowires electrolessly etched on the surface of silicon (100), (110), and (111) substrates for photovoltaic cell applications," *Photonics and Nanostructures - Fundamentals and Applications*, vol. 24, pp. 1–6, may 2017.

[80] J. J. Ibanes, M. H. Balgos, R. Jaculbia, A. Salvador, A. Somintac, E. Estacio, C. T. Que, S. Tsuzuki, K. Yamamoto, and M. Tani, "Terahertz emission from GaAs-AlGaAs core-shell nanowires on si (100) substrate: Effects of applied magnetic field and excitation wavelength," *Applied Physics Letters*, vol. 102, p. 063101, feb 2013.

[81] V. Trukhin, A. Bouravleuv, I. Mustafin, J. Kakko, and H. Lipsanen, "Optically excited THz generation from ordered arrays of GaAs nanowires," *Procedia Engineering*, vol. 201, pp. 100–104, 2017.

[82] A. Arlauskas, J. Treu, K. Saller, I. Beleckaitė, G. Koblmüller, and A. Krotkus, "Strong terahertz emission and its origin from catalyst-free InAs nanowire arrays," *Nano Letters*, vol. 14, pp. 1508–1514, feb 2014.

[83] A. Krotkus, K. Bertulis, L. Dapkus, U. Olin, and S. Marcinkevičius, "Ultrafast carrier trapping in be-doped low-temperature-grown GaAs," *Applied Physics Letters*, vol. 75, pp. 3336–3338, nov 1999.

[84] M. Tani, K.-S. Lee, and X.-C. Zhang, "Detection of terahertz radiation with low-temperature-grown GaAs-based photoconductive antenna using 1.55 μm probe," *Applied Physics Letters*, vol. 77, pp. 1396–1398, aug 2000.

[85] H. Liu, J. Yu, P. Huggard, and B. Alderman, "A multichannel THz detector using integrated bow-tie antennas," *International Journal of Antennas and Propagation*, vol. 2013, pp. 1–8, 2013.

[86] N. T. Yardimci and M. Jarrahi, "High sensitivity terahertz detection through large-area plasmonic nano-antenna arrays," *Scientific Reports*, vol. 7, feb 2017.

[87] Y. Cai, I. Brener, J. Lopata, J. Wynn, L. Pfeiffer, and J. Federici, "Design and performance of singular electric field terahertz photoconducting antennas," *Applied Physics Letters*, vol. 71, pp. 2076–2078, oct 1997.

[88] C. Winnewisser, P. U. Jepsen, M. Schall, V. Schyja, and H. Helm, "Electro-optic detection of THz radiation in LiTaO3, LiNbO3 and ZnTe," *Applied Physics Letters*, vol. 70, pp. 3069–3071, jun 1997.

[89] Q. Wu and X.-C. Zhang, "7 terahertz broadband GaP electro-optic sensor," *Applied Physics Letters*, vol. 70, pp. 1784–1786, apr 1997.

[90] R. Adomavičius, A. Krotkus, J. Kois, S. Bereznev, and E. Mellikov, "Terahertz radiation from nonstoichiometric CuInSe2 films excited by femtosecond laser pulses," *Applied Physics Letters*, vol. 87, p. 191104, nov 2005.

[91] A. Arlauskas, V. Pačebutas, R. Butkutė, R. Norkus, B. Čechavičius, E. Pozingytė, and A. Krotkus, "Semiconductor band structure characterization by terahertz excitation spectroscopy," in *2018 43rd International Conference on Infrared, Millimeter, and Terahertz Waves* (*IRMMW-THz*), IEEE, sep 2018.

[92] I. Beleckaitė, R. Adomavičius, R. Butkutė, V. Pačebutas, G. Molis, V. Bukauskas, A. Selskis, and A. Krotkus, "Non-stoichiometric GaAs – prospective material for compact THz emitters," *Electronics Letters*, vol. 52, pp. 1954–1956, nov 2016.

[93] I. Beleckaitė, R. Adomavičius, G. Molis, A. Šiušys, A. Reszka, T. Wojciechowski, J. Sadowski, and A. Krotkus, "Characterization of non-vertically aligned semiconductor nanowires by THz emission measurements," in *2016 41st International Conference on Infrared, Millimeter, and Terahertz waves* (*IRMMW-THz*), IEEE, sep 2016.

[94] M. Tonouchi, N. Kawasaki, T. Yoshimura, H. Wald, and P. Seidel, "Pump and probe terahertz generation study of ultrafast carrier dynamics in low-temperature grown-GaAs," *Japanese Journal of Applied Physics*, vol. 41, pp. L706–L709, jun 2002.

[95] K. J. Siebert, A. Lisauskas, T. Löffler, and H. G. Roskos, "Field screening in low-temperature-grown GaAs photoconductive antennas," *Japanese Journal of Applied Physics*, vol. 43, pp. 1038–1043, mar 2004.

[96] H. Nakanishi, A. Ito, K. Takayama, I. Kawayama, H. Murakami, and M. Tonouchi, "Visualization of photoexcited carrier responses in a solar cell using optical pump—terahertz emission probe technique," *Journal of Infrared, Millimeter, and Terahertz Waves*, vol. 37, pp. 498–506, dec 2015.

[97] I. Beleckaitė, L. Burakauskas, and R. Adomavičius, "Study of surface electric field and photocarrier dynamics in InAs by means of a modified double-pump-pulse terahertz emission method," *Lithuanian Journal of Physics*, vol. 58, mar 2018.

[98] L. Peters, J. Tunesi, A. Pasquazi, and M. Peccianti, "High-energy terahertz surface optical rectification," *Nano Energy*, vol. 46, pp. 128–132, apr 2018.

[99] T. Dekorsy, H. Auer, H. J. Bakker, H. G. Roskos, and H. Kurz, "THz electromagnetic emission by coherent infrared-active phonons," *Physical Review B*, vol. 53, pp. 4005–4014, feb 1996.

[100] N. Sarukura, H. Ohtake, S. Izumida, and Z. Liu, "High average-power THz radiation from femtosecond laser-irradiated InAs in a magnetic field and its elliptical polarization characteristics," *Journal of Applied Physics*, vol. 84, pp. 654–656, jul 1998.

[101] W. Lukosz, "Light emission by magnetic and electric dipoles close to a plane dielectric interface III radiation patterns of dipoles with arbitrary orientation," *Journal of the Optical Society of America*, vol. 69, p. 1495, nov 1979.

[102] W. Lukosz and R. E. Kunz, "Light emission by magnetic and electric dipoles close to a plane dielectric interface II radiation patterns of perpendicular oriented dipoles," *Journal of the Optical Society of America*, vol. 67, p. 1615, dec 1977.

[103] A. Y. Cho, "GaAs epitaxy by a molecular beam method: Observations of surface structure on the (001) face," *Journal of Applied Physics*, vol. 42, pp. 2074–2081, apr 1971.

[104] K. Alavi, "Molecular beam epitaxy," in *Encyclopedia of Materials: Science and Technology*, pp. 5765–5780, Elsevier, 2001.

[105] A. Bosacchi, S. Franchi, Y. Kanter, and S. Chikichev, "Study of GaAs MBE growth under ga-rich conditions by RHEED intensity oscillations," *Journal of Crystal Growth*, vol. 96, pp. 899–905, aug 1989.

[106] M. Kaminska, Z. Liliental-Weber, E. R. Weber, T. George, J. B. Kortright, F. W. Smith, B.-Y. Tsaur, and A. R. Calawa, "Structural properties of as-

rich GaAs grown by molecular beam epitaxy at low temperatures," *Applied Physics Letters*, vol. 54, pp. 1881–1883, may 1989.

[107] Z. Liliental-Weber, W. Swider, K. M. Yu, J. Kortright, F. W. Smith, and A. R. Calawa, "Breakdown of crystallinity in low-temperature-grown GaAs layers," *Applied Physics Letters*, vol. 58, pp. 2153–2155, may 1991.

[108] A. Krotkus, S. Marcinkevicius, J. Jasinski, M. Kaminska, H. H. Tan, and C. Jagadish, "Picosecond carrier lifetime in GaAs implanted with high doses of as ions: An alternative material to low-temperature GaAs for optoelectronic applications," *Applied Physics Letters*, vol. 66, pp. 3304–3306, jun 1995.

[109] C. Jagadish, H. H. Tan, J. Jasinski, M. Kaminska, M. Palczewska, A. Krotkus, and S. Marcinkevicius, "High resistivity and picosecond carrier lifetime of GaAs implanted with MeV ga ions at high fluences," *Applied Physics Letters*, vol. 67, pp. 1724–1726, sep 1995.

[110] A. Geižutis, R. Adomavičius, A. Urbanowicz, K. Bertulis, A. Krotkus, H. H. Tan, and C. Jagadish, "Carrier recombination properties in low-temperature-grown and ion-implanted GaAs," *Lithuanian Journal of Physics*, vol. 45, no. 4, pp. 249–255, 2005.

[111] A. Krotkus, K. Bertulis, R. Adomavičius, V. Pačebutas, and A. Geižutis, "Semiconductor materials for ultrafast optoelectronic applications," *Lithuanian Journal of Physics*, vol. 49, no. 4, pp. 359–372, 2009.

[112] M. Tani, S. Matsuura, K. Sakai, and S. ichi Nakashima, "Emission characteristics of photoconductive antennas based on low-temperature-grown GaAs and semi-insulating GaAs," *Applied Optics*, vol. 36, p. 7853, oct 1997.

[113] K. J. Siebert, H. Quast, R. Leonhardt, T. Löffler, M. Thomson, T. Bauer, H. G. Roskos, and S. Czasch, "Continuous-wave all-optoelectronic terahertz imaging," *Applied Physics Letters*, vol. 80, pp. 3003–3005, apr 2002.

[114] J.-M. Rämer, F. Ospald, G. von Freymann, and R. Beigang, "Generation and detection of terahertz radiation up to 4.5 THz by low-temperature grown GaAs photoconductive antennas excited at 1560 nm," *Applied Physics Letters*, vol. 103, p. 021119, jul 2013.

[115] A. Y. Elezzabi, J. Meyer, M. K. Y. Hughes, and S. R. Johnson, "Generation of 1-ps infrared pulses at 106 μm by use of low-temperature-grown GaAs as an optical semiconductor switch," *Optics Letters*, vol. 19, p. 898, jun 1994.

[116] F. Smith, A. Calawa, C.-L. Chen, M. Manfra, and L. Mahoney, "New MBE buffer used to eliminate backgating in GaAs MESFETs," *IEEE Electron Device Letters*, vol. 9, pp. 77–80, feb 1988.

[117] C.-L. Chen, F. Smith, B. Clifton, L. Mahoney, M. Manfra, and A. Calawa, "High-power-density GaAs MISFETs with a low-temperature-grown epitaxial layer as the insulator," *IEEE Electron Device Letters*, vol. 12, pp. 306–308, jun 1991.

[118] J.-W. Shi, Y.-H. Chen, K.-G. Gan, Y.-J. Chiu, C.-K. Sun, and J. Bowers, "High-speed and high-power performances of LTG-GaAs based metal-semiconductor-metal traveling-wave-photodetectors in 1.3-/spl mu/m wavelength regime," *IEEE Photonics Technology Letters*, vol. 14, pp. 363–365, mar 2002.

[119] Z. Wang, M. Pietz, J. Walowski, A. Förster, M. I. Lepsa, and M. Münzenberg, "Spin dynamics triggered by subterahertz magnetic field pulses," *Journal of Applied Physics*, vol. 103, p. 123905, jun 2008.

[120] A. D. Álvarez, T. Xu, G. Tütüncüoglu, T. Demonchaux, J.-P. Nys, M. Berthe, F. Matteini, H. A. Potts, D. Troadec, G. Patriarche, J.-F. Lampin, C. Coinon, A. F. i Morral, R. E. Dunin-Borkowski, P. Ebert, and B. Grandidier, "Nonstoichiometric low-temperature grown GaAs nanowires," *Nano Letters*, vol. 15, pp. 6440–6445, sep 2015.

[121] R. Adomavičius, J. Adamonis, A. Bičiūnas, A. Krotkus, A. Atrashchenko, V. Evtikhiev, V. Ulin, M. Kaliteevski, and R. Abram, "Terahertz pulse emission from nanostructured (311) surfaces of GaAs," *Journal of Infrared, Millimeter, and Terahertz Waves*, vol. 33, pp. 599–604, apr 2012.

[122] M. Birnbaum, "Semiconductor surface damage produced by ruby lasers," *Journal of Applied Physics*, vol. 36, pp. 3688–3689, nov 1965.

[123] D. C. Emmony, R. P. Howson, and L. J. Willis, "Laser mirror damage in germanium at 10.6 μm," *Applied Physics Letters*, vol. 23, pp. 598–600, dec 1973.

[124] F. Keilmann and Y. H. Bai, "Periodic surface structures frozen into CO2 laser-melted quartz," *Applied Physics A Solids and Surfaces*, vol. 29, pp. 9–18, sep 1982.

[125] H. M. van Driel, J. E. Sipe, and J. F. Young, "Laser-induced periodic surface structure on solids: A universal phenomenon," *Physical Review Letters*, vol. 49, pp. 1955–1958, dec 1982.

[126] J. Bonse, S. Hohm, S. V. Kirner, A. Rosenfeld, and J. Kruger, "Laser-induced periodic surface structures— a scientific evergreen," *IEEE Journal of Selected Topics in Quantum Electronics*, vol. 23, may 2017.

[127] F. Garrelie, J.-P. Colombier, F. Pigeon, S. Tonchev, N. Faure, M. Bounhalli, S. Reynaud, and O. Parriaux, "Evidence of surface plasmon resonance in ultrafast laser-induced ripples," *Optics Express*, vol. 19, p. 9035, apr 2011.

[128] T. J.-Y. Derrien, T. E. Itina, R. Torres, T. Sarnet, and M. Sentis, "Possible surface plasmon polariton excitation under femtosecond laser irradiation of silicon," *Journal of Applied Physics*, vol. 114, p. 083104, aug 2013.

[129] D. Puerto, M. Garcia-Lechuga, J. Hernandez-Rueda, A. Garcia-Leis, S. Sanchez-Cortes, J. Solis, and J. Siegel, "Femtosecond laser-controlled self-assembly of amorphous-crystalline nanogratings in silicon," *Nanotechnology*, vol. 27, p. 265602, may 2016.

[130] S. Höhm, A. Rosenfeld, J. Krüger, and J. Bonse, "Femtosecond laser-induced periodic surface structures on silica," *Journal of Applied Physics*, vol. 112, p. 014901, jul 2012.

[131] J. Bonse, J. Krüger, S. Höhm, and A. Rosenfeld, "Femtosecond laser-induced periodic surface structures," *Journal of Laser Applications*, vol. 24, p. 042006, sep 2012.

[132] T. Tomita, R. Kumai, S. Matsuo, S. Hashimoto, and M. Yamaguchi, "Cross-sectional morphological profiles of ripples on si, SiC, and HOPG," *Applied Physics A*, vol. 97, pp. 271–276, aug 2009.

[133] N. Wu, Z. Wang, X. Wang, Y. Shimotsuma, M. Nishi, K. Miura, and K. Hirao, "Nano-periodic structure formation on titanium thin film with a femtosecond laser," *Journal of the Ceramic Society of Japan*, vol. 119, no. 1395, pp. 898–901, 2011.

[134] A. Y. Vorobyev and C. Guo, "Colorizing metals with femtosecond laser pulses," *Applied Physics Letters*, vol. 92, p. 041914, jan 2008.

[135] B. Dusser, Z. Sagan, H. Soder, N. Faure, J. Colombier, M. Jourlin, and E. Audouard, "Controlled nanostructrures formation by ultra fast laser pulses for color marking," *Optics Express*, vol. 18, p. 2913, jan 2010.

[136] A. Y. Vorobyev, V. S. Makin, and C. Guo, "Brighter light sources from black metal: Significant increase in emission efficiency of incandescent light sources," *Physical Review Letters*, vol. 102, jun 2009.

[137] A. Y. Vorobyev and C. Guo, "Antireflection effect of femtosecond laser-induced periodic surface structures on silicon," *Optics Express*, vol. 19, p. A1031, jul 2011.

[138] A.-M. Kietzig, S. G. Hatzikiriakos, and P. Englezos, "Patterned superhydrophobic metallic surfaces," *Langmuir*, vol. 25, pp. 4821–4827, apr 2009.

[139] A. Y. Vorobyev and C. Guo, "Laser turns silicon superwicking," *Optics Express*, vol. 18, p. 6455, mar 2010.

[140] A. Y. Vorobyev and C. Guo, "Direct femtosecond laser surface nano/microstructuring and its applications," *Laser & Photonics Reviews*, vol. 7, pp. 385–407, aug 2012.

[141] F. Müller, C. Kunz, and S. Gräf, "Bio-inspired functional surfaces based on laser-induced periodic surface structures," *Materials*, vol. 9, p. 476, jun 2016.

[142] X. Wang, C. A. Ohlin, Q. Lu, and J. Hu, "Cell directional migration and oriented division on three-dimensional laser-induced periodic surface structures on polystyrene," *Biomaterials*, vol. 29, pp. 2049–2059, may 2008.

[143] E. Rebollar, I. Frischauf, M. Olbrich, T. Peterbauer, S. Hering, J. Preiner, P. Hinterdorfer, C. Romanin, and J. Heitz, "Proliferation of aligned mammalian cells on laser-nanostructured polystyrene," *Biomaterials*, vol. 29, pp. 1796–1806, apr 2008.

[144] J. R. Bush, B. K. Nayak, L. S. Nair, M. C. Gupta, and C. T. Laurencin, "Improved bio-implant using ultrafast laser induced self-assembled nanotexture in titanium," *Journal of Biomedical Materials Research Part B: Applied Biomaterials*, vol. 97B, pp. 299–305, mar 2011.

[145] A. Cunha, A.-M. Elie, L. Plawinski, A. P. Serro, A. M. B. do Rego, A. Almeida, M. C. Urdaci, M.-C. Durrieu, and R. Vilar, "Femtosecond laser surface texturing of titanium as a method to reduce the adhesion of staphylococcus aureus and biofilm formation," *Applied Surface Science*, vol. 360, pp. 485–493, jan 2016.

[146] H.-W. Chang, Y.-C. Tsai, C.-W. Cheng, C.-Y. Lin, Y.-W. Lin, and T.-M. Wu, "Nanostructured ag surface fabricated by femtosecond laser for surface-enhanced raman scattering," *Journal of Colloid and Interface Science*, vol. 360, pp. 305–308, aug 2011.

[147] R. Buividas, P. Stoddart, and S. Juodkazis, "Laser fabricated ripple substrates for surface-enhanced raman scattering," *Annalen der Physik*, vol. 524, pp. L5–L10, sep 2012.

[148] K. Lange, M. Schulz-Ruhtenberg, and J. Caro, "Platinum electrodes for oxygen reduction catalysis designed by ultrashort pulse laser structuring," *ChemElectroChem*, vol. 4, pp. 570–576, feb 2017.

[149] L. Romoli, C. Rashed, G. Lovicu, G. Dini, F. Tantussi, F. Fuso, and M. Fiaschi, "Ultrashort pulsed laser drilling and surface structuring of microholes in stainless steels," *CIRP Annals*, vol. 63, no. 1, pp. 229–232, 2014.

[150] Z. Wang, Q. Zhao, and C. Wang, "Reduction of friction of metals using laser-induced periodic surface nanostructures," *Micromachines*, vol. 6, pp. 1606–1616, oct 2015.

[151] A. Bičiūnas, "Puslaidininkinių medžiagų, skirtų 1 μm bangos ilgio femtosekundiniais lazerio impulsais aktyvuojamų terahercinių optoelektronikos sistemų komponentams, tyrimas," 2012.

[152] V. L. Al'perovich, V. I. Belinicher, V. N. Novikov, and A. S. Terekhov, "Surface photovoltaic effect in gallium arsenide," *Sov. Phys. JETP*, vol. 31, pp. 546–549, may 1980.

[153] V. L. Al'perovich, V. I. Belinicher, V. N. Novikov, and A. S. Terekhov, "Surface photovoltaic effect in solids. Theory and experiment for interband transitions in gallium arsenide," vol. 53, pp. 1201–1208, jun 1981.

[154] H. J. Joyce, Q. Gao, H. H. Tan, C. Jagadish, Y. Kim, J. Zou, L. M. Smith, H. E. Jackson, J. M. Yarrison-Rice, P. Parkinson, and M. B. Johnston, "III–v semiconductor nanowires for optoelectronic device applications," *Progress in Quantum Electronics*, vol. 35, pp. 23–75, mar 2011.

[155] Z. Fan, D. J. Ruebusch, A. A. Rathore, R. Kapadia, O. Ergen, P. W. Leu, and A. Javey, "Challenges and prospects of nanopillar-based solar cells," *Nano Research*, vol. 2, pp. 829–843, nov 2009.

[156] A. B. Greytak, L. J. Lauhon, M. S. Gudiksen, and C. M. Lieber, "Growth and transport properties of complementary germanium nanowire field-effect transistors," *Applied Physics Letters*, vol. 84, pp. 4176–4178, may 2004.

[157] R. G. Hobbs, N. Petkov, and J. D. Holmes, "Semiconductor nanowire fabrication by bottom-up and top-down paradigms," *Chemistry of Materials*, vol. 24, pp. 1975–1991, may 2012.

[158] G. Koblmüller and G. Abstreiter, "Growth and properties of InGaAs nanowires on silicon," *physica status solidi (RRL) - Rapid Research Letters*, vol. 8, pp. 11–30, dec 2013.

[159] A. Li, J. Zou, and X. Han, "Growth of III-v semiconductor nanowires and their heterostructures," *Science China Materials*, vol. 59, pp. 51–91, jan 2016.

[160] Y. Xia, P. Yang, Y. Sun, Y. Wu, B. Mayers, B. Gates, Y. Yin, F. Kim, and H. Yan, "One-dimensional nanostructures: Synthesis, characterization, and applications," *Advanced Materials*, vol. 15, pp. 353–389, mar 2003.

[161] R. S. Wagner and W. C. Ellis, "VAPOR-LIQUID-SOLID MECHANISM OF SINGLE CRYSTAL GROWTH," *Applied Physics Letters*, vol. 4, pp. 89–90, mar 1964.

[162] R. S. Dowdy, D. A. Walko, and X. Li, "Relationship between planar GaAs nanowire growth direction and substrate orientation," *Nanotechnology*, vol. 24, p. 035304, dec 2012.

[163] M. Yazawa, M. Koguchi, and K. Hiruma, "Heteroepitaxial ultrafine wire-like growth of InAs on GaAs substrates," *Applied Physics Letters*, vol. 58, pp. 1080–1082, mar 1991.

[164] J.-P. P. Kakko, T. Haggrén, V. Dhaka, T. Huhtio, A. Peltonen, H. Jiang, E. Kauppinen, and H. Lipsanen, "Fabrication of dual-type nanowire arrays on a single substrate," *Nano Letters*, vol. 15, pp. 1679–1683, feb 2015.

[165] F. Wang, A. Dong, J. Sun, R. Tang, H. Yu, and W. E. Buhro, "Solution-liquid-solid growth of semiconductor nanowires," *Inorganic Chemistry*, vol. 45, pp. 7511–7521, sep 2006.

[166] N. P. Dasgupta, J. Sun, C. Liu, S. Brittman, S. C. Andrews, J. Lim, H. Gao, R. Yan, and P. Yang, "25th anniversary article: Semiconductor nanowires - synthesis, characterization, and applications," *Advanced Materials*, vol. 26, pp. 2137–2184, mar 2014.

[167] C. Wilhelm, A. Larrue, X. Dai, D. Migas, and C. Soci, "Anisotropic photonic properties of III–v nanowires in the zinc-blende and wurtzite phase," *Nanoscale*, vol. 4, no. 5, p. 1446, 2012.

[168] M. J. L. Sourribes, I. Isakov, M. Panfilova, H. Liu, and P. A. Warburton, "Mobility enhancement by sb-mediated minimisation of stacking fault density in InAs nanowires grown on silicon," *Nano Letters*, vol. 14, pp. 1643–1650, feb 2014.

[169] W. Lu, P. Xie, and C. M. Lieber, "Nanowire transistor performance limits and applications," *IEEE Transactions on Electron Devices*, vol. 55, pp. 2859–2876, nov 2008.

[170] J. Goldberger, A. I. Hochbaum, R. Fan, and P. Yang, "Silicon vertically integrated nanowire field effect transistors," *Nano Letters*, vol. 6, pp. 973–977, may 2006.

[171] C. Thelander, T. Mårtensson, M. T. Björk, B. J. Ohlsson, M. W. Larsson, L. R. Wallenberg, and L. Samuelson, "Single-electron transistors in heterostructure nanowires," *Applied Physics Letters*, vol. 83, pp. 2052–2054, sep 2003.

[172] Y. Cui, Z. Zhong, D. Wang, W. U. Wang, and C. M. Lieber, "High performance silicon nanowire field effect transistors," *Nano Letters*, vol. 3, pp. 149–152, feb 2003.

[173] C. Yoon, G. Cho, and S. Kim, "Electrical characteristics of GaAs nanowire-based MESFETs on flexible plastics," *IEEE Transactions on Electron Devices*, vol. 58, pp. 1096–1101, apr 2011.

[174] J. Lieb, V. Demontis, D. Prete, D. Ercolani, V. Zannier, L. Sorba, S. Ono, F. Beltram, B. Sacépé, and F. Rossella, "Ionic-liquid gating of InAs nanowire-based field-effect transistors," *Advanced Functional Materials*, vol. 29, p. 1804378, nov 2018.

[175] J. in Hahm and C. M. Lieber, "Direct ultrasensitive electrical detection of DNA and DNA sequence variations using nanowire nanosensors," *Nano Letters*, vol. 4, pp. 51–54, jan 2004.

[176] Y. Hu, J. Zhou, P.-H. Yeh, Z. Li, T.-Y. Wei, and Z. L. Wang, "Supersensitive, fast-response nanowire sensors by using schottky contacts," *Advanced Materials*, vol. 22, pp. 3327–3332, may 2010.

[177] H. Kind, H. Yan, B. Messer, M. Law, and P. Yang, "Nanowire ultraviolet photodetectors and optical switches," *Advanced Materials*, vol. 14, pp. 158–160, jan 2002.

[178] M. S. Vitiello, L. Viti, L. Romeo, D. Ercolani, G. Scalari, J. Faist, F. Beltram, L. Sorba, and A. Tredicucci, "Semiconductor nanowires for highly sensitive, room-temperature detection of terahertz quantum cascade laser emission," *Applied Physics Letters*, vol. 100, p. 241101, jun 2012.

[179] B. Tian, X. Zheng, T. J. Kempa, Y. Fang, N. Yu, G. Yu, J. Huang, and C. M. Lieber, "Coaxial silicon nanowires as solar cells and nanoelectronic power sources," *Nature*, vol. 449, pp. 885–889, oct 2007.

[180] E. C. Garnett and P. Yang, "Silicon nanowire radial p-n junction solar cells," *Journal of the American Chemical Society*, vol. 130, pp. 9224–9225, jul 2008.

[181] M. Yao, N. Huang, S. Cong, C.-Y. Chi, M. A. Seyedi, Y.-T. Lin, Y. Cao, M. L. Povinelli, P. D. Dapkus, and C. Zhou, "GaAs nanowire array solar cells with axial p–i–n junctions," *Nano Letters*, vol. 14, pp. 3293–3303, may 2014.

[182] E. Garnett and P. Yang, "Light trapping in silicon nanowire solar cells," *Nano Letters*, vol. 10, pp. 1082–1087, mar 2010.

[183] J. Wallentin, N. Anttu, D. Asoli, M. Huffman, I. Aberg, M. H. Magnusson, G. Siefer, P. Fuss-Kailuweit, F. Dimroth, B. Witzigmann, H. Q. Xu, L. Samuelson, K. Deppert, and M. T. Borgstrom, "InP nanowire array solar cells achieving 13.8% efficiency by exceeding the ray optics limit," *Science*, vol. 339, pp. 1057–1060, jan 2013.

[184] W. Guo, A. Banerjee, P. Bhattacharya, and B. S. Ooi, "InGaN/GaN disk-in-nanowire white light emitting diodes on (001) silicon," *Applied Physics Letters*, vol. 98, p. 193102, may 2011.

[185] J. Bao, M. A. Zimmler, F. Capasso, X. Wang, and Z. F. Ren, "Broadband ZnO single-nanowire light-emitting diode," *Nano Letters*, vol. 6, pp. 1719–1722, aug 2006.

[186] A. Nadarajah, R. C. Word, J. Meiss, and R. Könenkamp, "Flexible inorganic nanowire light-emitting diode," *Nano Letters*, vol. 8, pp. 534–537, feb 2008.

[187] M. H. H. nad S. Mao, H. Feick, H. Yan, Y. Wu, H. Kind, E. Weber, R. Russo, and P. Yang, "Room-temperature ultraviolet nanowire nanolasers," *Science*, vol. 292, pp. 1897–1899, jun 2001.

[188] B. Hua, J. Motohisa, Y. Kobayashi, S. Hara, and T. Fukui, "Single GaAs/GaAsP coaxial core-shell nanowire lasers," *Nano Letters*, vol. 9, pp. 112–116, jan 2009.

[189] S. Gradečak, F. Qian, Y. Li, H.-G. Park, and C. M. Lieber, "GaN nanowire lasers with low lasing thresholds," *Applied Physics Letters*, vol. 87, p. 173111, oct 2005.

[190] S. Balci, D. A. Czaplewski, I. W. Jung, J.-H. Kim, F. Hatami, P. Kung, and S. M. Kim, "High efficient THz emission from unbiased and biased semiconductor nanowires fabricated using electron beam lithography," *IEEE Journal of Selected Topics in Quantum Electronics*, vol. 23, pp. 1–7, jul 2017.

[191] K. Peng, P. Parkinson, Q. Gao, J. L. Boland, Z. Li, F. Wang, S. Mokkapati, L. Fu, M. B. Johnston, H. H. Tan, and C. Jagadish, "Single n^+-i-n^+InP nanowires for highly sensitive terahertz detection," *Nanotechnology*, vol. 28, p. 125202, feb 2017.

[192] S. A. Baig, J. L. Boland, D. A. Damry, H. H. Tan, C. Jagadish, H. J. Joyce, and M. B. Johnston, "An ultrafast switchable terahertz polarization modulator based on III–v semiconductor nanowires," *Nano Letters*, vol. 17, pp. 2603–2610, mar 2017.

[193] R. Adomavičius, G. Molis, A. Krotkus, and V. Sirutkaitis, "Spectral dependencies of terahertz emission from InAs and InSb," *Applied Physics Letters*, vol. 87, p. 261101, dec 2005.

[194] S. A. Dayeh, E. T. Yu, and D. Wang, "Transport coefficients of InAs nanowires as a function of diameter," *Small*, vol. 5, pp. 77–81, jan 2009.

[195] M. Speckbacher, J. Treu, T. J. Whittles, W. M. Linhart, X. Xu, K. Saller, V. R. Dhanak, G. Abstreiter, J. J. Finley, T. D. Veal, and G. Koblmüller, "Direct measurements of fermi level pinning at the surface of intrinsically n-type InGaAs nanowires," *Nano Letters*, vol. 16, pp. 5135–5142, jul 2016.

[196] V. V. Karataev, M. G. Mil'vidsky, N. S. Rytova, and V. I. Fistui, "Compensation in n-type InAs," *Soviet Physics of Semiconductors*, vol. 11, no. 9, pp. 1009–1011, 1977.

[197] A. Lin, J. N. Shapiro, A. C. Scofield, B. L. Liang, and D. L. Huffaker, "Enhanced InAs nanopillar electrical transport by in-situ passivation," *Applied Physics Letters*, vol. 102, p. 053115, feb 2013.

[198] H. H. Wieder, "Transport coefficients of InAs epilayers," *Applied Physics Letters*, vol. 25, pp. 206–208, aug 1974.

[199] A. Brenneis, J. Overbeck, J. Treu, S. Hertenberger, S. Morkötter, M. Döblinger, J. J. Finley, G. Abstreiter, G. Koblmüller, and A. W. Holleitner, "Photocurrents in a single InAs nanowire/silicon heterojunction," *ACS Nano*, vol. 9, pp. 9849–9858, sep 2015.

[200] W. Lukosz and R. Kunz, "New method for determining refractive index and thickness of fluorescent thin films," *Optics Communications*, vol. 31, pp. 251–256, dec 1979.

[201] M. Lim, S.-J. Choi, G.-S. Lee, M.-L. Seol, Y. Do, Y.-K. Choi, and H. Han, "Terahertz time-domain spectroscopy of anisotropic complex conductivity tensors in silicon nanowire films," *Applied Physics Letters*, vol. 100, p. 211102, may 2012.

9. Publications

Publications

The main results of the dissertation were published in 5 scientific publications. All publications were prepared under author's maiden name (I. Beleckaitė).

P1 A. Arlauskas, J. Treu, K. Saller, **I. Beleckaitė**, G. Koblmüller and A. Krotkus. Strong terahertz emission and its origin from catalyst-free InAs nanowire arrays. *Nano Letters*, **14**(3), pp 1508–1514, 2014. DOI: 10.1021/nl404737r

P2 **I. Beleckaitė**, R. Adomavičius, R. Butkutė, V. Pačebutas, G. Molis, V. Bukauskas, A. Selskis and A. Krotkus. Non-stoichiometric GaAs – prospective material for compact THz emitters. *Electronics Letters*, **54**(23), pp 1954-1956, 2016. DOI: 10.1049/el.2016.2517

P3 **I. Beleckaitė**, J. Treu, S. Morkötter, M. Döblinger, X. Xu, R. Adomavičius, J. J. Finley, G. Koblmüller, and A. Krotkus. Enhanced THz emission efficiency of composition-tunable InGaAs nanowire arrays. *Applied Physics Letters*, **110**(20), p. 201106, 2017. DOI: 10.1063/1.4983641

P4 **I. Beleckaitė**, L. Burakauskas and R. Adomavičius. Study of surface electric field and photocarrier dynamics in InAs by means of a modified double-pump-pulse terahertz emission method. *Lithuanian Journal of Physics*, **58**(1), pp 116–125, 2018. DOI: 10.3952/physics.v58i1.3657

P5 **I. Beleckaitė** and R. Adomavičius. Determination of the terahertz pulse emitting dipole orientation by terahertz emission measurements. *Journal of Applied Physics*, **125**(22), p. 225706, 2019. DOI: 10.1063/1.5096952

The reprinted articles could be find in the following pages.

1st publication

Strong terahertz emission and its origin from catalyst-free InAs nanowire arrays

A. Arlauskas, J. Treu, K. Saller, I. Beleckaitė, G. Koblmüller and A. Krotkus

Nano Letters DOI: 10.1021/nl404737r

Reprinted with permission from NANO LETTERS. Copyright 2014 American Chemical Society. The article could be find online at https://doi.org/10.1021/nl404737r

NANO LETTERS

Letter

pubs.acs.org/NanoLett

Strong Terahertz Emission and Its Origin from Catalyst-Free InAs Nanowire Arrays

Andrius Arlauskas,[†] Julian Treu,[‡] Kai Saller,[‡,§] Ieva Beleckaitė,[†] Gregor Koblmüller,*[,‡] and Arūnas Krotkus*[,†]

[†]Center for Physical Sciences and Technology, 01180, A. Goštauto 11, Vilnius, Lithuania

[‡]Walter Schottky Institut, Physik Department, and Center of Nanotechnology and Nanomaterials, Technische Universität München, Garching, 85748, Germany

[§]Institute for Nanoelectronics, Technische Universität München, Munich, 80333, Germany

Supporting Information

ABSTRACT: The unique features of nanowires (NW), such as the high aspect ratio and extensive surface area, are expected to play a key role in the development of very efficient semiconductor surface emitters in the terahertz (THz) spectral range. Here, we report on optically excited THz emission from catalyst-free grown arrays of intrinsically n-type InAs NWs using THz time-domain spectroscopy. Depending on the aspect ratio, the THz emission efficiency of the n-type InAs NWs is found to be up to ∼3 times stronger than that of bulk p-type InAs, known as currently the most efficient semiconductor-based THz surface emitter. Characteristic differences from bulk p-type InAs are particularly revealed from excitation wavelength-dependent measurements, showing monotonously increasing THz pulse amplitude in the NW arrays with increasing photon energy. Further polarization-dependent and two-color pump−probe experiments elucidate the physical mechanism of the THz emission: In contrast to bulk p-type InAs, where the anisotropic photoconductivity in the surface electric field is the dominant cause for THz pulse generation, the origin of the intrinsic THz emission in the NWs is based on the photo-Dember effect. The strong THz emission from high aspect ratio NW arrays further suggests an improved out-coupling of the radiation, while further enhancements in efficiency using core−shell NW geometries are discussed.

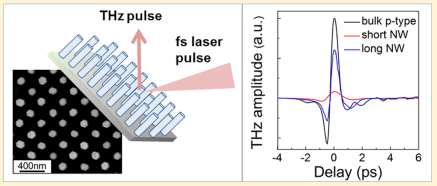

KEYWORDS: *InAs nanowires, catalyst-free site selective area epitaxy, THz emission, time-domain spectroscopy (TDS)*

The terahertz (THz) region of the electromagnetic spectrum, lying between microwave frequencies (100 GHz) and photonic frequencies (30 THz), is a potentially important region for a wide variety of applications, including imaging, time-domain spectroscopy, and material identification and characterization.[1] As effective sources for THz emission, the majority of direct band gap semiconductor crystals emits from their surfaces electromagnetic transients of subpicosecond (sub-ps) duration and spectral widths reaching several THz when excited by femtosecond (fs) laser radiation.[2,3] Although the amplitudes of these transients are by more than an order of magnitude lower than generated by electrically biased ultrafast photoconductors integrated with broad band antennas, surface emitters can find wide applications in THz time-domain-spectroscopy (TDS) systems due to a relatively large signal-to-noise ratio and an absence of the restrictions for activating a femtosecond laser wavelength.

The selection of proper material for a suitable THz surface emitter is determined by several properties, including high absorption coefficient, high saturation velocity, short carrier lifetime, large intervalley spacing to confine carriers in the high-mobility Γ valley, and appropriate band gap values. For these reasons the most efficient THz pulses are emitted from the surfaces of bulk InAs crystals,[4] p-type InAs being an order of magnitude more powerful surface emitter than n-type InAs.[5] Due to its narrow energy band gap of 0.35 eV, InAs emitters can be activated by femtosecond lasers with central wavelengths ranging from 600 to 2000 nm.[6] The main limitation of THz power emitted from bulk semiconductor samples though is their weak out-coupling from the crystal to the free space. Since photogenerated charge carriers excited by the laser pulse predominantly propagate in the direction of the surface normal, the radiation pattern of radiating dipole is primarily oriented parallel to the semiconductor surface. Out-coupling of THz radiation takes place in a narrow escape cone with an apex angle of $\theta_e = \arcsin(1/n) \approx 15°$ (n is the refractive index of a semiconductor at THz frequencies).

This problem caused by internal reflection at the air−semiconductor interface can be overcome by using semiconductor nanostructures as THz emitters. For instance, it was

Received: December 20, 2013
Revised: January 24, 2014
Published: February 6, 2014

ACS Publications © 2014 American Chemical Society

Nano Letters Letter

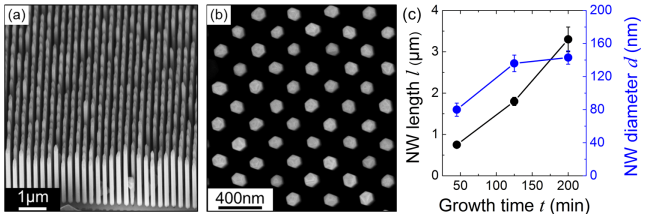

Figure 1. SEM micrographs of a representative InAs NW sample (t = 125 min) recorded (a) in bird's eye view and (b) in top-view. The hexagonal cross-section of the NWs as well as the excellent size uniformity is clearly visible. (c) Summarized dimensions of all three samples, giving the NW length and diameter as a function of growth time. The mean values and standard deviation are derived from a statistical analysis of 10 NWs measured per sample.

demonstrated that indium nitride (InN) nanorod arrays can generate THz pulses with at least three times larger amplitude than planar InN layers.[7] THz radiation was observed also from GaAs-AlGaAs core−shell NWs[8] and, surprisingly, even from Si NWs[9,10] excited by Ti:sapphire laser pulses, whereas bulk Si does not emit THz waves due to their indirect energy bandgap. Recently, THz emission was also observed from InAs NWs grown by metal−organic vapor phase epitaxy (MOVPE) using the gold-(Au)-catalyzed vapor−liquid−solid (VLS) growth mode.[11] The amplitude of the signal was found to be two times weaker than that from n-type InAs bulk crystal. Taking NW fill factor approximations into account, the authors estimated that the emitted THz power is increased by ∼15 times with respect to the n-type InAs substrate.[11] However, these estimations may to some extent be obscured by the rather inhomogeneous and strongly tapered NW growth, along with a very high density of parasitic islands, which further leads to large inhomogeneous broadening of the THz spectral shape. In addition, a comparison with n-type InAs bulk crystal may not provide the most appropriate benchmark, since the THz amplitude of n-type InAs is by far weaker than that of p-type InAs.[5] The origin of the THz emission was further attributed to an extrinsic nature due to surface plasmon polariton (SPP) waves excited by the laser pulses,[11] likely arising from the fact that the NWs were catalyzed by metallic Au droplets. To ultimately reveal the intrinsic physical mechanism of THz emission from InAs NWs and unambiguously explore the geometrical effects, investigations need to be performed on uniform, highly periodic NW arrays grown without any metal catalysts.

In this Letter, we present investigations of the intrinsic THz emission from high-uniformity, catalyst-free InAs NW arrays using THz time-domain spectroscopy (TDS). THz transients and their Fourier spectra measured on bulk p-type InAs and intrinsically n-type InAs NW arrays excited with femtosecond optical pulses of different wavelengths are compared. The efficiency of the THz emission from the n-type InAs NWs is remarkably high, with THz power up to ∼3 times stronger than that of bulk p-type InAs depending on NW aspect ratio. In addition, the physical mechanism of THz emission is studied by a two-color pump-and-probe technique. Analysis of the experiments suggests that the origin of the THz emission from NWs and bulk InAs is quite different: photoexcited electron and hole separation due to the photo-Dember effect in the former case and anisotropic photoconductivity in the latter case.

The InAs NWs investigated here were grown in a completely catalyst-free, selective area epitaxial growth (SAEG) mode on SiO_2/Si templates using solid-source molecular beam epitaxy (MBE).[12−14] The SiO_2/Si templates consist of commercially available 2″ p-type Si (111) wafers with a 20-nm-thick thermally grown SiO_2 dielectric mask layer prepatterned by nanoimprint lithography (NIL).[13−15] The prepatterned template thus exhibits a periodic pattern of 60 nm wide holes separated by a pitch of 250 nm across an area of ∼8 × 8 mm^2. This enables the growth of NWs in a site-selective, highly periodic manner with minimal size distribution and homogeneous NW densities of ∼2.5 × 10^9 cm^{-2},[16] further allowing unambiguous optical excitation experiments that are insensitive to the probed area within the entire array. The growth of the NWs was performed at a substrate temperature of 480 °C and material fluxes of Φ_{As} = 2.8 Å/s and Φ_{In} = 0.24 Å/s, corresponding to As-rich conditions (As/In ratio = 12). These growth conditions give rise to a microstructure dominated by a wurtzite (WZ) crystal phase interrupted by stacking faults.[14,17] The as-grown InAs NWs are intrinsically n-type with an estimated carrier concentration of ∼10^{17} cm^{-3} and electron mobilities of ∼800−2000 cm^2/(V s) at 300 K, as derived from transconductance measurements of single back-gated NW field effect transistors.[18,19] In total, a series of three InAs NW samples was grown with significantly different NW lengths (i.e., aspect ratio) by adjusting the growth time (t) among 45, 125, and 200 min.

Figure 1 shows exemplary scanning electron microscopy (SEM) images for the NW sample with medium growth time (t = 125 min), both in bird's eye view (a), where the high growth yield (>90%) and the excellent uniformity in NW length become evident, as well as in top-view mode (b), where the hexagonal cross-section and homogeneous distribution in diameter can be seen. The growth direction of the vertically aligned NWs corresponds to the [111] direction as expected from the epitaxial relationship with the underlying Si (111) substrate, while the six sidewall facets of the hexagon-shaped NWs are related to the {110} family of planes.[12−16] The dimensions of all three NW samples are evaluated based on the SEM images with their average values for both NW length and diameter given in Figure 1c. With increasing growth time (t) the average NW length and diameter increase from l = 0.75 μm/d = 80 nm (t = 45 min), l = 1.8 μm/d = 136 nm (t = 125 min), to l = 3.3 μm/d = 143 nm (t = 200 min), giving aspect ratios ranging from ∼9 to 23. Since obviously the NW length is the most distinctly varying parameter among the three samples,

dx.doi.org/10.1021/nl404737r | Nano Lett. 2014, 14, 1508−1514

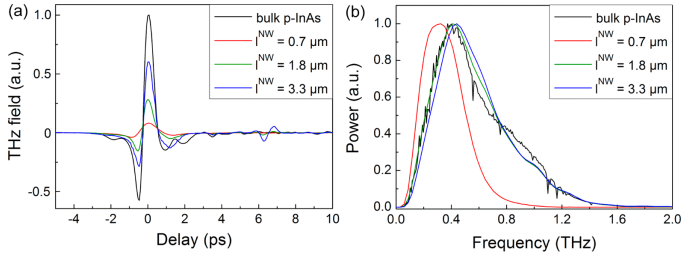

Figure 2. THz pulses (a) and their Fourier spectra (b) radiated from the surfaces of p-type bulk InAs and three n-type InAs NW samples excited by femtosecond Ti:sapphire laser pulses.

we simply refer to the NW length later on when comparing different samples.

To investigate the THz radiation pulses emitted by the InAs NWs we used a conventional THz TDS system, employing 76 MHz repetition rate pulses generated by a Ti:sapphire laser at 800 nm with a 150 fs pulse duration.[3,5,6] On the detection side, the emitted THz pulses were coherently detected by a photoconductive antenna fabricated from a low-temperature-grown GaAs epitaxial layer. The emitted THz pulses and the corresponding Fourier spectra are shown in Figure 2 for the three InAs NW samples in comparison with a p-type bulk InAs reference ([p] = 10^{18} cm^{-3}), known as currently the most efficient semiconductor THz surface emitter. We observe that the amplitude of the generated THz pulses is strongly related to the NW length and aspect ratio. In particular, by increasing NW length (aspect ratio) the amplitude of the THz pulses increases steadily, reaching a peak amplitude (at zero delay) in the sample with ~3.3 μm long NWs that is equal to ~60% of the amplitude emitted from the p-type bulk InAs reference. Taking the fill factor of this sample's surface by the NWs into account (FF ~ 0.2), we obtain an effective THz emissivity of the NWs that is ~3 times stronger than that of bulk p-InAs. In ref 11, where THz emission from Au-catalyzed InAs NWs was investigated using a similar excitation laser system, this ratio in peak amplitude between NWs and bulk InAs was similar (~50%)—however, the authors of this report used n-type bulk InAs as a reference, which emits several times lower amplitude THz pulses than p-type doped InAs crystals. Nevertheless, based on fill-factor considerations ref 11 suggests a more effective out-coupling of the THz radiation from NWs than from bulk, which in principle is also seen in the present data. To clearly identify how significant the enhanced out-coupling of the THz radiation is, one needs to, however, elucidate whether different mechanisms of THz emission are present from NW surfaces as opposed to bulk InAs (as shown below). In addition, the radiation out-coupling may also be strongly dependent on the NW geometry (i.e., NW length), as the relative peak amplitudes of the three investigated NWs in Figure 1a suggest. While the longest NW arrays (l^{NW} = 3.3 μm) exhibit the largest absolute peak amplitude (I), the relative radiative efficiencies of the other two NW arrays are decreased to ~0.5I (for l^{NW} = 1.8 μm) and ~0.13I (for l^{NW} = 0.75 μm) considering their much lower aspect ratios.

The Fourier spectra of the NW-related THz pulses presented in Figure 2b further show some interesting features with respect to bulk p-type InAs. Spectra corresponding to longer NWs (samples with l^{NW} = 1.8 μm and l^{NW} = 3.3 μm) are essentially equivalent to the spectrum obtained for the p-type bulk InAs reference, although their width is, most probably, limited by the temporal response of the detector used. In contrast, the Fourier spectrum of the THz pulse radiated from the other sample (l^{NW} = 0.75 μm) is distinctly narrower. This difference will be elucidated in more detail further below, when analyzing the physical mechanisms of the THz emission from InAs NWs and bulk, respectively.

To further identify characteristic differences in THz emission from NWs and bulk excitation, wavelength-dependent TDS measurements are performed using a specific ytterbium-doped potassium gadolinium tungstate (Yb:KGW) laser system (see Figure 3a and Supporting Information for experimental details). The corresponding THz excitation spectra of the three InAs NW samples together with the spectrum measured on p-type bulk InAs using an excitation pump fluence of ~50 nJ/cm^2 are presented in Figure 3b. The spectra are normalized to the same number of incident photons at different excitation wavelengths (i.e., photon energies). There are several distinct differences in the THz excitation spectra of the bulk and InAs NW samples. First of all, the THz pulse amplitude measured on the NW samples is monotonously increasing with increasing the laser photon energy, and no spectral maximum typical for the majority of bulk III–V semiconductor crystals is observed in the range of investigated photon energies. Second, the emission from the NW arrays sets in at larger photon energies as compared to the case of the bulk InAs crystal. Furthermore, the emitted THz transient becomes stronger with increasing length of the NWs, in accordance with the observations in Figure 2.

The origin of these distinct differences most likely stems from the impaired electron mobilities in intrinsic, unpassivated InAs NWs due to surface effects that dominate the charge carrier transport properties. Generally, electron mobilities in InAs NWs with diameters from 70 to 150 nm are in the range of ~800–2000 $cm^2/(V\ s)$,[19−21] values which are much smaller than the bulk electron mobility of InAs at room temperature (i.e., >20 000 $cm^2/(V\ s)$[22]). This means that the momentum relaxation time of electrons in NWs, $\tau_m = \mu m_n^*/e$, will be very short, on the order of several tens of femtoseconds. In bulk InAs, a maximum in the THz excitation spectrum appears when the excess energy of photoexcited electrons becomes comparable to the energy separation between the main, high mobility conduction band Γ valley and subsidiary L and X valleys with large effective electron masses and low mobilities.[23] Because values of τ_m in InAs NWs are comparable or even

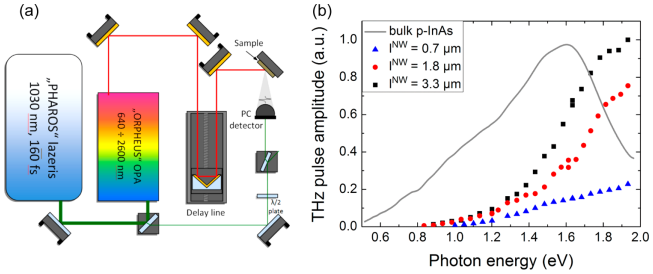

Figure 3. (a) Experimental setup of THz excitation spectroscopy (further details are described in the Supporting Information); (b) THz excitation spectra of all three InAs NW samples and bulk p-type InAs reference measured under different laser photon energies with a pump fluence of ~50 nJ/cm^2. The spectra are normalized to the same number of incident photons.

shorter than intervalley scattering times, which are on the order of ~50 fs for Γ−X scattering and ~300 fs for Γ−L scattering, the intervalley transitions will have only a minor effect on the photoexcited electron movement and on the characteristics of surface THz emission that is caused by this movement. This implies also that if one can increase the momentum relaxation time, that is, by increasing the electron mobility in the NWs, intervalley transitions will become more pronounced and may affect the THz emission more strongly. This could be realized by using surface-passivated InAs NWs, such as core−shell InAs-In(As)P with much higher electron mobilities.[21,24,25]

The surface properties have another important consequence on the electronic structure of InAs NWs. It is well-known that the surface Fermi energy in InAs is pinned in the conduction band,[26] which causes the formation of a surface electron accumulation layer.[27] This surface electron accumulation, with its origin caused by high densities of donor-type surface states at the native-oxide/InAs surface, has electron densities that can exceed 10^{18} cm^{-3} and is therefore responsible for a large intrinsic electron density in NWs.[24,28] For instance, in NWs with diameters of less than ~100 nm, this intrinsic electron density exceeds easily 10^{17} cm^{-3}.[20] Since the spectral characteristics presented in Figure 3b were measured using 3 mW of average laser power, the photoexcited carrier densities in the NWs are expected to be of similar order of magnitude or even lower than these electron densities. It is therefore suggested that the observed blue-shift of the onset of THz emission in the InAs NW arrays is caused by a conduction band filling and/or by an efficient screening of the photocarrier movement due to background electrons. To alleviate these effects caused by the intrinsic surface states, again surface-passivated core−shell NWs or even remotely p-type doped core−shell InAs-InP NWs[29] may be appropriate.

In the following, we provide a discussion and further use additional experiments to verify the underlying mechanism for THz emission in the InAs NW arrays with respect to bulk InAs. It has been shown in refs 4, 30, and 31 that the THz emission from fs-laser excited InAs surfaces can be phenomenologically described in terms of a third-order nonlinear optical effect, that is, electric field induced optical rectification (EFIOR). The electric field at the surface of InAs arises due to the spatial separation of photoexcited electrons that are quasi-ballistically moving toward the bulk of the crystal and less mobile holes staying at the illuminated surface. In p-type InAs the surface field and EFIOR effect are stronger than in n-type crystals because of the presence of a built-in electric field in the surface inversion layer having the same polarity as the photo-Dember field. Microscopically, the EFIOR effect in InAs was further described in ref 32 as a consequence of anisotropic photoconductance caused by optical alignment of photoexcited electrons in a nonparabolic conduction band.[33] In cubic semiconductors an absorption of linearly polarized radiation with a photon energy larger than the band gap results in the momenta of electrons excited from the heavy-hole valence band lying mainly in the plane perpendicular to the electric field of light wave (see Figure 4), while the momenta of electrons excited from the light hole band are predominantly aligned along the vector of polarization.

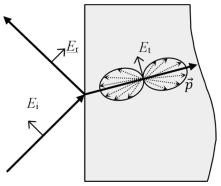

Figure 4. Orientation of the momenta of electrons after photoexcitation from heavy-hole band; E_i, E_r, and E_t denote incident, reflected, and transmitted optical field vectors, respectively; p and dashed arrows show the electron momenta distribution.

For a stationary excitation this effect is small because the anisotropic part of the photocarrier distribution function is damped on a short time scale (at 10^{-13} to 10^{-12} s) determined by the carrier momentum relaxation rate. However, in semiconductors excited by fs-laser pulses, the photocurrent reaches its peak value on a time scale smaller or comparable to the carrier momentum relaxation time; hence the optical momentum alignment effect will be more noticeable. Moreover, optical alignment of electron momenta can result in the appearance of a lateral (parallel to the illuminated semiconductor surface and perpendicular to the surface electric field) component of the photocurrent transient.[34] THz radiation induced by this transient is predominantly directed perpendicular to the illuminated surface, and hence it will be more efficiently out-coupled from the semiconductor.

dx.doi.org/10.1021/nl404737r | Nano Lett. 2014, 14, 1508−1514

The characteristic THz radiation caused by the EFIOR (or anisotropic photoconductivity) effect has a strong dependence of radiated THz field amplitude on the azimuthal angle ϕ between the crystal axes and the optical field direction. Figure 5

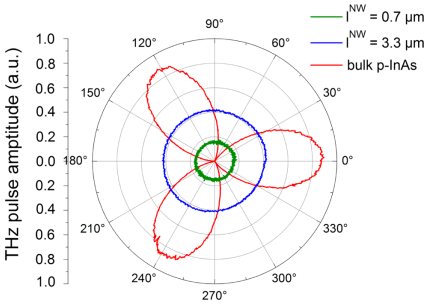

Figure 5. THz amplitude dependence on azimuthal angle for different samples. Measurements were performed at 760 nm wavelength and 50 mW average power. The data for the sample with shortest NWs (l^{NW} = 0.75 μm) are multiplied by a factor of 3 to increase resolution.

shows the azimuthal angle dependences measured for a p-type bulk InAs crystal cut parallel to (111) plane and for two InAs NW samples (for NWs with l^{NW} = 0.75 μm and l^{NW} = 3.3 μm). The recorded azimuthal angle dependences of bulk and NW samples are strikingly different. In the case of bulk InAs, the azimuthal dependence is modulated by a clear cos 3ϕ function as expected,[30] whereas for the NW arrays these dependences are fully isotropic. This means that the physical mechanisms responsible for THz emission are completely different for the two cases. In particular, the anisotropic photoconductivity loses its importance in NW arrays, where the lateral movement of photoexcited electrons is restricted by the NW size (diameter) and by a much larger momentum relaxation rate than in the bulk material. Such independence of the azimuthal angle in the THz emission from semiconductor surfaces is usually attributed to one of two effects related to the origin of ultrafast photocurrent transients: A photocurrent surge due to photo-excited electron and hole separation by (i) a built-in surface field or (ii) by their different diffusion rates (i.e., so-called photo-Dember effect). Although photoexcited electron and hole separation is an important factor to generate THz emission in bulk and NW samples, its role is very different in both cases: Dynamically changing electrical polarization in NW arrays is itself the cause of THz pulse radiation, whereas in the bulk InAs it induces an additional effect—that is, anisotropic conductance of ballistically moving photoelectrons. The latter effect is intrinsically faster than the photo-Dember effect caused by different electron and hole diffusion velocities in NWs, which manifests itself in a narrower spectrum of THz radiation emitted from NW arrays, as demonstrated, for example, in Figure 2b. The photo-Dember effect is therefore suggested to be the dominating intrinsic THz emission process in catalyst-free grown InAs NWs, which is further supported by recent measurements of the photocurrents of individual InAs NW-based circuits.[35]

In the following the different roles of photo-Dember electric field in InAs NW arrays as compared to bulk will be displayed by the results of an additional experiment, that is, surface THz emission excited by two-color fs-laser pulses ("pump-probe TDS"). In this experiment, the samples are excited by two femtosecond optical beams of different wavelength coming from the fs-OPO system as indicated in Figure 3a: a part of 1030 nm wavelength beam generated by the laser oscillator (probe-beam) and variable wavelength beam from the OPO (pump-beam). The first beam is mechanically chopped, and the THz pulse amplitude dependence on delay between pump and probe pulses is measured. The results of these measurements obtained for the p-type bulk InAs reference and an InAs NW array (sample with l^{NW} = 3.3 μm) are highlighted in Figure 6 for two pump-beam wavelengths. It is important to note, that when the pump beam impinges on the sample before the probe-beam, the amplitude of THz pulses generated by the latter becomes smaller in all cases, because of its screening by carriers created by the pump-beam. As obvious from Figure 6, the shape of the two-color pump-and-probe curves measured on bulk and NW samples is different at the first few picoseconds after their simultaneous excitation by two optical beams. For the bulk sample one can observe an increase of the THz pulse amplitude, whereas in contrast the NW array exhibits a reduction right at the temporal overlap of both laser pump and probe pulses (first ∼5 ps). These differences are more significant for shorter pump-beam wavelengths. At longer delays, however, the THz signal is reduced since an electron−hole plasma is created by the pump-beam causing screening

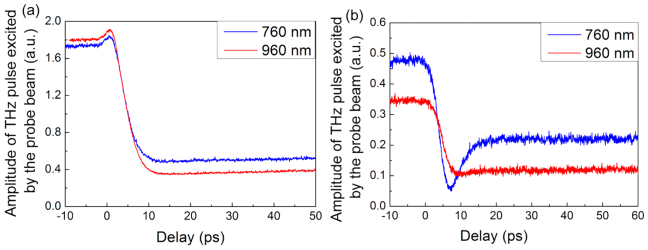

Figure 6. THz pulse amplitude dependence on the delay between pump and probe pulses for different pump wavelengths: (a) bulk p-type InAs and (b) InAs NW array (sample with l^{NW} = 3.3 μm). Average pump and probe beam powers are 75 mW and 18 mW, respectively. The probe wavelength was 1030 nm for all measurements.

dx.doi.org/10.1021/nl404737r | Nano Lett. 2014, 14, 1508−1514

effects. The slow recovery of the THz signal at longer delays (as seen in Figure 6b) further indicates that the photogenerated carrier lifetimes are much longer than the transient times right after excitation.

Note that in these experiments, the pump beam was illuminating the sample at normal incidence to its surface, while the incident angle of the probe pulses was set at 45°. This type of experimental arrangement was chosen, because it eliminates THz pulses created by a pump pulse, which interferes with the measurements in a collinear configuration. This configuration reduces slightly the temporal resolution of the measurement, because opposite pump-beam edges arrive at the sample at different times, creating about 8 ps excitation delay between the opposite beam edges. Reduced temporal response of the two-color pump-and-probe measurement hampers thus a full quantitative description of the distinct minimum of the trace shown in Figure 6b in terms of the NW plasma frequency. This interesting characteristic of the NW material will be investigated in more detail after modifying the experimental setup.

Nevertheless, these measurements allow us to determine how an additional electric field induced by the pump pulse influences the process of THz pulse generation by the probe pulse. Both pulses create a dynamically changing electric field at the illuminated surface due to photoexcited electron and hole spatial separation, with a field strength being stronger for shorter optical pulse wavelengths resulting in a stronger light absorption at the surface. In bulk InAs, where THz pulses are emitted as a result of anisotropic photoconductance in a surface field, one should expect an increase of THz pulse amplitude, because the electric fields induced by both laser beams are added together with the built-in surface field. On the other hand, if photoexcited carrier diffusion, that is, the photo-Dember effect is the main cause of THz pulse generation, the additional electric field appearing at the surface due to illumination by pump beam pulses will impede the diffusive motion of the carriers and reduce the THz pulse amplitude. This phenomenon is exactly observed for the InAs NW sample, confirming unambiguously that the photo-Dember effect is the leading mechanism for THz emission in NWs. Furthermore, this reduction in THz pulse amplitude is more pronounced for shorter pump beam wavelengths with stronger absorption, larger photoexcited carrier density gradient, and stronger pump-induced field strength.

In summary, we have investigated the THz emission characteristics from high-periodicity, intrinsically n-type InAs NW arrays using time-domain spectroscopy and compared these with results obtained from bulk p-type InAs crystals, known as the most efficient semiconductor-based THz surface emitter to date. The results presented here elucidate, in particular, also the intrinsic nature of the dominant THz emission process since the NW arrays are grown completely catalyst-free with surfaces free of any metallic droplets or adlayers. Depending on the aspect ratio, the THz emission efficiency of the n-type InAs NWs is surprisingly good, with THz powers up to ~3 times higher than for bulk p-type InAs, especially for NWs with lengths >3 μm. Further quite interesting differences in the THz emission between NWs and bulk are observed from excitation wavelength dependent measurements: the THz emission from NWs appeared at larger laser photon energies than in the case of bulk InAs, and the THz pulse amplitude was monotonously increasing with increasing photon energy without a maximum at energies corresponding to the onset of electron transitions into subsidiary conduction valleys. Based on this and supporting polarization-dependent as well as two-color pump−probe TDS experiments, we conclude that the physical mechanisms responsible for THz emission from InAs NWs and bulk are very different: anisotropic photoconductivity in the surface electric field being the prevailing cause of THz generation in the case of bulk InAs crystals, and dynamic polarization due to different diffusion velocities of photoexcited electrons and holes (so-called photo-Dember effect) in the case of InAs NWs. Although the latter mechanism of THz radiation from semiconductor surfaces is less efficient than the former one, NWs are yet very efficient THz emitters most likely due to an improved out-coupling of the radiation. Further enhancement of the THz emission from InAs NWs is expected by reducing their large background electron densities via surface-passivated or remotely p-type doped core−shell heterostructures.

■ ASSOCIATED CONTENT

Ⓢ Supporting Information

Experimental details on excitation wavelength-dependent measurements. This material is available free of charge via the Internet at http://pubs.acs.org.

■ AUTHOR INFORMATION

Corresponding Authors

*E-mail: gregor.koblmueller@wsi.tum.de.
*E-mail: krotkus@pfi.it.

Notes

The authors declare no competing financial interest.

■ ACKNOWLEDGMENTS

This work is in part supported by the Research Council of Lithuania (grant No. VP1-3.1-SMM-07-K-01-058). The authors also gratefully acknowledge financial support by the Marie Curie FP7 Reintegration Grant, the DFG excellence program Nanosystems Initiative Munich, and the collaborative research center SFB 631.

■ REFERENCES

(1) Mittleman, D. M.; Jacobsen, R. H.; Nuss, M. C. *IEEE J. Sel. Top.* **1996**, *2*, 679.
(2) Zhang, X.-C.; Auston, D. H. *J. Appl. Phys.* **1992**, *71*, 326.
(3) Krotkus, A. *J. Phys. D: Appl. Phys.* **2010**, *43*, 273001.
(4) Sarukura, N.; Ohtake, H.; Izumida, S.; Liu, Z. *J. Appl. Phys.* **1998**, *84*, 654.
(5) Adomavičius, R.; Urbanowicz, A.; Molis, G.; Krotkus, A.; Šatkovskis, E. *Appl. Phys. Lett.* **2004**, *85*, 2463.
(6) Arlauskas, A.; Krotkus, A. *Semicond. Sci. Technol.* **2012**, *27*, 115015.
(7) Ahn, H.; Ku, Y.-P.; Wang, Y.-C.; Chuang, C.-H.; Gwo, S.; Pan, C.-L. *Appl. Phys. Lett.* **2007**, *91*, 132108.
(8) Ibanes, J. J.; Balgos, M. H.; Jaculbia, R.; Salvador, A.; Somintac, A.; Estacio, E.; Que, C. T.; Tsuzuki, S.; Yamamoto, K.; Tani, M. *Appl. Phys. Lett.* **2013**, *102*, 063101.
(9) Hoyer, P.; Theuer, M.; Beigang, R.; Kley, E.-B. *Appl. Phys. Lett.* **2008**, *93*, 091106.
(10) Jung, G. B.; Cho, Y. J.; Myung, Y.; Kim, H. S.; Seo, Y. S.; Park, J.; Kang, C. *Opt. Express* **2010**, *18*, 16353.
(11) Seletskiy, D. V.; Hasselbeck, M. P.; Cederberg, J. G.; Katzenmeyer, A.; Toimil-Molares, M. E.; Léonard, F.; Talin, A. A.; Sheik-Bahae, M. *Phys. Rev. B* **2011**, *84*, 115421.
(12) Hertenberger, S.; Rudolph, D.; Bichler, M.; Finley, J. J.; Abstreiter, G.; Koblmüller, G. *J. Appl. Phys.* **2010**, *108*, 114316.

(13) Hertenberger, S.; Funk, S.; Vizbaras, K.; Yadav, A.; Rudolph, D.; Becker, J.; Bolte, S.; Döblinger, M.; Bichler, M.; Scarpa, G.; Lugli, P.; Zardo, I.; Finley, J. J.; Amann, M.-C.; Abstreiter, G.; Koblmüller, G. *Appl. Phys. Lett.* **2012**, *101*, 043116.
(14) Morkötter, S.; Funk, S.; Liang, M.; Döblinger, M.; Hertenberger, S.; Treu, J.; Rudolph, D.; Yadav, A.; Becker, J.; Bichler, M.; Scarpa, G.; Lugli, P.; Zardo, I.; Finley, J. J.; Abstreiter, G.; Koblmüller, G. *Phys. Rev. B* **2013**, *87*, 205303.
(15) Treu, J.; Bormann, M.; Schmeiduch, H.; Döblinger, M.; Morkötter, M.; Matich, S.; Wiecha, P.; Saller, K.; Mayer, B.; Bichler, M.; Amann, M.-C.; Finley, J. J.; Abstreiter, G.; Koblmüller, G. *Nano Lett.* **2013**, *13*, 6070.
(16) Koblmüller, G.; Abstreiter, G. *Phys. Status Solidi RRL* **2013**, DOI: 10.1002/pssr.201308207.
(17) Zardo, I.; Yazji, S.; Hörmann, N.; Hertenberger, S.; Funk, S.; Mangialardo, S.; Morkötter, S.; Koblmüller, G.; Postorino, P.; Abstreiter, G. *Nano Lett.* **2013**, *13*, 3011.
(18) Yang, T.; Hertenberger, S.; Morkötter, S.; Abstreiter, G.; Koblmüller, G. *Appl. Phys. Lett.* **2012**, *101*, 233102.
(19) Becker, J., et al. Unpublished.
(20) Dayeh, S. A.; Yu, E. T.; Wang, D. *Small* **2009**, *5*, 77.
(21) Lin, A.; Shapiro, J. N.; Scofield, A. C.; Liang, B. L.; Huffaker, D. L. *Appl. Phys. Lett.* **2013**, *102*, 053115.
(22) Wieder, H. H. *Appl. Phys. Lett.* **1974**, *25*, 206.
(23) Adomavičius, R.; Molis, G.; Krotkus, A.; Sirutkaitis, V. *Appl. Phys. Lett.* **2005**, *87*, 261101.
(24) Jiang, X.; Xiong, Q.; Nam, S.; Qian, F.; Li, Y.; Lieber, C. M. *Nano Lett.* **2007**, *7*, 3214.
(25) Van Tilburg, J. W. W.; Algra, R. E.; Immink, W. G. G.; Verheijen, M.; Bakkers, E. P. A. M.; Kouwenhoven, L. P. *Semicond. Sci. Technol.* **2010**, *25*, 024011.
(26) Mead, C. A.; Spitzer, W. G. *Phys. Rev. Lett.* **1963**, *10*, 471.
(27) Noguchi, M.; Hirakawa, K.; Ikoma, T. *Phys. Rev. Lett.* **1991**, *66*, 2243.
(28) Lind, E.; Persson, A. I.; Samuelson, L.; Wernersson, L.-E. *Nano Lett.* **2006**, *6*, 1842.
(29) Li, H.-Y.; Wunnicke, O.; Borgström, M. T.; Immink, W. G. G.; van Weert, M. H. M.; Verheijen, M. A.; Bakkers, E. P. A. M. *Nano Lett.* **2007**, *7*, 1144.
(30) Reid, M.; Cravetchi, I. V.; Fedosejevs, R. *Phys. Rev. B* **2005**, *72*, 035201.
(31) Malevich, V. L.; Adomavičius, R.; Krotkus, A. *C. R. Phys.* **2008**, *9*, 130.
(32) Malevich, V. L.; Ziaziulia, P. A.; Adomavičius, R.; Krotkus, A.; Malevich, Y. V. *J. Appl. Phys.* **2012**, *112*, 073115.
(33) Zakharchenya, B. P.; Mirlin, D. N.; Perel', V. I.; Reshina, I. I. *Usp. Fiz. Nauk.* **1982**, *136*, 459 [*Sov. Phys. Usp.* **1982**, *25*, 143].
(34) Belinicher, V. I.; Novikov, V. N. *Fiz. Tekh. Poluprov. (Leningrad)* **1981**, *15*, 1957 [*Sov. Phys. Semicond.* **1981**, *15*, 1138].
(35) Erhard, N.; Seifert, P.; Prechtel, L.; Hertenberger, S.; Karl, H.; Abstreiter, G.; Koblmüller, G.; Holleitner, A. W. *Ann. Phys.* **2013**, *525*, 180.

2nd publication

Non-stoichiometric GaAs – prospective material for compact THz emitters

I. Beleckaitė, R. Adomavičius, R. Butkutė, V. Pačebutas, G. Molis, V. Bukauskas, A. Selskis and A. Krotkus

Electronics Letters DOI: 10.1049/el.2016.2517

This paper is a postprint of a paper submitted to and accepted for publication in *Electronics Letters* and is subject to Institution of Engineering and Technology Copyright. The copy of record is available at the IET Digital Library. The article could be find online at https://doi.org/10.1049/el.2016.2517

Non-stoichiometric GaAs – prospective material for compact THz emitters

I. Beleckaitė✉, R. Adomavičius, R. Butkutė, V. Pačebutas, G. Molis, V. Bukauskas, A. Selskis and A. Krotkus

A non-stoichiometric (NS) GaAs layer by the means of terahertz (THz) emission spectroscopy is investigated. THz emission azimuthal dependencies and THz pulse amplitude dependence on the excitation angle were measured. Obtained results were explained by the existence of parallel to the sample surface components of THz radiating electric dipoles. The results were compared with those gained investigating GaAs nanowires. In addition, it was shown that a NS GaAs layer could be a very promising material for a compact bias-free THz emitter with good spectral characteristics.

Introduction: Despite a great progress in terahertz (THz) technology, fabrication of effective compact THz emitters without external bias is still a big challenge. Enhanced THz emission was observed from various semiconductor nanostructures like nanowires (NWs) [1], nanorods [2] and needle-shaped surface structures [3] after illuminating them with a laser beam. One of the biggest challenges of effective surface THz emitters is that a THz radiating dipole should be preferentially oriented parallel to the surface. Typically, the dipole is oriented perpendicularly to the surface in semiconductors and in most nanomaterials (e.g. vertically-aligned NWs), this results in parallel to the surface radiation direction and low THz signal outcoupling from the sample. Parallel dipoles do not have this limitation thus they are more effective and preferable but hardly realisable. One way to overcome this problem is to use nanomaterials with more complex geometry or unusual physical properties. Recently, it was reported about strong THz emission from (111)-cut p-InAs where the origin of THz radiation was explained by lateral photocurrent transients appearing due to a crystal anisotropy [4]. Yet in order to use InAs as a THz emitter in the transmission geometry one has to reduce the layer thickness down to ~80 μm due to a strong THz radiation absorption in an InAs crystal. On the other hand, it was reported on enhanced THz emission from tilted semiconductor NWs [5] which have both parallel and perpendicular components of the same electric dipoles leading to strong THz emission at the 0° excitation angle. In this Letter, we report enhanced THz emission from a non-stoichiometric (NS) Ga-rich GaAs layer. We also demonstrate that THz pulse polarisation depends on the azimuthal angle. This feature could be used for simple rotation of polarisation in a broad THz spectral region.

Sample preparation and experimental details: The investigated NS GaAs layer was grown by solid source molecular beam epitaxy using a SVTA reactor equipped with a metallic Ga and a two-zone arsenic valved-cracker source to produce As_2 dimers. The semi-insulating (100)-oriented GaAs wafers were used as substrates. GaAs layers were grown at a substrate temperature of 540°C and As_2 and Ga beam equivalent pressure ratio close to 5.8. The thickness of GaAs layer was about 5–6 μm. It was demonstrated by AFM investigations that under these conditions GaAs islands in diameter of 3 μm and height 400 nm have been formed on the sample surface. The SEM investigation revealed the existence of a specific growth direction which is tilted with respect to the substrate surface (Fig. 1*a*). Besides, our sample was proved to be Ga-rich as the elemental Ga/As ratio was found to be 1.6, 1.4 and 1.2 in the regions 1, 2 and 3, respectively (Fig. 1*b*).

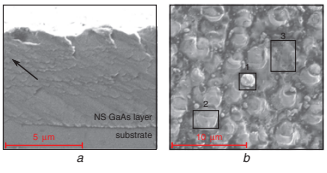

Fig. 1 *SEM image of NS Ga-rich GaAs layer*
a Side view
b Top view. The black arrow in (a) indicates the crystallisation direction

Experiments have been performed using a Ti:sapphire oscillator generating 150 fs, 800 nm pulses at a repetition rate of 76 MHz and pulse energy was 6.5 nJ. THz electric field transients were detected with a polarisation sensitive low temperature grown GaAs antenna. THz emission measurements were carried out in transmission and quasi-reflection geometries. THz pulse amplitude dependencies on an angle between the incident laser beam and a normal to the sample surface (excitation angle) have been measured. In addition, the samples were rotated around the normal to the sample surface, hence THz pulse amplitude azimuthal dependencies were measured. An NS GaAs layer was mounted onto a standard Teravil Ltd THz emitter holder with adjustable silicon lens and tested side-by-side with a commercial THz emitter antenna.

Results: Fig. 2*a* shows emitted THz pulse amplitude dependencies on the excitation angle (scheme in Fig. 2*b*) for the NS GaAs layer and bulk GaAs. Measurements were done in transmission geometry where an excitation beam and a THz beam are parallel and due to small sample thickness are almost on the same axis. The main difference occurs at the 0° excitation angle, where THz emission from bulk GaAs equals zero while for the NS GaAs layer it is reduced only by 36% in comparison with THz emission maximum obtained at 50° excitation angle. These results could be explained by the orientation of THz radiating dipoles. In a bulk semiconductor these dipoles are oriented perpendicularly to the sample surface. According to the Hertzian electric dipole theory electromagnetic radiation in the direction perpendicular to the dipole axis is forbidden, which results in low emissivity at 0° excitation angle (Fig. 2*c*). On the other hand, the results obtained from the NS GaAs layer suggest that there may exist parallel to the surface THz radiating dipoles responsible for enhanced THz emission at 0° excitation angle (Fig. 2*d*).

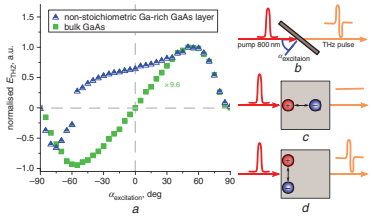

Fig. 2
a THz emission pulse dependencies on an excitation angle for NS Ga-rich GaAs layer and bulk GaAs
b Measurements were done in transmission geometry, THz detector was positioned to detect only p-polarised THz radiation. For more convenient comparison, the results of bulk GaAs were multiplied by the factor of 9.6
c, d Schematic illustrations of THz emission at 0° excitation angle for perpendicular and parallel to the surface electric dipole

The existence of parallel electric dipoles in the NS GaAs layer was also verified by measuring emitted THz pulse amplitude azimuthal dependencies (scheme in Fig. 3*b*). In Fig. 3*a*, one can see azimuthal dependence in $\sin(\theta)$ law for s and p polarised THz pulse emitted from the NS GaAs layer. In our experiments, p and s polarisations are defined by a THz electric field vector oriented parallel and perpendicularly to the plane of the optical table, respectively. It should be pointed out that when there is THz emission maximum for p THz polarisation, for s THz polarisation no THz emission is observed and vice versa. To understand the mechanism behind these results we consider that the THz electric field vector in the far field is parallel to the radiating dipole. The THz detector – a dipole antenna – detects an electric field oriented parallel to the antenna, and is not sensitive for the perpendicularly oriented electric field. Let us assume that the electric dipole is parallel to the surface and the orientation of this dipole is fixed in the sample, i.e. the dipole is rotating together with the sample when the azimuthal angle is changing. The maximum THz pulse amplitude will be detected when the THz radiating dipole is parallel to the detector antenna (Fig. 3*c*). Rotating the detector for detecting s polarisation, the electric dipole will be oriented perpendicularly to the antenna, and no THz signal will be detected (Fig. 3*d*). This is precisely what can be seen in Fig. 3*a*. The measured THz emission azimuthal dependencies are

evidencing parallel to the sample surface THz radiating electric dipoles in the NS GaAs layer. In addition, it is obvious that the orientation of these dipoles is fixed by the crystallography of the sample. The same results were obtained from tilted GaAs NWs [5]. It was shown in [5] that THz radiating dipoles are bonded with the NW and oriented along its axis as the origin of THz emission is photoexcited carriers moving along NW. Then in the case of tilted NWs two components of the same THz radiating dipoles, perpendicular and parallel (the latter one is responsible for THz emission azimuthal dependencies), appear. The same experiment was done with bulk GaAs at 45° excitation angle due to imperceptible THz radiation at the normal to the surface direction. In bulk GaAs exist only perpendicular to the surface electric dipoles and the radiated THz electric field vector is always fixed independently on the azimuthal angle. As a consequence the detected THz pulse amplitude was constant.

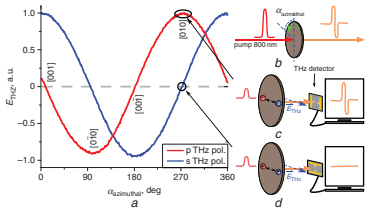

Fig. 3

a THz emission pulse dependencies on an azimuthal angle for the NS Ga-rich GaAs layer and bulk GaAs

b Measurements were done in transmission geometry at 0° excitation angle for s and p polarised THz radiations. The azimuthal angle is measured starting from the sample crystallographic direction [001] being parallel to the THz detector antenna

c, *d* Schematic illustrations explaining azimuthal dependencies

To understand the origin of the parallel to the surface THz radiating dipole in the NS GaAs layer theoretical calculations based on Lukosz theory [6] were adjusted. Comparing theoretical simulations and experimental results of THz pulse amplitude dependence on the excitation angle it was found that there are tilted electric dipoles with ∼8° heeling angle to the surface normal. One of the possible explanations of such dipoles could be the anisotropy of electrons mobility caused by existence of specific crystallisation axis in the NS GaAs layer. Tilted electric dipoles in the NS GaAs layer could be divided into two components: perpendicular and parallel to the surface. The latter one is responsible for THz emission features discussed above.

As it was mentioned above parallel to the surface THz radiating dipoles are more preferable for compact effective THz surface emitters due to better THz radiation outcoupling into free space and possibility to be activated by the laser beam perpendicularly. Since the NS GaAs layer corresponds to this requirement (there is a parallel to the surface component of THz radiating dipole) we have compared the emitted THz pulses from our sample with those obtained from other THz surface emitters operating at 0° excitation angle like tilted GaAs NWs and (111)-cut p-InAs. As one can see from Fig. 4*a*, NS GaAs emits at least two times higher THz pulse amplitude than the other two materials. Furthermore, the NS GaAs layer has been tested as a bias free THz emitter in Teravil Ltd THz spectroscopy system. For this purpose, the NS GaAs layer was mounted into a commercial THz emitter holder with silicon lens and placed into a THz spectrometer. Emitted THz pulses were detected using a 16-bit analogue to digital converter based coherent detection system. In addition, the low noise amplifier connected directly to the detector antenna was used to amplify the THz signal to the measurable level. 116 ps range was scanned ten times per second using a voice coil driven delay line with a feedback loop for speed control. The average of a 1000 curves was used to obtain the THz spectra (Fig. 4*c*). The obtained results were similar to the results of a standard THz emitter – GaAs dipole antenna biased with a 100 V DC (Fig. 4*b*). Despite the smaller amplitude of THz pulse emitted from the NS GaAs layer, the obtained spectrum was up to 3 THz and the dynamic range was more than ∼50 dB. In addition, in comparison with commercial THz sources (biased antennas) our suggested THz emitter based on the NS GaAs layer has some important advantages. First, no external bias is necessary for device opera which opens the possibility to make smaller, compact and easily r ageable THz emitters suitable for THz microscopy and moun together with a detector. Secondly, one can simply change the pol ation of emitted THz pulse by rotating the emitter around the no to the surface. These advantages are very important for optical c ponents capable to control polarisation in a broad THz spectrum reg

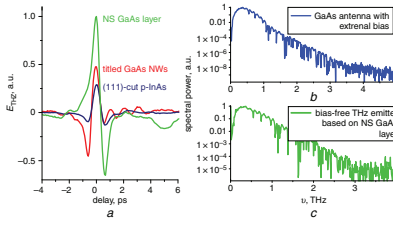

Fig. 4

a Emitted THz pulses from the NS GaAs layer, tilted GaAs NWs [5] and (111)-cut p-InAs [4] at 0° excitation angle

b Emitted THz pulse spectra for the commercial biased GaAs antenna

c Bias free THz emitter based on NS GaAs layer

Conclusion: In conclusion, we have investigated THz emission f the NS GaAs layer. Emitted THz pulse amplitude dependence on e tation and azimuthal angles were measured. Obtained results showe existence of a parallel to the surface component of the THz radia dipole witch rotates together with the sample when the azimu angle is changing. Also, it was shown that the characteristics of THz surface emitter based on the NS GaAs layer are good enc and close to those of commercial GaAs antennas with applied exte bias. Our suggested THz emitter based on nanomaterials is potent more compact, does not require an external bias as well as allowin change emitted THz pulse polarisation by simply rotating the em around normal to the surface.

Acknowledgment: This work was funded by a grant (no. MIP–54/2 from the Research Council of Lithuania.

© The Institution of Engineering and Technology 2016

Submitted: *8 July 2016* E-first: *25 October 2016*
doi: 10.1049/el.2016.2517
One or more of the Figures in this Letter are available in colour on

I. Beleckaitė, R. Adomavičius, R. Butkutė, V. Pačebutas, G. Molis Bukauskas, A. Selskis and A. Krotkus (*Center for Physical Scie and Technology, Saulėtekio av. 3, Vilnius, Lithuania*)

✉ E-mail: ieva.beleckaite@ftmc.lt

G. Molis: Also with TeraVil Ltd, Savanoriu pr. 235, LT-01108 Vil Lithuania

References

1 Arlauskas, A., Treu, J., Saller, K., Beleckaitė, I., Koblmüller, G., Krotkus, A.: 'Strong terahertz emission and its origin from catalyst InAs nanowire arrays', *Nano Lett.*, 2014, **14**, (3), pp. 1508–1514

2 Ahn, H., Ku, Y.-P., Wang, Y.-C., Chuang, C.-H., Gwo, S., and C.-L.: 'Terahertz emission from vertically aligned InN nanorod arr *Appl. Phys. Lett.*, 2007, **91**, (13), p. 132108

3 Hoyer, P., Theuer, M., Beigang, R., and Kley, E.-B.: 'Terahertz emis from black silicon', *Appl. Phys. Lett.*, 2008, **93**, (9), p. 091106

4 Cicėnas, P., Geižutis, A., Malevich, V.L., and Krotkus, A.: 'Teral radiation from an InAs surface due to lateral photocurrent transie *Opt. Lett.*, 2015, **40**, (22), p. 5164

5 Beleckaite, I., Molis, G., Adomavicius, R., *et al.*: 'Terahertz emis from non-vertically aligned semiconductor nanowires'. 40th Int. C on Infrared, Millimeter, and Terahertz waves (IRMMW-THz), 2 Available at: http://dx.doi.org/10.1109/irmmw-thz.2015.7327903

6 Lukosz, W.: 'Light emission by magnetic and electric dipoles close plane dielectric interface. III. Radiation patterns of dipoles with arbi orientation', *J. Opt. Soc. Am.*, 1979, **69**, (11), p. 1495

3rd publication

Enhanced THz emission efficiency of composition-tunable InGaAs nanowire arrays

I. Beleckaitė, J. Treu, S. Morkötter, M. Döblinger, X. Xu, R. Adomavičius, J. J. Finley, G. Koblmüller, and A. Krotkus

Applied Physics Letters DOI: http://dx.doi.org/10.1063/1.4983641

Reprinted from Applied Physics Letters, 110, 20, (2017), with the permission of AIP Publishing. The article could be find online at https://doi.org/10.1063/1.4983641

APPLIED PHYSICS LETTERS **110**, 201106 (2017)

Enhanced THz emission efficiency of composition-tunable InGaAs nanowire arrays

I. Beleckaitė,[1] J. Treu,[2] S. Morkötter,[2] M. Döblinger,[3] X. Xu,[2] R. Adomavičius,[1] J. J. Finley,[2] G. Koblmüller,[2,a)] and A. Krotkus[1,a)]
[1]*Center for Physical Sciences and Technology, 01180, A. Goštauto 11, Vilnius, Lithuania*
[2]*Walter Schottky Institut, Physik Department, Center of Nanotechnology and Nanomaterials, Technische Universität München, Am Coulombwall 4, Garching 85748, Germany*
[3]*Department of Chemistry, Ludwig-Maximilians-Universität München, Munich 81377, Germany*

(Received 30 March 2017; accepted 3 May 2017; published online 16 May 2017)

We report the terahertz (THz) emission properties of composition-tunable, intrinsically n-type InGaAs nanowire (NW) arrays using THz time-domain spectroscopy. By tuning the alloy composition of $In_{1-x}Ga_xAs$ NWs from pure InAs (x(Ga)=0) up to the intermediate composition (x(Ga)∼0.5), a substantially enhanced (>3-fold) THz emission efficiency is found, which is ascribed to a reduction in electron accumulation at the NW surface and respective electron scattering at donor-type surface defects. These findings are also confirmed by photoexcitation wavelength dependent measurements, while the THz emission characteristics are further found to be different from corresponding bulk-type planar InGaAs. In particular, NWs exhibit no distinct maxima in THz excitation spectra as caused by electron scattering to subsidiary conduction band valleys and commonly observed in the majority of bulk semiconductors. The wavelength-dependent emission spectra further reveal distinct signatures of modified intervalley scattering, revealing the underlying polytypism of intermixed wurtzite and zincblende phases in the investigated InGaAs NWs. *Published by AIP Publishing.* [http://dx.doi.org/10.1063/1.4983641]

To date, it is well known that semiconductor crystals excited by ultrashort pulses of laser radiation emit from their surface electromagnetic transients of sub-picosecond duration and with spectral widths reaching several terahertz (THz).[1,2] The amplitudes of these transients are typically an order of magnitude lower than those achieved by electrically-driven, broadband-antenna integrated ultrafast photoconductors.[3,4] Nevertheless, surface THz emitters find promising applications in THz time-domain-spectroscopy (TDS) systems owing to their relatively large signal-to-noise ratio and their straightforward activation of fs-laser radiation.[4] In general, in surface emitters, the efficiency of the optical-to-THz power conversion is limited by two main factors: the intrinsic properties of the emitter material and the out-coupling of THz radiation into free space. Intrinsically, THz emission from semiconductor surfaces is caused by either ultrafast photocurrent surge in the built-in electric field[1] or dynamic dipoles created by the spatial separation of photoexcited electrons and holes at the illuminated surface (the photo-Dember effect[2]). In both cases, the fs-laser photon quanta need to have energies larger than the energy bandgap of the semiconductor, and simultaneously, the material should exhibit a high electron mobility and large energetic distance to the subsidiary low mobility conduction band valleys. These requirements are best met by the narrow-gap semiconductors such as InAs or InSb that are also photosensitive at all technologically relevant fs-laser wavelengths.[4] On the other hand, the axis of the dynamic dipole appearing at the photoexcited surface is perpendicular to it, and hence, only a small part of the THz signal propagating at angles smaller than the total internal reflection angle will be out-coupled from the semiconductor. This out-coupling could be enhanced by exciting crystallographic planes for which the non-parabolicity and non-sphericity of the electron dispersion law lead to the appearance of the anisotropic photoconductivity and significant lateral ultrafast photocurrent components.[5,6]

Alternatively, the limitations given by the internal reflection at the air-semiconductor interface can also be surpassed by employing high aspect-ratio nanostructured materials such as nanowires (NWs). Indeed, THz emission has been observed from various different NW materials, including InN NWs,[7] GaAs-AlGaAs core-shell NWs,[8] and InAs NWs.[9–11] Even Si and Ge NWs were found to emit THz waves upon fs-laser excitation[12–14] although their bulk forms do not emit THz radiation due to the indirect energy bandgap. InAs NWs are considered as one of the most appealing materials, since their bulk phase—especially in the form of p-type InAs—is known as the most efficient THz surface emitter.[15] Recently, we studied THz emission from n-type InAs NWs and elaborated the underlying physical mechanisms responsible for THz emission in comparison to the bulk counterpart.[10] We found that while anisotropic photoconductivity in the surface electric field is the prevailing cause of THz pulse generation in bulk InAs, the origin in NWs lies in the dynamic polarization due to the photo-Dember effect.[10,16] THz emission via the photo-Dember effect is, however, considered much less efficient than the exploitation of anisotropic photoconductivity effects—still, THz pulse amplitudes from InAs NWs were found to be remarkably high, suggesting the highly efficient out-coupling of THz radiation from the NW surfaces.[10] The out-coupling

a)Electronic addresses: gregor.koblmueller@wsi.tum.de and arunas.krotkus@ftmc.lt

TABLE I. The summarized data of investigated samples listing the Ga-content (x(Ga)), average NW length (L) and diameter (D), aspect ratio (L/D), and predominant microstructure. The average values and standard deviation for L and D are derived from the statistical analysis of >10 NWs/sample using SEM. The microstructure as evaluated by TEM is adapted from Ref. 18.

Sample	x(Ga)	L (μm)	D (nm)	Aspect ratio	Microstructure
InAs	0	1.9 ± 0.4	98 ± 7	19 ± 5	WZ + SFs
InGaAs	0.28	1.1 ± 0.2	119 ± 10	10 ± 2	WZ + disorder
InGaAs	0.40	0.9 ± 0.1	121 ± 5	7 ± 1	WZ/ZB disorder
InGaAs	0.48	0.7 ± 0.1	138 ± 6	5 ± 1	WZ/ZB disorder
InGaAs	0.63	0.9 ± 0.1	131 ± 5	7 ± 1	ZB twins/disorder

efficiency is further found to directly scale with the NW aspect ratio, with longer InAs NWs producing stronger THz emission.[10,11]

In this letter, we demonstrate the control of the second important parameter that governs the THz emission efficiency, namely, the electronic properties of the intrinsic InAs NW. In particular, donor-type surface states and electron accumulation existing at n-type InAs NW surfaces[17] are considered a substantial limitation for efficient THz emission due to the associated large background electron densities and related charge carrier scattering.[10] By alloying InAs NWs with gallium (Ga) to produce composition-tunable InGaAs NWs, we effectively reduce the surface electron accumulation and thereby show how to achieve pronounced increases in THz emission efficiency. A total of five InGaAs NW samples are investigated with different Ga-contents ranging from x(Ga)=0 (pure InAs) to x(Ga) ~0.63, as determined by high-resolution x-ray diffraction (HR-XRD).[18] Each sample consisted of $\sim 8 \times 8\,\mathrm{mm}^2$ large, high-uniformity arrays of vertical InGaAs NWs grown by a catalyst-free, selective area growth (SAG) process on nano-imprinted SiO_2/Si(111) substrates via solid-source molecular beam epitaxy (MBE).[18,19] To minimize the effect of different out-coupling strengths of THz radiation, NWs were grown to comparable lengths (L), diameter (D), and hence the aspect ratio for most samples (Table I). The highly periodic arrangement of all NW samples as characterized by a fixed interwire distance of 250 nm, a NW density of $2.5 \times 10^9\,\mathrm{cm}^{-2}$, and an area fill factor of 0.2 enables further a comparative study of THz pulse amplitudes insensitive to the optically probed area. A typical NW array (InGaAs NWs with x(Ga) = 0.48) is illustrated in Fig. 1(a), demonstrating the high uniformity. Interestingly, the as-grown InGaAs NWs crystallize by mixed polytypical phases of wurtzite (WZ) and zincblende (ZB) type layer stackings as illustrated by the high-resolution transmission electron microscopy (HR-TEM) image and the selected area diffraction (SAD) pattern in Figs. 1(b) and 1(c). While such a highly disordered microstructure with intermixed WZ/ZB-phases is very common for catalyst-free InGaAs NWs,[18,19] the relative fraction of WZ versus ZB stacking varies with the Ga-content (Table I). From systematic TEM investigations performed recently on a series of InGaAs NWs grown under similar conditions,[18,19] we found that InAs NWs and In-rich InGaAs NWs exhibit a WZ-dominant phase with many stacking faults (SFs) and very short ZB segments. With the Ga-content increasing towards mid-composition ranges (x(Ga) ~0.4–0.5), the layer stacking becomes highly disordered and changes to a ZB-dominant phase for x(Ga) > 0.5 with small WZ inclusions and a high number of twin defects.[18]

The THz radiation pulses emitted by the InGaAs NW samples are shown in Fig. 2 and compared with bulk p-type InAs, known as the best semiconducting THz surface emitter. The measurements were performed at room-temperature in a conventional THz TDS system using a Ti:sapphire laser at a wavelength of 800 nm, with a short pulse duration of 150 fs and with a repetition rate of 76 MHz, while on the detection side, a photoconductive antenna fabricated from low-temperature-grown GaAs was used.[10] From the THz pulse spectra [Fig. 2(a)] and the corresponding amplitudes normalized to the peak amplitude of bulk p-type InAs [Fig. 2(b)], we find that InGaAs NWs with the increased Ga-content exhibit much higher THz emission efficiency compared to binary InAs NWs or highly In-rich InGaAs NWs. Quantitatively, while InGaAs NWs with x(Ga) < 0.3 show a THz amplitude as low as ~30% of the respective peak amplitude of bulk p-type InAs, InGaAs NWs with x(Ga) ~0.4–0.5 yield a ~2–3-fold increase in the THz pulse amplitude up to ~80% compared to bulk p-type InAs. The increase in apparent efficiency compared to non-alloyed InAs NWs is considered to be even higher, given the fact that the Ga-rich InGaAs NWs have a slightly lower aspect ratio, which, in general, limits out-coupling of THz radiation.[10] When considering the fill factor of the NW array, the increased THz efficiency translates to an effective THz emissivity of the Ga-rich InGaAs NWs that is ~4× stronger than that of bulk p-type InAs. Further increases in the Ga-content beyond x(Ga) > 0.6 lowers again the THz amplitude, suggesting that highly Ga-rich InGaAs NWs become less efficient due to the increased bandgap values and associated lower carrier lifetime and mobilities, as well as increased intervalley scattering when approaching the limit of GaAs.[20]

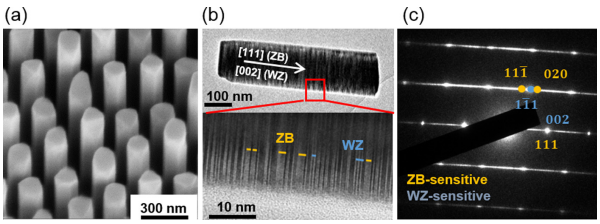

FIG. 1. (a) SEM image of a representative InGaAs NW array (x(Ga) = 0.48) along with the corresponding TEM data obtained from a single NW from the same sample, showing (b) the disordered layer stacking composed of ZB- and WZ-polytypes and (c) their respective diffraction signatures in a typical SAD pattern.

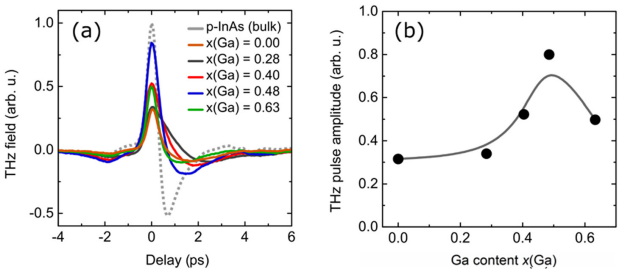

FIG. 2. (a) THz pulses radiated from the surfaces of InGaAs NW arrays after excitation by fs-short Ti:sapphire laser pulses in comparison to a bulk p-type InAs reference. (b) Corresponding amplitude normalized to the peak amplitude of bulk p-type InAs. The excitation fluence was 27 nJ/cm^2 for all measurements. The line is the guide to the eye.

To interpret the remarkable increases in THz emission efficiency from binary InAs NWs to InGaAs NWs in the mid-compositional range, we suggest the underlying cause in the elimination of a surface electron accumulation layer commonly present at InAs and In-rich InGaAs NW sidewall surfaces that induces excess electron screening of the photo-Dember field.[10] Indeed, recent x-ray photoemission spectroscopy studies and correlated semi-quantitative space charge calculations of the surface electronic structure of the {110}-terminated sidewalls of as-grown In-rich InGaAs NWs revealed that native In-suboxides cause donor-type surface states which pin the surface Fermi level in the conduction band and lead to large surface electron sheet densities of $>2\times10^{12}\,\mathrm{cm}^{-2}$ (Ref. 17). In contrast, for Ga-contents approaching the mid-compositional range, the elimination of surface electron accumulation is observed,[17] leading to flat-band conditions and further slightly acceptor-type surface state densities with increased x(Ga).

To obtain further insights into the characteristic THz pulse generation from InGaAs NW arrays, photon energy dependent measurements of the THz pulse amplitude were performed (Fig. 3). These dependences were measured using a THz TDS set-up based on an amplified ytterbium-doped potassium gadolinium tungstate (Yb:KGW) laser system (PHAROS, Light Conversion Ltd.) operating at 1030 nm with a pulse duration of 160 fs and a repetition rate of 200 kHz. Hereby, an average laser power of 6 W was directed into a cavity-tuned optical parametric oscillator that has generated 140–160 fs duration pulses with a central wavelength tunable from 640 nm to 2600 nm. In the THz-TDS arrangement activated by this laser system, the investigated surface emitters are excited by the output beam from OPO, whereas the radiated THz signals are detected by a photoconductive antenna manufactured from a GaAsBi epitaxial layer. The THz detector was illuminated by a small part (~5 mW) of the Yb:KGW laser beam delayed by different times with respect to the optical beam that activates the THz emitter. Radiated THz pulse shapes were then determined by measuring the photocurrent induced in the detector with a lock-in amplifier at different delays.

Figure 3 compares the obtained THz excitation spectra of four different InGaAs NW samples (symbols) with their corresponding photoluminescence (PL) spectra (lines of corresponding color). We note that the onset for THz emission occurs at slightly lower photon energies than the respective PL maxima. Also, at photon energies close to the energy bandgap, THz pulse amplitudes emitted by NWs with Ga-rich composition increase faster than those emitted by NWs with a low Ga-content. This can be explained in terms of differences in the band bending at the surface of InGaAs NWs with different compositions.[17] On the one hand, in In-rich InGaAs NWs, built-in surface electric fields are absent, and thus, THz emission is solely caused by the photo-Dember effect that shows up prominently at shorter wavelengths where carrier density gradients and photoexcited electron energy are higher. On the other hand, Ga-rich InGaAs NW surfaces exhibit upward band bending, and the photoexcited electron and hole separation in the existing surface electric field contributes to the radiated THz signal from the very beginning of the optical absorption. Most importantly, we also observe that the THz excitation spectra of the InGaAs NW arrays do not exhibit a distinct maximum at high photon energies, which is indicative of electron scattering to subsidiary conduction band valleys as typical for bulk semiconductors.[21] Only two samples with $x(\mathrm{Ga})=0.4$ and $x(\mathrm{Ga})=0.48$ may indicate a slight onset for such maximum in the high-energy part of the spectra.

To illustrate this behavior more closely, Fig. 3(c) compares the THz excitation spectra of InGaAs in the bulk and the NW form for similar Ga-contents (x(Ga) ~0.47–0.48). Two main features are evident from the displayed dependence. First of all, the spectrum obtained from the NW array has a maximum in the vicinity of ~1.6 eV, which is close to the position of the maximum measured for the bulk InGaAs reference layer and as explained in terms of intervalley scattering of photoexcited electrons.[21] In detail, increasing fs-laser photon energy leads first to an enhancement in THz pulse amplitude due to increases in initial electron velocity; this statement is valid as long as the photoexcited electron excess energy in the main Γ valley does not reach the energy position of the subsidiary L or X minima. At that point, however, the THz pulse amplitude starts to decrease due to electron transitions to the valleys with larger effective masses and due to the randomization of their quasi-momenta after scattering to equivalent valleys located at different crystal axes. Second, another less pronounced peak near 1.25 eV can also be identified from the spectrum of the NW array in Fig. 3(c). The presence of this peak cannot be explained in terms of the electronic band structure of ZB-type crystals. Instead, this peak is most likely a signature of the inherent intermixing of ZB and WZ crystal phases within the investigated NWs. In particular, in the case of WZ-type InAs, the

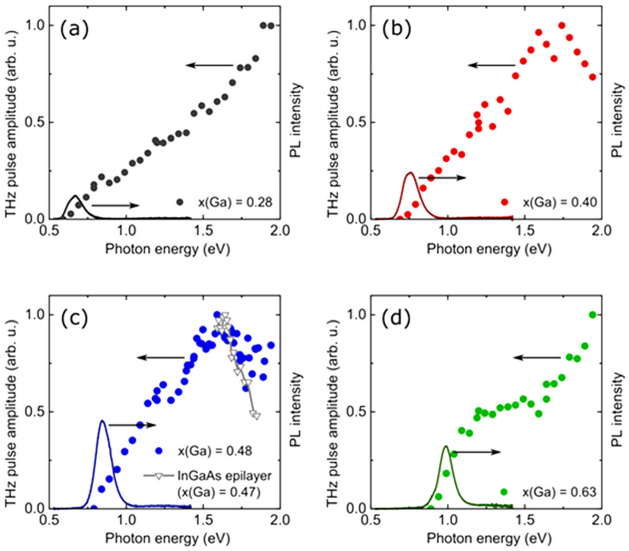

FIG. 3. THz excitation spectra of InGaAs NW samples with different Ga-contents (a)–(d) measured as a function of laser photon energy with a pump fluence of 60 nJ/cm^2 (symbols) and PL spectra from the same samples (lines of corresponding color). In (c), THz excitation spectra of Ga-rich InGaAs NWs are compared to a conventional ZB-phase bulk layer of a similar Ga-content, x(Ga) ~0.47–0.48.

energetic distance between the valence band maximum and the minimum of the secondary valleys in the conduction band is approximately equal to 1 eV.[22] The corresponding value obtained for ZB-phase InAs is of the order of 1.4 eV.[21] A similar difference in intervalley energy separation by ~0.4 eV between WZ and ZB phases can be expected also for the case of InGaAs NWs. Thus, the peak (or shoulder) near 1.25 eV can be ascribed to the presence of WZ-phase segments in InGaAs NWs, whereas the maximum at ~1.6 eV evidences the intervalley scattering of the electrons excited in ZB parts of the NWs. This is plausible since in contrast InAs NWs contain no extended ZB segments[18,19] (Table I), hence leading to the absence of the characteristic peak maximum at 1.6 eV. Moreover, it has to be pointed out that, due to the Brillouin zone folding in NWs containing the WZ-phase, the optical transitions to the secondary conduction band valleys become direct.[23] As a result, electrons photoexcited to these valleys will propagate quasi-ballistically similar to the electrons excited in the main conduction band valley, but their movement can be slower due to larger electron effective mass and smaller excess kinetic energy. This would explain the less pronounced character of the 1.25 eV maximum.

To further explore the role of the absorption strength of fs-short excitation pulses along the length of the free-standing InGaAs NWs, measurements of the THz transients at three technologically relevant excitation wavelengths were performed using the same tunable wavelength laser system. In detail, we focused on the central wavelengths of 780 nm, 1030 nm, and 1500 nm as often deployed in THz-TDS systems. The resultant THz transients are depicted in Fig. 4, illustrating several interesting features. First, the THz pulse amplitudes decay towards longer wavelength consistent with the data presented in Fig. 3. Second, however, the most intriguing feature is the apparent phase change in the THz field at the longest wavelength of 1500 nm for NW samples with larger bandgap energy, i.e., Ga-rich InGaAs NWs with $x(\mathrm{Ga}) = 0.4$ and $x(\mathrm{Ga}) = 0.48$ [Fig. 4(c)]. Note that the signal obtained at 1500 nm for the sample with $x(\mathrm{Ga}) = 0.63$ was too weak and thus is not shown. The observed phase change indicates that the laser excitation at this wavelength is absorbed less efficiently by the NW body and that the dominant THz signal is generated at the NW/Si substrate interface rather than the upper part of the NW. As a result, the built-in electric field of the NW/Si heterojunction moves photoexcited electrons in a direction opposite to the ballistic propagation of the electrons in the upper part of the NW.[24] Moreover, the data in Fig. 4 also evidence that the THz pulse amplitudes generated from the NW arrays exhibit, in general, a similar dependence on the InGaAs composition as obtained in Fig. 2 where Ti:sapphire laser pulses were employed. However, the mere difference here in Fig. 4 is that the largest THz pulse amplitudes are emitted from NWs with $x(\mathrm{Ga}) = 0.4$ rather than from NWs with $x(\mathrm{Ga}) = 0$. 48. This inconsistency can be explained by different optical pulse energy fluences typical for the experiments using Ti:sapphire laser oscillators (~27 nJ/cm^2) compared to the amplified OPO system (> 60 nJ/cm^2).

In conclusion, we investigated the THz pulse emission from high-uniformity InGaAs NW arrays with various different alloy compositions and different excitation wavelengths by THz-time domain spectroscopy. When subjected to fs-short excitation pulses, NW arrays with intermediate composition, i.e., a Ga-content of $x(\mathrm{Ga})$ ~0.4 – 0.5, are found to

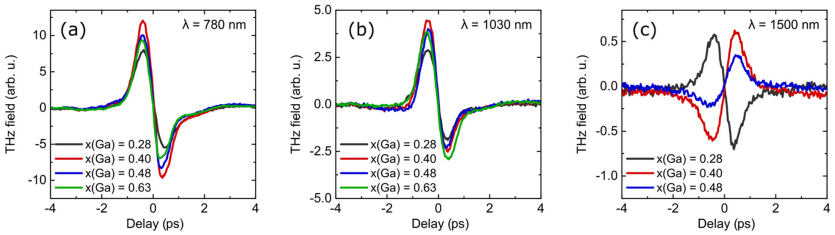

FIG. 4. THz pulses radiated from the surfaces of InGaAs NWs with different Ga-contents x(Ga) as excited by fs-short pulses of different wavelengths using the OPO system. Samples were excited under an angle of 45° with a pump fluence of 60 nJ/cm^2, while the THz pulses were monitored in the quasi-reflection direction.

radiate THz pulses much more efficiently (factors of ∼2–3 higher THz amplitudes) compared to InAs NWs and In-rich InGaAs NWs, despite their slightly lower NW aspect ratios. This unique behavior is attributed to the elimination of donor-type surface states and associated surface electron accumulation at the {110} NW sidewall facets, which reduces the otherwise considerably higher background electron concentrations and the corresponding charge carrier scattering. A comparison with bulk p-type InAs, the best planar THz surface emitter, illustrated distinct differences in the photoexcitation wavelength dependences and modified intervalley scattering due to wurtzite and zincblende phase intermixing in the InGaAs NWs. The wavelength-dependent studies also gave insights into the absorption characteristics of NWs and photoexcited carrier motion influenced by the built-in electric fields at the NW/substrate interfaces.

This work was supported in part by the Research Council of Lithuania (Grant No. MIP–54/2014). The authors also gratefully acknowledge the financial support by the DFG excellence program Nanosystems Initiative Munich, the collaborative research center SFB 631, and the Technische Universität München, Institute for Advanced Study, funded by the German Excellence Initiative. The authors wish to thank H. Riedl for the technical support during molecular beam epitaxy growth.

[1]X. C. Zhang and D. H. Auston, J. Appl. Phys. **71**, 326 (1992).
[2]T. Dekorsy, H. Auer, H. J. Bakker, H. G. Roskos, and H. Kurz, Phys. Rev. B **53**, 4005 (1996).
[3]K. A. McIntosh, E. R. Brown, K. B. Nichols, O. B. MsMahon, W. F. DiNatale, and T. M. Lyszczarz, Appl. Phys. Lett. **67**, 3844 (1995).
[4]A. Krotkus, J. Phys. D.: Appl. Phys. **43**, 273001 (2010).
[5]V. L. Malevich, P. A. Ziaziulia, R. Adomavičius, A. Krotkus, and Y. V. J. Malevich, J. Appl. Phys. **112**, 073115 (2012).
[6]P. Cicėnas, A. Geižutis, V. L. Malevich, and A. Krotkus, Opt. Lett. **40**, 5164 (2015).
[7]H. Ahn, Y. P. Ku, Y. C. Wang, C. H. Chuang, S. Gwo, and C. L. Pan, Appl. Phys. Lett. **91**, 132108 (2007).
[8]J. J. Ibanes, M. H. Balgos, R. Jaculbia, A. Salvador, A. Somintac, E. Estacio, C. T. Que, S. Tsuzuki, K. Yamamoto, and M. Tani, Appl. Phys. Lett. **102**, 063101 (2013).
[9]D. V. Seletskiy, M. P. Hasselbeck, J. G. Cederberg, A. Katzenmeyer, M. E. Toimil-Molares, F. Léonard, A. A. Talin, and M. Sheik-Bahae, Phys. Rev. B **84**, 115421 (2011).
[10]A. Arlauskas, J. Treu, K. Saller, I. Beleckaite, G. Koblmüller, and A. Krotkus, Nano Lett. **14**, 1508 (2014).
[11]D. W. Park, Y. B. Ji, J. Hwang, C.-R. Lee, S. J. Lee, J. O. Kim, S. K. Noh, S. J. Oh, S.-H. Kim, T.-I. Jeon, K.-U. Jeong, and J. S. Kim, Sci. Rep. **6**, 36094 (2016).
[12]P. Hoyer, M. Theuer, R. Beigang, and E.-B. Kley, Appl. Phys. Lett. **93**, 091106 (2008).
[13]G. B. Jung, Y. J. Cho, Y. Myung, H. S. Kim, Y. S. Seo, J. Park, and C. Kang, Opt. Express **18**, 16353 (2010).
[14]W.-J. Lee, J.-W. Ma, J.-M. Bae, K.-S. Jeong, M.-H. Cho, C. Kang, and J.-S. Wi, Sci. Rep. **3**, 1984 (2013).
[15]R. Adomavičius, A. Urbanowicz, G. Molis, A. Krotkus, and E. Šatkovskis, Appl. Phys. Lett. **85**, 2463 (2004).
[16]N. Erhard, P. Seifert, L. Prechtel, S. Hertenberger, H. Karl, G. Abstreiter, G. Koblmüller, and A. W. Holleitner, Ann. Phys. **525**, 180 (2013).
[17]M. Speckbacher, J. Treu, T. J. Whittles, W. M. Linhart, X. Xu, K. Saller, V. R. Dhanak, G. Abstreiter, J. J. Finley, T. D. Veal, and G. Koblmüller, Nano Lett. **16**, 5135 (2016).
[18]J. Treu, M. Speckbacher, K. Saller, S. Morkötter, M. Döblinger, X. Xu, H. Riedl, G. Abstreiter, J. J. Finley, and G. Koblmüller, Appl. Phys. Lett. **108**, 053110 (2016).
[19]S. Morkötter, S. Funk, M. Liang, M. Döblinger, S. Hertenberger, J. Treu, D. Rudolph, A. Yadav, J. Becker, M. Bichler, G. Scarpa, P. Lugli, I. Zardo, J. J. Finley, G. Abstreiter, and G. Koblmüller, Phys. Rev. B **87**, 205303 (2013).
[20]J. N. Heyman, N. Coates, A. Reinhardt, and G. Strasser, Appl. Phys. Lett. **83**, 5476 (2003).
[21]G. Molis, A. Krotkus, and V. Vaičaitis, Appl. Phys. Lett. **94**, 091104 (2009).
[22]C. Hajlaoui, L. Pedesseau, F. Raouafi, F. B. ChekhLarbi, J. Even, and J. M. Jancu, J. Phys. D: Appl. Phys. **46**, 505106 (2013).
[23]B. Ketterer, M. Heiss, E. Uccelli, J. Arbiol, and A. F. i Morral, ACS Nano **5**, 7585 (2011).
[24]A. Brenneis, J. Overbeck, J. Treu, S. Hertenberger, S. Morkötter, M. Döblinger, J. J. Finley, G. Abstreiter, G. Koblmüller, and A. W. Holleitner, ACS Nano **9**, 9849 (2015).

4th publication

Study of surface electric field and photocarrier dynamics in InAs by means of a modified double-pump-pulse terahertz emission method

I. Beleckaitė, L. Burakauskas and R. Adomavičius

Lithuanian Journal of Physics DOI: 10.3952/physics.v58i1.3657

Reprint from *Lithuanian Journal of Physics* with the permission of LMA. The article could be find online at https://doi.org/10.3952/physics.v58i1.3657

Lithuanian Journal of Physics, Vol. **58**, No. 1, pp. 116–125 (2018)
© Lietuvos mokslų akademija, 2018

STUDY OF SURFACE ELECTRIC FIELD AND PHOTOCARRIER DYNAMICS IN InAs BY MEANS OF A MODIFIED DOUBLE-PUMP-PULSE TERAHERTZ EMISSION METHOD

I. Beleckaitė [a], L. Burakauskas [b], and R. Adomavičius [a]

[a] *Center for Physical Sciences and Technology, Saulėtekio 3, 10257 Vilnius, Lithuania*
[b] *Department of Physics, University of Oxford, Parks Rd, Oxford OX1 3PU, UK*
Email: ieva.beleckaite@ftmc.lt

Received 31 January 2018; accepted 22 March 2018

In this study we report the investigation of terahertz (THz) emission efficiency dynamics in p-type InAs using a double-pump-pulse (DPP) THz emission method. We also suggest a novel modification of the standard DPP method which allows us to measure the indirectly modulated THz pulse. The obtained results reveal that the first optical pulse increases the free carrier concentration and enhances the surface electric field. This field prevents perpendicular but improves parallel to the surface electric dipole formation after sample excitation with the second optical pulse. Our suggested method is shown to be a more precise and sensitive way to study electric fields and photocarrier dynamics in semiconductors after photoexcitation.

Keywords: photo-Dember effect, THz emission from semiconductors, InAs

PACS: 07.57.Hm, 78.47.D-, 78.47.J-

1. Introduction

During the last decades of the 20th century the technology of femtosecond lasers was highly improved. It opened a possibility to investigate physical processes that last less than 1 ps. For the first time in 1984 Auston et al. used a femtosecond laser for the registration of electromagnetic pulse with the duration of a few picoseconds transmitted through free space [1]. A few years later, in 1988, the first terahertz time-domain spectroscopy (THz TDS) system was presented [2]. Since then such systems have become more accomplished and have found many application areas. One of the most important components of the THz TDS system is a THz pulse emitter commonly activated with femtosecond laser pulses. THz emitters could be various semiconductors, their compounds and nanostructures or optoelectronic switches – semiconductors with metallic contacts that require external bias for operation. In order to gain a better understanding of THz generation mechanisms and create more effective THz emitters, various THz TDS system modifications are used. The main idea of one of rarely used modifications is to use two excitation pulses instead of one: the first pulse (pump) changes the carrier concentration and electric fields inside the semiconductor while the other (probe) arrives with a time delay and generates the THz pulse which reflects changes of the mentioned parameters. For the first time such double-pump-pulse terahertz emission (DPP THz) method was mentioned by Tanouchi el al. in 2002 [3]. They

investigated a low-temperature-grown GaAs (LT-GaAs) optoelectronic switch and reported the decrease in THz generation efficiency due to the screening of the bias electric field by generated photocarriers. The recovery of the THz signal was ascribed to the electron relaxation and recombination processes. A few years later Siebert et al. [4] basically repeated Tanouchi's results [3] but the authors elucidated the decrease of THz signal intensity due to changes in the voltage distribution in the biasing circuit. Later works by this group were intended to investigate the carrier recombination in LT-GaAs optoelectronic switches [5, 6]. Recently Murakami et al. [7] have expanded the potential of the DPP THz method by using a very sharply focused probe beam that allowed them to scan the whole area of an optoelectronic switch with a resolution of 1.5 μm. This upgraded DPP THz method was proved to be an excellent candidate for the investigation of electric field distribution dynamics in THz emitters after photoexcitation. In all previously cited works the electron drift was caused by an external bias which forced them to move parallel to the semiconductor surface. Speaking about the unbiased THz emitters, there is a greater variety of materials for samples. Optical reflection and DPP THz methods were compared in an article [8] where both of them were used for the investigation of LT-GaAs layers grown at different temperatures. While using the DPP THz method for the investigation of $CuInSe_2$ it was shown for the first time that the pump pulse could increase the THz emission efficiency [9]. The enhancement in the THz signal was also observed in GaAs nanowires (NWs) grown by the MOCVD method [10]. In addition, the DPP THz method was used to investigate the main principles of THz generation in InAs NWs [11]. The same technique but with a sharply focused probe beam was applied for the investigation of photovoltaic cells [12].

To our knowledge, there are no previous works where the temporal shape of the THz electric field transient ($E_{THz}(t)$) at different time delays between two excitation pulses has been investigated. In this work we show that $E_{THz}(t)$ strongly depends on the time delay between two optical excitation pulses. We reveal the main principles of the $E_{THz}(t)$ variation and suggest a more accurate method for THz emission DPP measurements. This method is applied to investigate a p-type InAs substrate that is known as one of the most efficient semiconductor-based THz surface emitters. It is shown that THz emission dynamics in InAs strongly depends on the polarization of an optical pulse that activates the THz generation process. From the obtained results we conclude that the sample excitation with the first optical pulse enhances its surface electric field. This field has a different effect upon the capability of the photocarriers created by the second excitation pulse to form parallel and perpendicular to the sample surface THz radiating electric dipoles.

2. Experimental details

In this article we report two types of double-pump-pulse excitation methods: standard (DPP) and our suggested modified (MDPP). All experiments were based on the experimental set-up that is shown in Fig. 1(a). Measurements have been performed using a Ti:sapphire oscillator generating 800 nm wavelength pulses at 76 MHz repetition rate, 6.5 nJ pulse energy and 150 fs pulse duration. The laser beam is divided into three parts: one part (≈20 mW) is directed towards a polarization sensitive GaAs THz detector (*Teravil Ltd*) for THz transient measurement; the other part is directed at the sample for THz pulse generation (the so-called Probe beam); the last part is also directed towards the sample for the generation of free carriers (Pump beam). In order to change Pump and Probe beam polarization, half-wave plates were used. During the DPP experiment the Pump Delay Line is fixed at the desirable time delay between the Pump and Probe pulses while the Detector Delay Line is used to coherently scan a temporal shape of the THz signal. The detected signal is analysed with a lock-in amplifier and transferred to the computer.

3. Results and discussion

The THz pulse dependence on the time delay between optical Pump and Probe pulses (Δt) measured with the standard DPP method (Fig. 1(b)) is shown in Fig. 2. The positive time delay ($\Delta t > 0$) means that the optical Pump pulse reaches the sample surface before the Probe pulse, and the negative time delay ($\Delta t < 0$) means

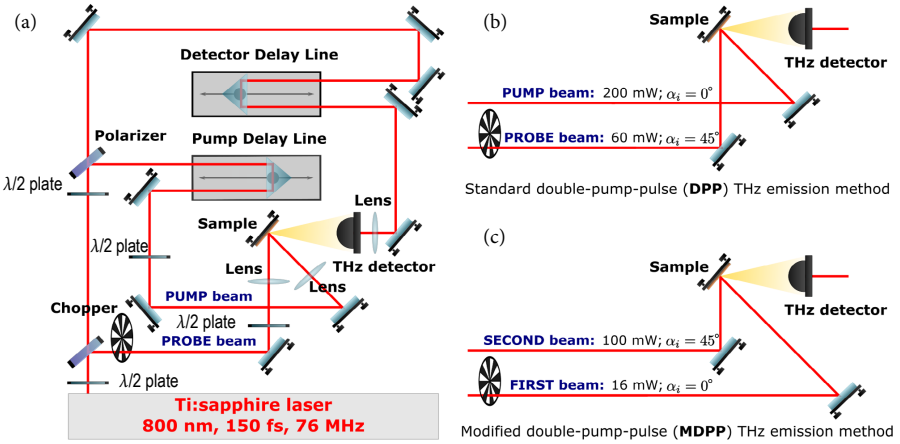

Fig. 1. Standard double-pump-pulse terahertz emission set-up. (a) Experimental set-up in general. (b) Standard double-pump-pulse terahertz emission method. (c) Modified double pump-pulse terahertz emission method.

that the Probe pulse comes before the Pump. In Fig. 2(a) it is possible to see a single THz pulse at different positive Δt. Generally speaking, both Pump and Probe pulses generate a THz pulse, but as the Probe beam is mechanically chopped due to the condition of synchronous detection, only the THz pulse generated by the Probe beam should be measured. Indeed, only the THz pulse generated by the Probe pulse is visible in Fig. 2(a). In this case the Pump beam only changes the conditions of the THz pulse generation. This effect is inert, thus with increasing Δt the registered THz pulse is more and more affected: the Pump pulse reduces the efficiency of THz generation. This is a typical result of the standard DPP THz measurement discussed in the previous works. In contrast,

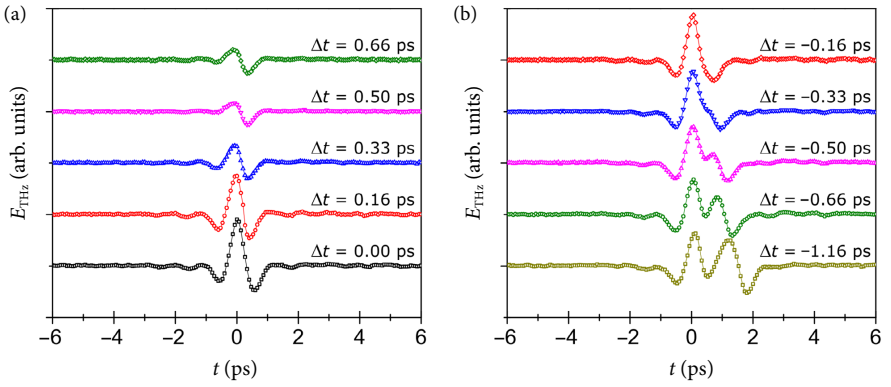

Fig. 2. THz pulse dependence on the positive (a) and the negative (b) time delay between optical Pump and Probe pulses. For positive time delays only the directly modulated THz pulse could be seen while for negative time delays both directly and indirectly modulated THz pulses are visible.

for negative Δt values the structure of the registered THz signal becomes more complicated (Fig. 2(b)). Overall, two kinds of THz pulses can be seen in Fig. 2: the first one is visible at all time delays and has a fixed position in the time scale; the second occurs only when the optical Probe pulse reaches the sample before the Pump pulse. The second pulse position in the time scale corresponds to the Δt, which suggests that we have the THz pulse generated by the Pump pulse. However, as mentioned before, the Pump beam is not mechanically chopped and due to the conditions of synchronous detection the THz pulse generated by the Pump pulse should not be registered. Nevertheless, a deeper analysis suggests that the generation of THz radiation with the Pump pulse is indirectly modulated. At negative time delays, when the Probe pulse reaches the sample before the Pump pulse, it creates photocarriers with the frequency of a mechanical chopper and affects the THz generation process initiated by the Pump pulse. So, as a result, the indirectly modulated THz pulse generated by the optical Pump pulse could be registered. Hence during the experiment we register the THz pulse generated by the Probe pulse and the indirectly modulated THz pulse corresponding to the difference in the THz emission generated by the Pump pulse due to the photocarriers created by the Probe pulse (the upper (green online) curve in Fig. 3). In comparison, the lower (red online) curve in Fig. 3 represents the same difference in THz generation but measured in a different way. Here the Pump pulse is chopped and the THz pulse measured with and without the additional excitation with the Probe pulse. Then both THz signals are subtracted from each other resulting in the difference in THz emission initiated by the Pump pulse due to the Probe pulse induced generation of the photocarriers. It is important to note that the position in the time scale of the indirectly modulated THz pulse in Fig. 2(b) is shifting during the experiment because the position of the Pump Delay Line is changing (Fig. 1).

It is obvious that the THz pulse registered due to the indirect modulation unavoidably affects dynamics measured by the traditional DPP THz method. When the Probe pulse arrives at the sample a few picoseconds earlier than the Pump pulse, the directly and indirectly modulated THz pulses are separated in the time scale (Fig. 4(a)). When

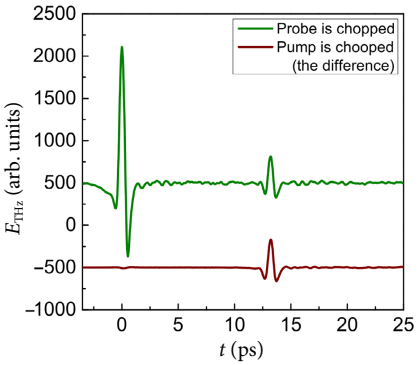

Fig. 3. THz pulses measured with different chopper positions at the time delay $\Delta t = -13$ ps. The upper (green online) curve represents the THz signal measured when the Probe beam is chopped. The lower (red) curve shows the difference in the THz signal with and without the Probe when the Pump beam is chopped.

the delay Δt approaches subpicosecond values, those two pulses overlap (Fig. 4(b)) and this pulse interference may seem like an increased THz pulse generated by the Probe laser pulse. Meanwhile, the Pump pulse reaching the semiconductor surface 0.5 ps later than the Probe pulse cannot affect the THz pulse generation process. Nevertheless, the indirectly modulated THz pulse is unique as it requires both Pump and Probe optical pulses for detection: if one of the pulses is blocked, this THz pulse vanishes. In addition, indirectly modulated THz pulse measurements at different Δt makes it possible to observe changes in the THz pulse generated due to the optically excited photocarrier relaxation.

The main idea of this work is to use indirectly modulated THz pulses for the investigation of THz generation dynamics. For this purpose, the set-up in Fig. 1(b) was modified to Fig. 1(c) as follows. The lower intensity mechanically chopped optical beam is directed perpendicular to the sample surface (the incidence angle equals 0°), while the higher intensity optical beam impinges on the sample surface at the 45° incidence angle. In order to detect the indirectly modulated THz pulse, the chopped optical pulse must be the first to reach the sample surface; therefore this pulse will be called the First pulse and the other will be called

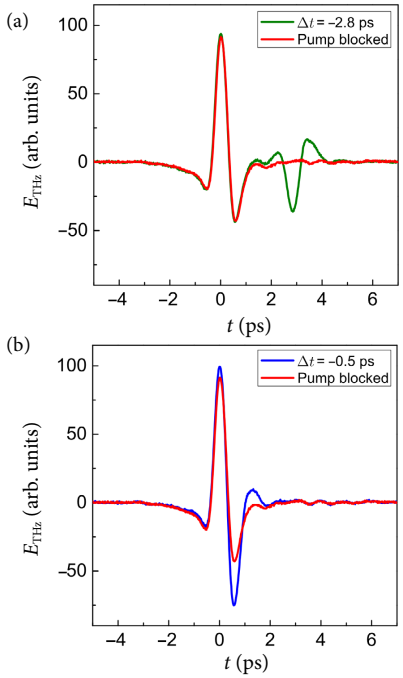

Fig. 4. Directly and indirectly modulated THz signals measured at different negative time delays (Δt = –2.8 ps (a) and Δt = –0.5 ps (b)). The repeating in (a) and (b) (red online) curve represents the directly modulated THz pulse created by the Probe pulse when the Pump pulse is blocked, the other (green online) curve in (a) shows the directly and indirectly modulated pulses separated in time and the other (blue online) curve in (b) presents the interaction of directly and indirectly modulated THz pulses that might be mistaken as enhancement of the Probe generated THz pulse.

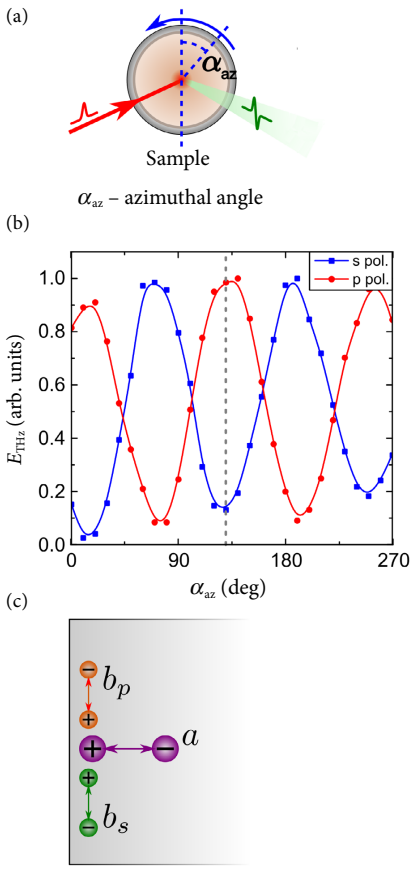

Fig. 5. (a) Schematic illustration of the THz emission efficiency dependence on an azimuthal angle measurement. The sample is rotating around the normal to the surface. (b) THz pulse amplitude dependence on an azimuthal angle for the s-polarized and the p-polarized optical pulse. (c) Schematic illustration of the electric dipoles formed in the sample after photoexcitation at an azimuthal angle ≈130°. There a corresponds to the perpendicular electric dipole while b_p and b_s to the parallel dipole excited with p or s light polarization.

the Second pulse. Before the DPP THz experiments the THz emission efficiency dependence on an azimuthal angle (Fig. 5(a)) in p type InAs (p-InAs) was measured using only the Second optical pulse: the First pulse was blocked and the chopper was moved to modulate the p-polarized Second pulse (the (red) curve with dots in Fig. 5(b)). The azimuthal angle for the maximum THz emission efficiency was determined and fixed for subsequent measurements (the dotted line in Fig. 5(b)). In Fig. 6(a, b) indirectly modulated THz pulses at different time delays between two optical excitation pulses are shown. THz pulse amplitudes (peak-to-valley) of these pulses are summarized in Fig. 6(c).

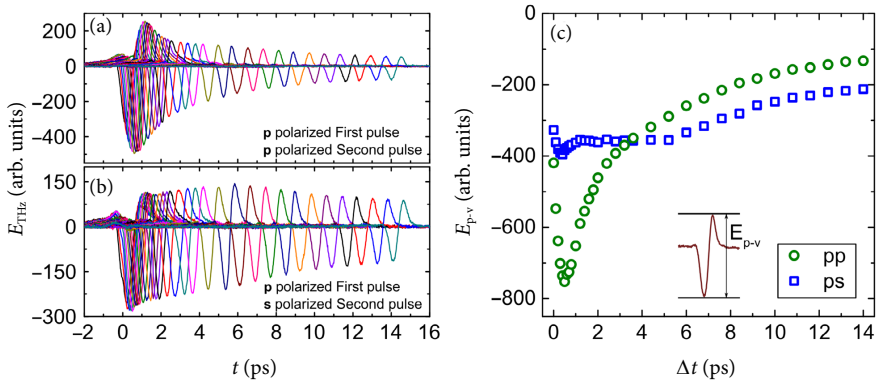

Fig. 6. Indirectly modulated THz pulses measured at different time delays for the p-polarized (a) and the s-polarized (b) Second pulse. The First pulse was always p-polarized. (c) The summarized THz pulse amplitudes (peak-to-valley) of these THz pulses.

The obtained curves show the influence of the First optical pulse to the THz generation process initiated by the Second pulse. It could be seen from the figure that THz generation properties strongly depend on the polarization of the Second pulse. It is worth mentioning that such dependence was not observed in other samples investigated by our introduced DPP THz method.

It should be noted that the ratio between optical pulse powers (the power of the Second pulse is a few times larger than that of the First pulse) is chosen intentionally. When the power of the First pulse exceeds 30 mW (that corresponds to 0.4 nJ energy and the concentration of photocarriers 3.4×10^{16} cm^{-3}), the shape of the measured kinetics changes dramatically. On the contrary, no such changes were observed for the increasing power of the Second pulse.

In order to understand the indirectly modulated THz pulse kinetics and its difference upon p and s optical polarization, it must be understood how the Second optical pulse generates the THz pulse. In all standard semiconductors photoexcited electrons and holes are separated in the surface electric field (field effect [13]) and/or compelled to move along the surface gradient at different velocities (photo-Dember effect [14]). Both effects result in the perpendicular to the sample surface electric dipole which emits THz radiation. It is also possible that the parallel to surface dipole will form. This could happen due to nonlinear optical effects [15] and most importantly due to anisotropic photocurrent effects [16] that are very important for narrow band-gap semiconductors (like InAs). In InAs electrons with high excess energy are created upon the excitation of 800 nm wavelength laser radiation. The motion of such electrons in the strong surface electric field leads to the formation of a parallel to the surface electric dipole due to the non-parabolicity [16] and non-sphericity [17] of the conduction band. When we rotate a sample around the normal to the surface, strength and orientation of the parallel electric dipole changes thus determining the THz emission efficiency dependence on an azimuthal angle. The orientation of the THz radiating electric dipole depends on the polarization of the excitation beam. It could be seen from the measured azimuthal dependences that under the p-polarized and s-polarized excitation the electric dipoles parallel to the surface are oriented in opposite directions (Fig. 5(c)). The THz emission from perpendicular to the surface electric dipole is supposed to remain constant. Then the registered THz radiation could be determined as the sum of the two components: $a + b_p$ and $a - b_s$. There a corresponds to the perpendicular electric dipole radiation, while b_p and b_s to the radiation of a parallel dipole excited

by p or s light polarization, respectively. Under the assumption that all the abovementioned electric dipoles always radiate the same form of THz pulses, the curves in Fig. 6(c) could be expected to be proportional to the $a + b_p$ and $a - b_s$ (here a, b_p, b_s are functions of the time delay Δt). Then the difference of these curves will be proportional to the $b_p + b_s$, while the sum could be described as $2a + b_p - b_s \approx 2a$ (we assume that $b_p \approx b_s$). It is obvious that the difference (sum) of the dependences in Fig. 6(c) describes the change in the THz radiation from the parallel (perpendicular) to the surface electric dipole initiated by the Second pulse and induced by the photocarriers excited by the First pulse.

The sum and difference of the curves in Fig. 6(c) is shown in Fig. 7. It should be noted that the results in Fig. 6(c) mean that the First pulse always reduces the THz pulse generated by the Second pulse. However, from the difference of the mentioned curves it could be seen that the THz emission from the parallel to the surface electric dipole is enhanced for the time interval of 3 ps after the surface excitation with the First pulse. To verify that the THz emission enhancement is real, measurements for the s-polarized THz electric field were performed. Many semiconductors form only a very weak parallel to the surface electric dipole and no s-polarized THz pulse could be detected. That is why usually polarization sensitive THz detectors are oriented to detect the p-polarized THz radiation. However, the (111) crystallographic orientation InAs emits a strong enough s-polarized THz pulse. It is important to mention that the perpendicular to the surface electric dipole has no influence over the s-polarized THz radiation. Figure 8(a) shows the indirectly modulated s-polarized THz pulse dynamics. To confirm the nature of the jump between positive and negative values, the chopper was moved to modulate the Second pulse. The bubble (blue) curves in Fig. 8(b) represent THz pulses when the First pulse is blocked, the dot (red) curves represent the results of the THz generation process affected by the First pulse. The results shown in Fig. 8(b) confirm that the THz emission efficiency can be enhanced using the additional excitation of the semiconductor surface. However, in our case this statement is true only for the parallel to the surface THz radiating electric dipole.

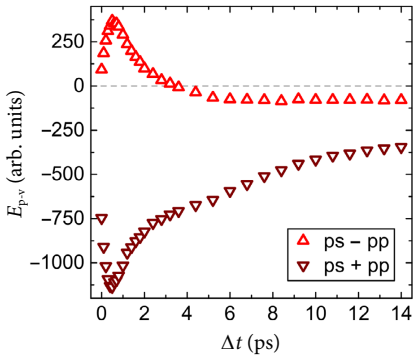

Fig. 7. Sum and difference of the curves shown in Fig. 6(c). The difference (sum) describes THz radiation from the parallel (perpendicular) to the surface electric dipole created by the Second pulse and modulated by the photocarriers excited by the First pulse.

The obtained results could be explained in terms of the two-kind influence of the photocarriers on the THz generation process. After the photoexcitation with the First pulse carrier motion is determined by the gradient and surface electric field. Within a few picoseconds after excitation, the surface electric field becomes stronger due to the carrier diffusion that is a dominant process at the beginning [18]. Then the motion of photocarriers created by the Second pulse is mostly controlled by the enhanced surface electric field. A stronger field obstructs the diffusion of new photocarriers [19] but stimulates the formation of the parallel to the surface electric dipole. Nevertheless, it must be kept in mind that photocarriers always affect THz generation even if they do not change the surface electric field. While photocarriers created by the Second pulse form an electric dipole, the photocarriers created by the First pulse move in the electric field of this dipole and create their own dipole of the opposite orientation. It means that free photocarriers always limit the THz generation process regardless of the THz radiating electric dipole orientation. It must be noted that the free carrier influence on the THz generation strongly depends on their energy relaxation time. Thus in narrow band-gap semiconductors the THz generation is almost unaffected due to

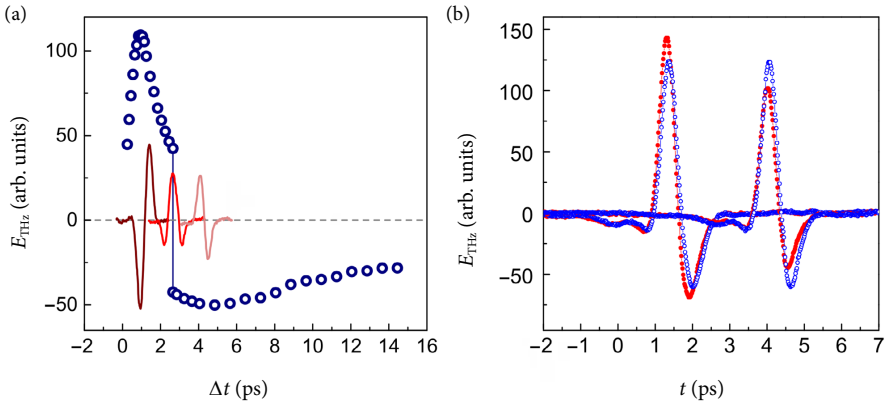

Fig. 8. (a) Bubble (blue online) dots represent the indirectly modulated s-polarized THz pulse amplitude (peak-to-valley) dynamics. Curves (red online) show the corresponding THz pulses. (b) Bubble (blue online) curves represent THz pulses when the First pulse is blocked, dot (red online) curves show the results of the THz generation process affected by the First pulse. THz emission enhancement (at t = 1.4 ps) and attenuation (at t = 4 ps) could be seen.

a relatively large electron mass during the first few picoseconds after the photoexcitation [20].

We have suggested the essential modification of the standard DPP THz emission method and showed its functionality by investigating p-type InAs. In the MDPP method registered THz pulse parameters depend on the versatile contribution of both optical pulses. For instance, the indirectly modulated THz pulse amplitude is proportional to the surface electric field alteration induced by the First pulse. This property allows us to investigate not only the electric field screening dynamics but also the dynamics of the Dember potential that is significant for the THz generation. Furthermore, our suggested MDPP method opens the possibility to investigate semiconductors at low excitation conditions when it is easier to separate physical mechanisms responsible for the THz generation. Additionally, the measurement of the indirectly modulated THz pulse is a novel promising contact-free method to investigate electric properties of photocarriers. Moreover, the time resolution of this method is a few hundreds of femtoseconds (the time period required for THz pulse generation), therefore rapid processes, for example, the ballistic electron transport dynamics, could be measured.

4. Conclusions

In conclusion, we have investigated the THz emission efficiency dynamics in InAs after sample excitation with the femtosecond optical pulse by means of the DPP method. Moreover, we have suggested a modification of the standard DPP method – whose main goal is to measure the indirectly modulated THz pulse. The analysis of the temporal shape of this pulse opens the possibility for a more precise and sensitive registration of changes in a semiconductor. We have shown that InAs excitation with the First pulse increases the free carrier concentration and enhances the surface electric field. This field prevents perpendicular but improves parallel to the surface electric dipole formation after sample excitation with the Second pulse. Free carriers screen both types of the dipole although their influence becomes noticeable over a few picoseconds after the excitation when the electron energy relaxation process is completed.

References

[1] D.H. Auston, K.P. Cheung, and P.R. Smith, Picosecond photoconducting Hertzian dipoles,

Appl. Phys. Lett. **45**(3), 284 (1984), https://doi.org/10.1063/1.95174

[2] P.R. Smith, D.H. Auston, and M.C. Nuss, Subpicosecond photoconducting dipole antennas, IEEE J. Quantum Electron. **24**(1), 255 (1988), https://doi.org/10.1109/3.121

[3] M. Tonouchi, N. Kawasaki, T. Yoshimura, H. Wald, and P. Seidel, Pump and probe terahertz generation study of ultrafast carrier dynamics in low-temperature grown-GaAs, Jpn. J. Appl. Phys. **41**(6B), L706 (2002), https://doi.org/10.1143/jjap.41.l706

[4] K.J. Siebert, A. Lisauskas, T. Löffler, and H.G. Roskos, Field screening in low-temperature-grown GaAs photoconductive antennas, Jpn. J. Appl. Phys. **43**(3), 1038 (2004), https://doi.org/10.1143/jjap.43.1038

[5] G.C. Loata, T. Löffler, and H.G. Roskos, Evidence for long-living charge carriers in electrically biased low-temperature-grown GaAs photoconductive switches, Appl. Phys. Lett. **90**(5), 052101 (2007), https://doi.org/10.1063/1.2436719

[6] G.C. Loata, M.D. Thomson, T. Löffler, and H.G. Roskos, Radiation field screening in photoconductive antennae studied via pulsed terahertz emission spectroscopy, Appl. Phys. Lett. **91**(23), 232506 (2007), https://doi.org/10.1063/1.2823590

[7] H. Murakami, S. Fujiwara, I. Kawayama, and M. Tonouchi, Study of photoexcited-carrier dynamics in GaAs photoconductive switches using dynamic terahertz emission microscopy, Photon. Res. **4**(3), A9 (2016), https://doi.org/10.1364/prj.4.0000a9

[8] V.K. Mag-usara, S. Funkner, G. Niehues, E.A. Prieto, M.H. Balgos, A. Somintac, E. Estacio, A. Salvador, K. Yamamoto, M. Hase, and M. Tani, Low temperature-grown GaAs carrier lifetime evaluation by double optical pump terahertz time-domain emission spectroscopy, Opt. Express **24**(23), 26175 (2016), https://doi.org/10.1364/oe.24.026175

[9] R. Adomavičius, A. Krotkus, J. Kois, S. Bereznev, and E. Mellikov, Terahertz radiation from non-stoichiometric $CuInSe_2$ films excited by femtosecond laser pulses, Appl. Phys. Lett. **87**(19), 191104 (2005), https://doi.org/10.1063/1.2126796

[10] V.N. Trukhin, A.D. Buravlev, V. Dhaka, G.E. Cirlin, I.A. Mustafin, M.A. Kaliteevski, H. Lipsanen, and Y.B. Samsonenko, Ultrafast carrier dynamics in GaAs nanowires, Lith. J. Phys. **54**(1), 41 (2014), https://doi.org/10.3952/physics.v54i1.2844

[11] A. Arlauskas, J. Treu, K. Saller, I. Beleckaitė, G. Koblmüller, and A. Krotkus, Strong terahertz emission and its origin from catalyst-free InAs nanowire arrays, Nano Lett. **14**(3), 1508 (2014), https://doi.org/10.1021/nl404737r

[12] H. Nakanishi, A. Ito, K. Takayama, I. Kawayama, H. Murakami, and M. Tonouchi, Visualization of photoexcited carrier responses in a solar cell using optical pump–terahertz emission probe technique, J. Infrared Millim. Terahertz Waves **37**(5), 498–506 (2015), https://doi.org/10.1007/s10762-015-0233-x

[13] X.-C. Zhang, B.B. Hu, J.T. Darrow, and D.H. Auston, Generation of femtosecond electromagnetic pulses from semiconductor surfaces, Appl. Phys. Lett. **56**(11), 1011 (1990), https://doi.org/10.1063/1.102601

[14] T. Dekorsy, H. Auer, H.J. Bakker, H.G. Roskos, and H. Kurz, THz electromagnetic emission by coherent infrared-active phonons, Phys. Rev. B **53**(7), 4005 (1996), https://doi.org/10.1103/PhysRevB.53.4005

[15] M. Reid, I.V. Cravetchi, and R. Fedosejevs, Terahertz radiation and second-harmonic generation from InAs: bulk versus surface electric-field-induced contributions, Phys. Rev. B **72**(3), 035201(2005), https://doi.org/10.1103/PhysRevB.72.035201

[16] V.L. Malevich, P.A. Ziaziulia, R. Adomavičius, A. Krotkus, Y.V. Malevich, Terahertz emission from cubic semiconductor induced by a transient anisotropic photocurrent, J. Appl. Phys. **112**(7), 073115 (2012), https://doi.org/10.1063/1.4758181

[17] P. Cicėnas, A. Geižutis, V.L. Malevich, and A. Krotkus, Terahertz radiation from an InAs surface due to lateral photocurrent transients, Opt. Lett. **40**(22), 5164 (2015), https://doi.org/10.1364/ol.40.005164

[18] V.M. Polyakov and F. Schwierz, Influence of band structure and intrinsic carrier concentration on the THz surface emission from InN and InAs,

Semicond. Sci. Technol. **22**(9), 1016 (2007), https://doi.org/10.1088/0268-1242/22/9/007

[19] A. Krotkus, R. Adomavičius, G. Molis, and V.L. Malevich, Terahertz emission from InAs surfaces excited by femtosecond laser pulses, J. Nanoelectron. Optoe. **2**(1), 108 (2007), https://doi.org/10.1166/jno.2007.011

[20] R. Adomavičius, R. Šustavičiūtė, and A. Krotkus, in: *Narrow Gap Semiconductors 2007*, eds. B. Murdin and S. Clowes (Springer, Dordrecht, 2008) pp. 41–43, https://doi.org/10.1007/978-1-4020-8425-6_10

InAs PAVIRŠINIO ELEKTRINIO LAUKO IR KRŪVININKŲ DINAMIKOS TYRIMAS MODIFIKUOTA DVIGUBO IMPULSINIO ŽADINIMO TERAHERCINĖS EMISIJOS METODIKA

I. Beleckaitė [a], L. Burakauskas [b], R. Adomavičius [a]

[a] *Fizinių ir technologijos mokslų centras, Vilnius, Lietuva*

[b] *Oksfordo universiteto Fizikos departamentas, Oksfordas, Jungtinė Karalystė*

Santrauka

Atlikome išsamią dvigubo žadinimo terahercinės emisijos metodo analizę, atskleidėme metodo trūkumus ir pasiūlėme, kaip patobulinti matavimo procedūrą. Taikant patobulintą metodiką ištirta terahercinės spinduliuotės generavimo dinamika p tipo InAs padėkle. Eksperimento metu registruotas terahercinis impulsas tiesiogiai atspindėjo pirmojo optinio impulso nulemtus pokyčius puslaidininkio paviršiuje. Prieita prie išvados, kad pirmąsias kelias pikosekundes po sužadinimo terahercinės spinduliuotės generavimo sąlygos labiausiai keičiasi dėl foto-Demberio efekto, o vėliau svarbesnis tampa ekranavimas šviesa sužadintais laisvaisiais krūvininkais. Eksperimento rezultatai parodė, kad terahercinės spinduliuotės generavimo dinamika labai priklauso nuo žadinančios šviesos poliarizacijos. Šis rezultatas paaiškinamas skirtinga elektrinio lauko pokyčių įtaka terahercinius impulsus spinduliuojančių elektrinių dipolių formavimuisi. InAs padėklo sužadinimas pirmuoju impulsu dėl foto-Demberio efekto sustiprina jo paviršinį elektrinį lauką. Šis laukas trukdo vėliau sužadintiems krūvininkams formuoti statmeną, bet padeda sudaryti lygiagretų paviršiui dipolį. Laisvieji krūvininkai ekranuoja bet kokio tipo dipolius, tačiau jų poveikis pasireiškia po kelių pikosekundžių, įvykus elektronų energijos relaksacijai.

5th publication

Determination of the terahertz pulse emitting dipole orientation by terahertz emission measurements

I. Beleckaitė and R. Adomavičius

Journal of Applied Physics DOI: 10.1063/1.5096952

Reprint from Journal of Applied Physics, 125, 22, (2019), with the permission of AIP Publishing. The article could be find online at https://doi.org/10.1063/1.5096952

Determination of the terahertz pulse emitting dipole orientation by terahertz emission measurements

Cite as: J. Appl. Phys. **125**, 225706 (2019); doi: 10.1063/1.5096952
Submitted: 21 March 2019 · Accepted: 22 May 2019 ·
Published Online: 11 June 2019

View Online Export Citation CrossMark

Ieva Beleckaitė[a)] and Ramūnas Adomavičius

AFFILIATIONS

Center for Physical Sciences and Technology, Saulėtekio av. 3, 10257 Vilnius, Lithuania

[a)]ieva.beleckaite@ftmc.lt

ABSTRACT

Terahertz pulse emission from the photoexcited semiconductor surface heavily depends on the orientation of the photo-induced electric dipole. Two methods to determine the orientation of the terahertz pulse emitting dipole have been demonstrated. Method I relies on the measurement of THz emission dependencies on the angle of incidence in the transmission geometry, while method II is based on the measurements of THz emission in the reflection geometry. Theoretical reasoning for both of these methods has been presented. Both of these methods have been tested with a semi-insulating GaAs substrate using an external magnetic field in order to change the tilt angle of the electric dipole. The investigation presented in this work leads to an assumption that the magnetic field induced change in the dipole tilt angle is proportional to the mobility of electrons. Thus, the suggested method may become a promising tool for testing the quality of substrates and epitaxial layers.

Published under license by AIP Publishing. https://doi.org/10.1063/1.5096952

I. INTRODUCTION

In recent years, terahertz time-domain spectroscopy[1] (THz TDS) has found its application in various fields. It could be used in security systems for detecting drugs and explosives,[2] in the field of medicine as a noninvasive way for cancer diagnostics,[3] in the food industry for quality control,[4] in arts for heritage restoration,[5] etc. Moreover, THz TDS spectroscopy is a good tool to investigate semiconductors and their nanostructures: it could be used to measure electron mobility,[6] as well as to determine the semiconductor bandgap and intervalley separation.[7] For all these applications, effective, compact, easy to use, and cheap THz emitters are desirable. Nowadays, semiconductor based photoconductive antennas with an applied external voltage are the most common laser driven THz sources. For example, semi-insulating GaAs is an ideal material for the THz pulse generation with femtosecond Ti:sapphire lasers. However, as these lasers are bulky and expensive, they are responsible for the high price of a spectroscopy system. The solution could be the use of materials with a narrower energy gap, together with cheaper and more compact lasers operating in the $1\,\mu$m–$1.5\,\mu$m wavelength range. Unfortunately, lower E_g determines a significantly higher dark conductivity of the semiconductor, which restricts the possibility of adding external voltage and reduces the reliability of photoconductive switch type THz emitters.

An alternative to the photoconductive antennas is the bare surface of semiconductors and semiconductor nanostructures (surface emitters). THz pulse emission from semiconductors after illumination with a femtosecond laser pulse[8] was observed soon after the discovery of optoelectronic THz pulse generation and coherent detection.[9] In some cases, semiconductor surface, especially those of narrow bandgap semiconductors, is a more universal THz pulse emitter than optoelectronic switches. Moreover, THz emission from semiconductors and their structures could deliver more information about the surface that emits the THz pulse.

THz pulses from semiconductor surfaces are usually a result of the electric current created due to the photo-Dember effect[10] or a surface electric field.[8] Both effects lead to the formation of a perpendicular to the surface THz emitting electric dipole. However, such a dipole orientation is not favorable for outcoupling THz radiation from a semiconductor into the free space, which is the main stimulus for exploration of ways in an effort to change the orientation of the electric dipole. An external magnetic field[11] as well as a certain configuration of metallic contacts[12] makes it

Published under license by AIP Publishing.

possible to create a parallel to the surface component of the THz emitting electric dipole and thus enhance THz emission from a semiconductor. Also, a parallel to the surface component is formed due to the laser induced strong nonlinear optical phenomena[13] or an anisotropic photocurrent effect.[14] Eventually, it is highly likely that nanostructuring of the semiconductor surface leads to the appearance of lateral photocurrent, which is responsible for THz emission enhancement in these structures.[15] Therefore, in order to use THz emission as a tool to investigate semiconductors and their structures, as well as to create effective THz emitters, it is necessary to have methods to determine the orientation of THz source (electric dipole/photocurrent) with respect to the semiconductor surface. Currently, there are a few methods to determine this orientation. In 2009, Inoue[16] suggested a method based on the measurement of the angular distribution of THz radiation in space using a sharply focused laser beam for the THz generation. In this case, the divergence of THz radiation is maximized and the angular distribution allows the characterization of the THz source. However, using such a method, only a very small part of the total radiation reaches the detector, which can greatly affect the accuracy of the experiment. In this work, we propose two new methods for the determination of the THz emitting electric dipole orientation. By applying these methods, the diameter of a laser beam at the surface of a semiconductor is higher than the THz radiation wavelength, so the divergence of THz radiation is small, and the majority of generated THz radiation is collected in the detector. Both experimental techniques are easier to implement than those described in the work of Inoue. Moreover, in this work, we present the theoretical reasoning for the experimental methods, demonstrate their operation in the study of THz emission from a GaAs substrate in an external magnetic field, and discuss the limitations and prospects of application of these methods. Furthermore, based on the results obtained, some considerations on the effect of the magnetic field on the THz emitting electric dipole are given.

II. EXPERIMENTAL SETUP

In this work, measurements were performed using a Ti:sapphire oscillator generating 800 nm wavelength pulses with the pulse duration of 150 fs. The diameter of the focused Gaussian beam at the surface is 1.5 mm. The central wavelength of THz radiation is 600 μm in air. THz radiation from the sample was detected by the THz time-domain spectroscopy method using a polarization sensitive THz detector (Teravil Ltd.). The THz radiation generated in the GaAs sample was collimated with a polyethylene lens having a focal length of 1.5 cm and a diameter of 1 cm. The collimated THz beam was directed to a detector where it was focused on the contact area of the photoconductive antenna with the help of a 1 cm diameter Si lens. The sample holder was made from Standa Ltd. rotational stage. In order to change the orientation of THz radiating electric dipole, the sample was placed in an electromagnet: the strength of the magnetic field varied from 0.0 T to 0.4 T. The magnetic field was parallel to the sample surface and perpendicular to the incidence plane. The experimental setup is shown in Fig. 1.

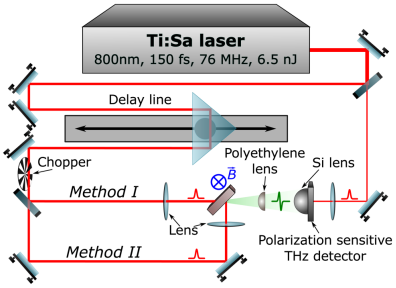

FIG. 1. Experimental setup. For method I, the sample was measured in the transmission geometry, and for method II, in the reflection geometry.

III. METHOD I: DEPENDENCE OF THz EMISSION ON THE ANGLE OF INCIDENCE OF LASER RADIATION

In the case of surface THz emitters, weak THz emission in a direction perpendicular to the sample surface is a result of the orientation of the THz emitting electric dipole. Thus, the sample is usually oriented so that the axis of a laser beam forms a 45° or higher angle (hereinafter referred to as the angle of incidence) to the normal of the sample surface. The authors of Ref. 17 have shown that the most effective THz emission from the InP substrate is achieved when the excitation light impinges the samples at the angle of incidence close to the Brewster angle. In general, the dependence of THz emission from semiconductor surfaces on the laser beam incidence angle may be completely different from that of the InP substrate.[18] If the test sample is transparent to the THz radiation, this dependence could be studied quite simply in the transmission geometry because then the laser beam axis, the sample, and the THz detector are in one straight line, and only the angle between the sample surface and the laser beam axis is changed during the experiment. The THz radiation generated in such a geometry is best assembled into the detector when the laser beam diameter exceeds the THz wavelength. Such a "soft" focusing mode is often applied in practice, because it is easy to predict and manipulate the direction of a THz beam generated under such conditions.

In this work, the THz emission dependencies on the angle of incidence of the laser beam were investigated. It was noticed that the above mentioned dependencies can be explained in terms of the model of electric dipole radiation proposed by Lukosz.[19,20] The main parameter of this model is the angle between the dipole axis and the normal to the sample surface (hereinafter referred to as the dipole tilt angle θ). Therefore, by knowing θ, it is possible to predict the spacial distribution of THz radiation as well as the efficiency of THz emitting electric dipole. The method determining the orientation of the THz emitting electric dipole presented here is based on this observation. For the demonstration of suggested

Published under license by AIP Publishing.

methods, a semi-insulating (SI) GaAs (100) substrate (Wafer Technology Ltd., $\mu \approx 5000\,\mathrm{cm^2/V\,s}$) in an external magnetic field was chosen, since θ could be easily controlled by the magnetic field and the wide-bandgap semiconductor–substrate system is closest to that described in the theoretical model proposed by Lukosz.

For the THz emission dependence on the angle of incidence experiments, s-polarized laser radiation was chosen, since this condition allows for better conformity between the theory and the experiment. In contrast, the THz detector was positioned to detect p-polarized THz radiation, as the GaAs substrate emits exclusively this polarization only. Before the start of experiments, the azimuthal dependencies of SI-GaAs sample were measured. Then, the alignment of crystal orientation was chosen so that the influence of nonlinear effects on THz emission would be largely suppressed. Therefore, the discussion could be focused on the THz pulse emission component caused by the electron motion due to the surface electric field and photo-Dember effect.

Experimentaly, the optically illuminated area of a semiconductor is larger than the terahertz radiation wavelength; therefore, this radiation is directional, diffraction limited, and can be completely collected on the THz detector, which allows achieving a good signal-to-noise ratio. The amplitude of the radiated field strongly depends on the incident angle and dipole orientation. The radiated field dependence has the following form:[17]

$$E_{\mathrm{THz}}(\alpha_1, \phi, \theta) = (1 - R_{opt}(\alpha_1))E_{td}(\alpha_1, \phi, \theta)t_{\mathrm{THz}}(\alpha_1), \qquad (1)$$

where ϕ and θ are the azimuthal and polar angles of the dipole, respectively, and α_1 is the angle between the laser beam and the normal to the semiconductor surface [Fig. 2(a)]. The first factor, $1 - R_{opt}$, comes from the photocarrier density, which is proportional to the optical absorption; the second factor, E_{td}, describes the radiation pattern of the dipole, and the third factor, t_{THz}, is the transmission coefficient for the THz wave field. The reflection coefficient of laser radiation, R_{opt}, strongly depends on polarization. For s-polarized light, R_{opt} can be expressed as

$$R_{opt}(\alpha_1) = \left(\frac{\cos\alpha_1 - n_{opt}\cos\alpha_{2,opt}}{\cos\alpha_1 + n_{opt}\cos\alpha_{2,opt}}\right)^2, \qquad (2)$$

where n_{opt} is the index of refraction of the semiconductor for laser radiation, and $\alpha_{2,opt}$ is the refracted optical beam angle, which can be calculated from Snell's law. For p-polarized terahertz radiation, the transmission coefficient through the semiconductor–air interface can be expressed as

$$t_{\mathrm{THz}}(\alpha_1) = \frac{2\sqrt{n_{\mathrm{THz}}\cos\alpha_{2,\mathrm{THz}}\cos\alpha_{1,\mathrm{THz}}}}{\cos\alpha_{2,\mathrm{THz}} + n_{\mathrm{THz}}\cos\alpha_{1,\mathrm{THz}}}, \qquad (3)$$

where n_{THz} is the index of refraction of semiconductor for terahertz radiation, $\alpha_{1,\mathrm{THz}}$ and $\alpha_{2,\mathrm{THz}}$ are the THz beam angles measured from the normal of the semiconductor–air boundary for propagation in air and semiconductor, respectively. In the case of semi-insulating GaAs, the refractive indexes of terahertz and optical waves have very close values: $n_{opt} = 3.65$[21] and $n_{\mathrm{THz}} = 3.59$;[22] then, according to Huygens's principle, the directions of THz and optical beams coincide inside the semiconductor; therefore, $\alpha_{2,opt} = \alpha_{2,\mathrm{THz}} \approx \alpha_2$ and $\alpha_1 \approx \alpha_{1,\mathrm{THz}}$. Thus, it was assumed that α_1, α_2, and n were the same for optical and THz radiation. In the calculations, $n = 3.6$ was chosen.

In this work, the terahertz radiation pattern inside the semiconductor sample was modeled on the basis of the Lukosz[19,20] theory. According to this theory, THz radiation going deeper in the semiconductor from the electric dipole located close to the semiconductor–air interface consists of two beams: one emitted in the transmission geometry and the second emitted to the reflection geometry and reflected back from the interface [Fig. 2(b)]. Then, the superposition of these two beams could be expressed as follows:

$$E_{td}(\alpha_1, \phi, \theta) = \frac{\cos\alpha_2(\cos\theta\sin\alpha_2 + n\sin\theta\cos\alpha_1\cos\phi)}{\cos\alpha_2 + n\cos\alpha_1}. \qquad (4)$$

At a certain angle $\alpha_1 = \alpha_{cr}$, the numerator of the right-hand side of Eq. (4) is equal to zero. Then, E_{td}, and as a result, E_{THz} become equal to zero too. If $\phi = 0$ (the dipole lies in the plane of incidence), the critical angle α_{cr} and angle θ are related by the equation

$$\tan\alpha_{cr} = n^2\tan\theta. \qquad (5)$$

Method I involves the experimental determination of the angle α_{cr}, at which the THz signal shifts to the opposite sign, and calculation of the angle θ.

Figure 3(a) shows experimental results: the dependence of THz pulse amplitude on the excitation angle. Most of THz pulses generated at various angles α_1 have two expressed extremes—peak and valley. The subtraction results between THz signal values in these extremes are displayed in blue dots. In the vicinity of α_{cr}, THz pulse is experiencing fundamental changes [Fig. 3(b)]; its complicated shape progressively changes from one polarity to another. Thus the points, where pulse polarity was not clear, were eliminated from Fig. 3(a), and linear approximation was used to determine α_{cr} value. Further, the angle θ was calculated using Eq. (5), and this value was inserted into Eq. (1); subsequently, the THz signal dependence on the incident angle α_1 was calculated [Fig. 3(a) gray dots].

As it will be shown below in this article, the recorded THz pulse results from the interference of two THz pulses of different origin and temporal shape. When the interference is constructive,

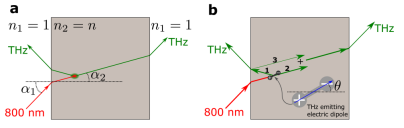

FIG. 2. The propagation of THz radiation after photoexcitation. (a) Propagation directions of optical and THz beams. (b) Formation of THz radiation in reflection and transmission directions according to the model represented in Ref. 20.

Published under license by AIP Publishing.

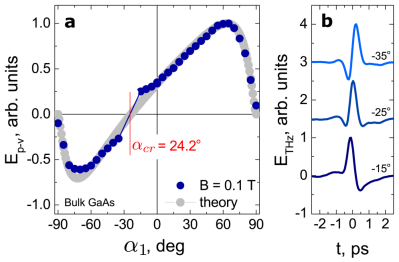

FIG. 3. (a) Dependence of THz pulse amplitude on the excitation angle. (b) THz pulse temporal shape at various excitation angles. Experimental results (represented in dots) show the THz pulse peak-to-valley amplitude and polarity. In the area $\alpha_1 \approx \alpha_{cr}$, a temporal shape of THz pulses changes drastically, so the values corresponding to their amplitudes are difficult to define. Theoretical curve was calculated by Eq. (1) using the electric dipole tilt angle θ that was calculated by (5) upon experimental determination of the angle α_{cr}.

the difference between these pulses does not play an important role and Eq. (1) accurately describes the dependence of the THz pulse amplitude on the angle of excitation. However, the last-mentioned pulses are of similar amplitude in the vicinity of α_{cr} and their interference is destructive. In this case, the difference in temporal shapes of those pulses results in a nonvanishing THz signal that can be recorded, contrary to what might be expected from Eq. (1). During our investigation, the THz generation mechanisms and resulting temporal shapes were identified for both the interfering THz pulses. However, decomposing the THz pulse into individual components is not always successful, so it is important to know

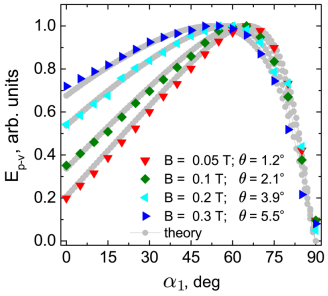

FIG. 4. THz pulse amplitude dependence on an excitation angle at various external magnetic fields.

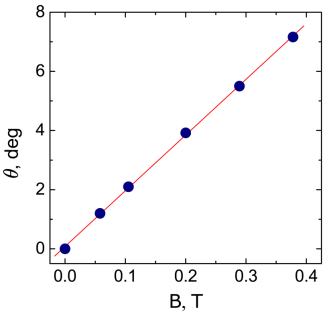

FIG. 5. THz radiating dipole tilt angle θ plotted as a function of the magnetic field.

whether the α_{cr} obtained from the procedure shown in Fig. 3 allows accurate determination of the electric dipole tilt angle θ.

During the investigation procedure, THz radiating dipole tilt angle θ was calculated from the α_{cr} value and later it was used in theoretical calculations of the dependence of THz pulse amplitude on the excitation angle. In order to compare these results with those achieved by Inoue *et al.*, the THz signal dependencies on the incident angle were displayed in the range of $0° < \alpha_1 < 90°$ (Fig. 4). As shown in Fig. 4, theoretical and experimental dependencies coincide quite well. This confirms that the α_{cr} determination procedure and further calculation of θ are appropriate.

In this study, the tilt angle θ determination procedure was repeated several times under a different magnetic field. The obtained tilt angles were plotted as a function of the magnetic field in Fig. 5. As shown in Fig. 5, the tilt angle is proportional to the magnetic field at least in the range of up to 0.4 T. Inoue *et al.*[16] also declared a linear relationship between the angle θ and the magnetic field; in the case of SI-GaAs, they found a proportionality constant equal to 10°/T. For comparison, the constant obtained by method I is higher and reaches 19°/T value. This mismatch and the unusual pulse alteration in the vicinity of α_{cr} [Fig. 3(b)] will be explained later in this work. Considering the $\theta(B)$ dependence, the article of Weiss *et al.*[23] should also be mentioned. In Ref. 23, the authors declared that the power enhancement caused by the magnetic field is proportional to the square of the applied field. This quadratic dependence correlates well with the linearity of $\theta(B)$.

IV. METHOD II: MEASUREMENT OF TWO THz PULSES IN THE REFLECTION GEOMETRY

During experiments with method II, THz radiation in the direction of reflection was measured. For this study, only the transparent for THz radiation and sufficiently thick samples could be used; for instance, standard high resistivity semiconductor substrates or

Published under license by AIP Publishing.

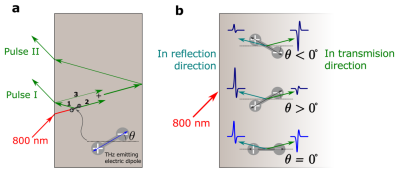

FIG. 6. (a) The illustration of THz pulse sequence formation in a semiconductor substrate. (b) The illustration of THz pulses emitted in transmission and reflection geometry at different electric dipole tilt angles.

epitaxial layers on top of them. For such samples, after the photoexcitation by the laser pulse, at least two THz pulses can be detected in the reflection direction. A THz wave emitted in the reflection direction forms pulse I (pulse I in Fig. 7), while the wave emitted in the transmission direction and reflected from the back surface of the sample is visible in pulse II [Fig. 6(a); pulse II in Fig. 7]. Keeping in mind the radiation pattern of the Hertzian dipole, it is obvious that the ratio between the electric field amplitudes of these two THz pulses strongly depends on the tilt angle of the dipole [Fig. 6(b)]. Estimating the reflection loss from the back surface of the sample, the ratio mentioned above could be calculated as follows:

$$\frac{E_{\mathrm{THz\_II}}}{E_{\mathrm{THz\_I}}} = \frac{-E_{td}(\alpha, \phi, \theta) r_{\mathrm{THz}}(\alpha_1) t_{\mathrm{THz}}(\alpha_1)}{E_{rd}(\alpha, \phi, \theta)}. \tag{6}$$

In Eq. (6), $E_{rd}(\alpha, \phi, \theta)$ refers to the amplitude of THz pulse emitted in the reflection direction (the transmission coefficient of the front interface is included), while $E_{td}(\alpha, \phi, \theta)$ is the amplitude

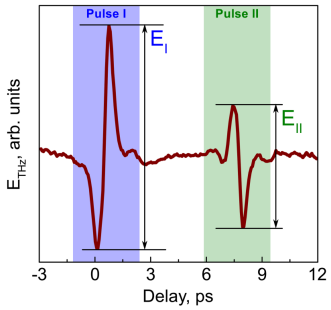

FIG. 7. Temporal shape of THz pulse detected in the reflection geometry.

of the THz pulse emitted in the transmission direction, respectively. $r_{\mathrm{THz}}(\alpha_1)$ and $t_{\mathrm{THz}}(\alpha_1)$ are the sample surface transmission and reflection coefficients for THz radiation. Expressions for $E_{td}(\alpha, \phi, \theta)$ and $r_{\mathrm{THz}}(\alpha_1)$ are described previously in Eqs. (4) and (7), while $E_{rd}(\alpha, \phi, \theta)$ and $t_{\mathrm{THz}}(\alpha_1)$ could be expressed as follows:

$$r_{\mathrm{THz}}(\alpha_1) = -\frac{\cos\alpha_2 - n\cos\alpha_1}{\cos\alpha_2 + n\cos\alpha_1} \tag{7}$$

and

$$E_{rd}(\alpha, \phi, \theta) = \frac{\sqrt{n\cos\alpha_1 \cos\alpha_2}(\cos\theta \sin\alpha_2 - \sin\theta \cos\alpha_2 \cos\phi)}{\cos\alpha_2 + n\cos\alpha_1}. \tag{8}$$

Figure 8 presents theoretical results for $E_{\mathrm{THz\_II}}$ and $E_{\mathrm{THz\_I}}$ and the ratios of the dependence of these amplitudes on the angle θ. Additionally, in Fig. 9, experimental results demonstrating the dependence of the aforementioned parameters on a magnetic field are shown. Figure 9 represents the ratio of the second and first THz pulse amplitudes for the GaAs sample measured at different magnetic field strengths, as well as the dependence of E_{II}/E_I. It is obvious that the theory poorly describes experimental results, when E_{II}/E_I approaches 0. It is not difficult to conclude that the sample is then activated at an angle of incidence close to α_{cr}, using the terminology described in method I. It also could be seen that the changing magnetic field strength affects the temporal shape of measured THz pulses, especially for the second pulse [Fig. 10(a)]. This change stimulates deeper analysis of THz radiation generation processes under the influence of the external magnetic field.

After the photoexcitation with a laser pulse, electrons move in the direction perpendicular (statistically) to the surface in the field of a depletion layer. The Lorentz force causes the appearance of a parallel to the sample surface component of electron motion, and it can be interpreted as a tilt of the perpendicular to the sample surface electric dipole.[24] However, such an image is not precise in

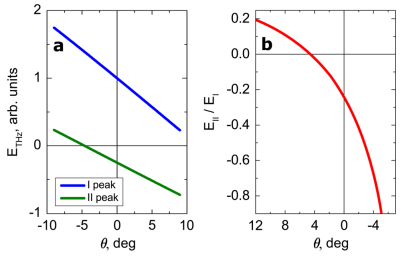

FIG. 8. (a) The THz pulse amplitudes of pulse I and pulse II and (b) their ratio dependence on the angle θ calculated by Eq. (6).

Published under license by AIP Publishing.

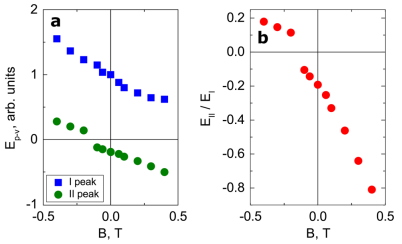

FIG. 9. Measurement of the first and second THz impulse amplitudes (a) and their ratio (b) dependence on the induction of the added magnetic field.

the case of THz pulses generation. It is important to note that the dynamics of the surface electric field and the Lorentz force are not alike, which results in two different temporal shapes of THz pulses originating from these two forces. This can be verified by subtracting the THz pulse measured without the magnetic field from the curves shown in Fig. 10(a). It is apparent that after elimination of the THz radiation determined by the electrostatic force, the temporal shape of THz pulse stays constant and the pulse amplitude becomes proportional to the magnetic field.

The results presented in Fig. 10(b) suggest that after the photoexcitation of the GaAs substrate in the external magnetic field, a THz emitting electric dipole of dual nature is formed. The electrostatic force determines the formation of a perpendicular to the surface electric dipole, while the Lorentz force determines the formation of the parallel one. These dipoles cause the emission of different temporally shaped THz pulses. In a THz detector, constructive or destructive interference of these pulses can occur depending on the values α_1 and B. In the case of constructive interference, the differences

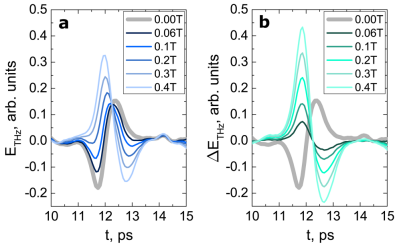

FIG. 10. Temporal shape of the second THz pulse measured at different magnetic field strengths: (a) as measured, (b) after subtraction of the reference pulse.

between THz pulses are not very important. Then, the total signal is well described by formulas (4) and (8) (Fig. 4). In the case of destructive interference, the signal amplitude decreases, and the temporal shape of THz pulse changes, but the signal does not disappear [Fig. 3(b)]. The destructive interference of two THz pulses explains the mismatch between the theoretical and experimental results obtained using method I in transmission (Fig. 3) and method II in reflection (Fig. 8) geometries. So, strictly speaking, the emission of THz radiation in a magnetic field should be described by the THz emission from two perpendicular to each other electric dipoles. However, the idea of a dipole tilted at the angle θ has proven to be workable and it is not necessary to abandon it. For the purpose of this work, it is continued with an assumption that $\tan\theta = p_x/p_y$, where p_x and p_y are the moments of a parallel and perpendicular to the surface electric dipoles, respectively.

The magnetic field changes the temporal shape of both pulses, $E_{\mathrm{THz\_I}}$ and $E_{\mathrm{THz\_II}}$. Pulses corresponding to these changes [Fig. 10(b)] were measured by varying the magnetic field from -0.4 to $+0.4$ T. Peak to valley values (ΔE_{p-v}) of these pulses are shown in Fig. 11(a). It contains the normalized ΔE_{p-v} values that are $\Delta E_{p-v}(B)/E_{p-v}(B=0)$, where $E_{p-v}(B=0)$ is the first or second pulse amplitudes measured without the magnetic field. In addition, Fig. 11 shows the curves, from Fig. 8(a), normalized in the same way. The experimental curves in Fig. 11 show only the influence of the parallel to the surface dipole, while the theoretical curves indicate the total operation of both dipoles, where the contribution of the perpendicular to the surface dipole is always equal to 1. By comparing the theoretical and experimental results of Fig. 11, the parameter $d\theta/dB$ can be determined. The value $20.5°/\mathrm{T}$ is obtained from the pulse I dependence on the magnetic field and it is in good agreement with the value obtained using method I. It should be noted that it is easy to separate the influence of the parallel to surface dipole induced by the magnetic field, while in other cases, it is usually impossible. In these cases, θ can be determined from Fig. 8(b) dependencies.

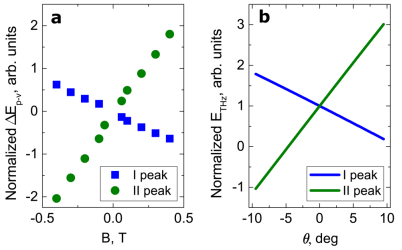

FIG. 11. (a) The magnetic field induced changes in THz pulses [see Fig. 10(b)] dependence on the magnetic induction. It is normalized to the amplitude of the THz pulse measured without the magnetic field. (b) THz pulse amplitude dependence on the dipole angle: the curves from Fig. 8(a) normalized to the corresponding $E_{\mathrm{THz}}(\theta = 0)$ values.

Published under license by AIP Publishing.

The value of parameter $d\theta/dB$, established in this work is approximately twice as high as that reported in the work of Inoue. Weiss *et al.* proposed in their work[23] that this parameter depends on the effective mass of the electron, but this does not explain why $d\theta/dB$ differs twofold in a GaAs substrate. However, based on a rather straightforward model, it is possible to explain which physical parameters determine the value of $d\theta/dB$ and predict it. Since most of the energy of THz radiation is emitted during the ballistic movement of electrons,[6,23] it is assumed that the electron motion is described by the equation of Paul Langevin.[24,26] In the case of weak magnetic fields, two equations can be written: for electrons moving perpendicular and parallel to the surface, where the forces responsible for the electron motion are eE and evB, respectively. The electric field of THz radiation near the detector is proportional to the current derivative, thus it is assumed that the THz pulse amplitude is proportional to the maximum electron acceleration or to the strongest force affecting electrons. Immediately after photoexcitation, the force acting in the direction perpendicular to the sample surface is the largest: $F_\perp = eE$. Meanwhile, the force acting in the parallel direction reaches its maximum later. The Lorentz force will gain its greatest value by settling electron drift velocity

$$v_\perp = \frac{eE\tau}{m}, \tag{9}$$

where τ is the electron momentum relaxation time.

Assuming that the maximum force operating in the direction parallel to the surface $F_\parallel$ is equal to the established Lorentz force, the following expression can be obtained:

$$\theta \approx \frac{F_\parallel}{F_\perp} \approx \frac{ev_\perp B}{eE} = \frac{e\tau B}{m}. \tag{10}$$

An analogous equation was obtained by Weiss *et al.*, where τ is referred to an average acceleration time without giving it any physical meaning. However, if τ is the electron momentum relaxation time, Eq. (10) could be simplified to $\theta = \mu B$ (μ is the electron mobility). Consequently, electron mobility, rather than electron effective mass, determines the value of parameter $d\theta/dB$. In this work, the electron mobility in the GaAs sample is $\approx 5000\ \mathrm{cm^2/V\,s}$; therefore, according to formula (10): $d\theta/dB = 28.7^\circ/\mathrm{T}$. Thus, Eq. (10) allows predicting the parameter $d\theta/dB$ with the accuracy of more than 30%.

In order to verify the relation $\theta = \mu B$, a few more semiconductor samples, possessing different mobilities, were investigated. The mobility values, obtained by the method introduced here, were compared with the ones obtained by other methods (optical pump terahertz probe and traditional Hall effect sensor). For all samples, the difference in the electron mobility values obtained by different methods did not exceed 33%. This accuracy is exceeding expectations, given that the above output is based on a very rough simplification of carrier dynamics. For example, the electric field at the semiconductor surface is considered to be constant. Meanwhile, spatial distribution of electrons and holes changes dramatically after photoexcitation, hereby, changes the distribution of the electric field. However, the simplified method explains the results quite well, as both forces, perpendicular to the surface electrostatic force and the parallel to the surface Lorenz force, depend on the strength of the surface electric field. Changes in the spatial distribution of charge carriers have a significant impact on F_E and F_L, but their ratio experiences only slight alterations. θ depends on the ratio of F_L and F_E, so the tilt angle of the dipole is hardly affected by the dynamics of the electric field on the semiconductor surface.

Returning to the $d\theta/dB$ value determination in this work and in the work of Inoue,[16] it can be stated that the difference in the obtained results is determined by different electron momentum relaxation times. The experiment in Ref. 16 was done under tight focus conditions; so a higher electron concentration could enhance electron scattering processes and could lead to lower τ and $d\theta/dB$. On the other hand, the specifications of the SI-GaAs substrate vary within a fairly wide range—τ in the SI-GaAs substrate may be different even under very low excitation conditions.

In this work, two methods to determine the angle θ were introduced and the performed experiments gave similar results. When these methods are compared, it is apparent that the $E_{\mathrm{THz}}(\alpha_1)$ measurement is more complicated. For example, the THz radiation transmission function begins to change when the laser beam diameter becomes comparable to the THz radiation wavelength. In addition, the aforementioned beam diameter depends on α_1, which results in drastically changing excitation conditions when α_1 approaches 90°. However, in certain cases, the $E_{\mathrm{THz}}(\alpha_1)$ measurement could be more informative than the measurement of two pulses. For instance, in the case of a very thin sample, method II is ineffective, because the pulses overlap in time. Another example—nanostructured semiconductor surfaces, in which θ often depends on the angle α_1. In this case, the measurement of $E_{\mathrm{THz}}(\alpha_1)$, together with the azimuthal dependencies $E_{\mathrm{THz}}(\phi)$, is the primary method for understanding the general picture of the THz emission characteristics of such a structure. As far as nanostructures are concerned, the determination of the angle α_{cr} is very important, since the dependencies of the optical radiation reflection and transmission functions on α_1 are generally not known; therefore, it is not possible to accurately describe the whole $E_{\mathrm{THz}}(\alpha_1)$ function. However, in most cases, method II is easier, faster, and more precisely described mathematically. In addition, it seems that it is suitable not only for the determination of angle θ. The statement that θ is proportional to μB, of course, still requires a detailed experimental check; nonetheless, if this proportionality would be proven, method II used together with an external magnetic field may become a promising tool for testing the quality of epitaxial layers. Using the fast delay line and the real time $E_{\mathrm{THz}}(t)$ analysis program, θ can be determined in seconds. This would make it possible to scan a two-inch sample in a few dozens of minutes. The 2D imaging of electron mobility can be particularly useful for new epitaxial growth techniques, when it is important to find optimum conditions for the production of layers of desired properties.

V. CONCLUSION

To sum up, two methods suitable for the determination of THz emitting electric dipole orientation have been presented. Method I is based on the measurement of THz emission

Published under license by AIP Publishing.

dependencies on the angle of incidence and determination of α_{cr}. The basis of method II is to measure THz emission in reflection geometry and determine the ratio between the second and the first THz pulses. Theoretical reasoning and calculations were also presented for both of these methods. Moreover, these methods were tested with the SI GaAs sample under an external magnetic field and gave very close $d\theta/dB$ values. In addition, the advantages and drawbacks of both of these methods have been discussed, and possible applications of each method have been suggested.

ACKNOWLEDGMENTS

The authors thank Dr. Irena Mirvienė for the improvement of the English language of the paper.

REFERENCES

[1]M. van Exter, C. Fattinger, and D. Grischkowsky, "Terahertz time-domain spectroscopy of water vapor," Opt. Lett. **14**, 1128 (1989).
[2]M. Tonouchi, "Cutting-edge terahertz technology," Nat. Photonics **1**, 97–105 (2007).
[3]M.-A. Brun, F. Formanek, A. Yasuda, M. Sekine, N. Ando, and Y. Eishii, "Terahertz imaging applied to cancer diagnosis," Phys. Med. Biol. **55**, 4615–4623 (2010).
[4]H. Tao, M. A. Brenckle, M. Yang, J. Zhang, M. Liu, S. M. Siebert, R. D. Averitt, M. S. Mannoor, M. C. McAlpine, J. A. Rogers, D. L. Kaplan, and F. G. Omenetto, "Food sensors: Silk-based conformal, adhesive, edible food sensors," Adv. Mater. **24**, 993 (2012).
[5]M. Picollo, K. Fukunaga, and J. Labaune, "Obtaining noninvasive stratigraphic details of panel paintings using terahertz time domain spectroscopy imaging system," J. Cult. Herit. **16**, 73–80 (2015).
[6]A. Urbanowicz, R. Adomavičius, A. Krotkus, and V. L. Malevich, "Electron dynamics in Ge crystals studied by terahertz emission from photoexcited surfaces," Semicond. Sci. Technol. **20**, 1010–1015 (2005).
[7]G. Molis, A. Krotkus, and V. Vaičaitis, "Intervalley separation in the conduction band of InGaAs measured by terahertz excitation spectroscopy," Appl. Phys. Lett. **94**, 091104 (2009).
[8]D. H. Auston, K. P. Cheung, and P. R. Smith, "Picosecond photoconducting hertzian dipoles," Appl. Phys. Lett. **45**, 284–286 (1984).
[9]X.-C. Zhang, B. B. Hu, J. T. Darrow, and D. H. Auston, "Generation of femtosecond electromagnetic pulses from semiconductor surfaces," Appl. Phys. Lett. **56**, 1011–1013 (1990).
[10]T. Dekorsy, H. Auer, H. J. Bakker, H. G. Roskos, and H. Kurz, "THz electromagnetic emission by coherent infrared-active phonons," Phys. Rev. B **53**, 4005–4014 (1996).
[11]N. Sarukura, H. Ohtake, S. Izumida, and Z. Liu, "High average-power THz radiation from femtosecond laser-irradiated InAs in a magnetic field and its elliptical polarization characteristics," J. Appl. Phys. **84**, 654–656 (1998).
[12]G. Klatt, F. Hilser, W. Qiao, M. Beck, R. Gebs, A. Bartels, K. Huska, U. Lemmer, G. Bastian, M. Johnston, M. Fischer, J. Faist, and T. Dekorsy, "Terahertz emission from lateral photo Dember currents," Opt. Express **18**, 4939 (2010).
[13]M. Reid, I. V. Cravetchi, and R. Fedosejevs, "Terahertz radiation and second-harmonic generation from InAs: Bulk versus surface electric-field-induced contributions," Phys. Rev. B **72**, 035201 (2005).
[14]V. L. Malevich, P. A. Ziaziulia, R. Adomavičius, A. Krotkus, and Y. V. Malevich, "Terahertz emission from cubic semiconductor induced by a transient anisotropic photocurrent," J. Appl. Phys. **112**, 073115 (2012).
[15]I. Beleckaitė, R. Adomavičius, R. Butkutė, V. Pačebutas, G. Molis, V. Bukauskas, A. Selskis, and A. Krotkus, "Non-stoichiometric GaAs—Prospective material for compact THz emitters," Electron. Lett. **52**, 1954–1956 (2016).
[16]R. Inoue, K. Takayama, and M. Tonouchi, "Angular dependence of terahertz emission from semiconductor surfaces photoexcited by femtosecond optical pulses," J. Opt. Soc. Am. B **26**, A14 (2009).
[17]X.-C. Zhang and D. H. Auston, "Optoelectronic measurement of semiconductor surfaces and interfaces with femtosecond optics," J. Appl. Phys. **71**, 326–338 (1992).
[18]L. Beleckaite, G. Molis, R. Adomavicius, A. Siusys, A. Reszka, A. Krotkus, and J. Sadowski, "Terahertz emission from non-vertically aligned semiconductor nanowires," in *2015 40th International Conference on Infrared, Millimeter, and Terahertz Waves (IRMMW-THz)* (IEEE Xplore® digital library, 2015).
[19]W. Lukosz and R. E. Kunz, "Light emission by magnetic and electric dipoles close to a plane dielectric interface II radiation patterns of perpendicular oriented dipoles," J. Opt. Soc. Am. **67**, 1615 (1977).
[20]W. Lukosz, "Light emission by magnetic and electric dipoles close to a plane dielectric interface III radiation patterns of dipoles with arbitrary orientation," J. Opt. Soc. Am. **69**, 1495 (1979).
[21]D. E. Aspnes, S. M. Kelso, R. A. Logan, and R. Bhat, "Optical properties of $Al_xGa_{1-x}As$," J. Appl. Phys. **60**, 754–767 (1986).
[22]N. Katzenellenbogen and D. Grischkowsky, "Electrical characterization to 4 THz of N- and P-type GaAs using THz time-domain spectroscopy," Appl. Phys. Lett. **61**, 840–842 (1992).
[23]C. Weiss, R. Wallenstein, and R. Beigang, "Magnetic-field-enhanced generation of terahertz radiation in semiconductor surfaces," Appl. Phys. Lett. **77**, 4160–4162 (2000).
[24]R. Grondin, P. Lugli, and D. Ferry, "Ballistic transport in semiconductors," IEEE Electron Device Lett. **3**, 373–375 (1982).
[25]M. B. Johnston, D. M. Whittaker, A. Corchia, A. G. Davies, and E. H. Linfield, "Simulation of terahertz generation at semiconductor surfaces," Phys. Rev. B **65**, 165301 (2002).
[26]C. Williams, T. Glisson, M. Littlejohn, and J. Hauser, "Ballistic transport in GaAs," IEEE Electron Device Lett. **4**, 161–163 (1983).

Published under license by AIP Publishing.

Notes

Notes

Notes

Vilniaus universiteto leidykla
Saulėtekio al. 9, LT-10222 Vilnius
El. p. info@leidykla.vu.lt,
www.leidykla.vu.lt
Tiražas 20 egz.